Characterization and Investigation of Large-Area, Ultra-Thin Gravure Printed Layers

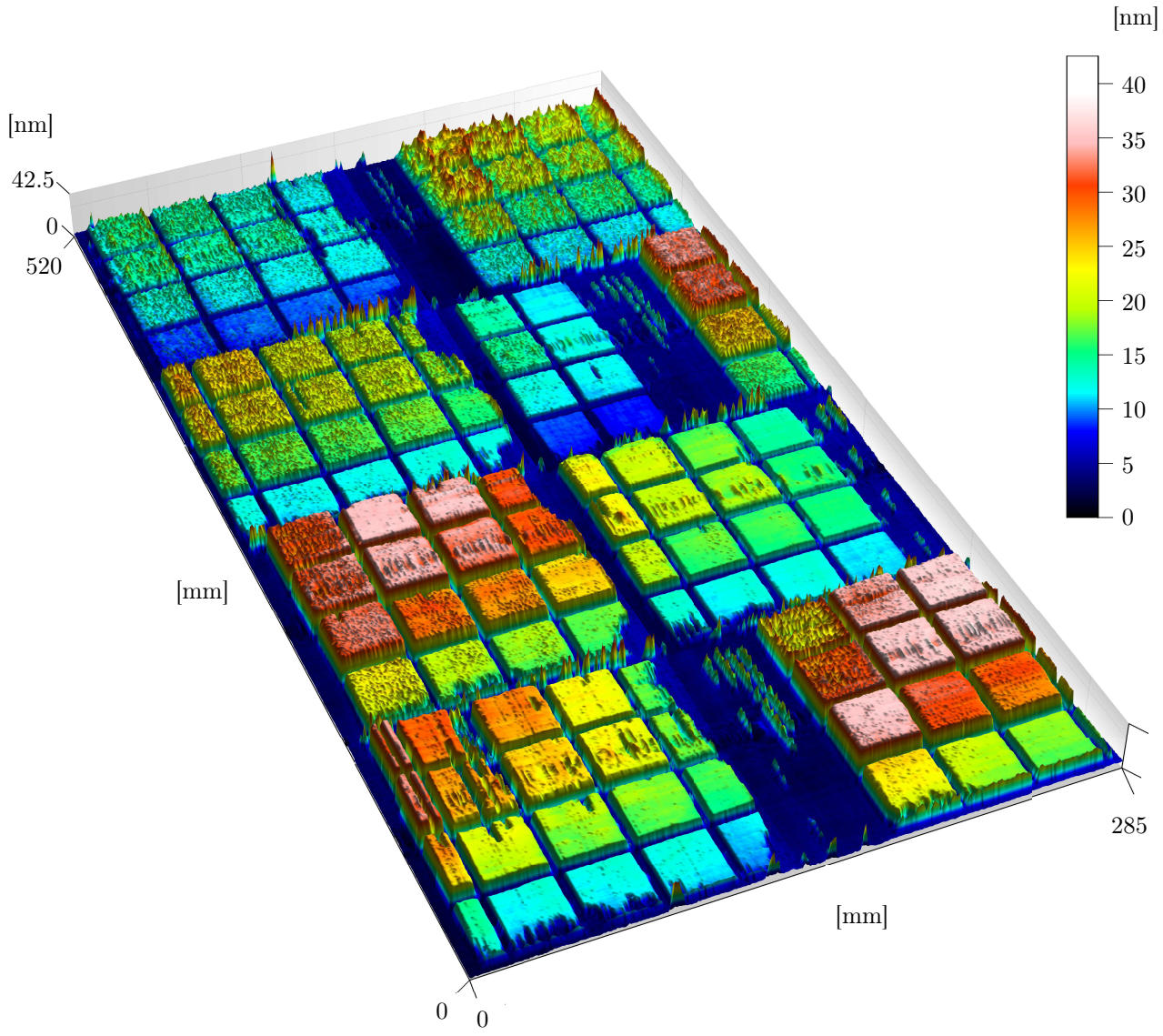

Nils Bornemann

Characterization and Investigation of Large-Area, Ultra-Thin Gravure Printed Layers

Beim Fachbereich Maschinenbau
an der Technischen Universität Darmstadt
zur
Erlangung des akademischen Grades
Doktor-Ingenieur (Dr.-Ing.)
genehmigte

DISSERTATION

vorgelegt von
Dipl.-Phys. Nils Bornemann
aus Celle

Berichterstatter:	Prof. Dr.-Ing. Edgar Dörsam, TU Darmstadt
Mitberichterstatter:	Prof. Dr.-Ing. Cameron Tropea, TU Darmstadt
Mitberichterstatter:	Prof. Dr. rer. nat. Uli Lemmer, Karlsruher Institut für Technologie

Datum der Einreichung:	21.08.2013
Datum der mündlichen Prüfung:	26.11.2013

Darmstadt, 2014
D17

Für Anni, Carla & Sarah

Acknowledgment

First of all I would like to thank Prof. Dörsam, who supervised and advised me the last 4 years and gave me a home for intense scientific work under best conditions. I thank the other members of the committee, Prof. Tropea and Prof. Lemmer, for spending so much of their valuable time. Without the staff, colleagues and friends from IDD, the present work would have been impossible, thank you all!

This thesis was supported by the German BMBF under grant number 13N10760 and 13N10759.

A special thanks goes to my parents, Ulrike and Werner, for their continuous support at any time.

Geliebte Sarah, ohne Deine stetige Unterstützung wäre nichts von dem hier möglich gewesen. Ich bin Dir für Deine nicht selbstverständliche Aufopferung zutiefst dankbar. Ich weiß, dass auch Dich die letzten Monate bis an die Grenzen Deiner Kräfte und darüber hinaus gebracht haben. Hiermit haben wir auch eine weitere Herausforderung in unserem gemeinsamen Leben gemeistert und wir können nun wieder Kraft sammeln für die nächste.

Kurzfassung

Das grafische Tiefdruckverfahren ist eine sehr zuverlässige Technologie, um kleinste Flüssigkeitsmengen in Form von Druckpunkten strukturiert auf ein Substrat zu übertragen. Dennoch stellt es eine erhebliche wissenschaftliche Herausforderung dar, dieses Druckverfahren für die Herstellung großflächiger, ultra dünner Schichten zu nutzen, wie sie z.B. in organischen Leuchtdioden (OLEDs) zum Einsatz kommen. Dies gilt nicht nur für die Drucktechnologie, sondern auch für die großflächige Messtechnik dieser Schichten.

Die Charakterisierung von sub-100 nm dünnen Schichten über die gesamte Druckfläche (∼DINA5) hinsichtlich ihrer Schichthomogenität ist eines der beiden Kernthemen der vorliegenden Arbeit. Durch die Ausnutzung der optischen Interferenz an dünnen Schichten wurde ein Verfahren erarbeitet, experimentell aufgebaut und erfolgreich an organischen Halbleitern evaluiert, das Schichtdicken von bis zu DINA5 großen Proben binnen Sekunden auf unter 5 nm genau bestimmt. Sowohl ein Mikroskop als auch ein modifizierter Flachbettscanner wurden verwendet, um herkömmliche $\mathcal{RGB}$-Bilddaten der Dünnschichtproben mit Hilfe eines weiterentwickelten physikalischen Modells, das in MATLAB implementiert wurde, auszuwerten. Das vorgestellte Verfahren bietet die Möglichkeit einer Inline Prozesskontrolle für die Herstellung großflächiger, ultra dünner Schichten.

Der zweite Schwerpunkt dieser Arbeit liegt in der Erarbeitung eines Modells, das es erlaubt, experimentell gefundene Prozessparameter für die erfolgreiche Verwendung des Tiefdruckverfahrens für die Herstellung ultra dünner Schichten aus niedrigviskosen Tinten auf Basis Kleiner Moleküle zu verifizieren. Dazu wurden Tiefdruckexperimente mit variierenden Prozessparametern auf je zwei hintereinander montierten 150×150 mm^2 großen ITO-beschichteten Glasscheiben durchgeführt, die einen Parameterraum von 128 verschiedenen gedruckten Feldern der Größe 30×30 mm^2 bilden. Die entwickelte Messtechnik ermöglichte es, alle sub-100 nm Schichten vollflächig hinsichtlich ihrer Schichtdicke zu charakterisieren (insgesamt ~ 1800 cm^2), um sie einer genauen, topographischen Analyse zu unterziehen. In dieser Analyse werden verschiedene Schichtparameter, darunter die Rauigkeit, die dominante laterale Wellenlänge, die Schiefe (Skewness) und die Kurtosis ausgewertet und mit fluiddynamischen Modellen des Druckprozesses und deren Auswirkungen auf die gedruckte Schicht verglichen. Für das Drucken homogener, ultra dünner Schichten lassen sich zwei Prozessfenster identifizieren, die auf Farbspaltungsmechanismen im Druckspalt −die Punkt- und die Filmspaltung−, die Nivellierung des flüssigen Films und die Trocknungszeit zurückzuführen sind.

Durch die Verknüpfung der beiden zugrunde liegenden Forschungsthemen werden erstmalig die in der Literatur und der vorliegenden Arbeit experimentell nachgewiesenen Prozessfenster für das erfolgreiche Herstellen ultra dünner Schichten mittels Tiefdruck theoretisch verifiziert.

Abstract

Graphical gravure printing is a very reliable process to transfer smallest amounts of fluid droplets to a substrate. Nevertheless, enabling this printing technique to produce large-area, ultra-thin layers for applications such as organic light emitting diodes (OLEDs) is a challenging task. This application not only imposes strong requirements on the printing technology but also on large-area measurement methods. Characterizing the homogeneity of sub-100 nm thin layers across the total printing area is one of the two central topics of the present investigation.

Utilizing optical interference from the thin film samples I developed and evaluated a method which successfully determined the thickness of thin, organic semiconductor layers with an accuracy better than 5 nm. Sample sizes of up to 150×150 mm^2 could be characterized within seconds using two hardware setups. I enabled a microscope and a modified flatbed scanner to acquire conventional $\mathcal{RGB}$-images of the thin film samples. These images were then compared to a corresponding physical model using MATLAB resulting in a laterally resolved thickness map. The method is predestinated for being part of an inline process control.

In the second part of the thesis, I deduced a physical understanding of gravure printing to produce ultra-thin, homogeneous layers from low viscous ink solutions which are based on small molecules dissolved in toluene. To this purpose, I processed on two consecutively mounted 150×150 mm^2 ITO-coated glass substrates with varying process parameters, resulting in a total number of 128 different gravure printed fields, each 30×30 mm^2 in size. Applying the large-area characterization method developed in the first part, I measured the thicknesses of all sub-100 nm printed layers (with a total area of ~ 1800 cm^2). This thickness data was analyzed regarding several surface parameters, such as roughness, dominant lateral wavelength, skewness and kurtosis. These surface parameters were referred to the physical models of fluid and thin film dynamics with respect to the underlying process parameters. As a consequence, two distinct process windows for the gravure printing process to produce homogeneous, ultra-thin layers were identified. The process windows were defined by two types of ink transfer mechanisms, namely single cell transfer and film splitting transfer, as well as appropriate film leveling and drying times.

The two process windows for producing homogeneous, ultra-thin layers using gravure printing have been reported in the literature and were demonstrated through the present experiments. By combining the two different topics, for the first time, these experimentally observed process windows were theoretically verified.

Contents

Chapter 1

Introduction

1.1 Motivation, objectives and methods

Electric lighting is one of the most important scientific achievements in daily life. The three main families of artificial electric light sources are incandescent light bulbs, electrical gas-discharge lamps and light emitting diodes (LEDs). Light bulbs are less efficient and possess shorter lifetimes compared to the other two and have therefore been partly taken off the market by the European Commission. Gas-discharge lamps and LEDs may have drawbacks regarding color spectrum, costs and illuminants design.

A fourth technology which is believed to play a major role in future lighting applications is based on organic light emitting diodes (OLEDs). They are already implemented in most premium cell phones as high brightness, low energy consuming displays. The OLED technology offers advantages regarding thin and low weight device structure possibly on flexible substrates, low production cost and efficient illumination for general lighting purposes [182]. However, the fabrication techniques that are used for OLED displays are based on expensive vacuum deposition methods and are not suitable to deliver cost-efficient OLED lighting panels.

There are basically two different types of organic semiconductors used for OLEDs: polymers with a molecular weight of > 10000 g/mol and small molecules with a molecular weight of < 10000 g/mol [216]. While only the small molecule semiconductors can be processed by vacuum deposition techniques, both types are also available as dilute solutions in organic solvents. This offers the possibility of low cost solution processing as an alternative method to produce most parts of an OLED. Especially conventional high-throughput printing technologies which were the foundation in delivering information in the 20th century could be utilized for OLED modules.

Three main technical and scientific challenges interfere this approach:

1. Over the past century, conventional mass printing technologies have been empirically developed and optimized. This has often led to a disregard of an exact physical understanding of the associated sub-process and has complicated the transfer of the printing methods to new fields of applications such as organic electronics.

2. According to the printing process itself, the demands that apply to the semiconducting organic layers are different and more strict than for graphical products. This is related to the cleanliness of the process, to the homogeneity and thickness of the layers and to the ink formulation.

Especially, the layer thicknesses for OLEDs which should be of the order of 100 nm are at least a factor of 20 smaller than for graphical applications.

3. Large-area thickness determination of the ultra-thin layers (below 100 nm) is very difficult to accomplish, and therefore process optimization and process control is hindered.

When considering a conventional mass printing method to produce large-area, organic, ultra-thin films for an OLED, I came to the conclusion that gravure printing is ideally suited for two main reasons. On the one hand, the range of solvents which are suitable for ink formulation is limited and those solvents are often chemically very aggressive. Compared with this, in gravure printing the ink only comes in contact with stainless steel which is chemically resistent against most solvents. On the other hand, the viscosity of the inks is usually very low, like water, especially when dissolving small molecule instead of polymer based materials. For that, gravure printing is the mass printing method most suited for very low viscosities [91, 136].

Several authors have shown that gravure printing is capable of producing ultra-thin semiconducting layers for OLEDs [102, 131, 140, 156], consistently using polymeric ink formulations. Only Hambsch et al. reported about gravure printed small molecule based semiconductor solutions without additives, not for OLEDs but for organic field-effect transistors (OFETs) [96]. To my knowledge regarding OLEDs, gravure printing has neither been utilized to produce small molecule semiconducting or emitting layers, nor has been investigated in detail for processing these low viscous (~ 1 mPa·s) inks for large-area electronic applications yet. Additionally to its low viscosity, the difficulty in printing small molecule solutions is the tendency of the wet printed film to dewet or evolve surface instabilities on a very short timescale after printed on the substrate [27]. These thin films with layer thicknesses of around 50 nm usually show dominant surface undulations in the millimeter range [27]. Understanding the origins of these pattern phenomenons is among other aspects a central part of the present work.

Guiding question. Within the context mentioned above, the main focus of the present thesis is addressed by the following guiding question:

- What are the "optimal" process parameters to produce defined, homogeneous, large-area and ultra-thin gravure printed layers using a low viscous ink formulation?

In particular this involves the following:

- analyzing results of ultra-thin printed layers,
- defining reproducible quality measures for printed semiconductor layers
- minimizing the quality measures according to a stable process window of the input parameters,
- applying a physical model to relate the stable process window to the minimized quality measures.

Methodology and approach. The approach to achieve the afore mentioned aspects was to define a suitable measurement method for large-area ultra-thin thickness determination first. Standard measurements techniques capable of measuring nanometer layers were limited to small areas while facing long acquisition times and high initial costs. I developed a large-area thickness measurement

method which resolved printed layers on sample size of up to 150×150 mm^2 with sub-5 nm vertical resolution within seconds of acquisition time.

Besides the root mean square roughness, I determined additional statistical and geometrical surface parameters. From preliminary printing experiments, I defined the input parameter space for the subsequent experiments. Applying the new measurement method to determine the complete, laterally resolved thickness maps of the printing results was followed by identifying the chosen set of surface parameters. The latter revealed distinct indicators for "optimal" layers and therefore "optimal" process parameters. I related the latter to physical models of surface instabilities and thin film dynamics and found strong correlating aspects. From this, I developed a process model within the set of parameters and found good agreement with results from previous studies with parameters outside the present range. This confirmed that the model is extendable.

1.2 Outline of the thesis

The thesis is organized as follows:

In Chapter 2, I develop a fast optical measurement method which is capable of quantifying layer thicknesses in the nanometer range on a large lateral scale. The physics of the underlying multi-layer thin film interference are introduced and a algorithm is developed. I present the type of thin film samples which were used for evaluating and validating the method and the resulting thickness maps I determined with the proposed method. The results obtained with a microscope and a modified, commercial scanner are compared. Additionally, I present a measurement of a structured sequentially processed double-layer thin film example shown as a "vertical stitched" 3D representation. Small errors to selected and motivated quantities are induced and the effect on the estimated thicknesses discussed. The chapter closes with an outlook of the method and its capability as an inline inspection system.

In Chapter 3, I divide gravure printing into sub-process classifying different fluid-dynamical regimes while referring to the literature. I introduce important fluid parameters followed by presenting the governing hydrodynamic equations and common models of printing nip instabilities and thin film dynamics. Results of preliminary printing experiments using color inks are presented which give important insights into the underlying ink transfer mechanisms.
In Chapter 4, I present direct gravure printing experiments of ultra-thin, small molecule based layers on glass with thicknesses in the range of 10 to 70 nm on a laboratory printing unit. I give details on the printing experiments and motivate and introduce the surface parameters used for the analysis. Potential driving mechanisms for the observed surface undulations are discussed. I conclude with a possible process window and compare it to results from the literature. The chapter closes with the outlook.
The thesis closes with the conclusion in Chapter 5.

Chapter 2

Imaging color reflectometry: A fast method for large-area thin film metrology

Abstract

Imaging and measuring solution-processed, large-area, ultra-thin layers for various applications is often a challenging task. Measurement techniques for thickness determination are usually limited to small areas while facing long acquisition times and high initial costs. In this chapter, I introduce a fast measurement method which is capable of quantifying layer thicknesses in the nanometer range on a large lateral scale using standard optical hardware setups. The measurement principle is based on optical interference effects which occur at interfaces of semi-transparent thin film stacks according to its film thicknesses and refractive indices. I enabled an optical microscope and a modified flatbed scanner to acquire red-green-blue ($\mathcal{RGB}$) images of the sample. Comparing contrast values and implementing a theoretical optical model, I estimated the most probable thickness for each pixel to obtain an overall thickness map of the top layer of a thin film stack. The proposed method is evaluated and validated by analyzing and comparing thicknesses of different test samples to the ones determined by reference methods. A detailed sensitivity analysis related to selected variables was performed revealing the predominant perturbation terms. Since I use standard hardware components and a simple optical setup this technique could be a powerful and easily applicable method for large-area inline inspection of ultra-thin layers produced by printing processes in general. The proposed measurement method was intensively used for inspecting and analyzing layer thickness and film quality of printing results in Chapter 4.

Parts of this work were published in *Optics Express* vol. 21, issue 19 with:
Bornemann, N., and Dörsam E. "A flatbed scanner for large-area thickness determination of ultra-thin layers in printed electronics",

and have been applied for a German patent:
Bornemann, N., et al. "Verfahren zur Messung einer Schichtdicke". German Patent Application number (DRN) 2013071815340800DE. July 18, 2013.

2.1 Introduction

The quality of printed products is essentially determined by the physics of ink deposition in the printing press. This is commonly rated by the printer, or by a camera-based optical inspection system in terms of visual perception. For adapting printing techniques to the field of large-area organic electronics requiring sub-100 nm thick layers, conventional visual criteria are usually not applicable. Therefore, I encounter a deficiency of a corresponding fast and reliable method for layer inspection.

Concerning for example organic light emitting diodes (OLED), not only the ultra-thin functional layers are transparent, but also the substrates made of glass or polymer foils. Printing results using low viscous inks for such applications might exhibit strong layer undulations [27]. This requires an inspection method which not only detects the thickness but also quantifies the undulations on top of the thin film in the sub-10 nanometer range.

In the following, I briefly discuss several possible methods for quantifying surface or thickness undulations under the above-mentioned conditions.

Layer qualities might be indirectly evaluated from the electrical or optical characteristics of the completed device [251], but this is not always practical. There are different direct measurement principles for determining thicknesses of organic ultra-thin layers.

Principally, we can divide the measuring techniques by two categories, a destructive and a non-destructive one. This implies that the sample either cannot or can be further processed after inspection. With no claim to completeness, I list measurement techniques which can be potentially applied to large-area thin films in the following.

X-ray and electron-beam based thin film characterization techniques belong to the category of destructive methods. The exposure to such high-energy radiation usually degrades organic layers. X-ray photoelectron spectroscopy (XPS) for thickness determination destroys the sample by successive sputtering [268], whereas transmission electron microscopy (TEM) requires usually not only an additional thin metal layer but also an edge or a layer step to determine the layer thickness [224]. For large films, the latter is provided by breaking the sample or scratching the thin film. The same conditions have to be established when using contact-based methods such as tactile profilometry with a stylus or atomic force microscopy (AFM) [21]. Both are less destructive than the two principles mentioned before. Nevertheless, AFM is inappropriate for measuring large-areas because the maximum lateral range is usually below 1 mm^2 [205] and tactile profilometry would have inadequate measurement times for sample area in the square-centimeter regime.

The second category of non-destructive methods mainly consists of optical characterization techniques. Here, different measuring principles can be identified. Optical profiling techniques which reconstruct the topography of the top surface such as confocal microscopy, white-light and phase-shifting interferometry (as described in Appendix A) require layer steps to determine film thicknesses and have drawbacks in measurement times for large-areas [17, 154]. Digital holographic microscopy (DHM) also is a powerful tool which successfully resolves ultra-thin layers in the nanometer range [128, 134, 154, 170]. Its variable depth-of-focus and short measurements times predestinate the method for robust inline measurements [74, 198] and large-area characterization. To my knowledge, large-area thin film characterization using DHM has not been investigated yet and remains a challenging task. It will therefore not be further discussed here.

Basically, there are two optical methods which are capable of in-depth thin film thickness measurements not requiring layer steps or edges. Ellipsometry and spectroscopic reflectometry analyze

the change of light properties after being reflected from the layer stack [45, 106]. This change is based on reflections from external and internal interfaces of semi-transparent thin films on a substrate and strongly depends on layer thicknesses and refractive indices. The lateral resolution is usually limited to a single millimeter-sized pixel or spot and therefore the characterization of large-areas is based on scanning the sample laterally resulting in long measurement times. The latter does not restrict imaging ellipsometry which is only limited by the resolution of the digital camera and the optical setup [9, 270]. Both methods could be applied to large-areas but mainly with stitching techniques and with a complex and cost-intensive setup.

Concerning spectroscopic reflectometry of ultra-thin films using a white-light source, reflections from different interfaces of the sample generate destructive or constructive optical interference of specific wavelengths at the detector. Usually, the detector is a spectrometer which is made of a grating and a photodiode array to split the light into spectral bands of 1 nm width and to measure the resulting spectral irradiance on each pixel separately. From the resulting spectral power distribution (SPD) or spectrum of the reflected light and prior knowledge of the refractive indices (real as well as imaginary values) the layer thicknesses can be reconstructed with resolution of down to ± 1 nm [106]. Replacing the spectrometer with an imaging $\mathcal{RGB}$ camera simplifies the setup and allows for laterally resolved thickness reconstruction.

Different authors have implemented this approach for analyzing several kinds of thin films. For example, Larson et al. [153] and Barth et al. [153] have applied this method to measure thicknesses of oxide layers on metals and silicon wafers. Roddaro, Chen, Jung and their co-authors used this method, which I term *imaging color reflectometry* (ICR) from now on, for quantifying the number of atomic mono-layers of graphene coatings [41, 123, 215]. However, these setups were limited to small sample areas.

Common substrate sizes of OLED panels in laboratory, advanced development and the present study are 30×30 mm^2 and above. Using stitching techniques of separately acquired pictures, optical bright field microscopes are capable of imaging such sample sizes within seconds or minutes. I therefore successfully adapted the concept of imaging color reflectometry to a microscope and additionally to a modified flatbed scanner. Besides scanning documents, the latter proved to be a useful device for different types of measurements from biological applications to the characterization of optical components [119, 138, 145, 175, 236, 265].

For the different hardware setups, I ensured approximately common normal optical paths of illumination and image detection of measurements on thin films. I spectrally characterized all components according to their optical response and implemented an algorithm that compared theoretical values to measured ones. Within specific limitations I was able to reconstruct laterally resolved thickness maps of large-area thin film samples.

This chapter is organized as follows. In Section 2.2, I describe the measurement principle in detail and formulate the underlying optical model. The physics of multi-layer thin film interference is introduced and integrated in the model. Additionally, the estimation algorithm is described at the end of this section.

Section 2.3 introduces the different hardware setups which were adopted and the characterization of their optical properties resulting in the optical spectral transfer functions of the setups.

Summarizing and incorporating the previous sections, a flow chart of the complete measurement procedure is presented in Section 2.4.

In Section 2.5, I present the type of thin film samples which were used for evaluating and validating the method and the resulting thickness maps I determined with the proposed method. The results obtained with the microscope and the scanner are compared. Additionally, I present a measurement of a structured sequentially processed double-layer thin film example shown as a "vertical stitched" 3D representation.

Section 2.6 addresses the effects on the resulting thickness map of inducing small errors to selected and motivated quantities. The physical model is extended with the polarization of light to account for opening angles of the optical system. Additionally, measurements with the microscope using different objectives are compared.

In Section 2.7, I summarize the investigation of the method and draw concluding remarks.

Section 2.8 closes with an outlook and presents possible improvements of the method and its capability as an inline inspection system.

2.2 Measurement principle

The following simple example explains the basic idea of the measurement principle. Figure 2.1a shows an original photograph of a printed glass substrate with an ultra-thin (< 100 nm) organic layer positioned on a laboratory table. There is a barely visible layer on the substrate and this impression would be identical if we observed the sample under normal conditions by eye. But when we set the observing angle of the camera to be equal to the incident angle of the illumination (here to the fluorescent bulbs at the ceiling) we suddenly observe dominant color differences as depicted in Figure 2.1b. The strong appearance of these colors is based on optical interference originating

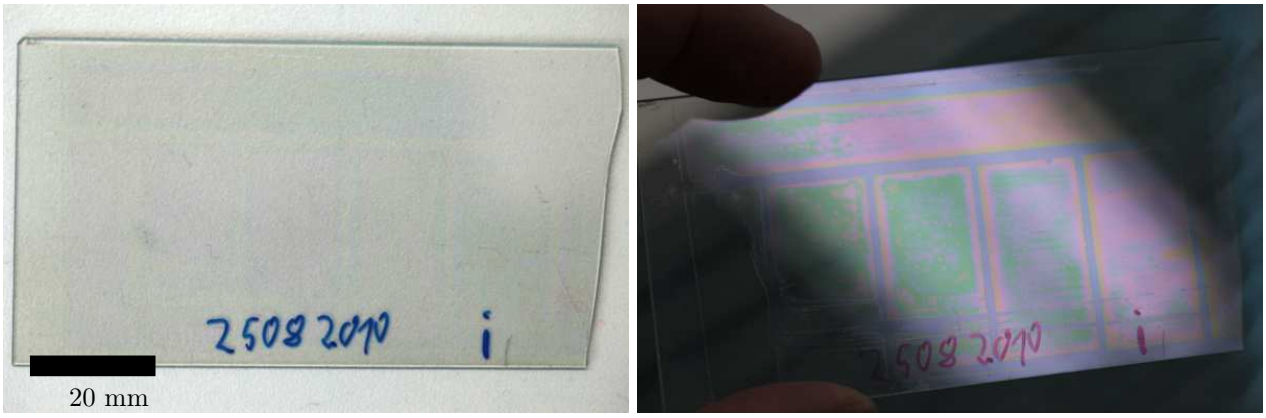

(a) **(b)**

Figure 2.1: Photographs of a printed glass substrate with an ultra-thin (< 100 nm) organic layer placed on a laboratory table (a) and positioned to image with an observing angle of the camera equal to the incident angle of the illumination (b).

from the interfaces of the thin film and the substrate. This is the main physical effect underlying the present method. Optical thin film interference is a phenomenon utilized in, for example, antireflection coatings of eyeglasses or in effect pigments. It appears in daily life for example as the origin of the striking colors of butterflies and of the rainbow colors of soap bubbles. Max Born introduced a consistent formula based on the Maxwell equations for single layer systems in 1932 [23].

The basic concept of the thickness measurement method is to compare the $\mathcal{RGB}$ color values of an image of a thin film sample to values predicted by a theoretical physical model. I describe the

equivalent optical model of the experimental setup first, followed by the physics of optical thin film interference on page 21 and the algorithm for the thickness reconstruction on page 25. The basic optical setup of the measurement principle is illustrated in Figure 2.2. In the following, the light propagation is described by focusing on the spectral power distributions (dimensionless quantities) rather than on radiometric quantities such as radiance, irradiance or exitance.

A white-light source emits a spectrum, which is denoted with $L(\lambda)$ depending on the wavelength λ,

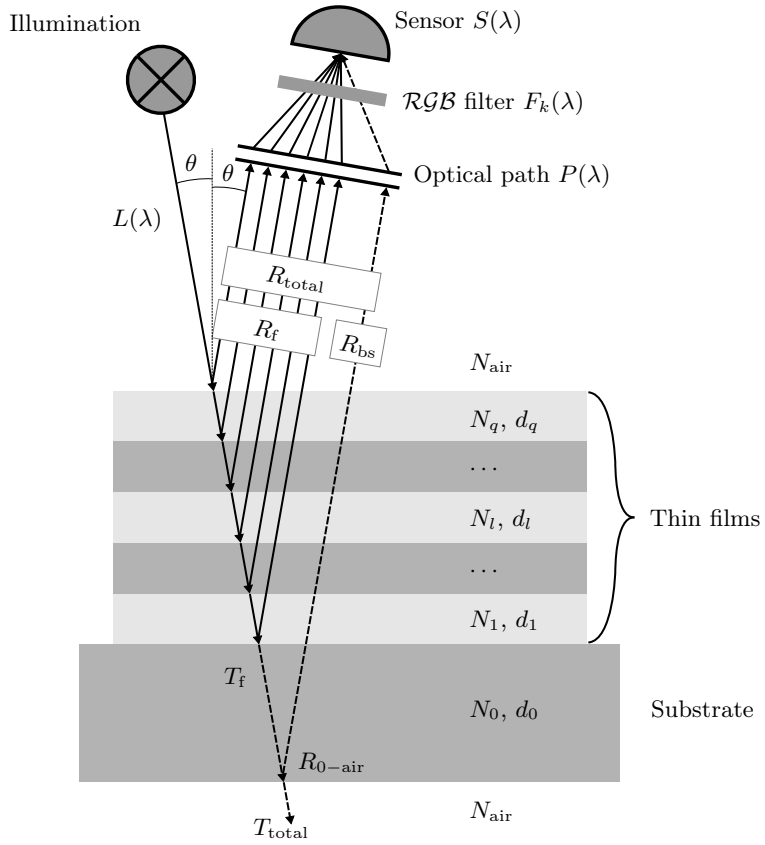

Figure 2.2: Basic optical setup of the measuring principle including quantities such as the angle of incidence and reflection θ, the spectrum of the light source $L(\lambda)$, transmittances of $T_{\text{f}}(\lambda)$, the optical path $P(\lambda)$, the color filters $F_k(\lambda)$, the optoelectronic transfer function of the sensor $S(\lambda)$, the reflectances $R_{\text{total}}(\lambda)$, $R_{\text{bs}}(\lambda)$, $R_{\text{f}}(\lambda)$, $R_{0-\text{air}}(\lambda)$, the complex refractive indices $N_l(\lambda)$ and the layer thicknesses d_l of the sample.

and illuminates the sample with its incident angle θ. According to the thicknesses d_l and refractive indices N_l of the $l = 0, \ldots, q$ different materials of the sample, a characteristic spectrum is reflected with the same angle θ (incident angle equals reflected angle) back from the sample. The latter is defined by its spectral reflectance R_{total}. For transparent substrates, I distinguish between two contributions to the total reflectance: on the one hand, the reflectance R_{f} originating from the thin films on top of the substrate material which cause the dominant colors, and on the other hand, the reflectance R_{bs} resulting from the backside of the substrate. The reflected light propagates through the lenses and objectives of the optical unit whose spectral transmittances are summarized by $P(\lambda)$. Then, the light passes through the three $\mathcal{RGB}$ filters in front of the corresponding sensor pixels which are characterized by the transmittances $F_k(\lambda)$, $(k = \mathcal{R})$ for red, $(k = \mathcal{G})$ for green and $(k = \mathcal{B})$ for blue. Finally, electronic signals are generated in the camera sensor which are described by the linear optoelectronic transfer function $S(\lambda)$.

2.2.1 Camera model

In an operating image sensor, photons are passing to the pixel area of the camera sensor during the exposure time. A number of electrons is generated in the photo sensitive semiconductor which causes a charge flow. The charge is converted by a capacitor to a voltage which is amplified by an electronic circuit. This analogue voltage is converted to a digital, discrete value per color channel and pixel.

Assuming a linear response of the sensor implies that the electronic signal or number of electrons is proportional to the number of photons reaching the sensor, i.e. doubling the number of photons causes twice the number of electronic charges in the detector. This assumption is justified if the sensor is not saturated with photons and the intensity causes a photo current that exceeds the dark current generated from fluctuations within the photo detector of the camera. By adjusting the exposure time, which defines the temporal window in which the sensor detects photons, and the total spectral power of the light source, one can usually ensure operation within this linear window of the sensor.

Laterally resolved imaging is commonly performed by either complementary metal oxide semiconductor (CMOS) or charge-coupled device (CCD) sensors. Details on the properties and architectures of the different types of sensor chips can be found in [20, 33, 64, 167].

Although CMOS and CCD sensors are linear devices according to their optoelectronic transfer function, they possess different sensitivities for photons with different energies or wavelengths. The quantum efficiency $S_{\mathrm{QE}}(\lambda)$, which is defined as the ratio of the number of electrical charges generated in the sensor and the number of photons that shine on the sensor, describes the spectral sensitivity of the device. Because the actual sensitivity curves of the sensors used in the present study were not available, the monochrome[1] KAF-8300 CCD and KAC-00401 CMOS chips from Truesense Imaging, Inc., USA, serve as examples to illustrate this non-constant behavior in Figure 2.3, re-plotted from [40, 44]. Within the regime of linear response of the sensors to photon detection, the quantum

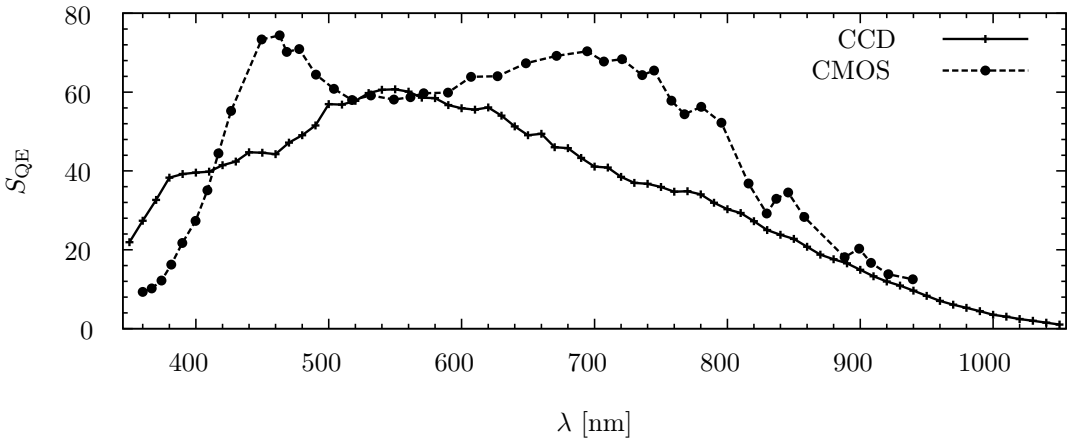

Figure 2.3: Comparison of the quantum efficiency S_{QE} of typical monochrome CCD (Truesense Imaging KAF-8300) and CMOS (Truesense Imaging KAC-00401) camera sensors, re-plotted from [40, 44].

efficiency is equal to the optoelectronic transfer function

$$S(\lambda) = S_{\mathrm{QE}}(\lambda). \tag{2.1}$$

Each image which is generated by a sensor is afflicted by different types of noises. These mainly originate from three sources. The *shot noise* affected by the statistical fluctuations of photons and

[1] i.e. no color filters in front of the sensor

predominantly of electrons in the photo semiconductor. The electronic circuit can be attributed a *readout noise* with contributions from various electronic parts. The third main source for noise in the image is the *quantization noise* originating from the conversion of the analogue continuous signals to quantized digital ones. More sophisticated sensor models could include far more noise sources [31, 98, 117]. Aside from the importance of noise treatment for a specific camera, I neglect noise sources of the optoelectronic system to keep the complexity of the over-all physical model reduced. Nevertheless, in Section 2.6, I analyze the propagation of small variations of selected quantities including the $\mathcal{RGB}$ signals from the sensor to the resulting thickness estimation.

Imaging color sensors possess three different kind of filters F_k in front of an usually even number of square ordered pixels in a block. The distribution for which a color filter appears within a block varies according to the type of filter arrangement [163]. A single block represents a single effective lateral pixel with its three colors as additional attribute. The effective lateral pixel position within the sensor array is denoted with $i \times j$ (short ij) ranging from 0 to i_m and 0 to j_m, respectively. Adding the dimension of the three colors, the effective dimension of the resulting image is $(i_\mathrm{m}+1) \times (j_\mathrm{m}+1) \times 3$, whereas $(i_\mathrm{m}+1) \times (j_\mathrm{m}+1)$ is often referred to as image pixel resolution.

The conversion from the analogue, amplified voltage to the digital value is usually performed with a resolution of 8-bit or 16-bit (2^8 or 2^{16} values) per pixel and channel ranging between 0 and $2^8 - 1 = 255$ or 0 and $2^{16} - 1 = 65535$, respectively.[2] The latter upper limit per channel is termed as O_max from now on. The full range of all channels is often denoted as color depth Cd, thus $\mathrm{Cd} = 3(O_\mathrm{max}+1)$ equals 24-bit or 48-bit. Depending on the type of sensor model, the settings for the color depth can be also controlled by the image acquisition software. Throughout the thesis, I used a color depth of 24-bit, hence $O_\mathrm{max} = 255$.

Color line sensors which are often used in scanning devices such as flatbed scanners or inline inspections systems in industrial roll-to-roll printing machines exhibit a high pixel resolution in direction of the substrate width (denoted with $i_\mathrm{m}+1$) but a low number of pixels in moving direction (here $j_\mathrm{m}+1$, at least 3 for the three $\mathcal{RGB}$ color channels). The image pixel resolution in printing direction is defined by the scan length and is usually matched to the other one accomplishing pixel aspect ratios[3] of 1. Therefore, the resulting image resolution is dependent on the distance which is actually scanned.

2.2.2 System model

In real hardware setups, the quantities $S_\mathrm{QE}(\lambda)$, $F_k(\lambda)$ and $P(\lambda)$ can not be determined separately[4] because the sensor, the color filters and the optical path are usually mounted in a single fixed optical unit. Therefore, I define the combined optoelectronic transfer filter function $U_k(\lambda)$ per color channel as

$$U_k(\lambda) \equiv S_\mathrm{QE}(\lambda) \cdot F_k(\lambda) \cdot P(\lambda) \tag{2.2}$$

Thus, I arrive at a theoretical description for the optical setup shown in Figure 2.2 from which the total optoelectronic response O_k^{ij} at pixel position ij is modeled within the visible spectrum from λ_min to λ_max with

$$O_k^{ij}(N_l, d_l^{ij}) \equiv K^{ij} \cdot \int_{\lambda_\mathrm{min}}^{\lambda_\mathrm{max}} U_k(\lambda) \cdot R_\mathrm{total}(\lambda, N_l, d_l^{ij}) \cdot L(\lambda)\ \mathrm{d}\lambda. \tag{2.3}$$

[2] bit: binary digit

[3] ratio of the lateral side lengths per pixel

[4] unless determined and provided by the different manufacturers

Here, d_l^{ij} represents the thicknesses of the thin films ($l = 1, \ldots, q$) including the substrate ($l = 0$) of the region on the sample that is projected onto pixel ij of the sensor. K^{ij} serves as a normalization and calibration constant for different purposes of reducing the formula to governing quantities. By using contrast values, as shown in Section 2.2.4, the constant K^{ij} is canceled under certain assumptions. To motivate the latter, I separate K^{ij} into a product of a scalar value K_0 and a pixel-dependent constant K_1^{ij}

$$K^{ij} \equiv K_0 \cdot K_1^{ij}. \tag{2.4}$$

K_0 ensures that O_k^{ij} is dimensionless and normalized either to the range $[0, 1]$ or, if matched to the color depth Cd of the sensor (usually 24-bit), to the range $[0, O_{\max}]$ per channel. Additionally, K_0 could be assigned proportionality to exposure time and image gain originating from camera settings and the size of the active surface area of the pixels. On the other hand, K_1^{ij} could represent lateral variations of the light intensity resulting from distortions of optical elements such as lenses and from heterogeneous illumination. Furthermore, the sensitivities of pixels could vary across the sensor which can also be described by this constant. The variations mentioned before should be almost constant in time compared to typical measurement times (in the range of seconds to minutes).

In summary, the constant K^{ij} illustrates the main difficulty in formulating an exact theoretical model that predicts the absolute $\mathcal{RGB}$ values of an image acquired by a defined hardware system. However, analyzing contrast values instead, as discussed in Section 2.2.4, provides the possibility to neglect the absolute values of K^{ij}. Therefore, I define the quantity

$$o_k^{ij}(d_l^{ij}) \equiv \int_{\lambda_{\min}}^{\lambda_{\max}} U_k(\lambda) \cdot R_{\text{total}}(\lambda, N_l, d_l^{ij}) \cdot L(\lambda)\, \mathrm{d}\lambda, \tag{2.5}$$

which is basically Equation 2.3 for $K^{ij} \stackrel{!}{=} 1$. The bounds of integration in Equation 2.3 and 2.5 to the visible spectrum ($\lambda_{\min} = 380$ nm to $\lambda_{\max} = 780$ nm) is justified because either the spectrum of the light source or the transmittances of the $\mathcal{RGB}$ filters vanish outside this range. In anticipation of the characterization of the optical components presented in Section 2.3, the spectra and the transmittances of the two underlying hardware setups depicted in Figure 2.5, 2.7 on page 28 and Figure 2.10, 2.11 on page 32 confirm this assumption.

Since the quantity of interest is the thickness distribution d_q^{ij} of the top layer, I assume that all refractive indices N_l and the thicknesses $d_{l=1,\ldots,q-1}^{ij}$ of the layers below as well as all spectral quantities defining the light source and the optical unit are determined in advance (using the measurement techniques discussed in Section 2.3 or provided by the manufacturer).

Simplifying the dependency to the thickness of the top layer d_q^{ij} results in the following total optoelectronic response function for the present system

$$O_k^{ij}(d_q^{ij}) = K^{ij} \cdot \int_{\lambda_{\min}}^{\lambda_{\max}} U_k(\lambda) \cdot R_{\text{total}}(\lambda, d_q^{ij}) \cdot L(\lambda)\, \mathrm{d}\lambda = K^{ij} \cdot o_k^{ij}(d_q^{ij}). \tag{2.6}$$

In the following paragraph, I review the underlying physical model of optical thin film interference to find a theoretical formulation for total reflectance $R_{\text{total}}(\lambda, N_l, d_l^{ij})$.

2.2.3 Thin film interference

The Maxwell equations describe the physics of electromagnetic interactions and allow to derive a differential wave equation for the propagation of light [23, 176]. A possible solution of this equation

is a harmonic, planar wave propagating in z-direction and in time t with an amplitude A proportional to

$$A(z,t) \propto e^{\mathrm{i}(\omega t - \frac{2\pi n}{\lambda} z + \Phi^\circ)} \cdot e^{-\frac{2\pi\kappa}{\lambda} z} = e^{\mathrm{i}\Phi} \cdot e^{-\beta z/2}, \tag{2.7}$$

where λ is the wavelength, $\omega = 2\pi c/(n\lambda)$ the angular frequency with c as the speed of light in vacuum, Φ° a static phase offset, $\Phi = (\omega t - 2\pi n z/\lambda + \Phi^\circ)$ the total phase and β the absorption coefficient. Neglecting scattering effects, the latter defines the exponential decay[5] of the amplitude when propagating a distance in z-direction through a medium. The absorption coefficient is defined as $\beta = 4\pi\kappa/\lambda$. The parameters n and κ define the complex (i as the imaginary unit) refractive index N of the surrounding medium, which also depends on the wavelength, as follows

$$N(\lambda) = n(\lambda) - \mathrm{i}\kappa(\lambda). \tag{2.8}$$

Important for the resulting reflectance of a thin film sample is the fact that amplitudes of electromagnetic waves can be combined by superposition, for example $A = A_1 + A_2$. A photo-sensor is able to detect only an irradiance[6] I which is proportional to the square of the superposition of all amplitudes. Assuming equal wavelengths and amplitudes of the two waves, the resulting spectral irradiance at the photo-detector is alternating according to the phase difference as follows

$$I \propto |A|^2 = |A_1 + A_2|^2 \propto \cos^2\left(\frac{\Phi_1 - \Phi_2}{2}\right) = \cos^2\left(\frac{\Phi_1^\circ - \Phi_2^\circ}{2}\right). \tag{2.9}$$

This allows light to show constructive or destructive interference at the detector depending on the relative (static) phase difference of the two waves. In contrast to the illustration of the angle of incidence θ of light in Figure 2.2, I assume normally oriented incidence and detection to the sample surface in the system model ($\theta = 0\,^\circ$). This is motivated for two reasons. First, for normal incidence, I can omit to treat the light according to its different polarization states.[7] This simplifies the algorithm and allows to use a light source of undefined polarization state. Second, the hardware setups exhibit almost normal configuration of illumination and detection matching the conditions of the simplified model. I further discuss the validity of this assumption in Section 2.6.8 on pages 51 ff..

Reflection and transmission at a single interface. For normal incidence, reflection and transmission ($\theta = 0\,^\circ$) at a single interface of layer l and $l-1$, the Fresnel coefficients ϱ and τ relate the amplitudes A_r and A_t of the reflected and transmitted light to the incoming amplitude A_i [165]:

$$\varrho = \frac{A_\mathrm{r}}{A_\mathrm{i}} = \frac{N_l - N_{l-1}}{N_l + N_{l-1}} \tag{2.10}$$

$$\tau = \frac{A_\mathrm{t}}{A_\mathrm{i}} = \frac{2N_l}{N_l + N_{l-1}}. \tag{2.11}$$

The Fresnel coefficients for their parts are dependent on the complex refractive indices N_l and N_{l-1} of the corresponding materials of the layers.

Multi-layer interference. To formulate a model for the spectral reflectance of a multi-layer arrangement based on optical interference, I consider the phase differences of all transmitting and

[5] often referred to as Lambert-Beer's law

[6] power per surface area, here per active area of the photo-sensor

[7] However, in Section 2.6.8, I extend the model for the so-called s- and p-polarization of light [23].

reflecting amplitudes of the thin film interfaces. For the moment I exclude reflections R_{bs} from the bottom substrate-air interface as shown in Figure 2.2. This is treated in the next paragraph. The reflections from the thin film stack depend on the resulting constructive or destructive interferences from the interfaces. Applying this approach, I assume that, over the thicknesses of the thin layers, the light is coherent. As estimated in the following, this is valid for the present samples because the thin films possessed thicknesses below the coherent length of the light used for illumination.

Light reflected from different interfaces can only interfere if their optical distances do not greatly exceed the coherence length of the light. Assuming a Gaussian distributed spectrum, the coherence length $\mathcal{L}_c$ is defined as [165]

$$\mathcal{L}_c = \frac{\lambda_c^2}{2n\Delta\lambda_c}, \tag{2.12}$$

where n is the real refractive index of the film the light travels through. λ_c describes the location of the peak of the spectrum and $\Delta\lambda_c$ its width (or standard deviation) for $\lambda_c \pm \Delta\lambda_c$. Hence, the broader the spectrum the shorter is the coherence length of the light. For the present color sensors, the $\mathcal{RGB}$ filters separate the light into three distinct spectra. To estimate a typical coherence length of the present setups, I chose the green filter curve of the microscope shown in Figure 2.7 on page 29 as the spectrum defining element. Here, the mean wavelength is assigned to $\lambda_c \approx 530$ nm and the width is estimated to $2\Delta\lambda_c \approx 150$ nm. For the organic material, the real refractive index is $n \approx 1.7$ (@ $\lambda_c = 530$ nm) (see Figure 2.17a on page 38). Therefore I estimate the resulting coherence length to $\mathcal{L}_c \approx 1.1$ µm which is considerable above all layer thicknesses ($d_{q,\max} \sim 500$ nm) used in the present study. This justifies to assume constant phase relations of the different reflections from the thin film stack.

Otherwise the information of the phase relations of the waves would be lost and we could not expect interference effects. In the next paragraph on page 24, when treating backside reflections from a millimeter thick substrate, I split their phase relations from the front-side reflection discussed here.

Generally, I take into account two contributions to phase changes. First, the optical distance of each film the light travels through yields a phase differences of

$$\varphi_l = \frac{2\pi}{\lambda} N_l d_l. \tag{2.13}$$

where d_l is the film thickness of the l-th layer. Second, waves reflected at interfaces can experience a phase shift of π if the material the light is going to enter possesses a higher real refractive index than the material from which light is coming. The latter is already covered by Equation 2.10 when the real part of the numerator changes its sign depending on the relation of $\mathrm{Re}N_l$ and $\mathrm{Re}N_{l-1}$. Hence, a phase shift of π is represented by a negative sign of $\mathrm{Re}(\varrho)$, i.e. $\mathrm{Re}N_l < \mathrm{Re}N_{l-1}$.

To simplify modeling the interference of thin multi-layer systems, I use the matrix formalism introduced by Abeles [1]. Assuming normal incidence ($\theta = 0\,^\circ$), each layer in Figure 2.2 is represented by a 2-dimensional square matrix M_l as follows

$$M_l = \begin{bmatrix} \cos\varphi_l & \frac{\mathrm{i}}{N_l}\sin\varphi_l \\ \mathrm{i}N_l\sin\varphi_l & \cos\varphi_l \end{bmatrix}, \tag{2.14}$$

where φ_l is the phase change introduced in Equation 2.13. With this, the characteristic matrix M of the multi-layer system is the product of the single layer matrices

$$M = \begin{bmatrix} m_{11} & m_{12} \\ m_{21} & m_{22} \end{bmatrix} = \prod_{l=q}^{1} M_l, \tag{2.15}$$

where $m_{[1,2][1,2]}$ denotes scalar entries resulting from the matrix product on the right-hand side of Equation 2.15. By definition, the order in this matrix product from left to right equals the order of the layers from top to bottom compared to the situation in Figure 2.2. The corresponding reflection and transmission coefficients ϱ_f and τ_f of the thin film stack are given as follows

$$\varrho_\mathrm{f} = \frac{N_\mathrm{air} m_{11} - N_0 m_{22} + N_\mathrm{air} N_0 m_{12} - m_{21}}{N_\mathrm{air} m_{11} + N_0 m_{22} + N_\mathrm{air} N_0 m_{12} + m_{21}}, \tag{2.16}$$

$$\tau_\mathrm{f} = \frac{2N_\mathrm{air}}{N_\mathrm{air} m_{11} + N_0 m_{22} + N_\mathrm{air} N_0 m_{12} + m_{21}}, \tag{2.17}$$

where N_0 is the refractive index of the underlying substrate. Then, the total reflectance R_f and transmittance T_f relating the incoming spectral irradiance I_i, the reflecting spectral radiant exitance I_r and the transmitting spectral irradiance I_t for a desired wavelength are of the form [165]

$$R_\mathrm{f} = \frac{I_\mathrm{r}}{I_\mathrm{i}} = \left|\varrho_\mathrm{f}\right|^2, \tag{2.18}$$

$$T_\mathrm{f} = \frac{I_\mathrm{t}}{I_\mathrm{i}} = \frac{\mathrm{Re}N_0}{\mathrm{Re}N_\mathrm{air}} \left|\tau_\mathrm{f}\right|^2. \tag{2.19}$$

Backside reflections. In the previous paragraph, I introduced the model for spectral reflectance and transmittance of the thin film stack. Within the stack, I showed that the light can be assumed to be coherent. For non-transparent substrates, the model would be complete. For transparent ones, I have to take into account the backside reflection of the transmitted light in the substrate at the substrate-air interface. These reflections do not show a constant phase relation to the light directly reflected at the thin film stack. This is because the substrate thickness of 700 µm is far above the coherence length of the light with $\mathcal{L}_c \approx 1.1$ µm as estimated in the paragraph on page 22. Therefore, I treat these amplitudes separately and take into account only phase relations for the transmission back through the thin film stack from bottom to top (in Figure 2.2). The formalism is identical to the one presented before, but with T_f' and R_f' denoting the spectral reflectance (Equation 2.18) and transmittance (Equation 2.19) in reverse order of the layers. Hence, the spectral reflectance R_bs originating from the backside of the substrate is [264]

$$R_\mathrm{bs} = \frac{T_\mathrm{f} T_\mathrm{f}' R_{0\text{-air}}\ e^{-4|\mathrm{Im}(\varphi_0)|}}{1 - R_\mathrm{f}' R_{0\text{-air}}\ e^{-4|\mathrm{Im}(\varphi_0)|}}. \tag{2.20}$$

φ_0 denotes a phase change from traveling through the substrate (see Equation 2.13) and hence, the exponent equals $|\mathrm{Im}(\varphi_0)| = 2d_0\beta_0$, where β_0 is the absorption coefficient and d_0 the thickness of the substrate (the factor of 2 originates from the light traveling forth and back through the substrate). Therefore, the exponential function in Equation 2.20 represents optical absorption in the substrate. $R_{0\text{-air}}$ is the spectral reflectance inside the substrate from the backside defined by the Fresnel reflection coefficient in Equation 2.10 replacing the correct material parameters and inserted in Equation 2.18.

With this, I formulate the total spectral reflectance R_{total} of the thin film system depicted in Figure 2.2 simply as the sum of the reflectances defined in Equation 2.18 and 2.20 as follows

$$R_{\text{total}} = R_{\text{f}} + R_{\text{bs}}. \tag{2.21}$$

With Equation 2.6 and 2.21 the theoretical model of the underlying optical system is sufficiently described in order to compare it to measured values as shown in the next section.

2.2.4 Thickness estimation algorithm

The optical system captures a $\mathcal{RGB}$ image of the sample which can be understood as the measured total optoelectronic response denoted with $\tilde{O}_k^{ij}$ at pixel position ij and for color channel k. This is the equivalent to the theoretical values from the physical model $O_k^{ij}(d_q^{ij})$ formulated in Equation 2.6. On the basis of these two different quantities, a thickness estimation algorithm is presented in the following.

As a precondition, I assume that apart from the thickness of the top, q-th layer all other material parameters are known before the actual measurement, namely all refractive indices and layer thicknesses of up to the $(q-1)$-th layer including the substrate. Nevertheless, there remains a parameter which is difficult to determine quantitatively. That is the constant K^{ij} in Equation 2.6 which mainly involves slowly varying lateral deviations and inhomogeneities originating from the illumination, the optical setup or the sensor as discussed in Section 2.2.2.

To evaluate quantities that are determinable except for a constant, one can analyze relative instead of absolute values. For multi-dimensional vector-like variables such as the $\mathcal{RGB}$ data, I could perform this normalization for example by dividing each component $\tilde{O}_k^{ij}$ for $k \in \{\mathcal{R}, \mathcal{G}, \mathcal{B}\}$ by the sum of all $\mathcal{RGB}$ components according to

$$\frac{\tilde{O}_k^{ij}}{\tilde{O}_{\mathcal{R}}^{ij} + \tilde{O}_{\mathcal{G}}^{ij} + \tilde{O}_{\mathcal{B}}^{ij}}. \tag{2.22}$$

But then, the dimension of the $\mathcal{RGB}$ space is reduced from 3 to 2 because from Equation 2.22 it follows that

$$\sum_k \frac{\tilde{O}_k^{ij}}{\tilde{O}_{\mathcal{R}}^{ij} + \tilde{O}_{\mathcal{G}}^{ij} + \tilde{O}_{\mathcal{B}}^{ij}} = 1 \tag{2.23}$$

and therefore, each normalized value can be expressed as the sum of the other two. This could more probably result in a metamerism-like situation where different thicknesses correspond to similar normalized $\mathcal{RGB}$ values yielding miscalculations similarly to the failure mechanism presented in Section 2.6.1 on page 44.

A different approach to circumvent the reduction of the dimension of the signals is to use additional measurements (i.e. images) as reference to relate to. Utilizing those measurements for the thickness estimation, the corresponding reference thin film stack has to be known according to its refractive indices and its layer thicknesses. In practice, this usually involves capturing an image of the sample before printing the q-th layer and calculate theoretical values with a thickness of apparently $d_{q,\text{ref}}^{ij} = 0$ nm. These reference values are denoted with $\tilde{O}_{k,\text{ref}}^{ij}$ and $O_{k,\text{ref}}^{ij}$ for the $\mathcal{RGB}$ image of the un-printed sample and the theoretical values, respectively.

With this, I define contrast[8] values $\tilde{c}_k^{ij}$ for the measured $\mathcal{RGB}$ values introducing a similar formalism for the reference values $\tilde{K}_{\text{ref}}^{ij}$ and $\tilde{o}_{k,\text{ref}}^{ij}$ according to Equation 2.4 and 2.5 as follows

$$\tilde{c}_k^{ij} \equiv \frac{\tilde{O}_k^{ij} - \tilde{O}_{k,\text{ref}}^{ij}}{\tilde{O}_k^{ij} + \tilde{O}_{k,\text{ref}}^{ij}} = \frac{\tilde{K}^{ij}\,\tilde{o}_k^{ij} - \tilde{K}_{\text{ref}}^{ij}\,\tilde{o}_{k,\text{ref}}^{ij}}{\tilde{K}^{ij}\,\tilde{o}_k^{ij} + \tilde{K}_{\text{ref}}^{ij}\,\tilde{o}_{k,\text{ref}}^{ij}} \quad \begin{matrix} \tilde{K}^{ij} \overset{!}{=} \tilde{K}_{\text{ref}}^{ij} \\ | \\ = \end{matrix} \quad \frac{\tilde{o}_k^{ij} - \tilde{o}_{k,\text{ref}}^{ij}}{\tilde{o}_k^{ij} + \tilde{o}_{k,\text{ref}}^{ij}}. \tag{2.24}$$

The right term of this equation states that $\tilde{c}_k^{ij}$ is independent of the constants $\tilde{K}^{ij}$, $\tilde{K}_{\text{ref}}^{ij}$ which was the purpose of introducing the contrast values. But the underlying assumption in Equation 2.24 that $\tilde{K}^{ij} = \tilde{K}_{\text{ref}}^{ij}$ is a strong constraint to the experimental setup. This means that for the image acquisition of the un-printed and the printed sample, the conditions and settings, expressed by $\tilde{K}_{\text{ref}}^{ij}$ and $\tilde{K}^{ij}$, must be exactly the same. For example, this involves that the intensity and the spectrum of the illumination should be constant. Furthermore the recurring positioning of the samples below the acquisition setup should be equal. Effects of a deviation from these requirements are discussed in Section 2.6.

The basic algorithm for estimating a thickness map $d_{q,\text{est}}^{ij}$ from the contrast image data $\tilde{c}_k^{ij}$ is performed by least-square (LS) comparison to a list of theoretical contrast values $c_k(d_{q,r})$ within a defined range of possible thicknesses for the q-th layer. Discretized in steps of usually 1 nm, this look-up table is created from a list of p entries for thicknesses $d_{q,r}$ ranging from $d_{q,1}$ to $d_{q,p}$ for $r = 1, ..., p$ values. Using Equation 2.5 and 2.6, the list of theoretical $\mathcal{RGB}$ contrast values for $r = 1, ..., p$ is defined by

$$c_k(d_{q,r}) \equiv \frac{O_k(d_{q,r}) - O_{k,\text{ref}}}{O_k(d_{q,r}) + O_{k,\text{ref}}} = \frac{o_k(d_{q,r}) - o_{k,\text{ref}}}{o_k(d_{q,r}) + o_{k,\text{ref}}}. \tag{2.25}$$

The theoretical contrast values $c_k(d_{q,r})$ formulated in Equation 2.25 span a curve parameterized by the film thickness range $d_{q,r}$ of the q-th layer in the 3-dimensional $\mathcal{RGB}$ contrast space as exemplary shown in Figure 2.22 on page 45. In a second step of the algorithm, I determine the Euclidian distance δ^{ij} between the measured contrast vector $\tilde{\mathbf{c}}^{ij} = [\tilde{c}_\mathcal{R}, \tilde{c}_\mathcal{G}, \tilde{c}_\mathcal{B}]^{ij}$ of each pixel and the list of theoretical vectors $\mathbf{c}(d_{q,r}) = [c_\text{R}, c_\text{G}, c_\text{B},](d_{q,r})$ for all possible thickness values $r = 1, ..., p$ defined as

$$\delta^{ij}(d_{q,r}) \equiv \left\| \mathbf{c}(d_{q,r}) - \tilde{\mathbf{c}}^{ij} \right\|^{\frac{1}{2}}. \tag{2.26}$$

From this list of distances I determine the minimum for each pixel separately with

$$\delta_{\text{min}}^{ij} \equiv \min(\delta^{ij}(d_{q,r})) = \delta^{ij}(d_{q,\text{est}}^{ij}) \tag{2.27}$$

according to the most probable thickness estimation $d_{q,\text{est}}^{ij}$ per pixel. Therefore, the final thickness map $d_{q,\text{est}}^{ij}$ for the layer of interest is found by

$$d_{q,\text{est}}^{ij} \equiv \underset{d_{q,r} \in \{d_{q,r=1,...,p}\}}{\arg\min} \left\{ \delta^{ij}(d_{q,r}) \right\}. \tag{2.28}$$

[8] so-called Michelson contrast [180, 199]

The minimum distance $\delta_{\min}^{ij}$ defined in Equation 2.27 can serve as a quality measure or error of the estimation algorithm per pixel. By averaging $\delta_{\min}^{ij}$ over i and j with

$$\overline{\delta}_{\min} \equiv \frac{1}{ij} \sum_{i,j} \delta_{\min}^{ij} \tag{2.29}$$

I can assign a single (quality) number $\overline{\delta}_{\min}$ as an error for the estimation procedure of a complete thickness map, i.e. the smaller $\overline{\delta}_{\min}$ the more reliable the result.

Based on Equation 2.28, I implemented a MATLAB program which computes the thickness map of an unidentified top layer of a thin film sample for which all optical material properties and thicknesses up to the $(q-1)$-th layer are known in advance. The code for this estimation algorithm based on two input images (sample and reference) can be found in the Appendix B.3 on pages 159.

2.3 Hardware setups and optical characterization

The physical model and the algorithm presented in the previous section impose two major presets on the hardware system. First, the light source and the photo detector have to be arranged perpendicular to the sample surface (Figure 2.2 with $\theta = 0\,^\circ$). Second, the spectrum of the light source $L(\lambda)$ and the transfer filter function of the detector unit $U_k(\lambda)$ (see Equation 2.2) have to be characterized. I implemented the proposed method using an optical microscope and a commercial modified flatbed scanner.

2.3.1 Optical microscope: Leica DM4000M

In principle, an optical microscope operating in bright field mode satisfies the first condition of normal orientation. But besides magnification, microscope objectives are also characterized by their dimensionless numerical aperture (NA). For an air surrounding medium (refractive index $N_{\text{air}} \approx 1$) the latter is defined as

$$\text{NA} = N_{\text{air}} \sin\alpha, \tag{2.30}$$

where α is half of the maximum opening angle of light entering or exiting the objective as indicated in Figure 2.4. The NA characterizes an objective to which extent it is possible to image inclinations or declinations of a sample surface, i.e. for angles below α. Therefore, α is also the angle which

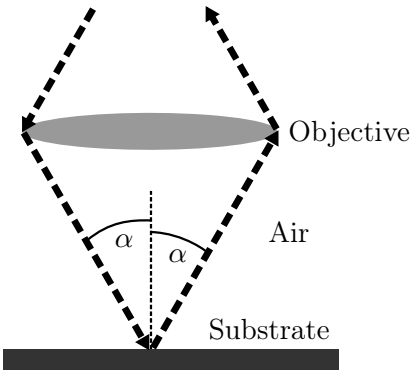

Figure 2.4: Geometrical representation of α, half the maximum opening angle, defining the numerical aperture in Equation 2.30. Dashed lines show the light exiting the objective (left ray) and entering it again (right ray) after reflection at the sample surface.

defines the maximum deviation from the assumption of normal illumination and detection stated above. The objective that was mainly used in the present study possessed a magnification of 2.5x and a numerical aperture of NA= 0.07 which results in an angle of only $\alpha = 4\,^\circ$. In Section 2.6.8, I discuss the error originating from this deviation by using objectives with numerical apertures of up to NA= 0.85 ($\alpha = 58.2\,^\circ$).
For the proposed method, I utilized a Leica DM4000M optical microscope for gathering image data of thin film samples. It was equipped with a color CCD sensor chip providing a maximum resolution of 2592×1944 pixels.

To characterize the light source spectral power distribution, I used a spectrophotometer CS1000A from Konica Minolta with 1 nm spectral resolution. The CS1000A was controlled by a MATLAB program which is given in the Appendix B.2 on page 156. I placed a white standard from Datacolor, Switzerland, which exhibits an almost constant spectral response within the visible spectrum, in the field of view of the objectives and measured the spectrum with the spectrophotometer CS1000A. Figure 2.5 illustrates the normalized measured spectrum $L(\lambda)$ of the light source exiting the 2.5x objective.

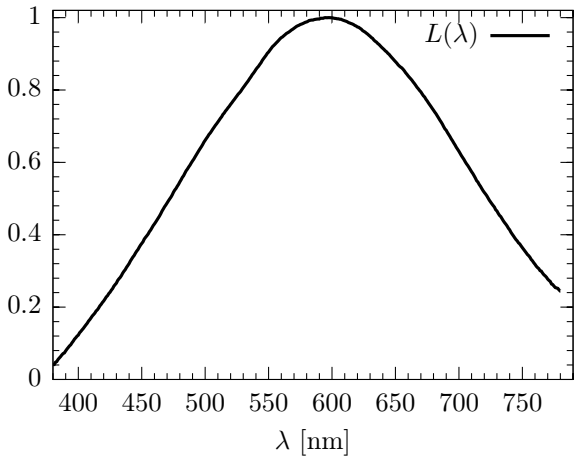

Figure 2.5: Measured normalized spectrum $L(\lambda)$ of the bright field illumination shining on the sample through the 2.5x objective of the Leica DM4000M microscope.

I determined the combined optoelectronic transfer function $U_k(\lambda)$, which is mainly the $\mathcal{RGB}$ response of the sensor chip to an incoming spectrum using a set of well-defined narrow transmission bandpass filters and the built-in transmission illumination of the microscope. Afore, I characterize the spectral transmittances of the interference filters which are shown in Figure 2.6. First, I measured the spectrum of the transmitting illumination from beneath the focal plane of the microscope. Then, I placed the 35 different optical interference filters in the focal plane of the microscope and captured the corresponding 35 images. Here, it was necessary to deactivate any image distortion feature of the camera's controlling software, most important parameter was the gamma correction. Details on the gamma correction and deviation from it are discussed in Section 2.6.7. I laterally averaged over the image data per color channel resulting in three $\mathcal{RGB}$ values, assigned each of them the peak wavelength of the band filters and weighted also with the integral of the corresponding filter transmittance. In this manner I deduced the normalized[9] optoelectronic transfer function $U_k(\lambda)$ for all three channels. The result within the visible spectrum is plotted in Figure 2.7. This direct

[9] to the maximum of each channel

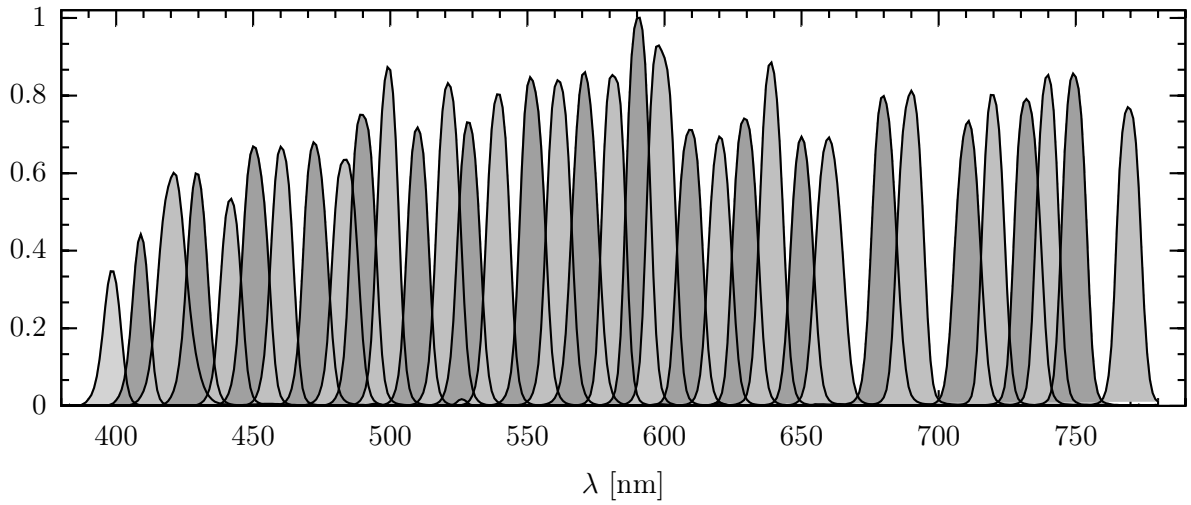

Figure 2.6: Measured normalized spectral transmittances of the 35 narrow-bandwidth interference filters that were used for spectral characterization of the microscope and scanner.

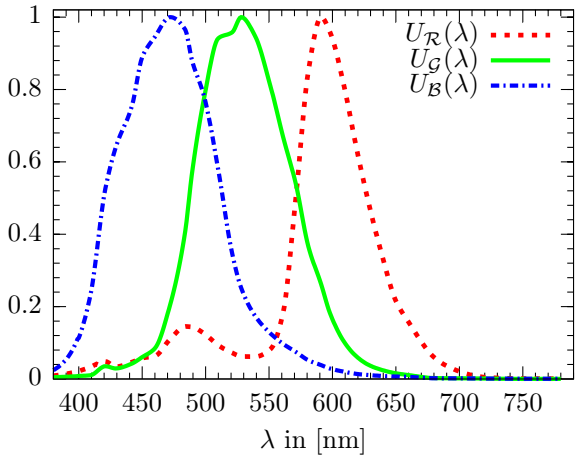

Figure 2.7: Measured normalized spectral optoelectronic transfer function $U_k(\lambda)$ for the three $\mathcal{RGB}$ channels of the Leica DM4000M microscope.

approach for spectral characterization is suitable because the filters possess narrow bandwidths and cover the total spectrum of interest. If the filter transmittance is arbitrary or the number of test samples with known spectral reflectance or transmittance is limited, alternative methods should be applied for spectral characterization as described for example by Hardeberg et al. or Urban et al. [98, 253].[10]

2.3.2 Modified flatbed scanner: Epson Perfection 3170

The second hardware setup, a commercial flatbed scanner (Epson Perfection 3170), was modified to match the condition of normal illumination ($\theta = 0\,^\circ$). Normal detection was implemented by default. I determined the deviation from the normal oriented incidence and detection in Section 2.6.8. A sketch of the optical setup of the modified flatbed scanner is shown in Figure 2.8. First, I removed

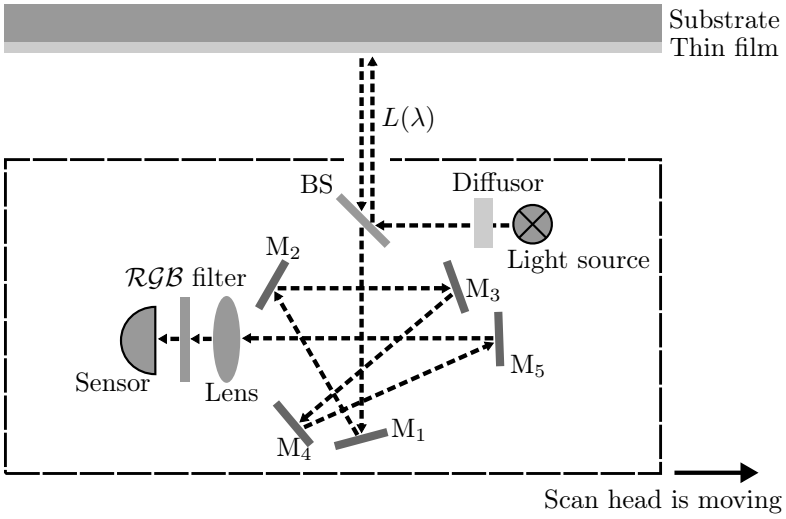

Figure 2.8: Setup of the optical elements and the optical path of the modified commercial flatbed scanner (Epson Perfection 3170). The beam-splitter (BS) and diffusor were additionally installed. $M_{1,\ldots,5}$ denotes the built-in mirrors. Light source and sensor were adjusted to be normal to the sample surface.

one of the two fluorescent bulbs for illumination which were originally positioned around $\pm 40\,^\circ$ off the normal to the sample surface. Second, I installed a beam-splitter (BS) from Edmund Optics[11] for the remaining bulb. This made it possible to match the optical path of the sample illumination to that of the detection, as illustrated in Figure 2.8. Furthermore, I included a diffusor to ensure a more homogeneous illumination, removed the glass support and mounted a substrate holder on top of the scanner to guarantee reproducible and adjustable sample position.

A picture of the scanner including the sample holder and a 150×150 mm^2 glass sample is shown in Figure 2.9. The optical detector of the flatbed scanner was a color CCD line-sensor with 6×13600 pixels [66]. The maximum optical resolution of the Epson scanner was specified by the manufacturer to 3200 dots per inch (DPI) [66]. The optical characterization of the illumination (fluorescent bulb) resulted in the spectrum $L(\lambda)$ depicted in Figure 2.10.

The optoelectronic response $U_k(\lambda)$ of the flatbed scanner was difficult to determine because it was neither possible to mount the transmission filter between light source and sensor nor to use the

[10] I have also tested the filter estimation based the *pseudoinverse* and *principal Eigenvector* method proposed by Hardeberg et al. [98] which gave even less reliable results than the direct approach.

[11] part no. NT46-583, 127mm X 178mm, 50R/50T, plate beam-splitter, from which I scribed and broke a part of 10mm X 178mm

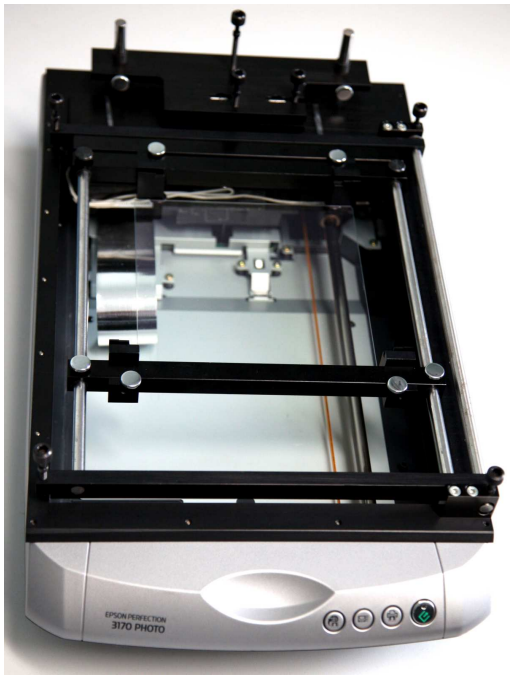

Figure 2.9: Photograph of the modified Epson flatbed scanner including the sample holder and a glass substrate.

filters in reflection. I positioned an external, characterized light source (1000 Watt halogen bulb) and the transmission filters above the scan head. But on the other hand, I had to switch off the internal light source while capturing images of the filters. This procedure was initially hindered because the internal control of the scanner which could not be modified, as mentioned before, frequently performed calibrating using the internal light source before operating. If this procedure failed, the scanner would refuse further operation. Therefore, I mounted a path-dependent switch connected to the internal light source to disable internal illumination only when the scan head was located beneath the filters. Using these modifications, I was able to perform the filter-dependent image acquisition and subsequent deduction of the optoelectronic response in the same manner as for the microscope before. The resulting measured normalized[12] optoelectronic response function $U_k(\lambda)$ for the three channels is plotted in Figure 2.11.

[12] to the maximum of each channel

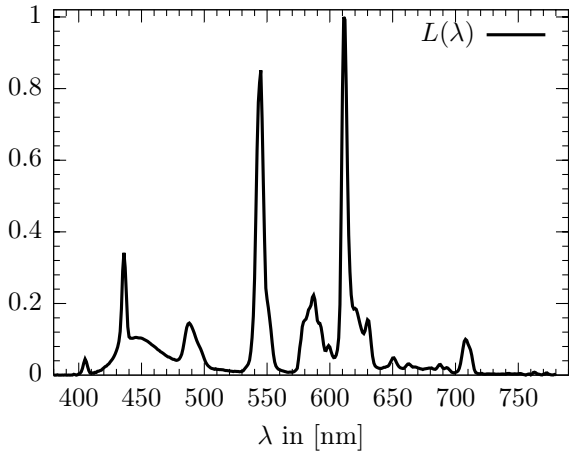

Figure 2.10: Measured normalized spectrum $L(\lambda)$ of the fluorescent bulb of the scanner illuminating the sample through the beam-splitter.

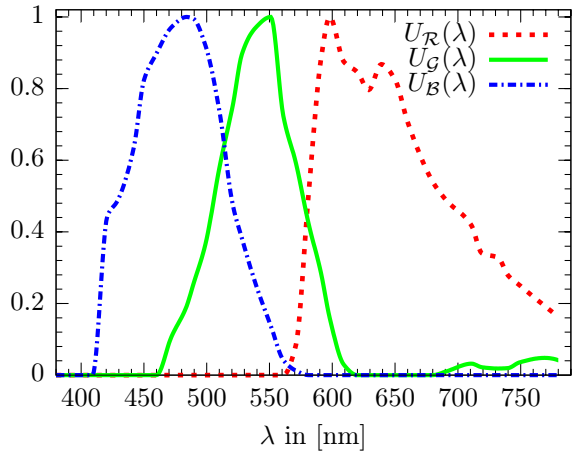

Figure 2.11: Measured normalized spectral optoelectronic transfer function $U_k(\lambda)$ for the three $\mathcal{RGB}$ channels of the modified flatbed scanner Epson Perfection 3170.

Fixed exposure time

The installation of the diffusor and the reduction to a single fluorescent bulb decreased the overall intensity. This caused a substantial drawback. On startup, the scanner sets its integration time for the sensor by referencing on an integrated white standard. This standard defined the integration time of the scanner for the subsequent scans. Several test scans had shown that this exposure time could not be significantly adjusted afterwards although the scanner performed a further calibration step before each scan. First, a problem arose for incorrect adjustment of the beam-splitter to the internal white standard. The intensity reflected by the standard was to low, therefore, the scanner reported a problem with the light source and refused operation. Second, for correct adjustment, the scanner successfully calibrated on startup, but this *long* exposure time resulted in a clearly overexposed image of the highly reflective samples. Because of lacking an alternative method for controlling the exposure time (i.e. by the computer software), I adjusted it by a hardware adaption. I replaced the internal white standard with an adjustable aluminum mirror. With this modification, I enabled the flatbed scanner to successfully image the thin film samples. Nevertheless, for the transparent glass substrates with the thin organic layer, the maximum measured $\mathcal{RGB}$ signals did not exceed 42% of its maximum accessible values. This aspect of the present scanner setup provides a considerable scope for improvement.

Rings in the scanned image

Occasionally, I faced the problem of extended rings in the scanned image, especially when using transparent and rigid 150×150 mm^2 glass samples which where used as test samples for the method (Section 2.5.2) and for printing experiments in Chapter 4.

A known issue of flatbed scanners is the appearance of so-called Newton rings in images when scanning transparent samples [237]. These usually occur for slightly curved transparent surfaces in contact to flat one [23]. The small distances between the surfaces below the coherent length of the light generate optical interference maxima and minima resulting in Newton rings. Since the glass

support of the scanner which usually serves as second surface for this optical effect was removed, the Newton rings might be excluded as origin.

A comparable optical effect, termed Haidinger rings or "Interferenzkurven gleicher Neigung", might appear at very plane-parallel plates with arbitrary absolute plate thicknesses, but with thickness variations below ~ 50 nm [23, 95, 164]. Raman showed [208], that this type of interference rings could also occur for rectilinear slit apertures and non-uniform plates which might be comparable to the present scanner setup and samples. According to this, I observed that the rings, only shown in the blue channel, have a smaller period than in the green color channel[13]. During completing this manuscript, I repeated some sample scanning experiments and could excluded that substrate curvatures or induced bending is responsible for the rings. The rings were also not significantly affected by relocating the substrate. Additionally, I realized that when I rotated the glass sample by $90\,^\circ$ to the scan direction, the rings were suppressed for all samples of this type[14]. Assuming that Haidinger rings were responsible for the fringes, would mean that the glass plates exhibit different thickness variation in the two lateral dimensions. But then, I would expect the rings to change when re-positioning the sample. The rings might also be generated by the modified optical setup with the beam-splitter, but then why did the rotation of the sample suppress the rings? Unfortunately, the main underlying mechanism creating the rings could not be resolved.

2.4 Measurement procedure

The combined procedure of a complete measurement to estimate the thickness map $d^{ij}_{q,\mathrm{est}}$ of a printed layer is summarized as a detailed flow chart in Figure 2.12. Apart from the input parameters (starting at the bottom left box of Figure 2.12) we can identify the four blocks described in the previous sections: *Theoretical model*, *Estimation algorithm*, *Hardware setup* and *Optical characterization* of the system.

[13] in the red channel I did not observe the rings

[14] ITO-coated glass substrate used in Section 2.5.2 and 4.2.1

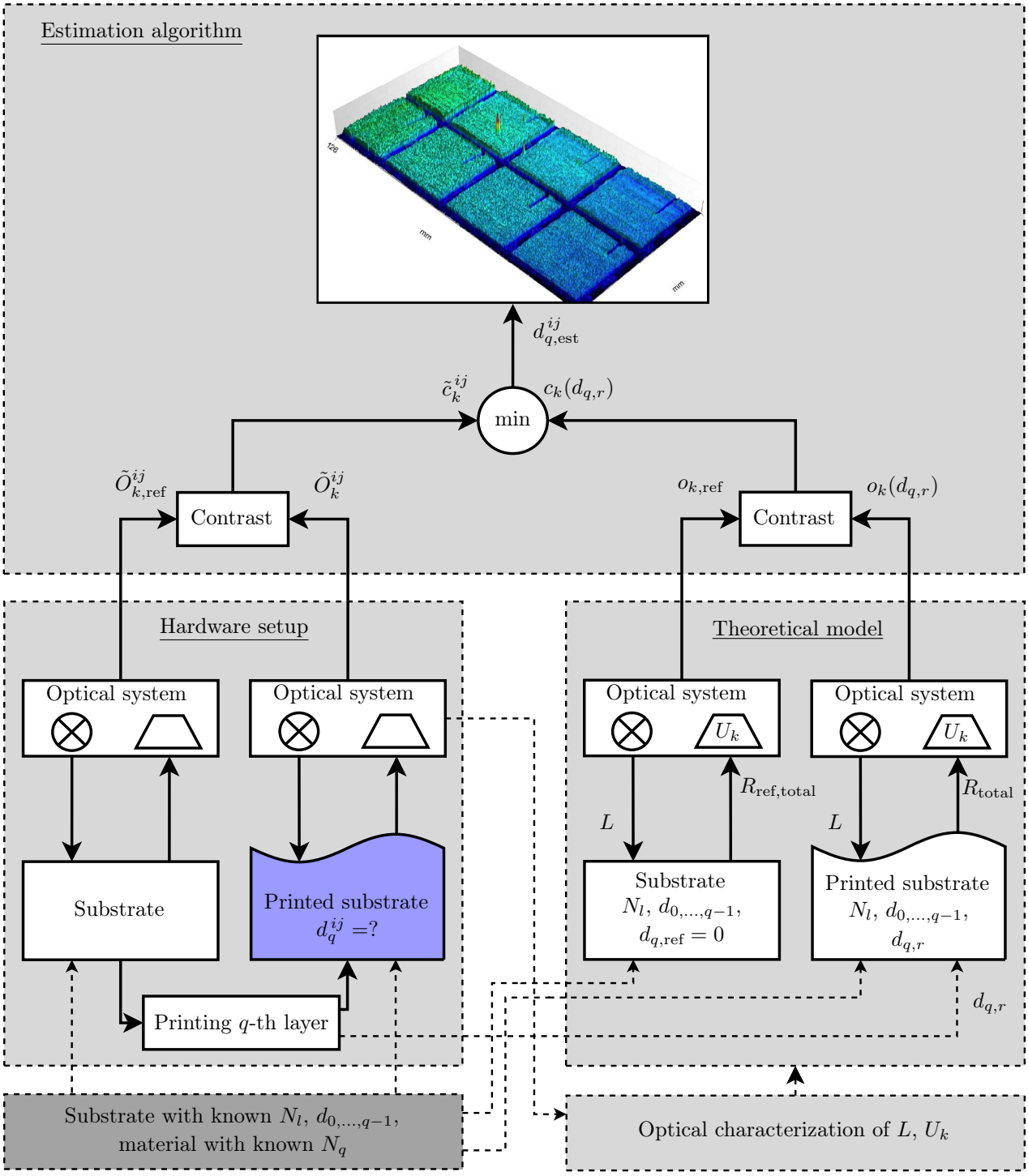

Figure 2.12: Overview of the measurement procedure to estimate the thickness map $d^{ij}_{q,\text{est}}$. On a substrate (bottom left box), which can possess already coated thin films ($l = 0, \ldots, q-1$), with known refractive indices (N_l) and thicknesses ($d_{0,\ldots,q-1}$), a q-th layer of known N_q and unknown thickness d_q is printed. The printing step suggests a possible thickness range $d_{q,r}$ of the q-th layer for the theoretical model. The optical system has to be characterized (determination of the spectrum L of the light source $\otimes$ and the transfer function of the detector unit U_k) before the measurement. For each pixel ij, the measured $\mathcal{RGB}$ contrast values are compared to the list of theoretical values. The thickness associate to the nearest entry in the list is selected for the final thickness map $d^{ij}_{q,\text{est}}$ (represented by the 3D image).

2.5 Evaluation of the method

To evaluate the proposed method I used three different samples. The first one was a silicon (Si) wafer with different silicon dioxide (SiO_2) layers. The second and third test samples were transparent glass substrates with vacuum coated layers of indium tin oxide (ITO), whereas the ITO of the third sample had additionally been structured. On top of the ITO an organic semiconductor layer was deposited from solution processes.

The refractive indices of the organic semiconductor were externally determined by spectroscopic ellipsometry at a laboratory of a project partner (BASF SE, Ludwigshafen). For the other anorganic materials, I used the optical properties given in the materials library which was delivered with the spectroscopic reflectometry tool NanoCalc-2000 from Ocean Optics (formerly Mikropack GmbH), Germany, [186].

The three different samples were chosen to test the measurement method using the two hardware setups described above. In the following, I compare the thickness results of the microscope to the ones of the scanner, respectively, and to reference methods.

2.5.1 Thicknesses of the SiO_2 coated silicon wafer

The first sample, the non-transparent silicon wafer with 100 mm diameter, had been lithographically processed with six different fields of silicon dioxide (SiO_2) by the manufacturer, Ocean Optics. They had determined the thicknesses of the layers ranging from 0 to 500 nm by spectroscopic ellipsometry, as listed in Table 2.1 on page 37. The refractive indices of the these materials are depicted in Figure 2.13a for n and in Figure 2.13b for κ, from [186].

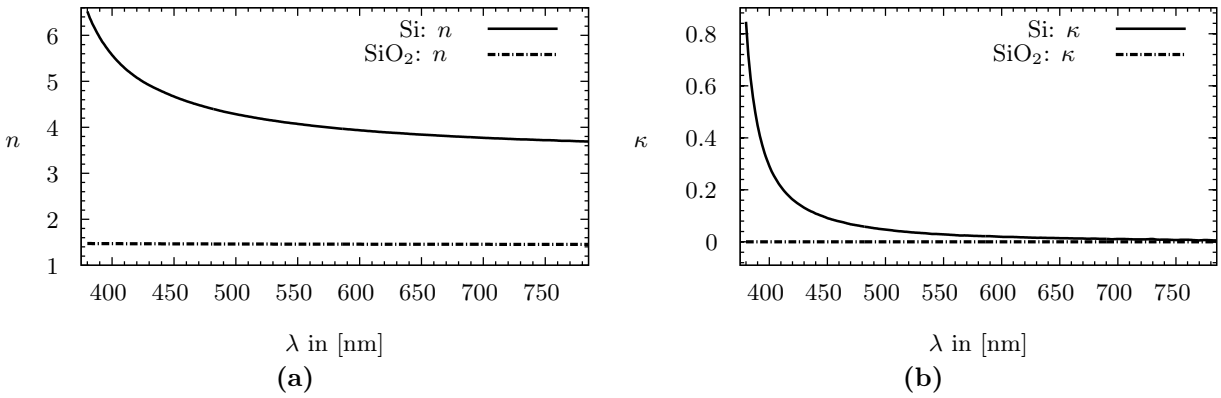

Figure 2.13: Refractive index components, n in (a) and κ in (b), of Si and SiO_2 for the wafer sample, from [186].

Since the silicon (Si) wafer was purchased and had been already coated with different thicknesses of silicon dioxide (SiO_2), I could not acquire a complete reference image of the wafer without the SiO_2 layers. I therefore extracted reference $\mathcal{RGB}$ values from the image of the test wafer of an un-coated area (bottom field #6 of Figure 2.14a and 2.14b) with a reference thickness of $d_{1,\mathrm{ref}} = 0$ nm[15].

To image most parts of the 100 mm sized wafer with the microscope's 2.5x objective, I scanned the sample with 342 single pictures which were combined by the Leica's capturing software, shown in Figure 2.14a. The image acquisition of the visible area of 94.0×78.3 mm^2 with 800×630 pixels[16]

[15] alternatively, I could have used the value given by the manufacturer of 1.2 nm

[16] reduced size

and 24-bit color depth took about 15 min. The grid which is visible in Figure 2.14a resulted from the stitching procedure and revealed the rotationally symmetric intensity variations of microscope objectives which are always present.

The modified flatbed scanner scanned the total wafer within 25 s with a reduced lateral resolution of 800×813 pixels, a scan area of 97.3×98.9 mm^2 and also 24-bit color depth. The acquired raw image of the SiO_2/Si wafer is shown in Figure 2.14b.

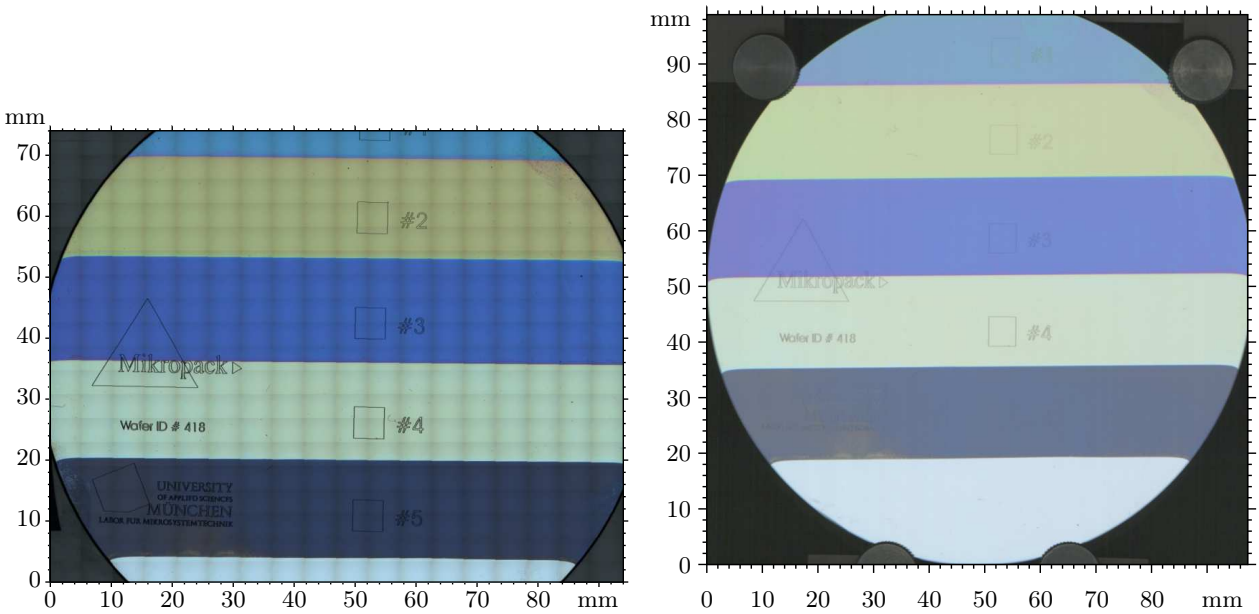

(a) Microscope **(b)** Scanner

Figure 2.14: Original images of the SiO_2/Si wafer acquired by the Leica microscope stitched from 342 single images in (a) and by a single scan of the modified Epson scanner in (b). Visible fields are labeled from #1 to #6 from top to bottom.

The theoretical contrast values $c_k(d_{1,r})$ (Equation 2.25) for the thickness of this single layer sample (i.e. $q = 1$) in the range of $d_{1,r} \in [0, 600]$ nm are plotted for both setups in Figure 2.15.[17] The reference thickness values were set to $d_{q,\mathrm{ref}} = 0$ nm for the calculated contrast values shown in Figure 2.15. For measured contrast values of the microscope, a single 2.5x image of the un-coated bottom field (#6) of the wafer was taken as reference. For the scanner, the reference $\mathcal{RGB}$ value which was used for measured contrast value determination of the image was found by averaging the $\mathcal{RGB}$ values of the bottom field #6 of Figure 2.14b.

The resulting thickness maps based on Equation 2.28 for the different fields of the SiO_2 layers on the silicon wafer are shown as pseudocolor images in Figure 2.16a for the microscope and in Figure 2.16b for the scanner. The averaged contrast residuals are of the same order for both setups, $\overline{\delta}_{\min} = 0.0209$ for the microscope and $\overline{\delta}_{\min} = 0.0259$ for the flatbed scanner. Average surface profiles of the topographies shown in Figure 2.16 for the microscope and the scanner yield the layer thicknesses summarized in Table 2.1. We can identify a maximum layer thickness difference of 3.5 nm and 2.5 nm between the proposed imaging color reflectometry method using the microscope and the scanner and the spectroscopic ellipsometry measurements by the manufacturer.

[17] Discussing the robustness of the method in Section 2.6.1, I show a 3-dimensional plot of the contrast values of the scanner in Figure 2.22 on page 45.

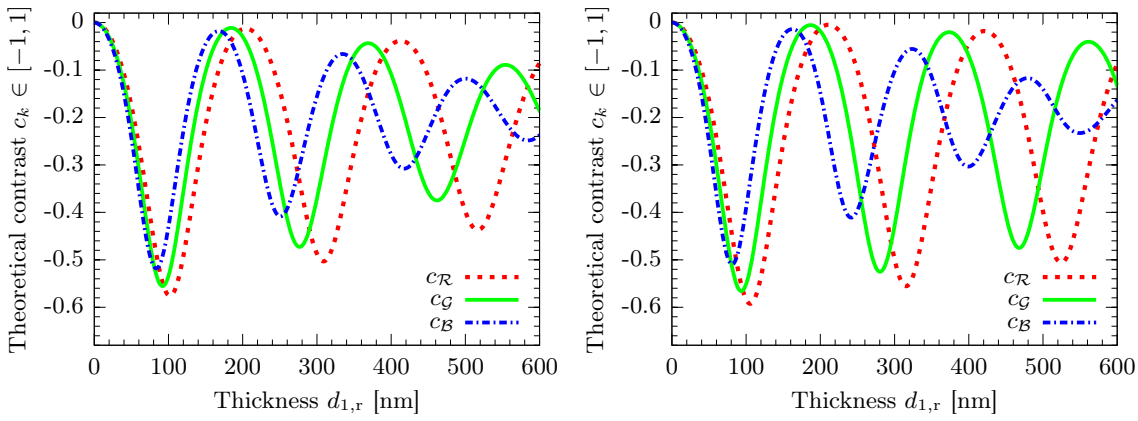

(a) Microscope **(b)** Scanner

Figure 2.15: Theoretical contrast values $c_k(d_{1,r})$ of the SiO_2/Si wafer according to Equation 2.25 for thicknesses in the range of $d_{1,r} \in [0, 600]$ nm for the microscope setup in (a) and the flatbed scanner in (b).

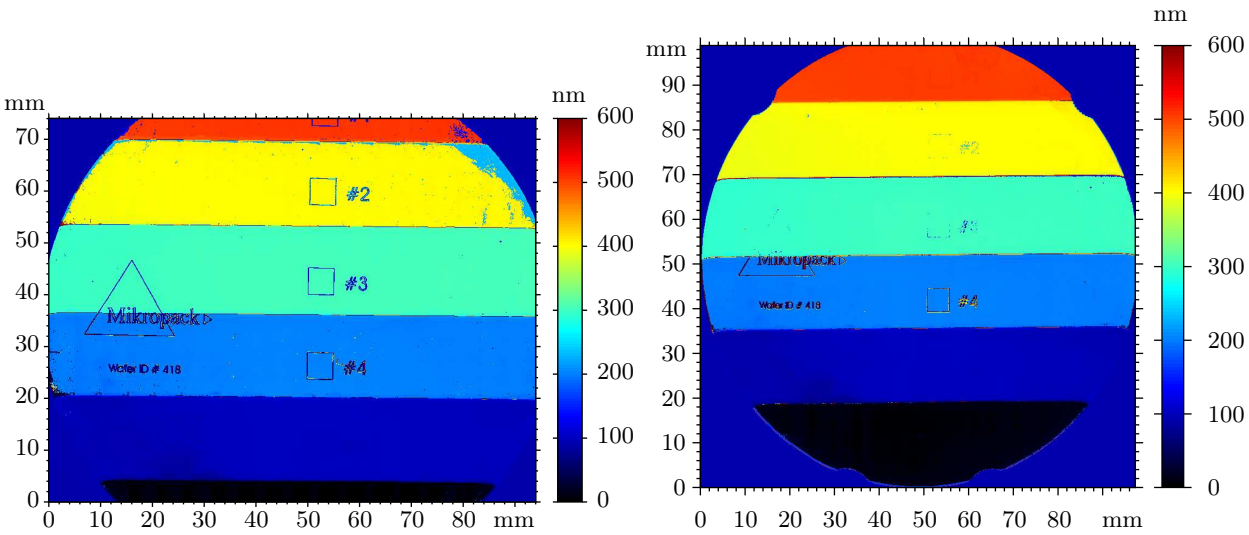

(a) Microscope **(b)** Scanner

Figure 2.16: Resulting pseudocolor images of the estimated thicknesses $d^{ij}_{1,\text{est}}$ of the silicon dioxide on the silicon wafer sample using the proposed measurement method with both hardware setups. The averaged contrast residuals are $\overline{\delta}_{\min} = 0.0209$ for the microscope (a) and $\overline{\delta}_{\min} = 0.0259$ for the flatbed scanner (b).

Table 2.1: Mean layer thicknesses of the different fields of SiO_2 on the silicon wafer measured by spectroscopic ellipsometry (SE) (from the manufacturer) and by the proposed imaging color reflectometry (ICR) using the microscope and the modified flatbed scanner.

	Field #1	Field #2	Field #3	Field #4	Field #5	Field #6
Spectroscopic ellipsometry (SE) [nm]	501.8	397.4	298.1	199.1	96.3	1.2
Microscope ICR [nm]	504.0 ± 2.4	400.5 ± 0.7	301.3 ± 0.4	201.5 ± 1.1	99.8 ± 0.8	3.1 ± 3.1
Difference to SE [nm]	2.2	3.1	3.2	2.4	3.5	1.9
Scanner ICR [nm]	502.7 ± 0.7	398.6 ± 1.1	298.8 ± 1.0	200.0 ± 1.1	98.8 ± 1.5	3.4 ± 3.1
Difference to SE [nm]	0.9	1.2	0.7	0.9	2.5	2.2

2.5.2 Thicknesses of a organic semiconductor printed on ITO coated glass

The transparent soda-lime glass substrate with the size of $150 \times 150 \times 0.7$ mm^3 had been vacuum coated with a thin layer of indium tin oxide (ITO) by Merck, Germany. They did not provide exact information of the layer thickness. Therefore, I determined the ITO thickness using the spectroscopic reflectometry tool NanoCalc-2000 from Ocean Optics which resulted in (160 ± 0.8) nm. On top of the ITO, I printed several 30×30 mm^2 square fields of the organic semiconductor spiro-MeOTAD ($C_{81}H_{68}N_4O_8$) dissolved in toluene using the gravure printing method as presented in Chapter 4. For reference, I measured the resulting organic thicknesses with phase-shifting interferometry (PSI) using a Plu Neox from Sensofar[18], Spain, at generated edges of swiped lines at several test positions. The resulting thicknesses ranged from 20 to 26 nm as listed in Table 2.2 on page 41. The corresponding (n, κ) values of the sample stack are shown in Figure 2.17a and 2.17b.

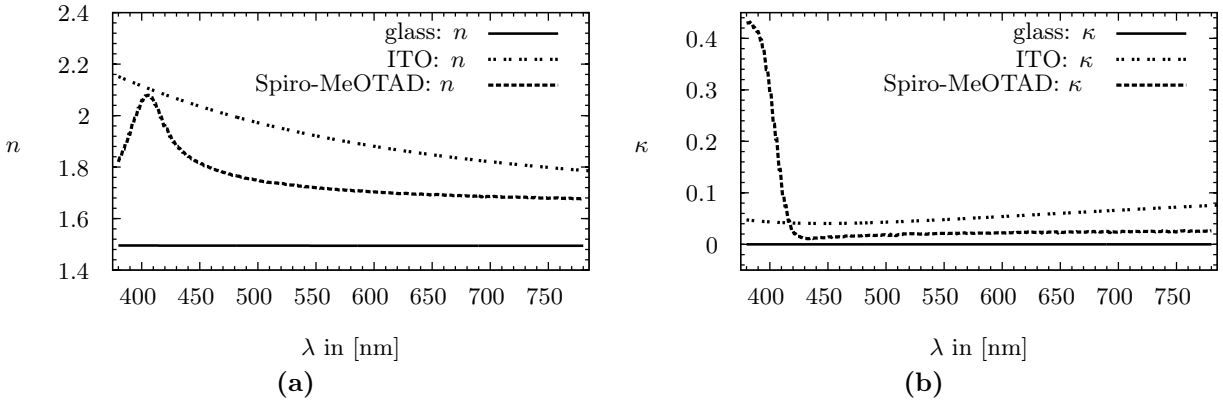

Figure 2.17: Refractive index components, n in (a) and κ in (b), of the three materials ITO, soda-lime glass and spiro-MeOTAD of the printed sample. Values for ITO, soda-lime glass from Ocean Optics [186], for spiro-MeOTAD from BASF SE.

The spiro-MeOTAD/ITO/glass sample was imaged with 323 combined single pictures using the Leica microscope, resulting in a recorded area of 66.1×93.0 mm^2 with a reduced lateral resolution of 711×1011 pixels, shown in Figure 2.18a. The same settings were used for acquiring an image of the substrate without the printed fields as reference.

The scan area of the Epson flatbed scanner was set to 65.2×127.0 mm^2 with a reduced resolution 519×1011 pixels to match the sizes of the pictures taken by the microscope. The image data from the desktop scanner of the printed sample is depicted in Figure 2.18b, whereas the box in the upper left corner shows the raw data and the remaining area was enhanced according to contrast and color for illustration. This reveals the previously discussed problem that the scanner sets the integration time using its internal calibration procedure dependent on the internal reference standard (the installed mirror) and independent of the type of the sample. Both, the printed sample and the bare ITO glass substrate were scanned with the same settings. Whereas the scanned image of the non-transparent wafer (Figure 2.14b on page 36) attained its maximum color value for the blue channel at 94 % of its theoretical maximum of $O_{\max} = 255$, the image of the transparent sample (Figure 2.18b) only reached its maximum value at 42 % of $O_{\max}$ for the blue channel. Hence, the image of the organic layer is too "dark" and the integration time should have been twice as long to acquire an optimal image for this sample by implementing a different type of internal reference.

[18] details on this profiling technique can be found in Appendix A on page 143

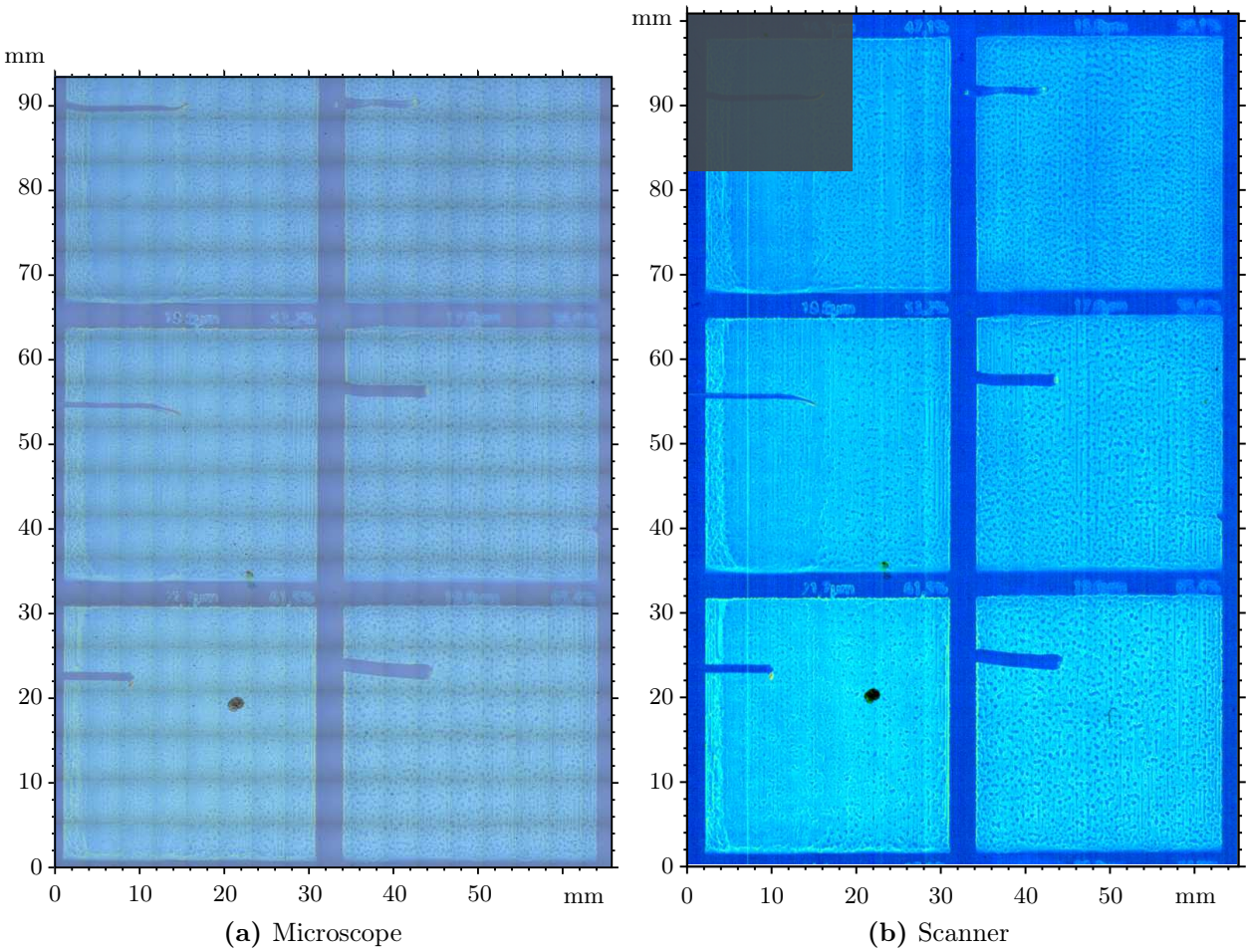

(a) Microscope **(b)** Scanner

Figure 2.18: Images of the spiro-MeOTAD/ITO/glass sample. Raw image data acquired by the Leica microscope stitched from 323 single images in (a) and by a single scan of the modified Epson scanner in (b) with the box in the upper left corner showing the raw data and the remaining area enhanced according to contrast and color for illustration.

Since this sample possessed two thin films (i.e. $q = 2$), a fully coated one (ITO) and a structured one (printed spiro-MeOTAD), I had to define two reference thicknesses. The ITO layer was measured using a different method (spectroscopic reflectometry with the NanoCalc-2000 from Ocean Optics) resulting in a reference thickness of $d_{1,\mathrm{ref}} = 160 \pm 0.8$ nm, and the thickness of the organic layer before the printing process was apparently set to zero thickness $d_{2,\mathrm{ref}} = 0$ nm. From known gravure cylinder parameters and known concentration of the solid content in the ink formulation, I could set the upper limit to $d_{2,p} = 60$ nm for the expected thickness of the organic layer.

I chose the theoretical thickness range for the contrast values of the organic layer to range within $d_{2,r} \in [0, 60]$ nm as depicted in Figure 2.19a for the microscope and in Figure 2.19b for the scanner.

The resulting estimated thicknesses $d^{ij}_{2,\mathrm{est}}$ of the printed spiro-MeOTAD on the ITO/glass substrate are depicted as pseudocolor images in Figure 2.20.

Contrary to the non-transparent wafer sample, the averaged contrast residuals of the organic layer of the least-square algorithm differ by a factor of about 3 for both setups, with $\overline{\delta}_{\mathrm{min}} = 0.0679$ for the microscope and $\overline{\delta}_{\mathrm{min}} = 0.1795$ for the flatbed scanner. This high residual of the flatbed scanner could originate from the underexposed image of the transparent substrate resulting in higher pixel noise.

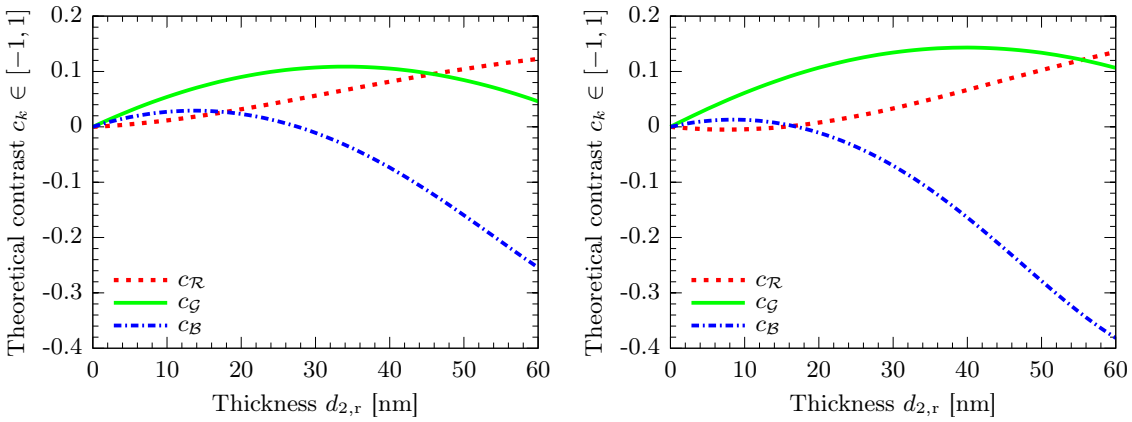

(a) Microscope **(b)** Scanner

Figure 2.19: Theoretical contrast values $c_k(d_{2,r})$ of the printed spiro-MeOTAD on the ITO/glass substrate for thicknesses ranging from $d_{1,r} \in [0, 60]$ nm for the microscope setup in (a) and the flatbed scanner in (b).

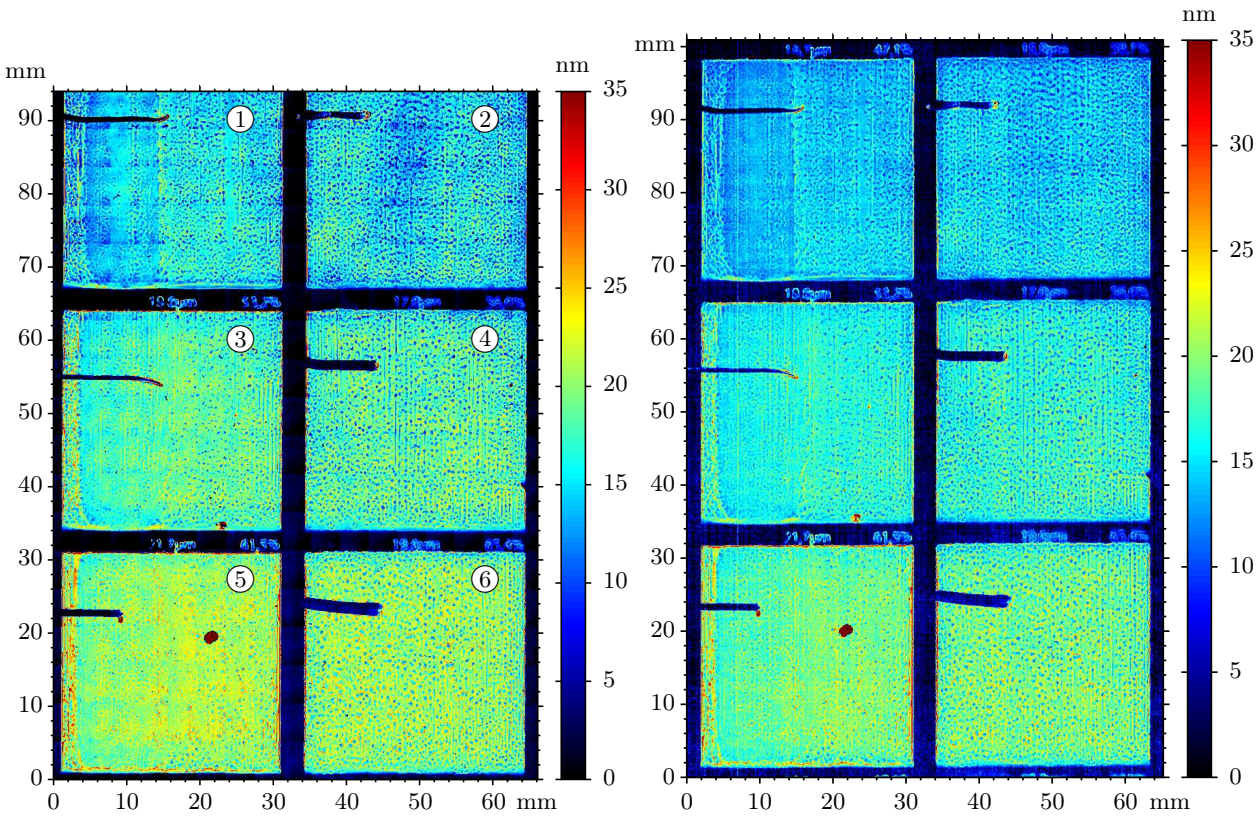

(a) Microscope. The mean contrast residual is $\overline{\delta}_{\min} = 0.0679$. The six different fields are labeled from ① to ⑥ .

(b) Scanner. The mean contrast residual is $\overline{\delta}_{\min} = 0.1795$.

Figure 2.20: Resulting pseudocolor images of the estimated thicknesses $d_{2,\mathrm{est}}^{ij}$ of the printed spiro-MeOTAD on the ITO/glass substrate. Mean thicknesses of the fields are listed in Table 2.2.

The different fields of the printed sample are numbered according to Figure 2.20a from ① to ⑥ .[19] By averaging linear surface profiles of the topography presented in Figure 2.20, I determined

[19]Please note that these field labels intentionally differ from the six fields of the wafer before where I used the # sign in front.

the mean thicknesses of the different fields in comparison to the ones acquired by phase-shifting interferometry listed in Table 2.2. From known printing process parameters I could assume the

Table 2.2: Mean layer thicknesses of the different printed fields of spiro-MeOTAD on the ITO/glass substrate measured by phase-shifting interferometry (PSI) and by the proposed imaging color reflectometry (ICR) using the microscope and the modified flatbed scanner.

	Field ①	Field ②	Field ③	Field ④	Field ⑤	Field ⑥
Phase-shifting interferometry (PSI) [nm]	18.7 ± 4.5	20.5 ± 7.3	21.0 ± 4.4	18.4 ± 3.5	20.2 ± 3.4	19.5 ± 6.6
Microscope ICR [nm]	15.1 ± 2.7	14.9 ± 3.4	18.3 ± 2.3	17.8 ± 3.1	20.9 ± 3.1	19.9 ± 2.3
Difference to PSI [nm]	3.6	5.6	2.7	0.7	-0.7	-0.5
Scanner ICR [nm]	14.0 ± 1.9	14.0 ± 2.3	16.4 ± 1.9	16.5 ± 2.5	19.0 ± 3.0	18.9 ± 2.7
Difference to PSI [nm]	4.7	6.5	4.6	1.9	1.2	0.6

thicknesses of the different fields to fulfill the relations

$$⑤ > ⑥ > ③ > ④ > ① > ②. \tag{2.31}$$

The phase-shifting interferometry (PSI) was difficult to apply on the organic test sample because only small areas of $254 \times 190 \mu m^2$[20] could be measured at a time. However, the surface undulations of the sample were in the millimeter range so that even four averaged measurements did not give reliable thickness results. Among others things, the inability of producing reliable results for this type of samples using existing optical profiling techniques prompted the development of the proposed ICR method.

From Table 2.2 I deduce that although the contrast residuals are different and strongly increased for the scanner, the estimated mean thicknesses ranging from 14.0 nm to 20.9 nm are quite similar for the two hardware setups. Compared to the reference PSI method which was problematic to apply, I found a maximum difference of up to 6.5 nm for field ② .

Comparing the results listed in Table 2.2 to the thickness relations in Equation 2.31 confirms that the proposed ICR method more plausible estimates the layer thicknesses than the reference PSI method. In summary, it can be concluded that the imaging color reflectometry is a reliable method for large-area characterization of printed ultra-thin organic and inorganic layers.

2.5.3 Vertically stitched thicknesses of a multi-layer sample

The results presented in this section demonstrate an extension of the MATLAB programm more than addressing details on the measurement parameters again. I implemented a multi-layer algorithm suitable for layer-by-layer processing with in-between image acquisition. The main improvement of the programm was that the results of the first thickness estimation were forwarded as reference image data with consigned thickness values to the second thickness estimation of the consecutively processed organic layer.

To measure different layers with the proposed method, I used a sample which was a $30 \times 30 \times 0.5$ mm^3 transparent soda-lime glass substrate vacuum coated and pre-structured with an ITO layer by the supplier Merck. On top of the ITO, which I partly covered by adhesive tapes, I spin-coated also the organic semiconductor spiro-MeOTAD dissolved in toluene. Phase-shifting interferometry at the generated edges at the removed tape resulted in an average thickness of (24.9 ± 1.8) nm.

[20] with a 50x objective

I used the microscope to image the 30×30 mm^2 ITO structured glass sample before processing the organic layer. Averaged $\mathcal{RGB}$ values of a non-structured area with the bare glass served as reference for the thickness estimation of the structured ITO layer. The determined thickness topography of the ITO layer is shown in Figure 2.21b. The mean thickness of the ITO fingers in Figure 2.21b resulted in $\overline{d}_{1,\mathrm{est}} = (144.1 \pm 1.2)$ nm using the ICR method and in (142.4 ± 0.6) nm using the spectroscopic reflectometry with the NanoCalc-2000.

After processing the organic layer, I imaged the sample with the same settings and at the same position beneath the microscope. The thickness map of the ITO layer (Figure 2.21b) was used as reference data for the algorithm. The resulting thicknesses distribution of the organic layer is depicted in Figure 2.21a. It is important to note that this 3D representation shows relative thickness values of the organic layer. This means that the steps generated by the ITO layer are not visible in the thickness of the organic layer, although it was deposited on the glass as well as on the ITO. For the organic layer, I determined the mean layer thickness to $\overline{d}_{2,\mathrm{est}} = (23.6 \pm 3.1)$ nm using the ICR method and to (24.9 ± 1.8) nm using the phase-shifting interferometry. These results again demonstrated the reliability of the method and its suitability for sequential thin film characterization as part of multilayer processing.

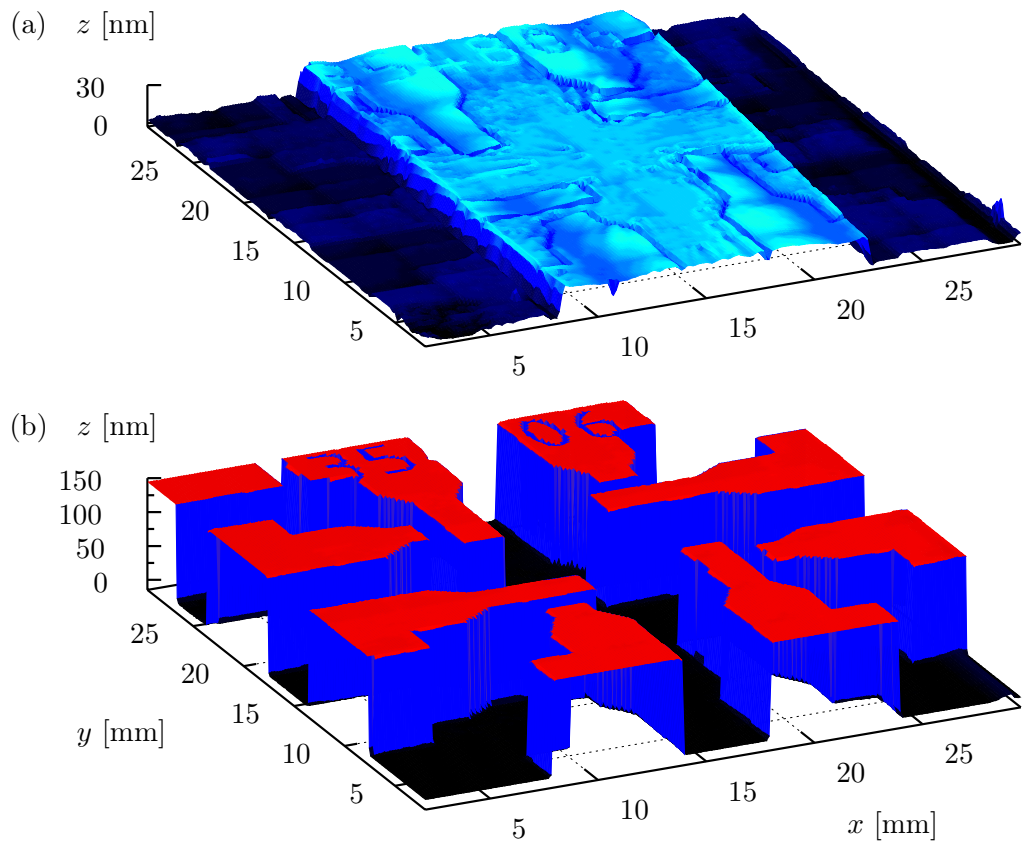

Figure 2.21: Relative layer thicknesses of the lithographically processed ITO layer in (b) and the consecutively spin-coated organic layer in (a) determined by the ICR method using the microscope. The thickness data in (b) was utilized as laterally resolved reference thicknesses for the estimation of the second layer in (a). The representations are aligned in x- and y-direction so that they can be understood as vertically stitched layer thicknesses.

2.6 Sensitivity/error analysis

In this section, I focus on the sensitivity of the proposed method related to errors originating either from the acquisition of the $\mathcal{RGB}$ raw data, the characterization of the optical hardware components or the adjustment of the theoretical model. This involves the variation of variables which initially were assumed to be constant. For a complete description of the problem, the dimension of the parameter space would expand from the 3-dimensional contrast space used before to a multi-dimensional one. Therefore, I avoided to analyze possible errors in terms of a Gaussian error propagation which would result in complex and excessive functional dependencies. I rather used the present measurements of the SiO_2/Si wafer with both setups and the existing estimation algorithm and induced errors to selected variables, i.e. to one specific variable at a time. Since the thicknesses are determined by exploring the minimum distance in the $\mathcal{RGB}$ contrast space, it is sufficient to change quantities in

the theoretical model without acquiring new images. Nevertheless, in Section 2.6.8, I performed new measurements of the SiO_2/Si wafer with the microscope using different objectives.

I reduced the analysis to those representative fields of the wafer which usually showed the most dominant behavior. However, the resulting thicknesses of all other fields related to the error propagation are included in the Appendix B.1 on pages 146 ff..

The layer thicknesses which were previously presented in Table 2.1 on page 37 of this section were determined based on average profiles of the complete thickness map of about 10^6 pixels. This equals the number of performed least-square estimation steps which were the most consuming time step within the calculation. To strongly reduced computation time for the present analysis, I averaged the image before I performed the thickness estimation, meaning I performed a single thickness estimation step. In this manner determined thickness values are shown in Table 2.3. Because of afore mentioned averaging step, these values slightly deviated from the ones previously given in Table 2.1.

The increment for the thickness estimation was set to 1 nm, in some cases it was reduced to 0.1 nm to give more accurate results. The initial upper and lower limits for the thickness range of the theoretical contrast values were set to $d_{1,r}^{\text{wide}} = 0, \ldots, 600$ nm (the same as for the calculation in Section 2.5.1) and additionally to a narrow window. This narrow window $d_{1,r}^{\text{narrow}}$ limited to ± 50 nm around the "true" thickness (manufacturer values given in Table 2.3) of each field was included to illustrate how prior knowledge of the sample improves the robustness of the method.

Apart from one example calculation, I chose field #6 with zero thickness of the SiO_2 as reference. When using a different field for reference, the resulting thicknesses slightly deviated from each other, as shown in Table 2.3 for reference fields #6 ($d_{1,\text{ref}} = 0$ nm) and #5 ($d_{1,\text{ref}} = 96.3$ nm).

Table 2.3: Layer thicknesses of the SiO_2 fields on the silicon wafer measured by spectroscopic ellipsometry (SE) (manufacturer) and by the proposed imaging color reflectometry (ICR) using the microscope and the modified flatbed scanner for different reference fields. $\mathcal{RGB}$ values were averaged and no errors were induced.

	Field #1	Field #2	Field #3	Field #4	Field #5	Field #6
Manufacturer (SE) [nm]	501.8	397.4	298.1	199.1	96.3	1.2
Microscope ICR Reference field #6 [nm]	503.4	399.0	299.0	199.0	98.7	Ref: 0
Microscope ICR Reference field #5 [nm]	502.7	403.5.2	297.1	204.0	Ref: 96.3	12.8
Scanner ICR Reference field #6 [nm]	502.5	398.1	298.3	198.8	98.2	Ref: 0
Scanner ICR Reference field #5 [nm]	500.4	406.9	296.0	202.1	Ref: 96.3	18.8

2.6.1 Robustness of the thickness estimation algorithm

Before going into detail about the error propagation for the present wafer sample, a possible origin for a failure of the algorithm is exemplary discussed.

The theoretical contrast values $c_k(d_{q,r})$ formulated in Equation 2.25 on page 26 span a curve parameterized by the film thickness range $d_{q,r}$ of the q-th layer in the 3-dimensional $\mathcal{RGB}$ contrast space. This is shown for SiO_2/Si wafer and the microscope setup in Figure Figure 2.22.

The measured, averaged contrast values of the six different fields of the sample are depicted as red triangles and the theoretical ones as black circles. For each thickness determination step (either per pixel or per averaged values), the algorithm finds the shortest distance between the measurements

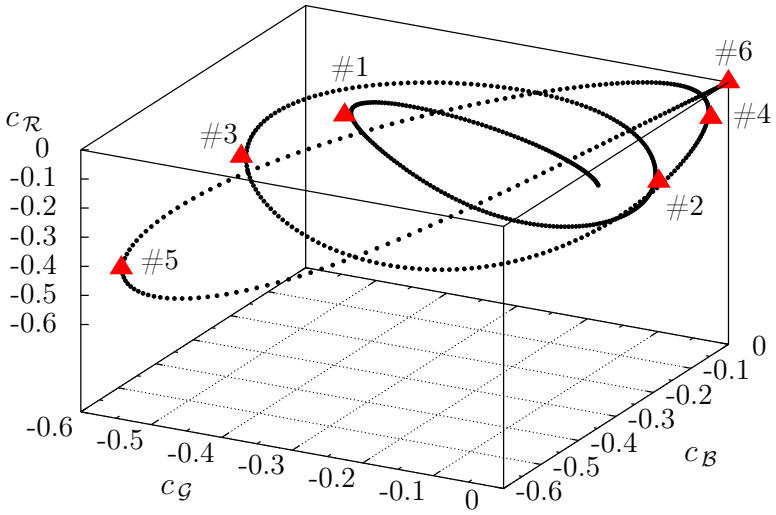

Figure 2.22: Theoretical contrast values $c_k(d_{1,r})$ of the SiO_2/Si wafer (black circles) according to Equation 2.25 for thicknesses ranging from $d_{1,r} = [0 \dots 600]$ nm for the microscope setup. Red triangles represent averaged measurements of contrast values of the reference wafer with thicknesses from 0 to 500 nm for fields #6 to #1 in steps of 100 nm.

(red triangles) and the point curve (black circles), and addresses the corresponding thicknesses to the measured values according to Equation 2.28. When the point curve has got a spiral structure in the 3D space such as shown in Figure 2.22, a failure of the algorithm occurs if the measured value (red triangle) is far from the "true" thickness. Then, the shortest distance can be close to a region of the curve of completely different thicknesses resulting in a value hundreds of nanometers off the "true" value. This failure is dependent on the length and the curvatures of the curve of the theoretical contrast values in the 3-dimensional space and will be less probable if the thickness range is reduced around the "true" value. The latter is recurringly illustrated in the following sections by simultaneously using the narrow range $d_{1,r}^{\text{narrow}}$ of the theoretical contrast values.

This failure mechanism might be strongly dependent on the number of dimensions of the imaging system, i.e. the number of color channels. For more channels the algorithm is more robust according to this miscalculation and for a smaller number of channels vice versa.

According to the propagation of errors (usually denoted with ε) into the estimated thicknesses of the SiO_2 layers on the wafer, the following seven main error sources motivate the choice of variables I varied.

2.6.2 Reference thickness value

The reference thickness which is required for the calculation of the theoretical contrast values (Equation 2.25) has to be determined by a separate type of measurement and can deviate from the "true" value. To analyze the sensitivity of the algorithm to a change of this thickness, I chose the un-coated field #6 and in a second step the field #5 as reference. For the first variation of the reference thickness in the estimation algorithm, I added an error of up to $\varepsilon = 10$ nm to the initial thickness which was set to $d_{1,\text{ref}} = 0$ nm of the un-coated field #6 according to Equation 2.32

$$d_{1,\text{ref}} \rightarrow d_{1,\text{ref}} + \varepsilon. \tag{2.32}$$

The effect on the resulting thickness values within the theoretical thickness range $d_{1,r}^{\text{wide}} = 0, \ldots, 600$ nm (0.1 nm steps) is depicted in Figure 2.23, here for the representative field #4. The blue circles repre-

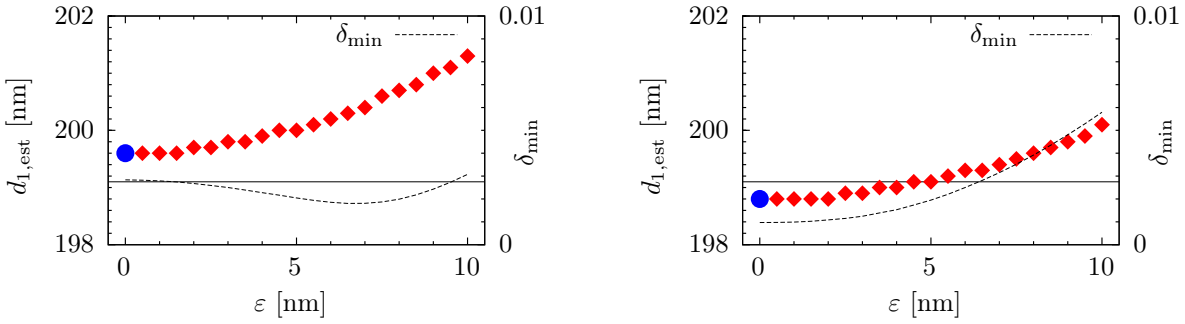

(a) Microscope: Field #4 (#6 as reference) **(b)** Scanner: Field #4 (#6 as reference)

Figure 2.23: Estimated thicknesses $d_{1,\text{est}}$ of SiO_2 of field #4 (red squares) in respect to a variation of the reference thickness $d_{1,\text{ref}} = 0$ nm of field #6 of up to $\varepsilon = 10$ nm. Blue circles depict the initial thickness values for $\varepsilon = 0$ nm. The black horizontal lines show the manufacturer thickness value for field #4. Residuals δ_{min} in contrast space are depicted as dashed curves.

sent the initial thickness values and the red squares the resulting thicknesses according to the variation ε. The black horizontal lines depict the thickness value of field #4 determined by the manufacturer (see Table 2.3). The dashed curves in Figure 2.23 show the residuals δ_{min} in contrast space, which, in the case of the microscope, exhibit a minimum at $\varepsilon_{\text{min}} = 7$ nm. However, the estimated thickness at this minimum is not approaching the "true" manufacturer value. For the scanner, the contrast residuals are monotonically increasing. The maximum absolute deviation gradient of the estimated thickness of field #4 according to the change of the reference thicknesses is only $|\frac{\Delta d_{1,\text{est}}}{\Delta \varepsilon}| = 0.2\ \frac{\text{nm}}{\text{nm}}$ for both the microscope (Figure 2.23a) and the flatbed scanner (Figure 2.23b). Here, $\Delta d_{1,\text{est}}$ and $\Delta\varepsilon$ denote the differences of that two data points for which the ratio $|\frac{\Delta d_{1,\text{est}}}{\Delta \varepsilon}|$ is maximized.

For the second variation, I used field #5 with a thickness set to $d_{1,\text{ref}} = 96.3$ nm as reference. The variation of the error ε added to the initial value ranged between $\varepsilon \in [-10, 10]$ nm. The change

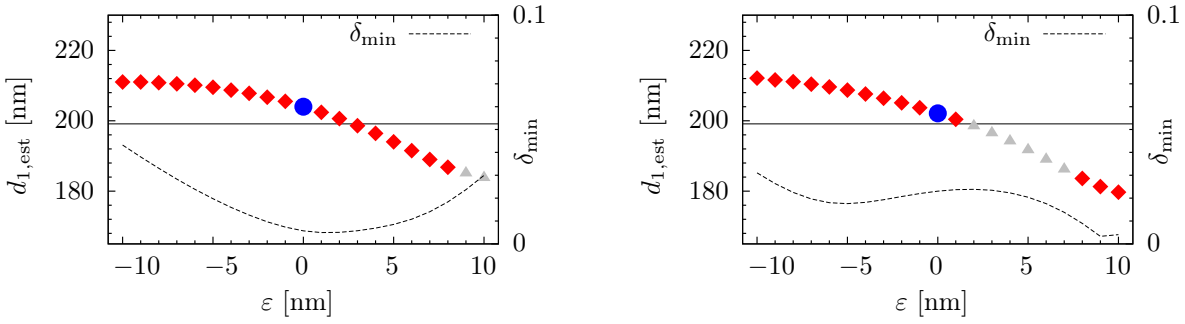

(a) Microscope: Field #4 (#5 as reference) **(b)** Scanner: Field #4 (#5 as reference)

Figure 2.24: Estimated thicknesses $d_{1,\text{est}}$ of SiO_2 of field #4 (red squares) in respect to a variation of the reference thickness $d_{1,\text{ref}} = 96.3$ nm of field #5 of up to $\varepsilon = \pm 10$ nm. Blue circles depict the initial thickness values for $\varepsilon = 0$ nm. Grey triangles show results using $d_{1,r}^{\text{narrow}}$ with simultaneous failure of the algorithm for $d_{1,r}^{\text{wide}}$. The black horizontal lines show the manufacturer thickness value for field #4. Residuals δ_{min} in contrast space are depicted as dashed curves.

of the estimated thicknesses is more pronounced than in the first case with a maximum deviation

gradient of $|\frac{\Delta d_{1,\text{est}}}{\Delta \varepsilon}| = 2.5\ \frac{\text{nm}}{\text{nm}}$ for the microscope (Figure 2.24a) and $|\frac{\Delta d_{1,\text{est}}}{\Delta \varepsilon}| = 2.8\ \frac{\text{nm}}{\text{nm}}$ for the flatbed scanner (Figure 2.24b).

Besides the red squares displaying results for the thickness range $d_{1,r}^{\text{wide}}$, the gray triangles show estimated thicknesses for the reduced thickness range $d_{1,r}^{\text{narrow}}$ where failure occurred when using the wide range (according to the mechanism described in Section 2.6.1). The reduced theoretical thickness range was narrowed to ±50 nm around the "true" (manufacturer) value. Hence, failure of the algorithm is avoided by reducing this range. In Figure 2.24, first failure within $d_{1,r}^{\text{wide}}$ occurred for a deviation of $\varepsilon = +9$ nm for the microscope and only $\varepsilon = +2$ nm for the scanner. This shows a possibly sensitive behavior of the estimation algorithm in respect to failure if the reference thickness value is uncertain.

2.6.3 Real part of the refractive index

The refractive indices of all materials have to be determined separately, for example by ellipsometric measurements. Especially the real part of those refractive indices which strongly influence the theoretical contrast values can differ from the "true" values. Additionally, solution-processed layers might vary according to their density. This directly change the refractive indices of the deposited material, as for example discussed by Bach et al. [249]. They summarize the variation of the real refractive index at $\lambda = 550$ nm of SiO_2 depending on various coating methods. Thereby, refractive indices of solution-processed layers vary about 2%.

Motivated by this, I varied the real part of the refractive indices of the top SiO_2 layer of the wafer by $\varepsilon = \pm 10\%$ in the theoretical model with field #6 as reference ($d_{1,\text{ref}} = 0$ nm). The induced error would shift the n-curve shown in Figure 2.13a on page 35 vertically up or down according to

$$n_1 \rightarrow n_1 + \varepsilon. \tag{2.33}$$

The variation of n_1 by ±10% resulted in the estimated layer thicknesses for field #1 shown in Figure 2.25 for the two setups. For both setups in Figure 2.25, we can identify a very high max-

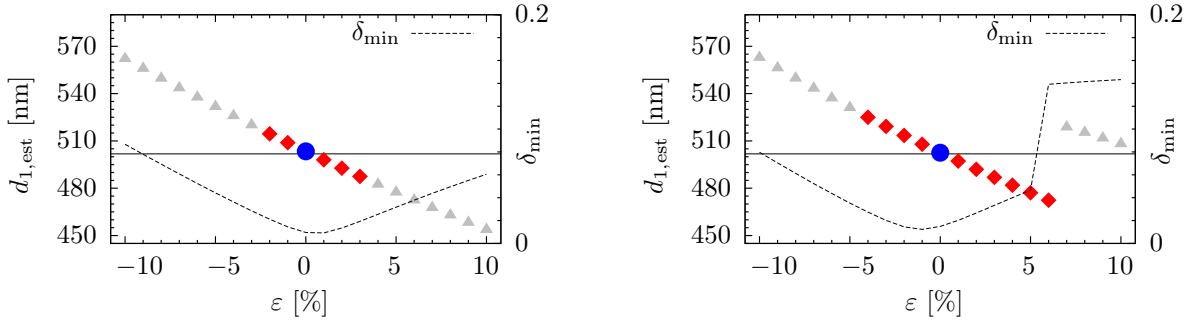

(a) Microscope: Field #1 **(b)** Scanner: Field #1

Figure 2.25: Estimated thicknesses $d_{1,\text{est}}$ (red squares) of the top SiO_2 layer in respect to the variation of its real refractive indices n_1 by $\varepsilon = \pm 10$ %. Blue circles depict thickness values for $\varepsilon = 0\%$. Grey triangles show results using $d_{1,r}^{\text{narrow}}$ with simultaneous failure of the algorithm for $d_{1,r}^{\text{wide}}$. The black horizontal lines show the manufacturer thickness value for field #1. Residuals δ_{min} in contrast space are depicted as dashed curves, the minima are located close to $\varepsilon_{\text{min}} = 0$ %.

imum gradient of $|\frac{\Delta d_{1,\text{est}}}{\Delta \varepsilon}| = 6.3\ \frac{\text{nm}}{\%}$ for the microscope and $|\frac{\Delta d_{1,\text{est}}}{\Delta \varepsilon}| = 6.6\ \frac{\text{nm}}{\%}$ (neglecting the step at $\varepsilon = 5$ %) for the scanner, respectively. This means that for the initially mentioned possible variation of the refractive index of 2%, the estimated thickness of the layers could differ by ±13 nm.

According to the wide range of theoretical thickness values $d_{1,r}^{\text{wide}}$, we observe failure of the thickness estimation for only $\varepsilon = -3$ % and $\varepsilon = -5$ %. However, the minima of the contrast residuals δ_{min} are both located at around $\varepsilon_{\text{min}} = 0$ % indicating that the initial n_1 values minimized the residuals.

2.6.4 Spectrum of the light source

All light sources degrade and change their spectra depending on the operation principle and on different timescales. Although degradation mechanisms of halogen bulbs usually arise within several hundreds of hours they tend to shift their peaks to lower wavelengths as I observed for the bulb of the present microscope for an operation period of four weeks. Those shifts are also present during the first minutes after switching on incandescent bulbs because of temperature rise rather than degradation. This type of short-time temperature dependent spectra shift occurs for all kind of light sources. I therefore analyzed the deviation of the thickness estimation with respect to a wavelength shift:

$$L(\lambda) \rightarrow L(\lambda + \varepsilon). \tag{2.34}$$

I shifted the complete spectrum of the microscope's halogen bulb and the scanner's fluorescent bulb (shown in Figure 2.5 and 2.10 on page 28 and 32) by $\varepsilon = \pm 5\%$[21] (± 20 nm). The resulting thicknesses of field #1 for the two hardware setups are depicted in Figure 2.26. For the microscope (Figure 2.26a),

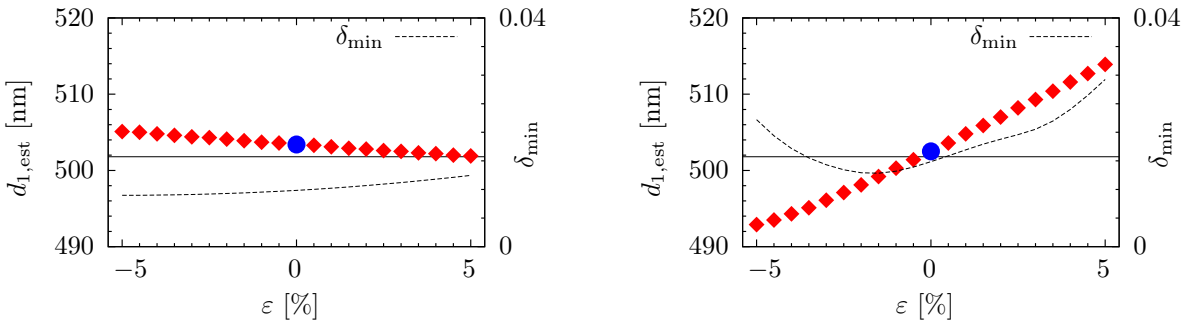

(a) Microscope: Field #1 **(b)** Scanner: Field #1

Figure 2.26: Estimated thicknesses $d_{1,\text{est}}$ (red squares) of the top SiO_2 layer in respect to a wavelength shift of the spectrum of the light sources $L(\lambda)$ by $\varepsilon = 5\%$ (20 nm). Blue circles depict thickness values for $\varepsilon = 0\%$. The black horizontal lines show the manufacturer thickness value for field #1. Residuals δ_{min} in contrast space are depicted as dashed curves.

the minimum of the contrast residuals is unpronounced and for the scanner, it is located at $\varepsilon = -1.5\%$ (-6 nm). The maximum deviation gradients of the estimated thicknesses for the microscope and the scanner in relation to the spectrum shift are $|\frac{\Delta d_{1,\text{est}}}{\Delta \varepsilon}| = 0.4 \ \frac{\text{nm}}{\%}$ and $|\frac{\Delta d_{1,\text{est}}}{\Delta \varepsilon}| = 2.4 \ \frac{\text{nm}}{\%}$. The reason for the higher deviation gradient of the scanner might originate from the different forms of the optical spectrum of the light sources. The spectrum of the incandescent bulb (Figure 2.5) of the microscope is continuous and broadband in contrast to the fluorescent bulb of the scanner (Figure 2.10) which mainly consists of several narrow-band wavelength peaks. On the other hand, a wavelength shift of $\varepsilon = \pm 5\%$ (± 20 nm) for a fluorescent bulb is very high and might not emerge to this extend in real measurements.

[21] in relation to the wavelength range of the visible spectrum from 380 nm to 780 nm

2.6.5 Positioning of the thin film sample

Acquiring the reference image of the desired sample with known thickness is usually performed before printing or coating the thin layer of interest. After the layer has been printed the positioning of the sample in front of the optical system may slightly change. This can lead to errors in the intensities being recorded by the sensors. To analyze this scenario, I induced errors only to the measured $\mathcal{RGB}$ values $\tilde{O}_k$ of the layer according to

$$\begin{aligned} \tilde{O}_k &\rightarrow \tilde{O}_k + \varepsilon \\ \tilde{O}_{k,\mathrm{ref}} &\rightarrow \tilde{O}_{k,\mathrm{ref}} \end{aligned} \tag{2.35}$$

with $\varepsilon = \pm 10\%$ and without changing the reference $\mathcal{RGB}$ values $\tilde{O}_{k,\mathrm{ref}}$. This approach would also take into account possible pixel- and time-dependent deviations of the camera sensor and intensity variations of the light source during early operation phases. The propagation of this type of error to the estimated thicknesses and the contrast residuals is shown in Figure 2.27. In this case, the

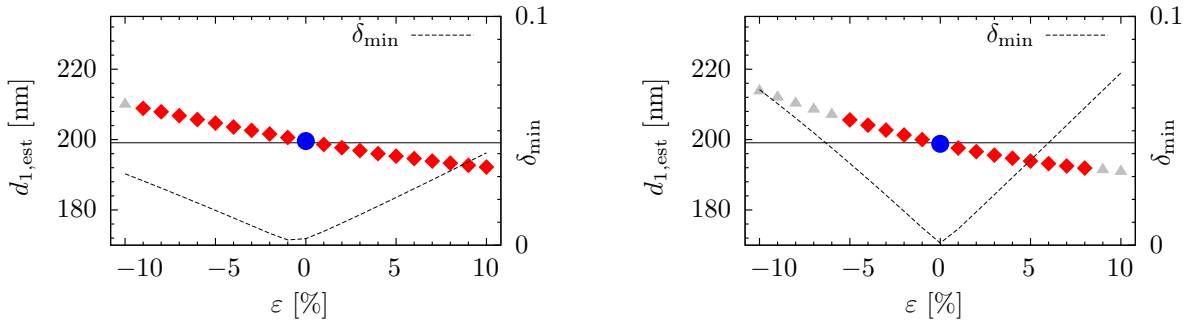

(a) Microscope: Field #4 **(b)** Scanner: Field #4

Figure 2.27: Estimated thicknesses $d_{1,\mathrm{est}}$ (red squares) of the top SiO_2 layer in respect to a variation of the measured $\mathcal{RGB}$ values of the layers by $\varepsilon = \pm 10\%$ apart from the reference field #6. Blue circles depict thickness values for $\varepsilon = 0\%$. Grey triangles show results using $d_{1,r}^{\mathrm{narrow}}$ with simultaneous failure of the algorithm for $d_{1,r}^{\mathrm{wide}}$. The black horizontal lines show the manufacturer thickness value for field #4. Residuals $\delta_{\min}$ in contrast space are depicted as dashed curves, both minima are at $\varepsilon_{\min} = 0$ %.

maximum gradients of the estimated thicknesses in relation to the addition of errors to the measured $\mathcal{RGB}$ values are $|\frac{\Delta d_{1,\mathrm{est}}}{\Delta \varepsilon}| = 1.1 \ \frac{\mathrm{nm}}{\%}$ for the microscope and $|\frac{\Delta d_{1,\mathrm{est}}}{\Delta \varepsilon}| = 1.8 \ \frac{\mathrm{nm}}{\%}$ for the scanner. Failure of the algorithm occurred for an error below $\varepsilon = -10$ % and $\varepsilon = -6$ %, respectively. Both contrast residuals $\delta_{\min}$ (dashed lines in Figure 2.27) show a pronounced minimum located at $\varepsilon_{\min} = 0$ % indicating reproducible sample positioning and intensities.

2.6.6 Scattered light

In real optical measurements, we always have to deal with light scattering effects originating from dust, surfaces, impurities of the optical elements and external illuminations. To estimate the influence of this error source on the resulting layer thicknesses, I added the same constant offset of up to

$\varepsilon = \pm 10\%$[22] to all measured $\mathcal{RGB}$ values ($\tilde{O}_k$ and $\tilde{O}_{k,\mathrm{ref}}$) of both the thin film sample and the reference field according to

$$\begin{aligned} \tilde{O}_k &\rightarrow \tilde{O}_k + \varepsilon \\ \tilde{O}_{k,\mathrm{ref}} &\rightarrow \tilde{O}_{k,\mathrm{ref}} + \varepsilon. \end{aligned} \tag{2.36}$$

Figure 2.28 presents the resulting layer thicknesses and the contrast residuals. From Figure 2.28 I

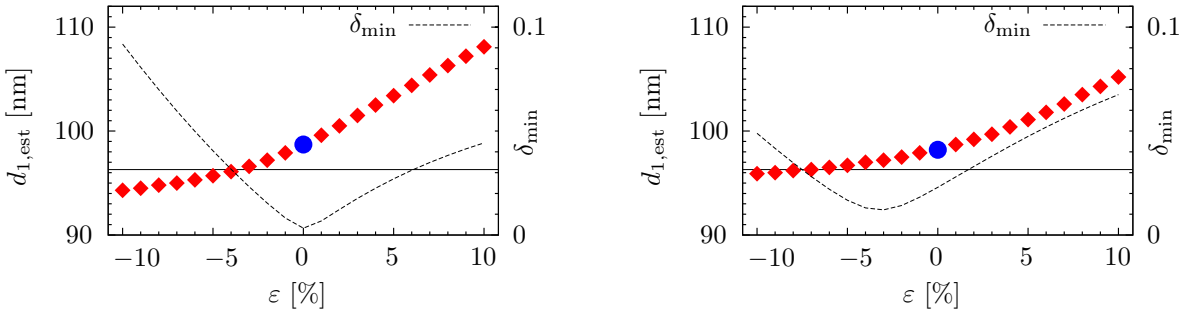

(a) Microscope: Field #5 **(b)** Scanner: Field #5

Figure 2.28: Estimated thicknesses $d_{1,\mathrm{est}}$ (red squares) of the top SiO_2 layer in respect to an offset added to all measured $\mathcal{RGB}$ values of $\varepsilon = \pm 10\%$. Blue circles depict thickness values for $\varepsilon = 0\%$. The black horizontal lines show the manufacturer thickness value for field #5. Residuals δ_{min} in contrast space are depicted as dashed curves.

deduce a maximum deviation gradient of $|\frac{\Delta d_{1,\mathrm{est}}}{\Delta \varepsilon}| = 1.0 \ \frac{\mathrm{nm}}{\%}$ for the microscope and $|\frac{\Delta d_{1,\mathrm{est}}}{\Delta \varepsilon}| = 0.9 \ \frac{\mathrm{nm}}{\%}$ for the scanner. The contrast residuals δ_{min}, shown as dashed lines in Figure 2.28, possess minima at $\varepsilon_{\mathrm{min}} = 0$ % and $\varepsilon_{\mathrm{min}} = -3$ %, respectively. For the microscope, the location of the minimum reveals the high quality of the optical setup and for the scanner, some small scattering or intensity issues.

2.6.7 Gamma correction

Usually, whenever images are recorded by a $\mathcal{RGB}$ camera or a flatbed scanner they are gamma (γ) encoded. This means that all digital $\mathcal{RGB}$ signals ($\tilde{O}_k$, $\tilde{O}_{k,\mathrm{ref}}$[23] and the image data used for hardware characterization) delivered by the camera or by the image acquisition software are normalized before and after raising to the power of $1/\gamma$ yielding

$$\tilde{O}_k = \left[\left(\frac{\tilde{O}_{k,\mathrm{raw}}}{O_{\mathrm{max}}} \right)^{1/\gamma} \right] \cdot O_{\mathrm{max}}, \tag{2.37}$$

where $\tilde{O}_{k,\mathrm{raw}}$ is the raw data of the image and O_{max} the maximum value per channel, usually 8-bit resulting in $O_{\mathrm{max}} = 255$. A displaying device actually performs the gamma correction of raising the signals to the power γ again to present the human observer an effective gamma of 1. Humans do not perceive changes in light intensity the linear way cameras do, they are more sensitive to changes in dark tones than to changes in bright tones. Therefore, the procedure of encoding and re-encoding allows the system to store more information of the dark tones in the digital image data without increasing the color depth. Since the present optical measurement method is based on a

[22] in relation to the overall maximum of all measured $\mathcal{RGB}$ values
[23] omitting the pixel-dependence ij

linear relation between light intensity impinging on the sensor and the corresponding digital values, a gamma of unity is required when analyzing the image data.

The software of the Leica microscope provided detailed options to control the image acquisition and the camera settings. Thereby, the gamma value was set to unity ($\gamma = 1$). Concerning the flatbed scanner setup, the software that controlled the movement of the scan head and reconstructed the image data provided settings stating to deliver a raw image. Although the documentation of the software and the hardware of the scanner did not contain information on the actual gamma value, the software indicated a gamma encoding[24] with $\gamma = 1.8$. Using the representative field #1 of the SiO_2/Si wafer imaged with the microscope and the flatbed scanner, I varied the exponent $\gamma_0 = 1.0$ and $\gamma_0 = 1.8$ of the microscope and the scanner by ± 0.2 and estimated the resulting thicknesses and corresponding distances in contrast space, as depicted in Figure 2.29. The gamma

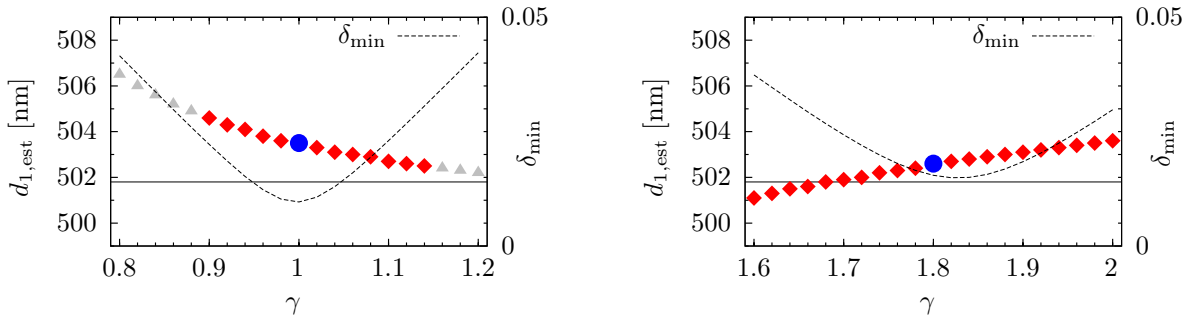

(a) Microscope: Field #1 with $\gamma_0 = 1$

(b) Scanner: Field #1 with $\gamma_0 = 1.8$

Figure 2.29: Estimated thicknesses $d_{1,\mathrm{est}}$ (red squares) of the top SiO_2 layers in respect to a variation of gamma around γ_0 (blue circles) by ± 0.2. Grey triangles show results using $d_{1,r}^{\mathrm{narrow}}$ with simultaneous failure of the algorithm for $d_{1,r}^{\mathrm{wide}}$. The black horizontal lines show the manufacturer thickness value for field #1. Residuals $\delta_{\min}$ in contrast space are depicted as dashed curves, their minima are located close to γ_0.

variation was also included in the characterization procedure of the optoelectronic transfer function of the microscope and the scanner which were based on 35 gamma-encoded images of well-defined interference filters, presented in Section 2.3. The maximum deviation gradients of the thickness values are only $|\frac{\Delta d_{1,\mathrm{est}}}{\Delta\gamma}| = 2.5\ \frac{\mathrm{nm}}{1}$ for the microscope and $|\frac{\Delta d_{1,\mathrm{est}}}{\Delta\gamma}| = 1.0\ \frac{\mathrm{nm}}{1}$ for the scanner. The curves of the minimum distances $\delta_{\min}$ for both setups shown as dashed lines in Figure 2.29 exhibit minima at gamma values of $\gamma_{\min} = 1.0$ and $\gamma_{\min} = 1.84$, respectively. Besides a deviation of 0.04 for the scanner, this proved that the gamma encoding of the systems behaved as expected, especially that the scanner raised the image data to the power of 1/1.8 which had to be corrected by the estimation algorithm with a gamma correction of the reciprocal value.

2.6.8 Deviation from normal oriented illumination and detection

Previously, I always assumed normal orientation of light source and detector relative to the sample surface ($\theta = 0\,^\circ$). In this section, I discuss deviations from this simplification by the following observations: First, inaccuracy in positioning the sample surface perpendicular to the optical path and second, real optical systems possess numerical apertures (NA) as mentioned in Section 2.3.1 and hence, distinct opening angles.

[24] here, with the exponent $1/\gamma$

Including this into the optical model requires an extension of the thin film interference (Section 2.2.3) concerning the polarization of light. The electric field vector of a light wave imping on a surface with an arbitrary incident angle θ (sketched in Figure 2.2) can be separated into two components. First, a vector component which is directed in the plane of the sample surface, denoted as s-polarization. And second, into a component which lies in the plane spanned by the incident and reflected light normal to the sample surface, denoted as p-polarization. These components exhibit different transitions for reflection and transmission at a surface. According to reference [152], I modify the phase shift within the thin layers previously described by Equation 2.13 and apply the so-called pseudo-indices instead of the refractive indices (Equation 2.8) in the optical interference model (Section 2.2.3) as described in the following.

The phase shift $\tilde{\varphi}_l$ originating from inside the layer l including an arbitrary incident angle of θ (see Figure 2.2) now yields [152]

$$\tilde{\varphi}_l = \frac{2\pi\, d_l}{\lambda}\sqrt{N_l^2 - N_{\text{air}}^2 \sin^2\theta}. \tag{2.38}$$

In Equation 2.14 which represents the Abele matrices of the thin film stack, (φ_l, N_l) should be replaced by $(\tilde{\varphi}_l, \tilde{N}_l^{\text{s}}, \tilde{N}_l^{\text{p}})$, where $\tilde{N}_l^{\text{s}}$ and $\tilde{N}_l^{\text{p}}$ are the pseudo-indices defined for the s- and p-polarization as follows [152]

$$\begin{aligned} \tilde{N}_l^{\text{s}} &= N_i \cos\theta \\ \tilde{N}_l^{\text{p}} &= N_i / \cos\theta. \end{aligned} \tag{2.39}$$

The reflection and transmission coefficients r_{f} and t_{f} (Equation 2.16 and 2.17) of the thin film stack are also separated into corresponding s- and p-components each. Therefore, all refractive indices occurring in Equations 2.16 and 2.17 should be replaced by the corresponding pseudo-indices defined in Equation 2.39. To account for backside reflections from the bottom of the substrate/air interface, I replace φ_0 in Equation 2.20 by $\tilde{\varphi}_0$. This results in a total θ-dependent spectral reflectance at the film stack of $\tilde{R}^{\text{s}}_{\text{total}}(\theta)$ and $\tilde{R}^{\text{p}}_{\text{total}}(\theta)$. The remaining question is how to implement the s- and p-components of the polarization and the θ-dependence into the optical system model (Equation 2.6). For this purpose, it is reasonable to assume that the polarization states of the light sources (halogen and fluorescent bulb) are randomly distributed. This was proven by imaging the light sources through a linear polarizer in front of the sensor which was rotated by 180°. The variation of the resulting $\mathcal{RGB}$ values was below 5 % for both setups. This allows me to simply integrate $\tilde{R}^{\text{s}}_{\text{total}}(\theta)$ and $\tilde{R}^{\text{p}}_{\text{total}}(\theta)$ from 0 to $\theta_{\max}$ for both polarizations and average them according to

$$R_{\text{total}} = \frac{1}{C}\int_0^{\theta_{\max}} \tilde{R}^{\text{s}}_{\text{total}}(\theta) + \tilde{R}^{\text{p}}_{\text{total}}(\theta)\ \mathrm{d}\theta, \tag{2.40}$$

where C is a normalization constant. Equation 2.40 is applicable if the aperture of the optical system is circular which is valid for the microscope. But in the case of the flatbed scanner, the aperture or the maximum opening angles are strongly non-circular and hence, $\theta_{\max}$ depends on the polar angle in the plane of the sample surface as it is discussed in the paragraph on page 54. In the following two paragraphs, I adapt the optical model including arbitrary incident angles θ to estimate thicknesses from images of the SiO_2/Si wafer acquired by the microscope with different objectives and the flatbed scanner.

Optical microscope

As discussed in Section 2.3.1, the numerical aperture defines half the maximum opening angle α of microscope objectives. Without changing the algorithm to include arbitrary incident angles θ, I performed the thickness estimation of the SiO_2/Si wafer as before but using objectives with different magnification (MA) and numerical apertures (NA) as shown in Table 2.4. Using the different

Table 2.4: Leica microscope objectives used in the present study with MA, NA, α and FOV denoting the magnification of the objectives, numerical aperture, the resulting maximum half opening angle (according to Figure 2.4 and Equation 2.30) and the field of view that is imaged with the camera chip.

Objective	MA	NA	α	FOV
1	2.5x	0.07	4.0 °	5222×3916 µm^2
2	5x	0.12	6.9 °	2611×1958 µm^2
3	10x	0.25	14.5 °	1305×979 µm^2
4	20x	0.40	23.6 °	653×490 µm^2
5	50x	0.75	48.6 °	261×196 µm^2
6	100x	0.85	58.2 °	131×98 µm^2

objectives with different maximum half opening angles α, I effectively induced a larger physical deviation from normal incidence and detection compared to the simple estimation algorithm that assumed $\theta = \alpha = 0$. Figure 2.30a shows the resulting thicknesses of field #1 (results for the other fields can be found in the Appendix B.1 on page 154) and the corresponding contrast residuals $\delta_{\min}$ using the simple model. Figure 2.30b depicts the thickness results estimated from the images but analyzed using the modified optical model in which θ-dependency was implemented as described in the previous paragraph. I set $\theta_{\max} = \alpha$ and performed the integration over θ according to Equation 2.40. As expected, the objective 1 with $\alpha = 4.0\,°$ exhibits the smallest minimal contrast residual

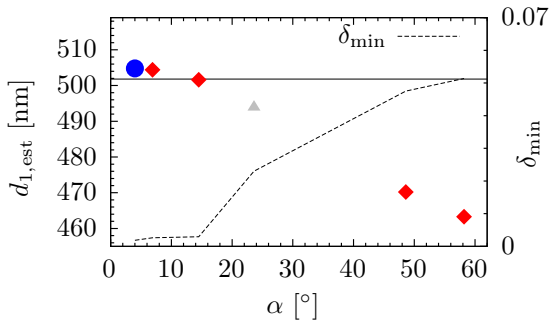

(a) Microscope: Wafer field #1 without θ-dependency ($\theta = 0$) in the algorithm. α denoting the maximum half opening angle of the different objectives.

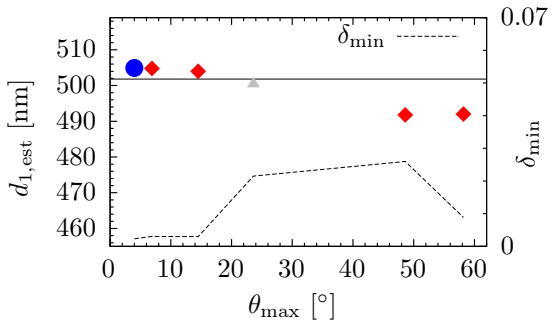

(b) Microscope: Wafer field #1 with θ-dependency in the algorithm, $\theta_{\max} = \alpha$ and using Equation 2.40 where the spectral reflectance was integrated from 0 to $\theta_{\max}$.

Figure 2.30: Estimated thicknesses $d_{1,\mathrm{est}}$ (red squares) of the top SiO_2 layers in respect to a variation of the microscope objectives and hence of the maximum physical half opening angles from $\alpha = 4\,°$ to $\alpha = 58.2\,°$ using different algorithms. Grey triangles show the result using $d_{1,r}^{\mathrm{narrow}}$ with simultaneous failure of the algorithm for $d_{1,r}^{\mathrm{wide}}$. The black horizontal lines show the manufacturer thickness value for field #1. Residuals $\delta_{\min}$ in contrast space are depicted as dashed curves.

and objective 6 with $\alpha = 58.2\,^\circ$ the largest one for the simple algorithm in Figure 2.30a. For the θ-dependent algorithm, the contrast residuals are clearly reduced for objectives 5 ($\alpha = 48.6\,^\circ$) and 6 ($\alpha = 58.2\,^\circ$) in Figure 2.30b. Additionally, I chose objective 5 to test whether the advanced algorithm minimized the contrast residual for varying the upper integration limit of $\theta_{\max}$ from $0\,^\circ$ to $70\,^\circ$. Then, I would expect a minimum of the contrast residual $\delta_{\min}$ at $\theta_{\max} = 48.6\,^\circ$. Figure 2.31 depicts the thickness results for wafer field #1 with the 50x objective 5 according to the variation of the upper integration limit $\theta_{\max}$. Indeed, the contrast residuals show a minimum at $\theta_{\max} = 55.0\,^\circ$ in Figure 2.31. Aside from a deviation of $6.4\,^\circ$, this result verified that the advanced algorithm with

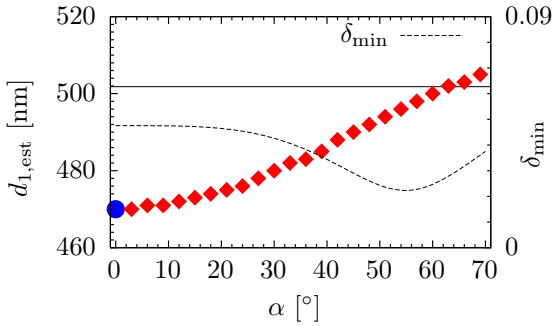

Figure 2.31: Estimated thicknesses $d_{1,\mathrm{est}}$ (red squares) of the SiO_2 layer of field #1 with respect to a variation of the upper angle of incidence $\theta_{\max}$ using the 50x objective 5 ($\alpha = 48.6\,^\circ$) and the θ-dependent algorithm. The black horizontal lines show the manufacturer thickness value for field #1. Residuals $\delta_{\min}$ in contrast space are depicted as dashed curves, the minimum of $\delta_{\min}$ is at $\theta_{\max} = 55\,^\circ$.

implemented θ-dependency is suitable for microscope objectives with high numerical apertures.

Based on the results for the SiO_2/Si sample shown in Figure 2.30, I conclude that the implementation of θ-dependency noticeably improves the outcome of the method for microscope objectives with NA> 0.25 ($\alpha > 14.5\,^\circ$). Below this value, the simpler and faster algorithm neglecting deviations to the normal orientation could be considered.

Modified flatbed scanner

In principle, the flatbed scanner was set up to operate with normal oriented illumination and detection. But just as the microscope or any other real optical detection system, the flatbed scanner images the sample with a deviation from the normal $90\,^\circ$ orientation to the sample surface. The numerical aperture was not specified by the manufacturer, therefore I developed a method to estimated the maximum half opening angle by scanning a well-defined metallic sphere with a diameter of 13.9 ± 0.03 mm. The acquired gray-scale image is shown in Figure 2.32, where the image was scanned in y-direction. Comparing the maximum size of the elliptical white area in x- and y-direction in the center of Figure 2.32 to the diameter and curvature of the sphere allowed an estimation of the maximum half opening angles. The half opening angles for which incident and reflecting angle of the light at the sphere surface were equal, obviously differ in x- and y-direction for a line scanner setup. Taking this into account, I denote the effective maximum half opening angles with $\alpha_{x,\mathrm{eff}}$ and $\alpha_{y,\mathrm{eff}}$ for the two directions. From image analysis and geometrical considerations of Figure 2.32, I determined a large angle of $\alpha_{x,\mathrm{eff}} = 40.9\,^\circ$ perpendicular to scan direction and a small angle $\alpha_{y,\mathrm{eff}} = 2.8\,^\circ$ in scan direction. I then assumed that these half opening angles equals the maximum angles of incidence $\theta_{\max,x} = \alpha_{x,\mathrm{eff}}$ and $\theta_{\max,y} = \alpha_{y,\mathrm{eff}}$. Hence, I faced the problem that $\theta_{\max}$ was not constant throughout the illuminated sample surface. I assumed that the latter is of elliptic shape and θ depends on the

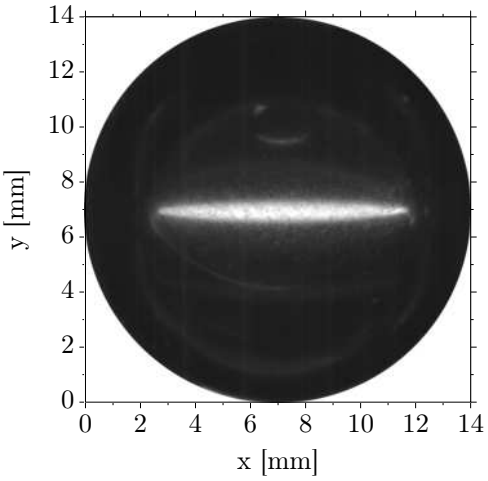

Figure 2.32: Acquired gray-scale image of a metallic sphere with a diameter of 13.9 ± 0.03 mm using the modified flatbed scanner. Equal angles of incidence and reflection at the surface of the sphere resulted in the white (bright) ellipse in the center. Geometric relations yielded $\alpha_{x,\mathrm{eff}} = 40.9\,^\circ$ in x and $\alpha_{y,\mathrm{eff}} = 2.8\,^\circ$ in y-direction.

polar angle ϕ as sketched in Figure 2.33. Therefore, the single integration in Equation 2.40 was not

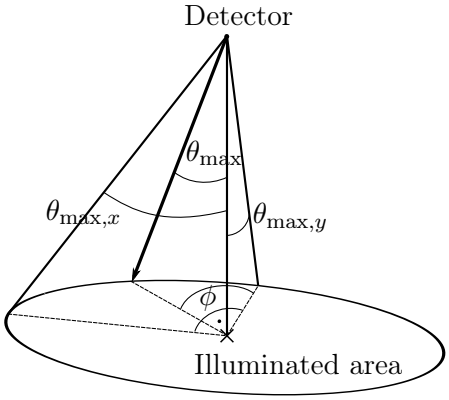

Figure 2.33: Geometrical relations between the maximum half opening angle θ_{max} and the polar angle ϕ for an elliptic illuminated and detected area according to the flatbed scanner setup.

applicable and I also integrated over the polar angle ϕ as follows

$$R_{\mathrm{total}} = \frac{1}{C}\left(\int_0^{2\pi}\int_0^{\theta_{\mathrm{max}}(\phi)} \tilde{R}^{\mathrm{s}}_{\mathrm{total}}(\theta) + \tilde{R}^{\mathrm{p}}_{\mathrm{total}}(\theta)\ \mathrm{d}\theta\ \mathrm{d}\phi\right), \tag{2.41}$$

where C is a normalization constant and $\theta_{\mathrm{max}}(\phi)$ is the half opening angle dependent on the polar angle ϕ in the plane of the illuminated surface as illustrated in Figure 2.33. Geometric considerations on the basis of an ellipse resulted in the following relation for θ and ϕ

$$\theta_{\mathrm{max}}(\phi) = \arctan\left(\frac{\tan\theta_{\mathrm{max},x}\tan\theta_{\mathrm{max},y}}{\sqrt{(\theta_{\mathrm{max},x}\sin\phi)^2 + (\theta_{\mathrm{max},y}\cos\phi)^2}}\right). \tag{2.42}$$

I then applied this formula to estimate the thickness of the different fields of the pixel-averaged wafer image (Figure 2.14) and compared the results to values that are compared to the ones estimated

without θ-correction and those given by the manufacturer in Table 2.5. From Table 2.5, I deduced

Table 2.5: Layer thicknesses of the different SiO_2 fields on the silicon wafer measured by spectroscopic ellipsometry (SE) (manufacturer) and by the proposed imaging color reflectometry (ICR) using the modified flatbed scanner with and without θ-dependence.

	Field #1	Field #2	Field #3	Field #4	Field #5
SE [nm]	501.8	397.4	298.1	199.1	96.3
ICR without θ [nm]	502.5	398.1	298.3	198.8	98.2
Residual $\delta_{\min}$	0.0149	0.0069	0.0202	0.0010	0.0229
ICR with θ [nm]	521.0	412.0	309.0	206.0	101.0
Residual $\delta_{\min}$	0.0104	0.0121	0.0026	0.0026	0.0169

that for the scanner setup the implementation of the θ-dependence did not improve the outcome of the algorithm, to the contrary, it deteriorated the results. The contrast residuals were only reduced for three of the five fields and the difference to the manufacturer values were increased in all cases. The reason for this remained unresolved, it might originated from the optical setup. In contrast to the microscope, the light source and detector of the scanner did not exhibit similar optical paths. Therefore, the assumption made above that half the opening angle determined in Figure 2.32 equals the maximum angle of incidence could be incorrect.

2.7 Summary and conclusion

For measuring laterally resolved ultra-thin organic or inorganic layers with thicknesses below 1 µm on a large scale (decimeter range and possibly above), I presented a method based on optical thin film interference. The method is denoted as *imaging color reflectometry* (ICR) because the imaging element is a standard $\mathcal{RGB}$ camera. As the only hardware requirement, the incident light angle and the observation angle of the optical setup should be equal and close to the normal of the sample surface. Optical microscopes operating in bright field mode match this condition by default with normally oriented illumination and detection. I successfully adopted a Leica microscope which was able to automatically image large areas of up to 98×80 mm^2 using a built-in stitching technique. Additionally, a commercially Epson flatbed scanner was modified to operate with normally oriented illumination by installing a beam-splitter.

A least-square based estimation algorithm was developed in MATLAB which compared measured $\mathcal{RGB}$ contrast values to theoretical ones predicted by an optical model. This model describes the thin film interference and the optical setup which had to be spectrally characterized. Using contrast values of an image of the thin film stack and a reference image of a well-defined sample, the algorithm provided a laterally resolved thickness map of the top unknown layer of interest.

The requirement the samples have to fulfill is that at least the top layer of interest is semi-transparent. The refractive indices of the layers have to be known and constant during the measurement and have to considerably differ from each other for the various layers. The present optical model neglects diffraction, scattering and non-linear optical effects as well as phosphorescent or fluorescent properties of the materials in the visible region.

Both setups revealed reliable thickness determination of the test samples matching the results of corresponding reference methods. The high quality optical system of the microscope gave slightly

better results than the modified scanner, but the scanner acquired the test samples within half a minute, a factor of 30 faster than the microscope. The scanner occasionally produced images with artifacts of rings whose origins remained unresolved and it was inflexible according to adjusting exposure times for different types of samples.

The method was successfully applied to measure the different thicknesses of a sequentially processed multi-layer sample as a vertically stitched representation.

A detailed sensitivity analysis for selected variables within the estimation algorithm and the setup was presented. The combined behavior and the resulting magnitude of error propagation in general might exceed the values shown in the analysis. But a relative classification according to the maximum gradient of the resulting thickness deviation and the robustness of the algorithm could be extracted.

This allows the conclusion that the proposed ICR method is most sensitive to deviations of the refractive indices of the layers. The method can also drastically react against variations of the reference layer thickness, if the absolute reference thickness is arbitrary. Whereas, for a reference layer thickness close to zero, the method produces robust results. The sensitivity analysis also revealed that the method is stable against spectral and intensity variations of the light source.

Initially, the underlying optical model neglected deviations from the normal optical orientation of the setups. But based on measurements with different objectives (and numerical apertures) of the microscope, I analyzed considerable deviations from the normal optical orientation both experimentally and in the physical model. As a consequence, I found that for incident (and observing) angles below $\theta = 14.5\,^{\circ}$, the simple estimation algorithm assuming normal incidence produced reliable results. The latter also implies that the method is suitable for substrate geometries which obey curvatures, slopes or wavy undulations enclosing angles to the mean surface below $14.5\,^{\circ}$.

2.8 Outlook

A drawback of the present measurement system is that I neglected noise terms in the system model and inaccurately characterized the optical unit. An improvement of these two aspects would strongly enhance the outcome of the method.

The principle of varying possible error-prone quantities, such as the gamma correction (Section 2.6.7), showed that by analyzing the residuals of the algorithm, I could perform a sort of optimization procedure. In this manner a more advanced thickness estimation algorithm could autonomously perform a multi-dimensional optimization procedure to compensate deficiencies of the optical system or inaccuracies of the properties of the sample. This would strongly improve the robustness and the reliability of the method.

Furthermore, an extended algorithm and an optically more precise setup could also estimate an additional quantity such as the refractive indices. This would open the possibility to determine the last stage of the drying phase of a thin liquid film whose refractive indices temporally approach the value of the solid material. It is assumed that the late stage of the drying of organic layers strongly affect the quality of the solid film. Thereby, this evolution could be captured by measuring the layer thickness dynamics.

The latter approach requires capturing video streams which either could be analyzed off-line afterwards or processed in real time. This leads to the most obvious enhancement of the method, to an inline large-area thickness determination method. For single layer processing, the method can easily be adapted by handling look-up tables of the desired thicknesses. The corresponding algorithm

could be implemented on a graphic card of a standard personal computer operating in a thickness "video" mode.

As I motivated in the discussion of the robustness of the method (Section 2.6.1), the number of color channels of the camera is a significant property of the setup. An analysis on how this number affects the potential of the method is an important aspect. It would be interesting if there exists a finite number of channels for which the method reaches a maximum of accuracy and reliability. Thereby, multi-spectral cameras with up to 12-channels[25], which possess still much lower initial cost than imaging spectrophotometers, and which might become standard inspection cameras for printing and coating processes, could be easily utilized for the present measurement principle.

[25]for example the 12 color channel camera truePIXA-12C from Chromasens, Germany

Chapter 3

Physical introduction to gravure printing

Abstract

Gravure printing might be a simple wet process at a first glance, but in detail, this printing technique combines different physical aspects whose mechanisms are still not completely understood. In industrial gravure printing, maximum velocities are 15 m/s on meter-sized substrate widths while the ink transfer proceeds in the micrometer range. This reveals a highly dynamic process which is difficult to observe or simulate directly. This chapter introduces the basic physics relevant for a detailed description of the main ink-based part of the printing process. Important aspects involve the characteristics of the ink and under which circumstances the ink is transferred to the substrate and wets its surface. Aside from the physical models, I present new modified printing setups with color inks which give important insights into the main ink transferring mechanisms. Furthermore, I separate gravure printing into five different sub-processes which categorize relevant phases from ink acquisition to solidification while involving important aspects from the literature and from afore mentioned printing experiments.

3.1 Introduction

Gravure printing is a very old technique to reproduce information. First inventions go back to the 18th century, when Thomas Bell applied an English patent for a cloth printing press [136]. Gravure printing with electromechanical engraved cylinders of nowadays mass production was introduced by Rudolf Hell in the nineteen sixties [136].

Main products of gravure printing are high quality magazines and packaging products with a high circulation. This is because the high initial costs of a gravure cylinder are only amortized after a large number of printed copies.

The basic operational principal of roto-gravure printing is that ink is filled in microscopic engraved cells (typical width of ~ 150 µm and depth of ~ 20 µm) reproducing the thereby screened image to a substrate by contact-based ink transfer. Colored products are commonly printed using consecutively arranged printing units, each for one type of color and with its own gravure cylinder.

The gravure printing method has been optimized for graphical applications and industrial printing machines for magazines achieve printing velocities of up to 15 m/s [136]. The typical ink volume which is transferred per gravure cell to the substrate is only 50 pl (picoliter) within ~ 1 ms at this fastest velocity.

This involves precisely optimized parameters for the printing process as well as for the inks and the substrates. The physical basics describing this complex interplay are introduced in the present chapter.

First, I divide gravure printing into sub-process classifying different fluid-dynamical regimes while referring to the literature. In Section 3.3, I introduce important fluid parameters followed by presenting the governing hydrodynamic equations and common models of printing nip instabilities and thin film dynamics. Section 3.7 presents the results of preliminary printing experiments using color inks which give important insights into the underlying ink transfer mechanisms. The chapter closes with a summary, an experimental outlook.

Gravure printing

Figure 3.1 shows the sketch of a typical gravure printing unit as used in the present study.

The main parts promoting the ink transfer from the gravure cells to the substrate are the ink reservoir, the doctor blade, the gravure cylinder and the impression cylinder (or roller). The gravure cylinder rotates and its cells are filled with ink from the reservoir. A doctor blade usually made of thin stainless steel which is oriented under a macroscopic blade angle $\alpha_{\mathrm{bl}} < 90\,^\circ$ to the tangent of the contact line, commonly $\alpha_{\mathrm{bl}} \sim 60\,^\circ$ [89], wipes off excess ink, as shown in Figure 3.1. The actual microscopic blade angle at the tip might be smaller because the blade is pressed against the cylinder which bends the blade.

The gravure cylinder is usually made of a steel core cylinder which has been plated with a $0.2, \ldots, 2$ mm thick copper layer [89, 136]. The screened image is electro-mechanically engraved using a diamond stylus whose tip is defined by its stylus angle α_{St} [189, 237]. The latter strongly influences the form of the square, inverted pyramids. This engraved copper layer is then plated with a thin (~ 10 µm) chromium layer and polished to exhibit a desired roughness. The roughness is intended to enable lubrication of the doctor blade and hence, extends its shelf life [89, 136]. Additional fabrication techniques to produce cell structures on gravure cylinders are laser writing and etching methods [89, 101, 136, 237]. However, such processed cylinders are not used in the present study and therefore, not further discussed.

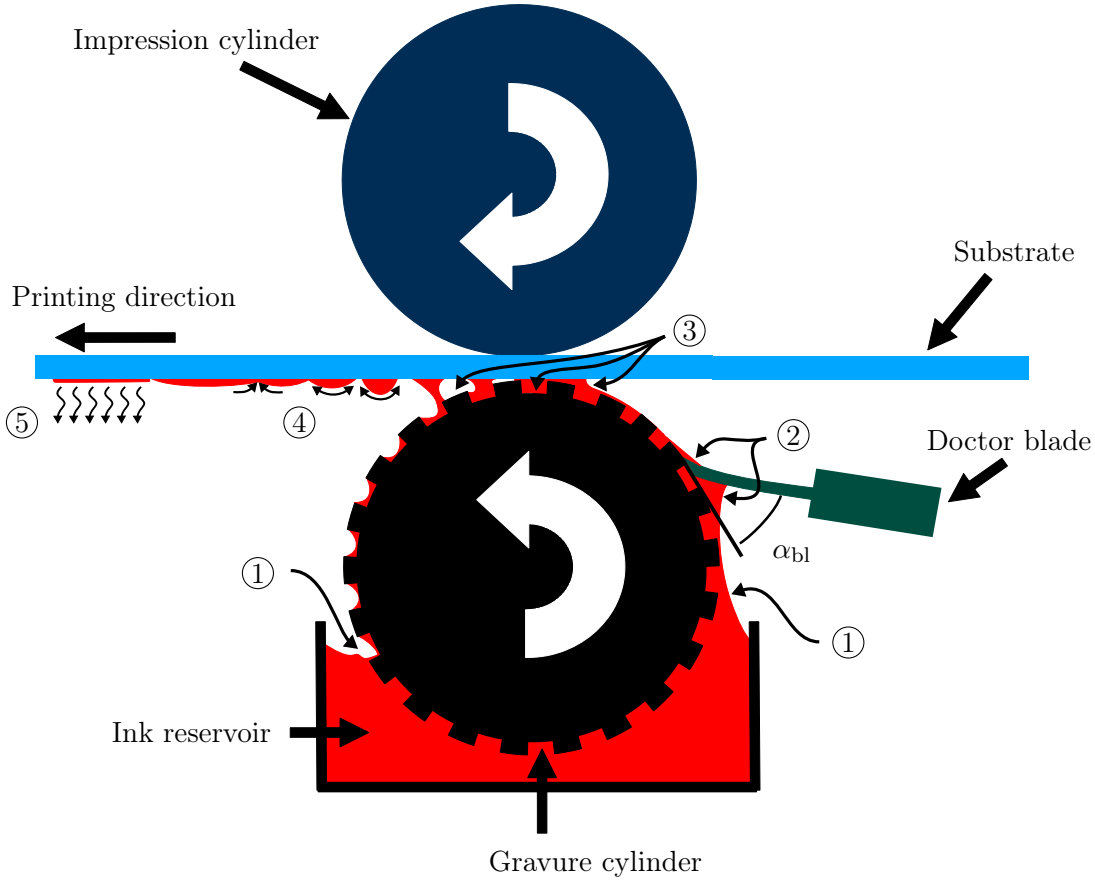

Figure 3.1: Sketch of a typical sheet-fed gravure printing unit. Main parts promoting the ink transfer to the substrate are the ink reservoir, the doctor blade, the gravure cylinder and the impression cylinder (or roller). The process is separated into five different regimes: ① Ink acquisition from the reservoir, ② Dosing of the ink (doctor blade process), ③ Ink transfer, ④ Fluid dynamics on the substrate, ⑤ Solidification (drying, curing), see text on pages 63 ff. for details.

A microscopic topography[1] of a typical electromechanical engraved gravure cylinder surface with its pyramidal cells is shown in Figure 3.2.

Important parameters describing the electromechanical engravings are the screen angle α_{SR}, the screen ruling SR with unit lines per centimeter [L/cm], the stylus angle α_{St}, the cell volume V_c in units milliliter per square-meter [ml/m^2], the cell depth d_c in micrometer [µm] and the tonal value in percent [%]. The screen angle α_{SR} defines the orientation of the cells with respect to the rotational axis of the cylinder. The screen ruling SR is the inverse of the distance between two gravure cells in the direction of the screen angle. The two parameters are illustrated in Figure 3.2.

The tonal values describe the area coverage of the cylinder surface with gravure cells and are normalized by a 100% field which is usually not exactly defined. Therefore, this parameter is not further discussed nor used in the present study. The cell volume V_c is equivalent to the volume which was removed to fabricate the cell. I chose to treat the two parameters screen ruling SR and cell volume V_c as main independent quantities for the further discussion because the stylus and the screen angle are not significantly changed in the present printing experiments.

[1] acquired by confocal microscopy, see Appendix A.1 for details on this technique

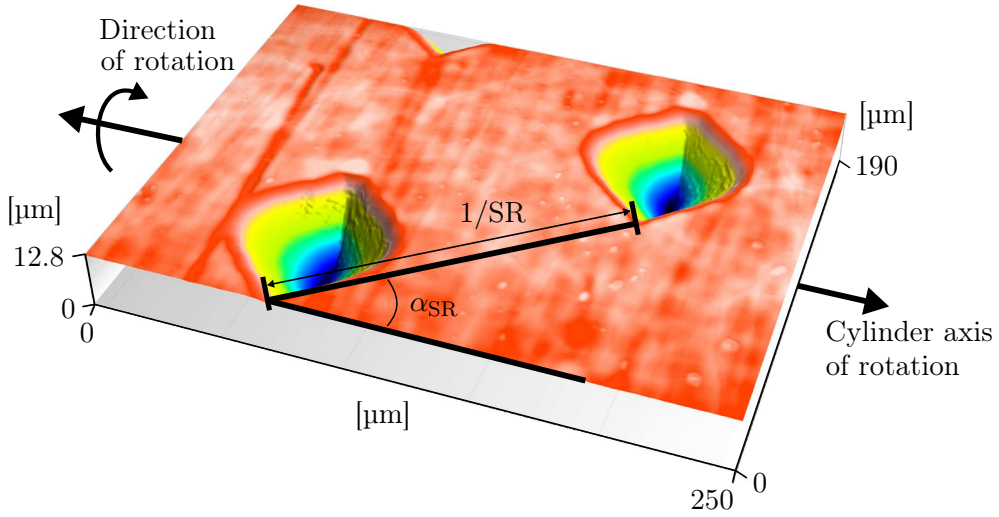

Figure 3.2: Topography of a typical electromechanically engraved gravure cylinder acquired by confocal microscopy. α_{SR} and SR denote the screen angle and the screen ruling (here 53 ° and 70 L/cm). The inverse of the screen ruling is the repeating distance along the screen angle between two adjacent gravure cells. Reprinted with permission of IS&T (The Society for Imaging Science and Technology) from [27].

3.2 Gravure printing separated into sub-processes

Gravure printing requires a complex interplay between different process and material parameters. In the following, I give a brief overview of the main mechanisms acting on the ink on its way through a gravure printing press onto a substrate. I restrict the introduction to non-absorbing substrates because of the underlying application of electronic devices which usually involves foils, glass or silicon substrates. For detailed implementations of gravure printing tools and their range of capabilities, I refer to textbooks of Kipphan [136] and the Gravure Association of America [89].

The most complete investigations capturing the main ink-relevant processes in gravure printing are given by Joyce [122], Kunz [144] and Bery [18, 19]. Bery separates gravure printing into five sub-processes [18, 19]: first, "gravure cylinder inking"; second, "doctoring"; third, "complex of physicochemical processes after doctoring and before impression"; fourth, "ink transfer"; fifth, "flow on the substrate after the filament rupture". Recently, Stahl [237], Fell [68] and Neff [187] give alternative summaries of the complete process involving some aspects of the other authors. Stahl gives a comprehensive list of important parameters affecting the gravure printing process which provides new aspects. Neff more focusses on the last process according to ink spreading on the substrate [187] and Fell experimentally analyze wetting aspects associated to gravure printing for complex fluids in detail [68].

Taking up Bery's phases, I also divide gravure printing into five regimes, but I count his third phase to the doctoring and graduate his last process into "fluid dynamics on the substrate" and "solidification (drying, curing)". Among others, this was motivated by defining a classification which should not only be applicable to gravure printing but also to flexographic, screen and ink-jet printing.[2] Additionally, the focus of the present study using gravure printing is on processing low viscous inks which tend to give rise to much faster dynamics on the substrate (see Section 3.6) before evaporation and drying.

[2] I introduced this approach first when I prepared the lecture notes for *Printing Technology for Electronics* [60], summer term 2011 at TU Darmstadt / University of Heidelberg, Germany, as an assistant/advisor.

While presenting the gravure printing process separated in sub-processes, I recurrently mention relevant investigations on this topic and refer to my results of the preliminary printing experiments in Section 3.7.[3] Based on Figure 3.1 and its marking numbers, I separated gravure printing into the following processes:

① Ink acquisition from the reservoir

The gravure cylinder dips into the ink in order to fill its cells. Here, macroscopic velocities and ink flow generated by the cylinder rotation are confronted with the microscopic ink dynamics in and at the cells. For very high velocities, the ink may slosh out of the ink reservoir if it is not closed or a strong entrapment of air into the ink bath may occur. On the micro-scale, if the gravure cells were not completely filled by the approaching fluid surface at the entrance of the cells into the ink [4], they might be trapped with microscopic air bubbles in their apex. The latter is experimentally confirmed in Figure 3.16 (on page 82) or qualitatively shown by simulations of Brethour [30]. The entrapped air might eventually leave the cells during the motion through the bath which often builds up ink foam on the entrance side of the ink reservoir which could again negatively influence the inking of the cells.

After the gravure cells of the cylinder have immersed into the ink, they are withdrawn from the bath on the other side of the ink reservoir, as illustrated in Figure 3.1. Usually, the ink filled in the cells is overlayed by an additional ink layer. For unstructured surfaces perpendicular leaving a liquid bath, Landau, Levich [149] and Derjaguin [55] show that the resulting layer thickness is proportional to the velocity v, the viscosity η (introduced in Section 3.3.1) and the surface tension σ (introduced in Section 3.3.2) of an ideal liquid as $\propto (\eta v/\sigma)^{2/3}$. Ramdane et al. and Afanasiev et al. investigated the thicknesses of wet layers on a plate dragging from a bath of complex liquids [2, 209]. For textured surfaces with micron-sized pillars, Seiwert and Quéré experimentally and theoretically analyzed the variation of the resulting wet layer thickness on the withdrawn plate as a function of the pillar geometries [232]. Krechetnikov investigated similar flow situations over structures and discussed a resulting effective flow with extended slip at the surface [142].

According to the fluid meniscus region, Manukyan [172] and Fell [68] recently investigated the immersion and the withdrawal of positive millimeter-sized pyramides (Manukyan) and unstructured cylinders (Fell) into a liquid bath of simple (Manukyan) and complex (Fell) fluids. Maleki et al. presented experiments and a physical model for the shape of the fluid meniscus when a plate with a pre-coated wet layer is immersed into a liquid bath [169]. Numerical simulations on the initial micro-cavity filling problem have been performed by Gramlich et al. [88] and Kalliadasis et al. [124].

② Dosing of the ink (doctor blade process)

Subsequent to the withdrawal of the gravure cells from the reservoir, excess ink above the cells and on the unstructured area of the gravure cylinder (also denoted as walls) is wiped off by a so-called doctor blade (Figure 3.1). During this 3-dimensional, highly dynamic process, the macroscopic ink flow in front of the blade faces the microscopic one in the cells and at the blade tip which is in close contact to the cylinder (distance < 2 µm). From the preliminary experiments I performed with two color inks at four different velocities presented in Section

[3] For those who are not familiar with the quantities of viscosity and surface tension, I refer the reader to Section 3.3.1 and 3.3.2 on pages 67 ff. first.

[4] compare dynamic contact angles and moving contact lines in Section 3.3.2

3.7.1, I analyzed the fill ratio after the doctor blade process as shown in Figure 3.15b (on page 81).

Hanamanthu performed extensive experimental and theoretical investigations of the blade wear during processing which he coupled to ink flow models at the tip considering the comparable gravure coating process [97]. He found that the wear of the tip changes its contact geometry to the cylinder and strongly influences the ink filling, respectively the ink transfer [97]. The theoretical models he adapted have been studied and experimentally confirmed by numerous authors[5] for blade coating and tape casting processes which directly wipe on substrates. Those studies revealed that an important parameter affecting the doctor blade process is the dynamic pressure in front of the tip which acts against the rigidly or flexibly fixed blade. The resulting velocity profiles of the ink flow beneath the blade might be either approximated by a Couette flow (maximum velocity component near the substrate [261]) or for high dynamic pressures comparable to a Poiseuille flow (maximum velocity in the middle between blade and substrate [261]. The latter would result in a thicker blade coated film [132] or equivalently to higher cell filling. Bery found that, in gravure printing, the fill ratio of the cells never achieves 1 (or 100%) [19].

Since the cylinder surface possesses induced micrometer sized roughnesses to promote blade lubrication [89], ink might wet the non-engraved regions of the cylinder after doctoring. Under certain conditions, low viscous inks might flow up the back of the doctor blade resulting in additional coating of the cell walls. In [25], I determined this layer thickness for a common gravure ink to ~ 100 nm.

After doctering and before first contact of the filled cells with the substrate, Bery accounts an separate phase. He experimentally estimated a cylinder surface temperature of up to 200 °C which possibly evolves at the blade tip [18, 19] and promotes faster evaporation of solvent based inks right after the blade. However, from aspects of ink flow, this phase is not that complex. The ink meniscus in the cells might tend to a more symmetric shape. Eventually, the ink may drain off the cells if the viscosity is too low or the velocity too high by emptying the cells by centrifugal forces to the outer environment.

③ Ink transfer

The ink transfer phase consists of three important regimes within the contact zone, also denoted as *printing nip*, according to the corresponding arrows in Figure 3.1. First, at the inlet of the contact area, the ink initially wets the substrate. Thereby, the negatively formed meniscus in the cells can produce an air void when the substrate contacts the cell. The void volume is proportional to (1 − fill ratio). Figure 3.18 on page 83 shows a microscope image of such an air bubble present after contact of an transparent substrate.

Second, the pressure promoted by the impression cylinder at the contact zone enhances the wetting of a flexible substrate by bending it into the inked cell. Additionally, higher printing force provides an increased contact area to a flexible substrate which on the other hand increases the contact time between gravure cells and substrate. This gives the ink more time to wet the substrate. If the ink meniscus in the cell was not able to contact the surface, the result would be a so-called “missing dot” [217].

[5] [116, 118, 132, 139, 146, 202, 206, 221]

Third, ink is actually separated at the outlet contact zone. A certain amount of ink is transferred to the substrate. Dependent on the ink's mobility in the printing nip and further system parameters, the ink transfer mechanism can take on two different types. First, ink is separated between each cell and the substrate isolatedly which I denote as *single cell splitting* or *single cell transfer*. For the second type, the ink from each cell primary entrains to an ink bead bounded at the printing nip which results in a continuous meniscus along the printing width. Thereby, I denoted this as *film splitting* or *film splitting transfer*. Kunz is the first and to my knowledge only one who provided impressive high speed microscope images of these distinct splitting classes of a conventional gravure process which is shown in Figure 3.3, with permission from [144]. Kunz argues that both extreme splitting situations shown in Figure 3.3 are not

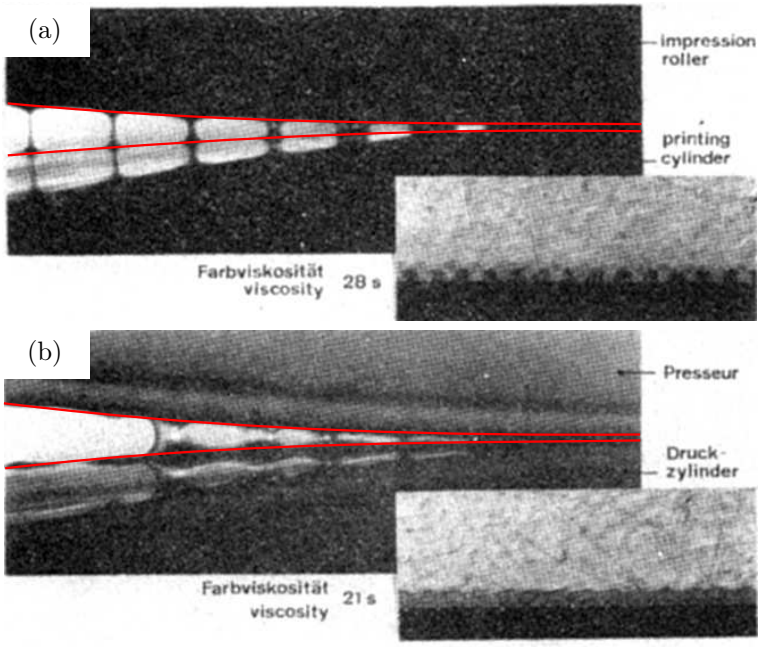

Figure 3.3: High speed microscope images of conventional gravure printing experiments performed by Kunz who imaged the ink splitting process in the nip from the side. Single cell ink splitting in (a) and film ink splitting (b). With printing velocity of 16 m/s and two different ink viscosities, 28 s in (a) and a lower one of 21 s in (b) (measured with a flow cup of unknown geometry). The red lines represent the position of the contact area where the ink menisci touch the cylinder and the substrate. The insets show equivalent printing results at the border of an engraved printed region. With permission from [144].

the optimal conditions for a successful printing process which should rather be a situation in between [144]. Hübner refers the two splitting types to as "ink splitting of first class", meaning ink is available on a "small" area (single cell splitting, see Figure 3.3a) and as "ink splitting of second class" meaning ink is available on a "large" area (film splitting, see Figure 3.3b) [115].

Ink transfer mechanisms in gravure printing have been studied by numerous authors, mainly focussing on setups of the single cell splitting type, experimentally for scale up configurations[6] and numerically usually for one single cell[7]. Considering the actual 3D nip geometry including the cells at realistic printing velocities for a possible hybrid splitting type as postulated by Kunz [144], has, to my knowledge, not been provided by the literature so far.

[6] [91, 125, 133, 222]
[7] [3–6, 30, 58, 61, 82, 114, 125, 135, 141, 159, 160, 228]

As indicated by the insets of Figure 3.3, from the printing result one might conclude on the underlying ink splitting type. On this basis, I deduce possible ink dynamics in the contact zone in Chapter 4. A common parameter in printing experiments to draw conclusions on ink transfer mechanisms is to determine the transfer ratio (transferred ink divided by cell volume), not only for gravure printing but also for other printing techniques[8]. This is a complex function of several system parameters. Figure 3.15a on page 81 shows this ratio in relation to the velocity for gravure printing experiments with two color inks.

From investigations on gravure coating and roll coating[9] operations with equal velocities of ink transferring cylinder and substrate, one might conclude some similar aspects on gravure printing. However, the transfer ratio is usually not comparable because in gravure printing it is a decreasing [65] and in gravure coating [16] an increasing function of velocity. This might originate from the different ink splitting classes which underly the respective processes: gravure printing more close to single cell splitting and gravure/roll coating mainly based on film splitting.

The different types of splitting classes involve different types of printing nip instabilities. Whereas single cell transfer might produce for example the afore mentioned "missing dots" [217], the film splitting transfer provides the onset for the so-called "viscous fingering" [13, 257], which is introduced in Section 3.5 and discussed in Chapter 4 in detail.

④ **Fluid dynamics on the substrate**

After the ink has been transferred to the substrate, it depends on the underlying ink transfer mechanism which dynamics mainly occur within the thin film before evaporation and drying become dominant. Transferred drops might spread and eventually coalesce which would be the desired process to produce closed layers [27, 187]. The film splitting might have already produced a closed film which, eventually with strong undulations [27, 102], might undergo leveling or rupturing dynamics during evaporation of the solvent. The theoretical basis for this thin film behavior without evaporation effects is introduced in Section 3.6 and applied in Chapter 4.

Evaporation of solvents might not only strongly influence the fluid properties. It might also have strong impact on the underlying thin film dynamics [245–247]. Gradients in surface tension (Marangoni effects) and viscosity, diffusion-limited or enhanced evaporation open a wide field of possible effects on the film morphology, in the nanometer, micrometer and millimeter range [22, 53, 54, 110–113, 193].

⑤ **Drying and solidification**

If the transferred film lost most of its liquid components, it could start to dry and solidify. In this regime, a strong topographic change above the micro-scale is not expected due to immobility of the layer but a change of the alignments of the molecules could be expected. The latter might be insignificant for graphical applications, but could strongly influence electric and optical properties. Additionally, chemical reactions and crystallization effects of the underlying solid compounds at the dry layer surface might occur during this phase [42, 143, 229].

[8] [18, 19, 51, 52, 56, 65, 80, 107, 122, 137, 144, 187, 242, 248, 269]
[9] [15, 16, 34, 35, 39, 47, 48, 75, 76, 104, 105, 155, 157, 196]

I leave Bery the last word in this section on sub-process of gravure printing [19]:
"Considering the complexity of the processes we just briefly described, it is rather surprising that gravure printing is possible after all. It works, and it works well."

3.3 Properties and interactions of fluids and solids

3.3.1 Viscosity

Fluid flow usually involves dissipation of energy due to friction within the fluid. This friction can be related to the viscosity of the fluid, which was firstly introduced by Isaak Newton in 1687 in his famous *Principia* [188]. A simple two-plate model describing the response of a viscous fluid which is confined between a fixed and a moving plate is shown in Figure 3.4 [174, 204]. The velocity U in

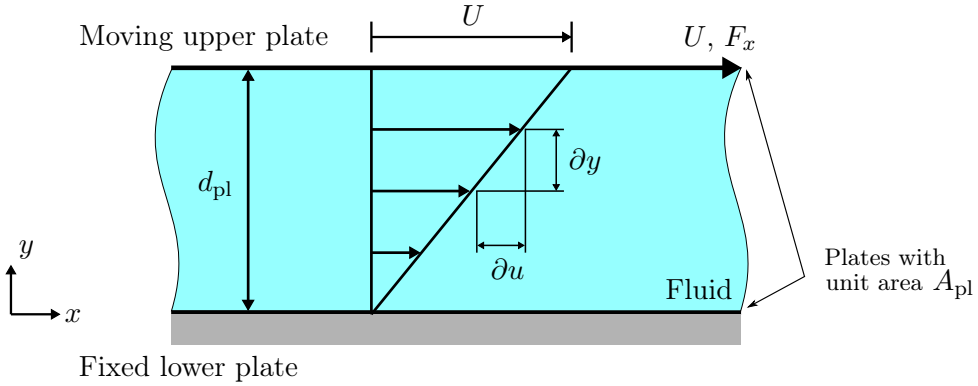

Figure 3.4: Two-plate model to introduce important parameters of a viscous fluid confined between a fixed and a moving plate with velocity U. The distance of the parallel plates is denoted with d_{pl}, the unit areas of the plates A_{pl}, the force directed in x with F_x, following [174, 204].

x-direction of the upper plate involves a force component F_x acting parallel on a unit area A_{pl} of the upper plate. In this model setup, the ratio of force F_x and area A_{pl} is defined as shear stress τ_{yx} [174] in units [Pa]

$$\tau_{yx} = \frac{F_x}{A_{\mathrm{pl}}}. \tag{3.1}$$

For the setup illustrated in Figure 3.4, it is assumed that the velocity of the fluid at the walls move with the wall's velocity and that the fluid between the walls exhibit only non-zero velocity components in x-direction. The first condition is known as the *no-slip condition* [204] and the second corresponds to a pure laminar flow in x-direction. Relating the infinitesimal velocity difference in ∂u to the corresponding difference in ∂y shown in Figure 3.4, results in the shear rate $\dot{\gamma}$ in units of [s^{-1}]

$$\dot{\gamma} = \frac{\partial u}{\partial y}. \tag{3.2}$$

The assumption of Newton's law of viscosity [188] is that the shear stress τ_{yx} is a linear function of the shear rate $\dot{\gamma}$ with

$$\tau_{yx} = \eta\,\dot{\gamma} \quad \Rightarrow \quad \boxed{\eta = \frac{\tau_{yx}}{\dot{\gamma}}}, \tag{3.3}$$

where the constant η is defined as the Newtonian dynamic viscosity [204] in units [Pa·s]. For the linear relation in Figure 3.4 and using Equation 3.1 and 3.3, we may write for the shear rate $\dot{\gamma} = U/d_{\mathrm{pl}}$

$$\eta = \frac{F_x d_{\mathrm{pl}}}{A_{\mathrm{pl}} U} \tag{3.4}$$

for the two-plate model. Water, for example, possesses a viscosity of $\eta \approx 1$ mPa·s under ambient conditions.

In arbitrary Cartesian coordinates, the shear stress and the shear rate might be written in tensor notation [204, 235]. The viscosity usually depends on temperature, pressure and density [204, 235]. In multi-component solutions, the viscosity might also be a function of the particular concentrations [213].

In the case that the linear relation in Equation 3.3 is not valid anymore, the class of fluids are termed as non-Newtonian fluids. Then, the viscosity is usually a function of the shear rate $\eta(\dot{\gamma})$ [204] and might show time-dependent relaxation effects. Prominent examples of non-Newtonian fluids are ketchup as shear-thinning and a cornstarch-water mixture as shear-thickening (dilatant) fluid.

But also color inks for gravure printing applications are commonly non-Newtonian, shear-thinning fluids. Recommended ink viscosities[10] for gravure printing range between $50, \ldots, 200$ mPa·s [136].

Strictly speaking, the afore mentioned concept is related to shear viscosities. One may attribute viscous friction to elongational problems, which originate from extensional stresses. For small elongational velocities and Newtonian fluids, the so-called extensional viscosity η_{e} can be related to the shear viscosity by [84, 200, 252]

$$\eta_{\mathrm{e}} = 3\eta. \tag{3.5}$$

Viscosity measurements

Shear viscosity measurements can be performed using different geometries and tools. In the printing industry, standardized flow cups with a defined hole are still a common tool to determine the viscosity in the unit seconds [s] defining the time the ink needs not empty the cup [73, 244]. More sophisticated methods measure the resulting forces in so-called rotational viscometers [166, 174]. For the present measurements, the rotational viscometer Haake Mars from Thermo Scientific, Germany, was used.

3.3.2 Surface tension and contact lines

Liquid free surfaces usually tend to form spheres. This can be observed for example for soap bubbles, gas bubbles raising in a water boiler or the water stream from a tap that decays into droplets. The reason for this behavior is the tendency of a fluid to minimize its free surface area. Physically, this originates from attractive forces of the liquid molecules. In the bulk, the forces are equally distributed and the resulting net-force on a molecule is zero. Molecules at the surface are missing half of their neighbors and hence, half of their attractive forces. The resulting net-force is directed into the fluid. To bring a molecule from the bulk to the surface is therefore energetically more costly than staying in the bulk [79]. The energy associated to the liquid surface area (energy per area) is denoted as the surface energy σ in units of [J/m^2]. This is equivalent to force per length with the unit [N/m], whereupon σ is usually denoted as surface tension.

Surface tensions of common oils exhibit values of $\sigma \sim 20$ mN/m and water under ambient conditions a value of $\sigma \sim 72$ mN/m [79].

[10] if not quoted otherwise for smallest shear rates

Different types of interactions may occur at liquid/liquid or liquid/solid interactions. They depend on van der Waals forces (also known as disperse forces) or polar forces [72]. Therefore, surface tension models might separate into the different components and assume different functional relations to the different (interfacial) surface tension values [72, 194].

Surface tension is usually dependent on temperature, pressure and for multi-component liquid solutions, it might also be a function of the particular concentrations [79, 120, 183, 219]. Thereby, gradients of surface tension might arise within the fluid if the temperature or the concentration locally varies, also possibly induced by chemical reactions or solvent evaporation. Those gradients might promote fluid flow [184], which was firstly described by Marangoni in the case of temperature induced surface tension gradients [173].

With no loss of generality, surface tension can be attributed to any type of surface, of liquids σ, gases σ_g and solids σ_s. For the latter, this quantity is usually termed as surface energy. For a liquid attached to a solid while sharing a common interface, the interfacial surface tension σ_{sl} was firstly introduced by Young [267]. Strictly speaking, surface tensions of liquids and solids are also interfacial surface tensions because they share their interfaces with the surrounding gas. But the energy difference is small, therefore it is usually justified to neglect the effect of the surrounding gaseous medium.

Static contact angles

A liquid drop which is in static (equilibrium) contact to a solid surface setups a macroscopic contact angle θ_E at the three-phase contact line (also denoted as triple line) dependent on the balance of surface tensions. The vectorial components of the corresponding surface tension of the fluid σ, the interfacial surface tension of the liquid-solid interface σ_{sl} and the surface energy of the solid σ_s are illustrated in Figure 3.5.

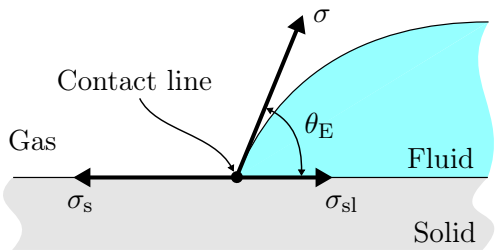

Figure 3.5: Equilibrium contact angle θ_E at the contact line of a fluid on a solid. With surface tension of the fluid σ, interfacial surface tension of the liquid-solid interface σ_{sl} and surface energy of the solid σ_s, following [204].

In the plane of the solid surface, the surface tensions must be equal in equilibrium resulting in

$$\sigma \cos\theta_E = \sigma_s - \sigma_{sl}, \tag{3.6}$$

which is known as Young's equation [267]. Thereby, the macroscopic contact angle is related to the surface tensions of the system.

Laplace pressure

Considering a spherical drop of surface area A, volume V and radius r, we may ask for the work to increase the drop's surface. Increasing the surface by $\mathrm{d}A$ against the surface tension results in the

work $\mathrm{d}W_\sigma = \sigma \mathrm{d}A$. On the other hand, the surface tension provides an additional pressure inside the drop of Δp. Therefore, the work to increase the surface area by $\mathrm{d}A$ also involves an increase of the volume by $\mathrm{d}V$ against the pressure Δp. This gives $\mathrm{d}W_{\mathrm{vol}} = \Delta p \mathrm{d}A$. These two contributions have to be equal,

$$\mathrm{d}W_\sigma = \mathrm{d}W_{\mathrm{vol}}. \tag{3.7}$$

Using the area and volume derivatives of a sphere $\mathrm{d}A = 8\pi r \mathrm{d}r$ and $\mathrm{d}V = 4\pi r^2 \mathrm{d}r$, Equation 3.7 results in

$$\Delta p = \frac{2\sigma}{r}, \tag{3.8}$$

which is known as the Young-Laplace equation or the Laplace pressure originating from the surface tension [151, 204, 267]. Sometimes, it is also denoted as capillary pressure. This means that positive curvatures of free liquid surfaces generate an additional pressure contribution. For non-spherical surfaces, the Laplace pressure can be described by two radii [79]

$$\Delta p = \sigma \left(\frac{1}{r_1} + \frac{1}{r_2} \right). \tag{3.9}$$

Measurement methods for surface tension

There are several methods available to determine surface tensions [59, 87]. For liquids, forces acting between a probe solid and the liquid of interest or pressure differences resulting from the Laplace pressure might be directly measured and analyzed. Other methods optically analyze drop-shape deviations. The latter is often accomplished by the pendant drop method as used with a DSA100 from Krüss, Germany, in the present study. Thereby, a non-spherical drop pending at a needle is formed by balancing forces of gravity and Laplace pressure [59, 79, 238].

For solids, common measurement devices such as the present DSA100 from Krüss dispense different drops of known liquids onto the unknown substrate and analyze the resulting contact angles to obtain the surface energies [87]. This technique is often referred to as sessile drop method.

Wetting

Contact angles of $\theta_{\mathrm{E}} = 0\,^\circ$ represent so-called *total* (or *complete*) *wetting* scenarios, as depicted in Figure 3.6a. Equivalent to this situation, one might introduce the spreading parameter S [79]

$$S = \sigma_{\mathrm{s}} - (\sigma_{\mathrm{sl}} + \sigma), \tag{3.10}$$

which is $S > 0$ for total wetting. For $S < 0$, the static contact angle is $\theta_{\mathrm{E}} > 0\,^\circ$ and the regime is denoted as *partial wetting*. Thereby, fluids with contact angles of $\theta_{\mathrm{E}} \leq 90\,^\circ$ are described as *mostly wetting*, Figure 3.6b, and of $\theta_{\mathrm{E}} > 90\,^\circ$ as *mostly non-wetting*, Figure 3.6c, following de Gennes [79].

Contact angles on real surfaces $\theta_{\mathrm{E,r}}$ with arbitrary roughnesses might change their values compared to ideal ones θ_{E}. According to Wenzel, mostly wetting regimes become more "wettable" ($\theta_{\mathrm{E,r}} < \theta_{\mathrm{E}}$) and mostly non-wetting regimes more "un-wettable" ($\theta_{\mathrm{E,r}} > \theta_{\mathrm{E}}$) [79, 260]. For chemically heterogeneous surfaces, models have also been developed and verified, first by Cassie and Baxter [37].

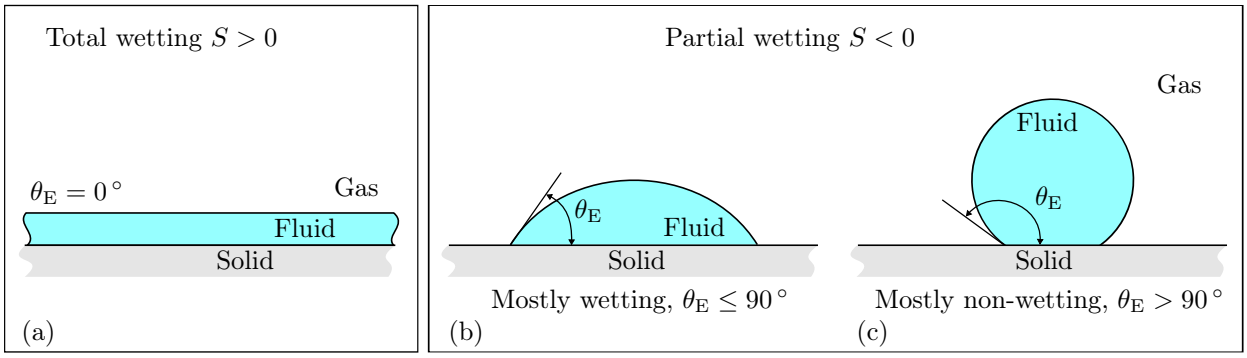

Figure 3.6: Different wetting regimes with equilibrium contact angle θ_E and spreading parameter S, following [79].

Dynamic contact angles

The contact angles at the triple line introduced above are assumed to represent static, equilibrium regimes. If the liquid or the substrate is in motion, the resulting *apparent* or *dynamic* contact angle θ_D would differ from the equilibrium value θ_E. This has been confirmed by numerous experiments

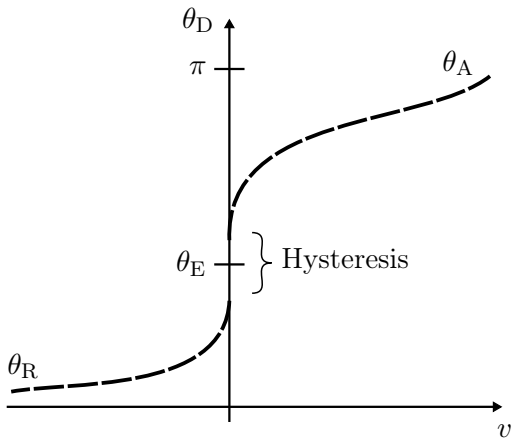

Figure 3.7: Exemplary curve of a dynamic contact angle θ_D on a real surface dependent on contact line velocity v. Hysteresis effects due to surface roughness. Receding contact angle θ_R for $v < 0$ and advancing contact angle θ_D for $v > 0$, after [78].

and models, still lacking a uniform theory, especially for real surfaces and complex fluids [22, 68, 78, 148, 172, 210].

For low velocities v, experiments usually agree with the proportionality of

$$\theta_D \propto v^{\frac{1}{3}}, \tag{3.11}$$

where for $v \to 0$ the angle $\theta_D \to \theta_E$, [22]. Real surfaces may produce hysteresis as illustrated in Figure 3.7 which originate from surface roughnesses [78, 172] and surfactants in the fluid might strongly modify apparent contact angles [68]. For positive velocities, the dynamic contact angle θ_D is often referred to as *advancing* contact angle θ_A and for negative contact line velocities as *receding* contact angle θ_R.

Pinning of the moving contact lines

As mentioned in the previous paragraph, moving contact lines on rough surfaces can influence the resulting apparent contact angles. If surfaces obey topographies in the form of sharp edges, advancing or receding contact lines could be pinned at these positions and be prevented from further movement [22, 83, 190]. This might be encountered in gravure printing because when the ink firstly contacts the substrate or when the gravure cylinder dips into the ink reservoir, fast contact line movement might occur.

Figure 3.8a illustrates this situation. An advancing triple line with contact angle θ_D passes a convex (falling) edge at point A in Figure 3.8a. Unless the contact angle stays below θ_E enclosed to the falling facet (yellow area), the contact line might be pinned. The apparent contact angle can obtain any value within the yellow region of Figure 3.8a. This can be associated to an additional force required to continue contact line movement [22]. For the concave edge at point B in Figure 3.8a the contact line passes without a pinning distortion [190]. For the receding fluid front shown in Figure 3.8b, the contact line is pinned at the same falling edge A as the advancing is pinned.

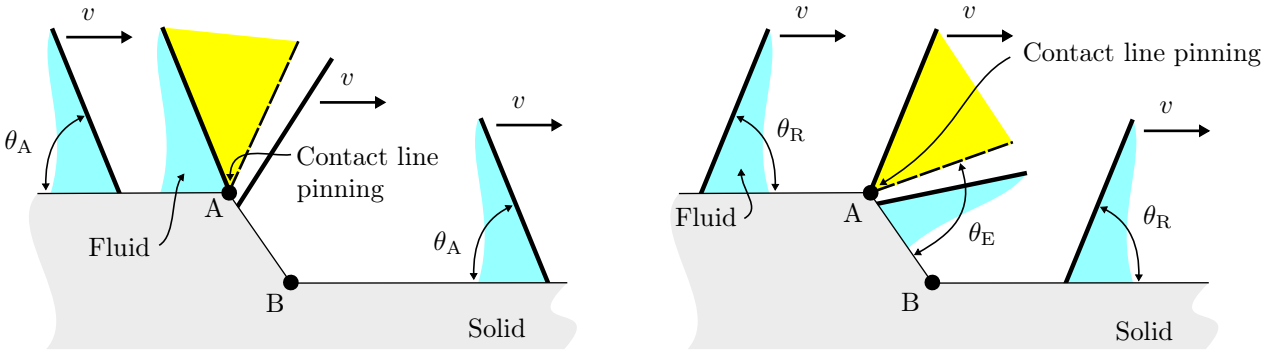

(a) Advancing contact line

(b) Receding contact line

Figure 3.8: Contact lines passing a falling, convex (A) and raising, concave (B) edge. Both advancing (a) and receding (b) contact lines are "pinned" at the falling edge, whereas raising edges are passed without preventing the contact line from further motion.

In Figure 4.21 on page 116, I discuss possible drawbacks of pinned contact lines at the edges of gravure cells.

3.4 Governing hydrodynamic equations

The governing equations describing the motion of fluids can be derived from conservation of mass, momentum and energy. First formulated by Claude Louis Navier and George Gabriel Stokes, the so-called Navier-Stokes equations (NSE) for an incompressible fluid ($\nabla \cdot u = 0$) in vectorial notation are of the form

$$\underbrace{\rho\left(\frac{\partial \vec{u}}{\partial t} + (\vec{u}\cdot\vec{\nabla})\vec{u}\right)}_{\text{Inertia}} = \underbrace{\eta\nabla^2\vec{u}}_{\text{Viscous friction}} - \underbrace{\vec{\nabla}p}_{\text{Pressure gradient}} + \underbrace{\rho\vec{g}}_{\text{Gravity force}} \tag{3.12}$$

where t is the time, g the gravitational acceleration and u, p, η, ρ the velocity, hydrodynamic pressure, viscosity and density of the fluid, [150]. Surface tension enters the equation when considering appropriate boundary conditions [150].

Equation 3.12 can be understood as a balance of forces per volume. The left term of Equation 3.12 represents the conservation of momentum (inertia forces) whereas on the right side of the NSE, we find contributions from viscous friction, hydrodynamic pressure and gravity.

Up to now, the existence and smoothness of a full set of analytical solutions of the Navier-Stokes equations has not been derived. It is one of the seven Millenium problems in mathematics announced by the Clay Mathematics Institute, Cambridge, Massachusetts [43].

In fluid dynamics, comparing experimental results to the physical model formulated in Equation 3.12 is often accomplished by discussing dimensionless numbers or groups [177]. They involve characteristic constants for velocity U, length L and time T. Thereby, dimensionless numbers might be defined, usually consisting of ratios of different types of forces which enter the different terms in Equation 3.12 as pre-factors.

From the fluid dynamical point of view, the following orders of forces can be mainly attributed to the gravure printing process.

$$\begin{aligned} \text{inertia forces} &\mathrel{\widehat{=}} \mathcal{O}\left(\rho U^2 L^2\right), \\ \text{gravity forces} &\mathrel{\widehat{=}} \mathcal{O}\left(\rho g L^3\right), \\ \text{viscous forces} &\mathrel{\widehat{=}} \mathcal{O}\left(\eta U L\right), \\ \text{surface tension forces} &\mathrel{\widehat{=}} \mathcal{O}\left(\sigma L\right), \end{aligned} \tag{3.13}$$

where ρ is the density, η the viscosity and σ the surface tension of the fluid/ink, following [197]. The characteristic velocity U is usually the printing velocity and the characteristic length strongly depends on the sub-process one considers. For the ink transfer, one might choose the length of the gravure cell ($L \sim 100$ µm) as characteristic length and for the flow in the ink reservoir the length of the tank ($L \sim 0.2$ m). Comparing the forces for the latter case, for $L \to 0$, the gravity force with $\propto L^3$ much stronger decreases like the viscous force with $\propto L$, whether we could possibly neglect gravity forces in this case.

Based on the forces in Equation 3.13, the following dimensionless numbers can be considered for the gravure printing process of Newtonian fluids [94, 261]:

$$\text{Reynolds number:} \quad \mathrm{Re} = \frac{\rho U L}{\eta} \quad \mathrel{\widehat{=}} \quad \frac{\text{inertia force}}{\text{viscous force}}, \tag{3.14}$$

$$\text{Capillary number:} \quad \mathrm{Ca} = \frac{\eta U}{\sigma} \quad \mathrel{\widehat{=}} \quad \frac{\text{viscous force}}{\text{surface tension force}}, \tag{3.15}$$

$$\text{Weber number:} \quad \mathrm{We} = \frac{\rho U^2 L}{\sigma} \quad \mathrel{\widehat{=}} \quad \frac{\text{inertia force}}{\text{surface tension force}}, \tag{3.16}$$

$$\text{Bond number:} \quad \mathrm{Bo} = \frac{\rho g L^2}{\sigma} \quad \mathrel{\widehat{=}} \quad \frac{\text{gravity force}}{\text{surface tension force}}. \tag{3.17}$$

In Section 4.4.4 on page 119 ff., I discuss effects of the Bond number on the ink transfer mechanism and define a modified number which is the ratio of the (pseudo) centrifugal force and the surface tension force. Additionally, I discuss the so-called Taylor number which relates the centrifugal force to the viscous force.

3.5 Printing nip instability

A very common instability in printing and coating applications and at moving fluid surfaces in confined geometries is the occurrence of regular undulations at the fluid front. This is often referred

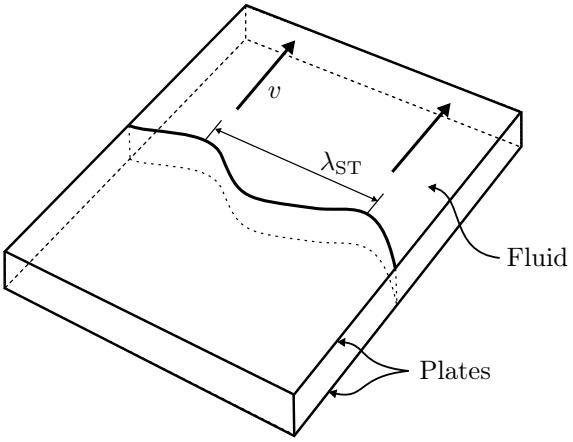

Figure 3.9: Rectangular Hele-Shaw cell with fluid confined between the plates and evacuated to one side. Undulations with wavelength λ_{ST} might evolve, following [226].

to as *viscous fingering*[11], *ribbing instability*[12] or *Saffman-Taylor instability*[13]. Since this rupture mechanism occurs at the nip region of the contact area of gravure cylinder and substrate, I also denoted the effect as *printing nip instability*.

Initially, in 1958, Saffman and Taylor formulated a model using linear perturbation analysis which predicted the wavelength of a periodic instability in the so-called rectangular Hele-Shaw geometry [69, 100, 220]. That is a fluid confined between parallel plates with a small spacing where the fluid is evacuated from one side and the initially straight receding fluid front breaks up into fingers, as shown in Figure 3.9.

A simple explanation can be drawn by considering the pressure balance at the initially straight free fluid interface. Due to the evacuation velocity of the bulk fluid, the hydrodynamic pressure at the interface is reduced. Balancing the reduced pressure to the outer one, the interface might tend to form positive curvature resulting in an compensating positive contribution from to the Laplace pressure. Therefore, a distorted free surface might be more favorable than a straight one.

Fields et al. extended the linear analysis to different geometries including a roller type one which is comparable to the underlying gravure printing process [70]. They determined the minimal critical wavelength λ_{ST} which might evolve along the ink meniscus for the geometry depicted in Figure 3.10 to

$$\lambda_{\mathrm{ST}} = \pi \sqrt{\frac{\sigma h_{\mathrm{nip}}^2}{\eta v}} \tag{3.18}$$

with surface tension σ, viscosity η, printing velocity v and nip height h_{nip} according to Figure 3.10. A comparable equation was also derived by Voss [257].

Referring to simple geometrical considerations, meniscus distance X_{nip} and nip height h_{nip} are related as follows

$$X_{\mathrm{nip}} = \sqrt{2Rh_{\mathrm{nip}} - h_{\mathrm{nip}}^2}. \tag{3.19}$$

[11] [13, 14, 36, 69, 85, 108, 127, 161, 162, 168, 185, 207, 223, 234]
[12] [11, 16, 38, 86, 90, 99, 158, 197, 254, 257]
[13] [46, 70, 181, 195, 220, 241, 256]

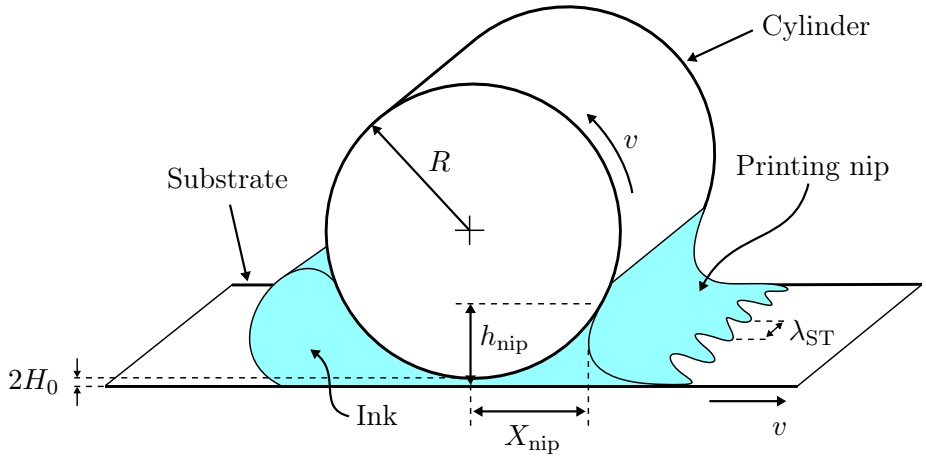

Figure 3.10: A rotating roller with radius R transports ink to a moving substrate with the same velocity v and a distance to the substrate of H_0. The forming ink meniscus at the outlet printing nip exhibits a nip height of h_{nip} and a distance to the tangential center of cylinder and substrate of X_{nip}. Along the printing nip, periodic undulations (fingers) with a dominant wavelength of λ_{ST} might evolve due to the so-called Saffman-Taylor instability.

The assumptions underlying the linear perturbation analysis performed by Fields et al. [70] are indicated in Figure 3.10, and are the following:

- unstructured cylinder, i.e. no gravure cells,
- continuous meniscus along the contact line of cylinder and substrate and along the printing nip.

This is a strong deviation from the present gravure cylinder setup which I compare to experiments and discuss in Chapter 4.

Aside from the linear perturbation analysis related to the Saffman-Taylor approach of Fields and others, comparable 3-dimensional numerical studies have been performed on ribbing in symmetric roll coating flows by Castillo et al. and Carvalho et al. [34, 38]. Their setups are comparable to the one shown in Figure 3.10[14] and they explicitly take account for the gap between cylinder and substrate $2H_0$, which is neglected by Fields. A simple equation relating the ribbing wavelength to velocity, viscosity, surface tension and gap height is not achieved, but their results show similar behavior to the velocity dependence of Equation 3.18 [34, 38]. A comparison of ribbing wavelength of the present study and obtained from Carvalho is shown in Figure 4.39 on page 133.

It is important to note at this point, that all ribbing or fingering structures introduced above are usually oriented in the direction of substrate motion.

3.6 Thin film dynamics

Solution-processed homogeneous, thin layers can only be fabricated if the wet film is homogeneous right before the phase transition from liquid to solid. Describing the dynamics of thin fluid films neglecting gravity and inertia effects, the Navier-Stokes equations (Equation 3.12) can be reduced to a differential equation also referred to as Landau-Levich or lubrication equation [149, 192]. For the derivation of the thin film equation, one applies the assumption that the liquid film is thin, meaning

[14] they used roll-to-roll instead of roll-to-sheet geometries, which is only a negligible geometrical variation at the nip

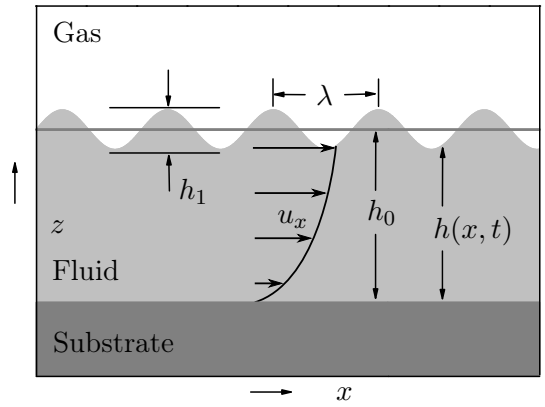

Figure 3.11: Geometry of a thin liquid film of thickness $h(x,t)$, mean thickness h_0 and with periodic surface undulations of amplitude h_1 and wavelength λ. With slowly varying film heights, i.e. $\partial h/\partial x \ll 1$ involving $|\partial u_x/\partial x| \ll |\partial u_x/\partial z|$ (lubrication approximation), [24].

that it has only slowly varying film heights along the surface. According to Figure 3.11 [24], this is equivalent to $\partial h/\partial x \ll 1$. It also involves that the main tangential velocity gradients of the fluid dominantly vary along the film thickness, meaning $|\partial u_x/\partial x| \ll |\partial u_x/\partial z|$. This assumption is referred to as lubrication approximation [78, 184, 193, 227, 239].

Thereby, the thin film equation is derived to [149]

$$\frac{\partial h}{\partial t} = -\frac{\sigma}{3\eta}\frac{\partial}{\partial x}\left(h^3\frac{\partial^3 h}{\partial x^3}\right). \tag{3.20}$$

This fourth-order nonlinear differential equation describes the spatial thickness evolution $h(x,t)$ in time of a thin liquid film under the influence of surface tension.

3.6.1 Leveling

One might consider an infinitely extended film with mean thickness h_0 and a small periodic undulation of amplitude h_1 and wavelength λ as depicted in Figure 3.11. Using the ansatz

$$h(x,t) = h_0 + h_1(t)\,\cos(2\pi/\lambda\, x), \tag{3.21}$$

the solution of the Landau-Levich Equation 3.20 linear in h_1, meaning to the order of $\mathcal{O}(h_1^2)$, results in a exponentially decaying amplitude $h_1(t) \propto \exp(-t/t_{\text{lev}})$. The corresponding decaying time or so-called *leveling time* t_{lev} is of the form [24, 192]

$$\boxed{t_{\text{lev}} = \frac{3\eta\,\lambda^4}{16\pi^4\sigma\,h_0^3}}. \tag{3.22}$$

It is important to note that this linear perturbation analysis and the lubrication approximation involve the long-wavelength limit with the constrains of $h_0 \gg h_1$ and $\lambda \gg h_0$.

Without the latter restriction on the wavelength but in the limit of small amplitudes, Orchard

[192] and Kheshgi [129] derived an exact solution of the equations of motion[15] resulting in a leveling time of [38, 129]

$$t_{\mathrm{lev}} = \frac{2\eta h_0}{\sigma \beta_0} \frac{1 + \mathrm{sech}^2 \beta_0}{\tanh \beta_0 - \beta_0 \mathrm{sech}^2 \beta_0}, \tag{3.23}$$

where β_0 is the dimensionless wavenumber defined as $\beta_0 = 2\pi h_0 / \lambda$, [38]. In the short-wavelength approximation [129], i.e. $\lambda \ll h_0$, Equation 3.23 reduces to [129]

$$t_{\mathrm{lev}} \propto \frac{\eta}{\sigma} \lambda. \tag{3.24}$$

In Section 4.4.7 on pages 128 ff., I compare the determined wavelengths of the printing results to leveling times predicted by the expression in Equation 3.23.

3.6.2 Spinodal dewetting

Since the intended dry layer thickness should be in the sub-100 nm range, also the liquid layer might reach those thicknesses while still mobile. In this ultra-thin thickness region, it has been shown, first by Vrij [258], that homogeneous thin liquid films are prone to a rupture mechanism based on long-range interactions. They originate from van der Waals forces between substrates and liquid films and contribute to the so-called disjoining pressure [193]. This might possibly amplify small fluctuations. Interestingly, the strength of this additional contribution (defined by the Hamaker constant A_{H}) can be estimated by corresponding refractive indices and dielectric constants of the liquid and the substrate using the so-called Lifshitz theory [8, 120].

Using linear perturbation analysis with the disjoining pressure entering the Landau-Levich equation [218, 258], one can derive a characteristic rupture time t_{spin} which favors a corresponding fastest growing wavelength λ_{spin} evolving at the liquid surface [12, 193, 212, 218, 230, 258, 262] as follows.

$$\text{Spinodal rupture time:} \quad t_{\mathrm{spin}} = 48\,\pi^2\,\eta\,\sigma\,\frac{h_0^5}{A_{\mathrm{H}}^2}, \tag{3.25}$$

$$\text{Spinodal wavelength:} \quad \lambda_{\mathrm{spin}} = \sqrt{\frac{16\,\pi^3\,\sigma h_0^4}{A_{\mathrm{H}}}}, \tag{3.26}$$

where A_{H} is the Hamaker constant of the system, η the viscosity, σ the surface tension and h_0 the mean liquid film thickness.

Referring to the denotation of sinusoidal decomposition of the phase separation in isotropic systems by Cahn [32], the rupture mechanism is named *spinodal dewetting*.

From Equation 3.26 it is obvious that spinodal dewetting can only occur for positive Hamaker constants, hence for negative ones, the liquid film is stable.

In Section 4.4.7, I compare the undulations determined from the printing results to theoretical values calculated from Equation 3.25 and 3.26.

3.6.3 Heterogeneous nucleation

When the spinodal dewetting is not favored because either of a negative Hamaker constant or the rupture time is quite large, Seemann et al. investigated that then *heterogeneous nucleation* might

[15] omitting inertia and gravity effects

be the favored rupture mechanism [231, 247]. This usually originates from nuclei in the fluid or on the substrate (heterogeneous nucleation) or from thermal fluctuations (thermal nucleation) and generates growing holes that finally coalesce and result in dry patches [130, 263]. The evolving film defects are, contrary to spinodal dewetting, Poisson distributed. Therefore, by analyzing the spatial distributions of undulations of fabricated films, one should be able to conclude on the underlying rupture mechanism.

Jacobs et al. show that this is a challenging task and common statistical surface analysis may lead to misinterpretation of experiments [121]. They propose and successfully apply the interesting concept of Minkowski functionals [171, 178, 225] to distinguish between the different types of undulations [12, 121].

In Section 4.3, I introduce the underlaying surface parameters to describe the film surface. Apart from a spectral analysis to determine the dominant wavelength, I applied the statistical surface parameters of skewness and kurtosis. I also tested the Minkowski functionals on some of the printed results presented in Chapter 4 with the program code published by Mantz [171], but I could not deduce relevant physical conclusions from the Minkowski functionals.

3.7 Preliminary printing experiments with color inks

In Section 3.2, I described the different phases of gravure printing and some issues related to them. However, measuring the different phases during operation is a big challenge because of the high velocities and the small length scales. Usually the printing outcome is analyzed to conclude on the underlying sub-processes. In this section, I present new experiments with a conventional printing proofer and an optical profilometer which revealed direct measurements of properties of the doctor blade process and issues related to the gravure cell – substrate contact and to the cell filling.

For the present preliminary printing experiments, I used the test print device K Printing Proofer from RK PrintCoat Instruments Ltd, United Kingdom, which is shown in Figure 3.12. It is important

Figure 3.12: K Printing Proofer, a test print device for gravure printing used for preliminary studies with color inks (source: IDD).

to note that usually this type of test tools requires a manual ink acquisition and therefore the gravure cells are not continuously inked unlike laboratory or industrial machines. Furthermore, the geometry of this tool differs from industrial machines especially according to its gravure "cylinder". This is flat

and the flexible substrate is bent around the impression cylinder. A sketch of the K Printing Proofer is illustrated in Figure 3.13. Stahl analyzed the applicability and drawbacks of the K Printing Proofer

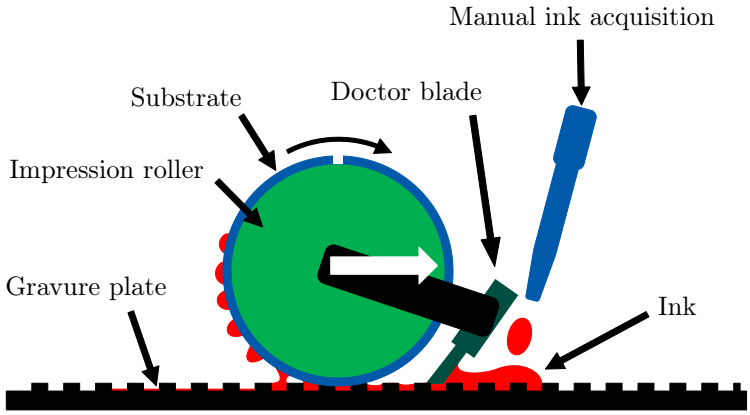

Figure 3.13: Sketch of the operation principle of the K Printing Proofer.

for electronic applications [237] and Elsayad et al. its characteristics for graphical applications in terms of parameter studies [65]. Furthermore, this tool was used in several studies related to printed electronics, for example for conductive polymer inks [109], for printed conductive anorganic ITO layers [187] or humidity sensors [211].

3.7.1 Experiments on the filling and emptying of gravure cells

The flat geometry predestinated the test device to investigate the filling and emptying of gravure cells. This is because the gravure plate could be easily removed and placed under a microscope to analyze the ink meniscus in the gravure cell.[16] However, positioning the plate after processing under a microscope was challenging since common inks evaporate so that the volume loss is huge in the first seconds after printing. Therefore, I used two different ultra-violet (UV) light curable color inks. The first one, denoted as I1, was a black ink (GT-Ink BLUN8-B Jetrion from Efi, USA) with a viscosity of 35 mPa·s at a shear rate of 1000 s^{-1} and a surface tension of 19.9 mN/m. The second model UV ink, denoted as I2, was a yellow ink (UV-Sicura Flex 36-2-1200 from Siegwerk, Germany) with a viscosity of 406 mPa·s at a shear rate of 1000 s^{-1} and a surface tension of 37.2 mN/m.[17] These inks showed almost no evaporation loss ($< 3\%$ within the first 30 min after printing), which was confirmed using a micro-balance. This gave enough time to perform the printing run and the positioning of the plate under a microscope.

I printed on a commercial polyethylene terephthalate (PET) foil (Hostaphan GN4600 from Mitsubishi Polyester Film GmbH, Germany) with the standard printing plate delivered with the printing proofer which was mechanically engraved with eight different fields. I used four of the eight fields which varied according to their tonal value from 75%, 80%, 85% to 90%. The screen ruling was 60 L/cm, the screen angle 37°. I determined the corresponding cell volumes V_c using the method presented in [26], resulting in values from 8 ml/m^2 to 10 ml/m^2.

I enabled the optical profiling microscope Sensofar Plu Neox with its confocal and white-light interferometry mode[18] to measure empty cells and the top ink meniscus of partly filled gravure

[16] I presented the results of these experiments as a poster at the Materials Science and Engineering Congress 2012 in Darmstadt, Germany [28].

[17] Viscosities and surface tensions of both inks were measured using a Haake Mars rotational rheometer from Thermo Scientific and a DSA100 from Krüss, respectively.

[18] for details on this methods see Appendix A on page 143

cells of the different fields on the gravure plate. Using automated recipes in combination with a 5x objective and the xy stage of the microscope, I determined ink menisci in gravure cells of four fields of the cylinder plate at three different positions resulting in approximately 500 single determined cell menisci per field.

Two different types of "printing" processes were performed. First, I raised the impression cylinder (compare Figure 3.13) while remaining the doctor blade process operational, followed by the determination of the ink meniscus topography in the gravure cells after doctoring. Second, I conventionally printed on the PET foil with a cleaned gravure plate and the same settings as before followed by analyzing the meniscus topography of the remaining ink in the gravure cells again. I varied the printing velocities by four different values from 0.3 m/s to 0.9 m/s.

Calculating the difference of the filled and empty gravure cells revealed the actual ink volume in the cells, as representatively illustrated for a corresponding data set in 2D in Figure 3.14. Using this

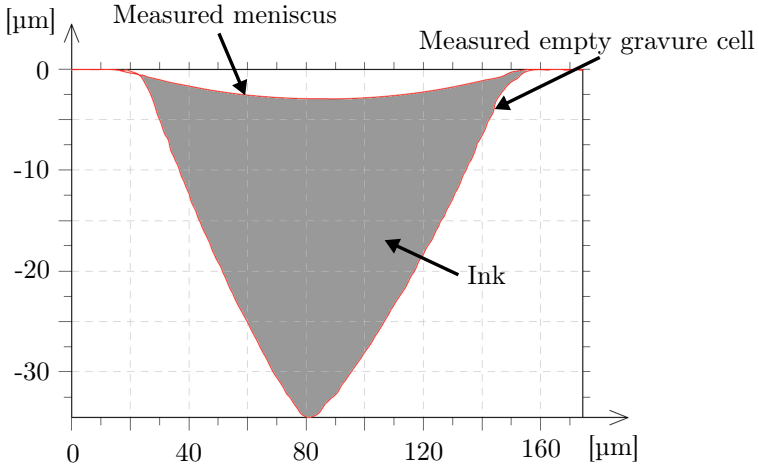

Figure 3.14: Representative, measured 2D topography of an empty and a filled gravure cell after a doctor blade process. Calculating the *difference* in 3D resulted in the fill volume of the cell (gray area).

procedure, I could determine the ink volumes in the gravure cells after the doctor blade process V_{fill} and after the conventional printing process V_{print}. This allowed me to determine important volume ratios. The filled ink volume divided by the empty gravure cell volume is denoted with "fill ratio" A_{fill}. The transferred (from gravure cell to substrate) ink volume V_{trans} normalized by the empty cell volume V_{c} is denoted as "transfer ratio" A_{TR}, whereas V_{trans} normalized by the actual ink volume before transfer V_{fill} as "effective transfer ratio" A_{eff}. Thereby, the transferred ink volume V_{trans} is calculated as the difference $V_{\text{trans}} = V_{\text{fill}} - V_{\text{print}}$.

These three ratios revealed almost no dependence on cell volume but a strong on printing velocity. Figures 3.15a, 3.15b and 3.15c show the corresponding ratios of the present preliminary experiments for the two different color inks averaged over cell volumes.

For the high viscous ink I2 in Figure 3.15, the transfer ratios revealed almost no dependence on printing velocity. For the low viscous ink I1, the normal transfer ratio A_{TR} (Figure 3.15a) is decreasing for increasing velocity as known from the literature [65, 242]. Figure 3.15b indicates that this strongly correlates with a reduced fill ratio A_{fill} for increased velocity. As a result, the effective transfer ratio A_{eff} remains constant for varying velocity in the present range as depicted in Figure 3.15c. This is a surprising observation for the present test print device and it remains an open question if this behavior is also present in industrial gravure printing processes.

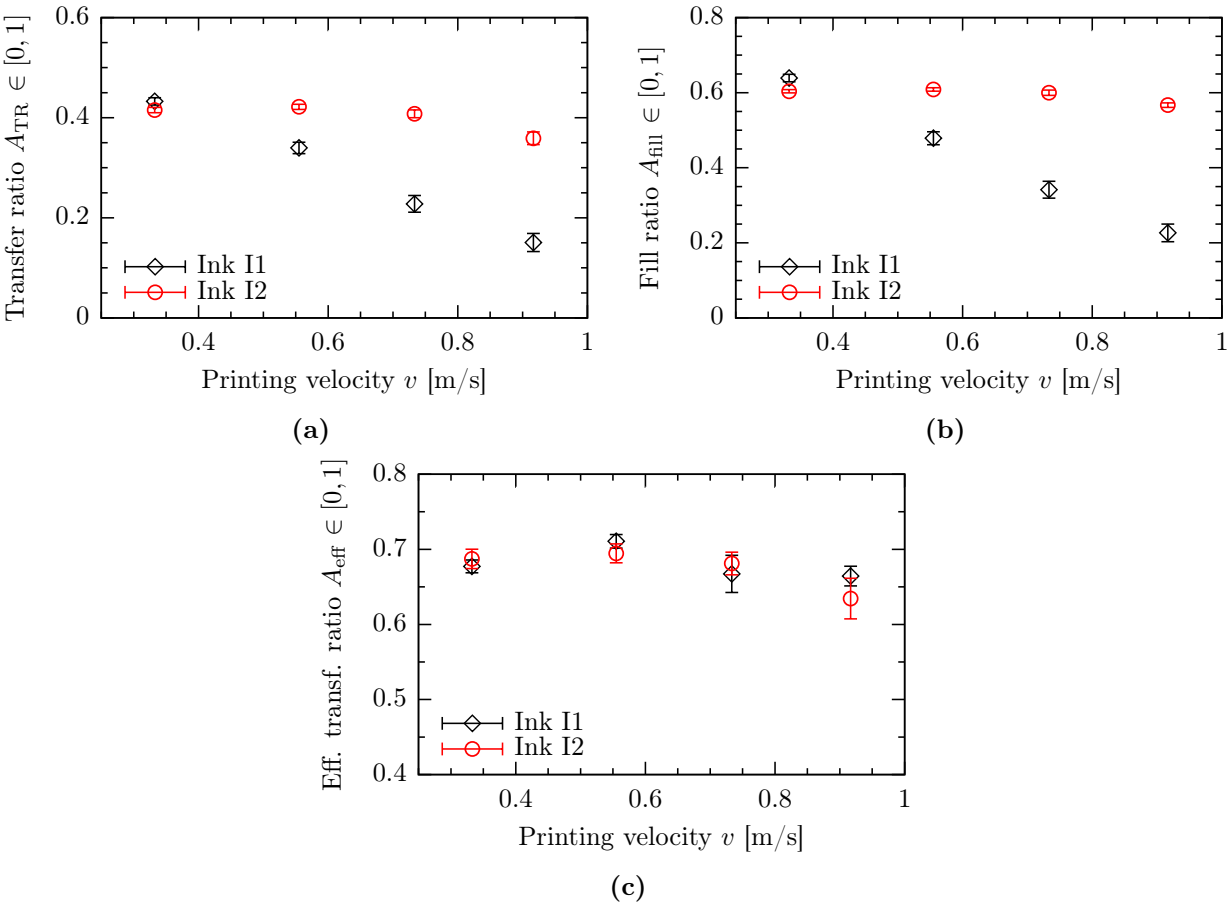

Figure 3.15: Different ink volume ratios of preliminary gravure printing experiments for different velocities and two different UV color inks performed on the K Printing Proofer. Transfer ratio A_{TR} in (a), fill ratio A_{fill} in (b) and effective transfer ratio A_{eff} in (c). The viscosity of ink I1 was 35 mPa·s at 1000 s^{-1} and of ink I2 406 mPa·s at 1000 s^{-1}.

3.7.2 Observation of air entrapment after doctor blade process

Under the same experimental conditions as presented in the section before (3.7.1) with raised impression roller, I used a high viscous (η = 1020 mPa·s at 1000 s^{-1}) transparent UV ink (Senolith KAT-UV-Lack 07-30-52-365010 V45 from Weilburger Graphics GmbH, Germany). Inspecting the filled cells through the transparent ink, I found air bubbles at the bottom of the cells. Figure 3.16 shows representative gravure cells filled with transparent ink after the doctor blade process and imaged with an conventional optical microscope focussing the bottom of the cell. A two-part small air

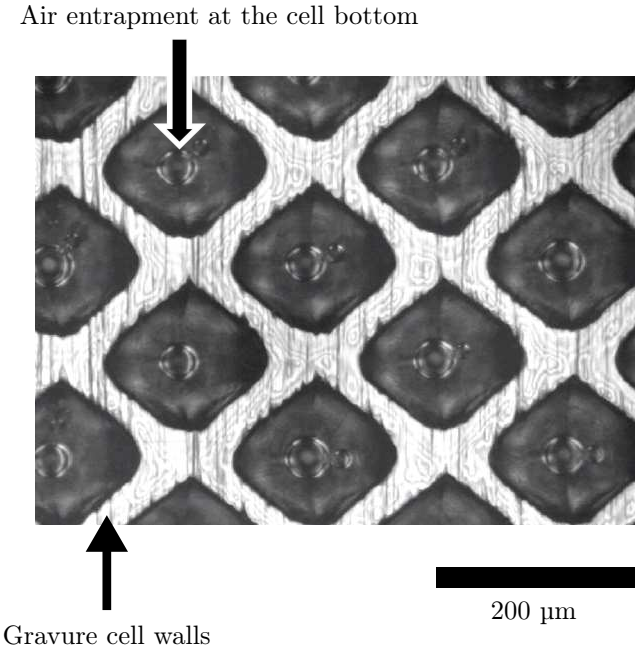

Figure 3.16: Air entrapment at the bottom of gravure cells after the doctor blade process.

bubble remains at the bottom of each cell. The two-part characteristics is an optical effect resulting from the flanks of the cell and confirms that the bubble is located at the apex of the inverted, engraved pyramid. For the present ink, I observed that the size of the air bubbles reduced in time, after 150 s no air entrapment was visible under the microscope. This could result from a dissolution of the air in the ink which originated from the type of the ink and might be not transferable to other inks.

3.7.3 Experiments on air entrapment during first contact of substrate and cell

The fill ratio A_{fill} is always below 0.65, as shown in Figure 3.15b, and the ink surface always contacted the upper boundary of the cells, as representatively illustrated in Figure 3.14. This resulted in a negative meniscus which might not only occur in the equilibrium state as illustrated in Figure 3.14 but also on average in the dynamic case between doctor blade process and ink transfer. When the substrate contacts the negatively curved ink in the filled gravure cell, air might be trapped in between. From the following experiments, I determined these air voids for the color inks I1 and I2 used in Section 3.7.1.

The printing setup was changed so that the PET foil was *laminated* onto the gravure plate, as illustrated in Figure 3.17. With this modification, I could analyze the area of the ink in the gravure cell contacting the substrate with a conventional microscope through the transparent foil. Figure

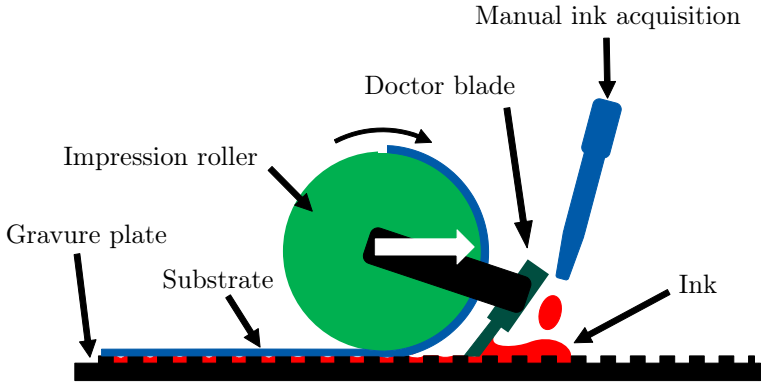

Figure 3.17: Sketch of the operation principle of the K Printing Proofer in the *lamination* mode.

3.18 shows a representative microscope image of a single gravure cell of this lamination process using ink I1, printing velocity $v = 0.3$ m/s and screen ruling SR = 60 L/cm. The dashed line encloses the void area of the air entrapment and the solid line the opening area of the gravure cell. The ratio of these two areas multiplied by 100 denotes the relative void area in percent. This is illustrated in Figure 3.19 versus printing velocity. Each data point in Figure 3.19 corresponds to the mean value of around 150 measurements.

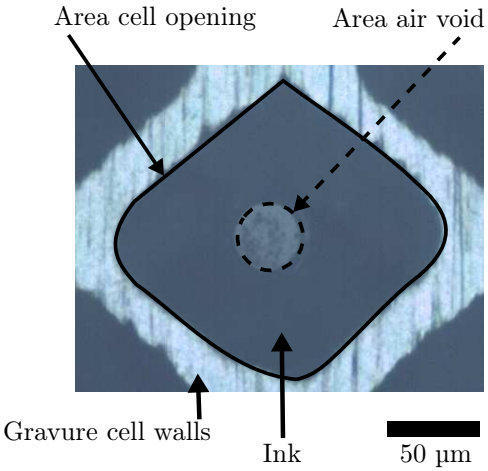

Figure 3.18: Representative microscope image of a single gravure cell after *lamination* of the foil with $v = 0.3$ m/s and SR = 60 L/cm. Dashed line encloses the void area of the air bubble and the solid line the opening area of the gravure cell.

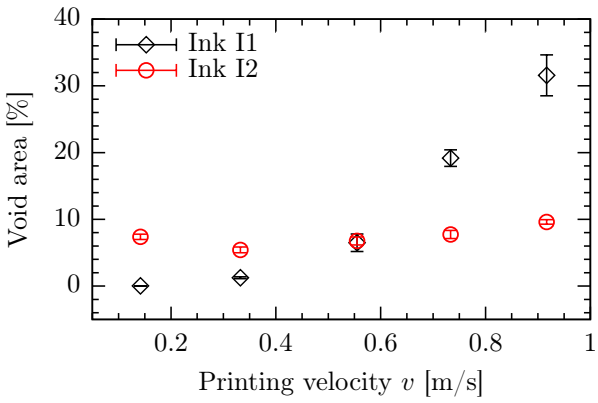

Figure 3.19: Void area of air entrapment in percent versus printing velocity for all cell volumes. The viscosity of ink I1 was 35 mPa·s at 1000 s^{-1} and of ink I2 406 mPa·s at 1000 s^{-1}.

For the high viscous ink I2 (black open squares), the relative void area is almost constant at 7.4%, whereas for the low viscous ink I1 (red open circles), the relative void area is increasing for increasing velocity. This behavior correlates with the reduced fill ratios A_{fill} shown in Figure 3.15b for both inks. For the low viscous ink I1, this means that the less the gravure cells are filled with ink the larger are the trapped air bubbles after contact between cell and substrate.

3.8 Summary

In this section, I introduced the relevant physics associated to the gravure printing process. Thereby, the complexity of gravure printing was reduced by descriptively separating the process into different phases, slightly modified compared to the literature. To the different phases, I associated aspects of other fields of research and provided a comprehensive list of relevant studies.

In anticipation of the application of low viscous inks for large-area electronic applications, I focussed the introduction on printing nip instabilities related to viscous fingering and on thin film dynamics on the substrate related to leveling and dewetting.

The results of the preliminary printing experiments with color inks revealed a new method for gaining insights into sub-process of gravure printing. The combination of the easily removable printing plate of the test device, the usage of non-evaporating inks, transparent substrates and an optical profilometer enabled these new types of measurement setups. For the first time, air bubbles trapped in the apex of gravure cells, theoretically not surprising, but experimentally not reported before, were demonstrated. Additionally, the dependence of the air voids originating from the first gravure cell – substrate contact were presented which correlated with the filling of gravure cell after doctoring.

3.9 Outlook

3.9.1 Air voids as a measure of fill ratio

Form the correlation between the air void and the fill ratio of the gravure cells, one could enable a simple measurement setup to determine the filling states of gravure cells. This might only involve to image an air void through a transparent substrate "laminated" on any gravure cylinder, even possibly for industrial machines. The absolute ink volume could also be estimated, if one assumes that the contact angle of the ink at the confined preferable spherical air void to the foil is constant and possible equal to the static one. Then, the absolute volume of the air bubble could be determined only by its measured contact area which could be reduced to the fill ratio.

Chapter 4

Ultra-thin, homogeneous layers processed by gravure printing low viscous inks

Abstract

In this chapter, I present direct gravure printing experiments of ultra-thin, small molecule based layers on glass with thicknesses in the range of 10 to 70 nm on a laboratory printing unit. The viscosity of the toluene-based ink was two orders below common values used in gravure printing. I chose a gravure cylinder with 32 different 30×30 mm^2 engraved fields to span a wide parameter space. By applying the thickness measurement method introduced in Chapter 2, I was able to determine nanometer thickness maps of all printed substrates, with a total area of 1800 cm^2 (analyzed printed fields 1150 cm^2). Apart from the mean layer thicknesses, I analyzed the relative RMS roughness, skewness, kurtosis and the isotropic dominant wavelength of the surfaces of the printed fields. I found that the layer thicknesses of the fields were affected by the adhesive tapes used for fixation the substrates. This gave surprising insights into the underlying physical mechanisms of the ink transfer. The wavelengths of undulations could be assigned to instabilities originated from the ink splitting process in the nip matching the prediction of the model. Two distinct minima of the relative roughnesses equivalent to most homogeneous layers were identified. As leading control parameter, I defined a normalized leveling time. This correlated with the optimal fields revealing a defined stable process window for ultra-thin homogeneous layers produced by gravure printing of low viscous inks.

Parts of this work have been published in:

Bornemann, N., Sauer, H. M., and Dörsam, E. "Gravure Printed Ultrathin Layers of Small-Molecule Semiconductors on Glass". In: *Journal of Imaging Science and Technology* 55.4 (2011), p.40201

4.1 Introduction

Utilizing gravure printing for printed electronic devices offer the following apparent advantages:

- resistivity against aggressive solvents because only nobel metals come in contact with the ink,
- high throughput capability,
- existing machine technology,

In contrast, the challenges associated to the gravure printing process mainly originate from the different requirements for this new application. Therefore, process optimization is hindered because of the following aspects:

- complex interplay and lacking exact physical knowledge of the different sub-processes as introduced in the previous chapter,
- graphical applications require color dots, functional ones closed and homogeneous layers,
- desired layer thicknesses are < 100 nm which are about two orders below the ones required for graphical applications,
- desired layer homogeneities should be significantly reduced compared to the ones of graphical layers
- ink formulations might possess viscosities far below the common values used for graphical application,
- for multi-layer processing, the subsequent layers could dissolve during the processing of further ones,
- cleanliness must be comparable to established inorganic semiconductor processes which greatly differ from established paper processes,
- industrial processes of organic electronic devices require sufficient yield factors.

The last point has been widely ignored in the literature so far and is very crucial aspect to achieve. That is because, for example, a missing color dot on a printed front page of a magazine does not exclude this product from sale. Instead to a printed OLED panel, this issue would possibly produce a short circuit or a nucleus for fast degradation of the device rejecting it from further use.

The scope of the present experiments and analysis is to define a process window and understand its underlying physical mechanisms for the processing of small molecule based binary solutions targeting layer thickness below 100 nm. The conditions for "optimal" layer qualities should be related to easily accessible machine and gravure cylinder parameters.

Previous work on the subject

Several authors have shown that gravure printing is capable of producing ultra-thin semiconducting layers for OLEDs [102, 131, 140, 156], consistently using polymeric ink formulations. Only Hambsch et al. reported about gravure printed small molecule based semiconductor solutions without additives, not for OLEDs but for OFETs [96]. However, they do not systematically relate process parameters to the layer quality.

To my knowledge regarding OLEDs, gravure printing has neither been utilized to produce small molecule semiconducting or emitting layers, nor has been investigated in detail for processing these low viscous (~ 1 mPa·s) inks for large-area electronic applications yet.

Printing small molecule solutions is difficult because of its low viscosity and with this its tendency to dewet or evolve surface instabilities on a very short timescale after printed on the substrate [27]. Understanding the origins of these pattern phenomenons to optimize the process parameters is among other aspects a central part of the present work.

For process optimization, one has to define quantities which should reach "optimal" values. In example, for OFETs and OLED displays, minimal and sharply contoured printed channels or pixels could be targeted. Whereas for OLED lighting and OPV panels, large and homogeneous layers are required. The latter is the focus of the present investigation. As leading quality parameter, I chose the relative root mean square (RMS) roughness S_{qr}. In the field of gravure printed organic electronics, among others, this quality parameter was recently investigated by several authors summarized in the following (and shown in the chart of Figure 4.1). The authors performed their experiments using small test print devices, processed on foils and used polymer-based ink formulations.

(i) Michels et al. used a neural network approach to optimize the homogeneity of gravure printed light-emitting polymer layers on foils [179]. Apart from the mean dry film thickness $\overline{h}$, they determined the relative RMS roughness S_{qr} and an additional developed "anisotropy" parameter A_{Mi} which quantifies the stripe-like pattern of the printed layers. Their input parameters were printing velocity ($v = 0.5, \ldots, 1.5$ m/s), cell volume ($V_{\mathrm{c}} = 0.2, \ldots, 12$ ml/m^2) and concentration ($c_{\mathrm{m}} = 2.2, \ldots, 3.0$ wt-%) of the photo-active polymer material (which changed the viscosity of the ink to around $\eta \approx 30$ mPa·s) in their ternary ink solution of solute and 30/70 (w/w) mixture of toluene and anisole. The screen ruling of SR = 60 L/cm remained constant throughout the experiments. For mean dry film thicknesses between $\overline{h} = 80$ nm and 220 nm, they obtained relative roughnesses between $\tilde{S}_{\mathrm{qr}} = 7.5\%$ and 13%. With a surface tension of approximately $\sigma = 30$ mN/m, the dimensionless capillary number (Ca $\widehat{=}$ viscosity × velocity/surface tension) ranges from Ca $= 0.5, \ldots, 1.5$.

(ii) Simon Stahl investigated the relative RMS roughness (also denoted as *coefficient of variation*) of gravure printed polymer layers on foils [237]. He chose model inks on the basis of toluene and anisole with comparable fluid properties to light-emitting polymer solutions and applied different molecular weights and concentrations ($c_{\mathrm{m}} = 5, \ldots, 20$ wt-%) to modify the viscosities in the range of $\eta = 5, \ldots, 100$ mPa·s. The other input parameters he varied were cell volume ($V_{\mathrm{c}} = 2.1, \ldots, 16.8$ ml/m^2) and screen ruling (SR $= 40, \ldots, 140$ L/cm) for constant printing velocity of $v = 0.8$ m/s. Stahl analyzed an impressive number of 864 different printed sample fields of a total area of 864 cm^2 and obtained mean layer thickness between $\overline{h} = 50$ nm and 1500 nm with relative RMS roughnesses between $\tilde{S}_{\mathrm{qr}} = 5\%$ and 30%. With surface tensions between $\sigma = 28$ mN/m and 37 mN/m, the capillary number ranges from Ca $= 0.14, \ldots, 2.2$. From his optical observation of the printed fields, he postulated a qualitative printing process model dependent on relative roughness and viscosity.

(iii) Hernandez-Sosa et al. fabricated polymer OLEDs and optimized the gravure printed emitting layer by modifying the ratio of two different solvents ($\sim c_{\mathrm{s}}$) and the concentration of the functional polymer c_m [103].[1] Therewith, they mainly modified the viscosity η and the drying time t_{d} of the wet layer $\overline{h}_{\mathrm{w}}$ after ink transfer promoting more time for leveling ($\sim t_{\mathrm{lev}}$). They used constant printing velocity ($v = 1.0$ m/s), cell volume ($V_{\mathrm{c}} = 14$ ml/m^2) and screen ruling (SR = 54 L/cm) and a surface tension and viscosity range of $\sigma = 25, \ldots, 35$ mN/m and

[1] I participated in this publication in measuring surface tensions and formulating parts of the section "2.2 Ink Surface Tension and Contact Angle" and "2.4. Printing Outcome and Film Leveling Time".

$10, \ldots, 600$ mPa·s. They obtained layer thicknesses from $\overline{h} = 36$ nm to 77 nm and found an "optimal" ink formulation yielding homogeneous light emission and correlating with a minimum leveling time associated to surface undulations. The capillary numbers ranged from Ca $= 0.42, \ldots, 24$.

Processing layers on foils hampers comparing different results with each other. This is because it assigns the machine-dependent quantity of printing pressure and elasticity of the impression cylinder a strong influence on the nip position and the ink dynamics in the nip affecting the printing results [34, 35, 266]. Additionally, determining layer thicknesses on foils in the nanometer range is often a challenging task because of the waviness of this type of substrate. Apart from Stahl, the thickness measurements carried out by the authors are limited to small sample areas (Michels) and 2D line scans (Hernandez-Sosa). Stahl adds a small amount of red dye to his model ink formulations and enabled a flatbed scanner in transmission mode to determine the absorbtion of the dye and therewith the layer thicknesses. He limits his analysis to parameters of mean dry film thickness $\overline{h}$, relative RMS roughness S_{qr} and deduced wet film thickness $\overline{h}_{\mathrm{w}}$ and transfer ratio A_{TR}.

A relation of their "optimal" parameters to physical models is not entirely covered by the authors (i) - (iii). Enabling their results to set up a model is also difficult because neither all important parameters such as wavelength of undulations are given nor relevant input parameters (i.e. printing velocity) are varied. It remains partly unresolved from the previous investigations, which machine and gravure cylinder parameters one should chose to process "optimal" ultra-thin layers.

I performed gravure printing experiments on glass, used a predefined low viscous ink formulation and varied printing velocity, cell volume and screen ruling. These three input parameters are easily accessible and adjustable for any kind of printing tool. From the laterally resolved thickness data of 128 printed fields (on total 1150 cm^2), I determined additional surface and statistical parameters as mentioned and compared to the other investigations in Figure 4.1. For the meaning of the parameters listed in Figure 4.1, I refer to the following section[2]. My analysis revealed two locally distinct "optimal" parameter ranges which could be related to physical models. The *process windows* stated by the authors (i) − (iii) could be assigned to either of them.

I found a surprising feature when printing over topography (adhesive tapes). This step on the substrate influenced the mean thicknesses of the printed fields behind it. I presented an explanatory model that gives insights into the possibly underlying ink transfer mechanisms assigning the process a dependence on its *printing history* per run.

The main structure of this chapter is shown in Figure 4.2. It is organized as follows. In Section 4.2, I give details on the printing experiments and in Section 4.3, I motivate and introduce the surface parameters used for the analysis. Section 4.4 presents the results and discusses possible driving mechanisms related to ink transfer and surface undulations. In Section 4.5, I conclude a possible process window and compare it to results of the afore mentioned authors (i)−(iii) [103, 179, 237]. Section 4.6 and 4.7 closes with the summary and outlook.

[2] apart from the anisotropy factor A_{Mi} developed by Michels [179]

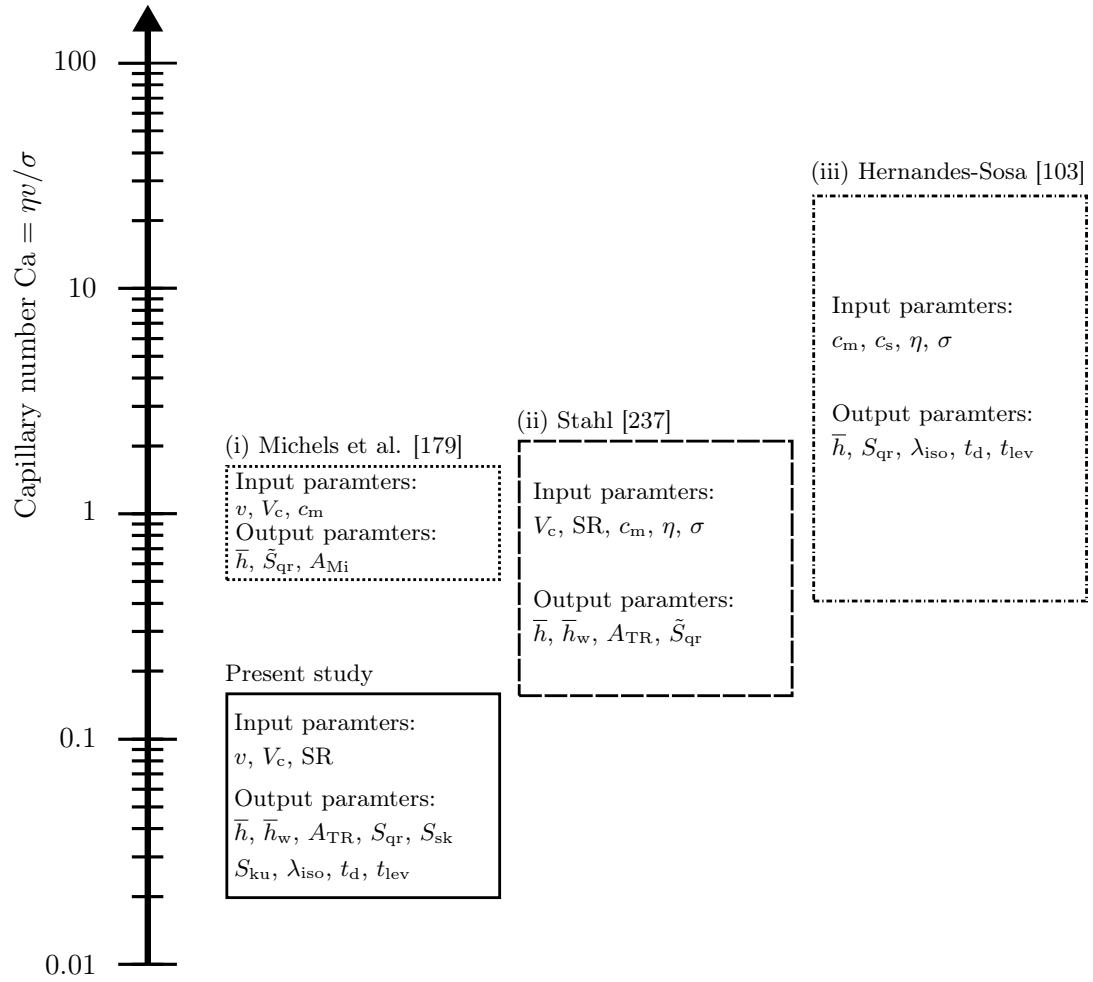

v: printing velocity
V_c: cell volume
SR: screen ruling
c_m: concentration of material
c_s: concentration of first solvent
$\overline{h}_w$: mean wet film thickness
$\overline{h}$: mean dry film thickness
η: viscosity
σ: surface tension

A_{Mi}: anisotry factor developed by Michels [179]
A_{TR}: transfer ratio of ink
S_{qr}: relative RMS roughness
$\tilde{S}_{qr}$: relative RMS roughness in [%]
S_{sk}: skewness
S_{ku}: kurtosis
t_d: drying time
t_{lev}: leveling time
λ_{iso}: isotropic dominant wavelength

Figure 4.1: Overview in terms of capillary numbers of relevant investigations by Michels [179], Stahl [237] and Hernandez-Sosa [103] according to parameter studies on gravure printing experiments for polymeric ink formulations. The present work using a low viscous small molecule based formulation approaches low capillary numbers which have not been covered by other studies yet. For more details on the experiments and the parameters of the authors (i) to (iii) and the present study see text and the following sections.

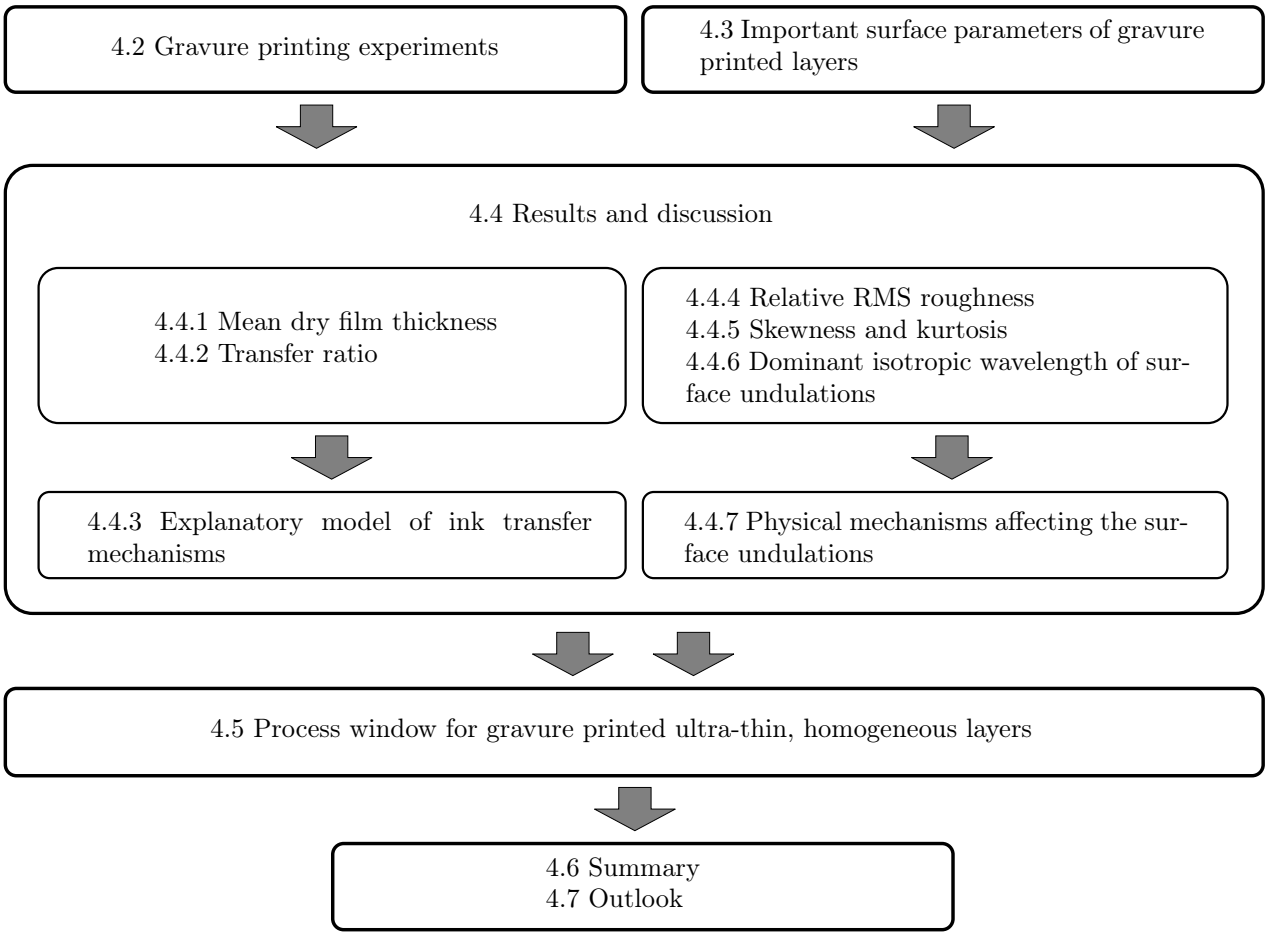

Figure 4.2: Main structure of the present Chapter 4.

4.2 Gravure printing experiments

4.2.1 Substrates

The printing experiments were performed on soda-lime glass substrates provided by Merck KGaA, Darmstadt. The initial size of the edge-polished substrates was $150 \times 150 \times 0.7$ mm^3 vacuum coated with a thin layer of indium tin oxide (ITO). I determined the layer thickness of the ITO using spectroscopic color reflectometry with the Nanocalc from Ocean Optics resulting in 160 ± 0.8 nm. For imaging color reflectometry measurements of the printed layers, the refractive indices of the ITO and the soda-lime glass were taken from the materials library delivered by Nanocalc's controlling software.

The surface energy of the ITO substrates as received, with previous cleaning in an industrial washing machine at Merck, was determined using a contact angle measurement system DSA100 from Krüss, Germany, to 40 mN/m. Immediately before printing, the substrates were treated in a vacuum plasma (Nano from Diener Electric, Germany) with oxygen for 4 minutes, increasing the surface energy to 69 mN/m.

4.2.2 Inks

The solvent of the binary ink solution was toluene, purity $\geq 99.5\%$, purchased from Sigma-Aldrich, Germany. The small molecule semiconductor material $2,2'7,7'$-tetrakis-(*N*,*N*-di-*p*-methoxyphenyl amine)-$9,9'$-spirobi-fluorene (spiro-MeOTAD) was used as solute, it was provided by BASF, Germany. Its molar weight is 1225.43 g/mole and its chemical formula $C_{81}H_{68}N_4O_8$. The refractive indices of solid spiro-MeOTAD spin-coated on glass were determined by spectroscopic ellipsometry at BASF SE, Germany. The viscosity η of the formulation was determined with a rotational rheometer HAAKE MARS from Thermo Scientific, Germany, and the surface tension σ with a pendant drop measurement device DSA100 from Krüss, Germany. For details on the measurement principles, I refer the reader to Macosko [166] and de Gennes [82]. The values resulted in a shear rate independent (Newtonian) viscosity of $\eta = 0.8$ mPa·s and a surface tension of $\sigma = 27.8$ mN/m which are comparable to the values of the pure solvent.

Under static conditions and before considerable evaporation effects, the contact angle of the ink formulation on the plasma-treated ITO glass substrates was $\theta_E = 8.1 \pm 3.8\,^\circ$.

Spiro-MeOTAD can be used as hole-transport material in OLEDs and in solid-state dye-sensitized solar cells [67].

I dissolved $c_{spiro} = 3.5$ wt-% spiro-MeOTAD in toluene. 60 ml of this ink formulation were filled into the ink reservoir before printing.

4.2.3 Printing unit

Figure 4.3: Prüfbau laboratory gravure printing machine used in the present study.

The printing experiments were performed using a laboratory gravure printing unit from Prüfbau, Germany, shown in Figure 4.3. Initially, the ink reservoir had to be filled with a minimum of 300 ml of ink to provide a sufficient ink level. We replaced this reservoir with a modified stainless steel vessel reducing the minimum ink volume to 60 ml. Ink is deposited on the substrate from below, as shown in the sketch of the Prüfbau printing machine in Figure 4.4.

Both the gravure cylinder and the impressing roller possessed a radius of $R = 46$ mm. Initially, the substrate carrier was bent at the impression roller, and deflected from horizontal movement by a specific angle. Using the non-flexible glass substrates, would result in a fracture of the substrate. Adjusting this angle to the horizontal, i.e. to the same guiding angle as in front of the contact zone, enabled a stable printing process on glass. The printing pressure was chosen such as to ensure sufficient contact between cylinder and substrate. A further increase above this value did not change

the printing result. This situation was different to the printing process on foil because the latter is deformable and is pressed into the gravure cells for higher printing pressure. This effect did not occur on glass which we can consider as completely rigid, at least on the length and timescales of the printing process.

Two glass substrates of $150 \times 150 \times 0.7$ mm^3 were consecutively mounted on the substrate carrier and fixed at their borders using adhesive tapes (Figure 4.4). The total printed area per run was therefore 150×300 mm^2.

The printing unit allows four discrete printing velocities of $v_1 = 0.62$ m/s, $v_2 = 1.25$ m/s, $v_3 = 2.5$ m/s and $v_4 = 5.0$ m/s. The printing took place in a climate controlled laboratory with constant temperature and relative humidity of 23 °C and 50%. The drying time of the ink on the substrate was estimated analyzing a video recording of the optical interference patterns of the drying liquid film using a Canon EOS 5D Mark II camera.

I characterized all printed samples using the flatbed scanner setup with the imaging color reflectometry introduced in Chapter 2.

4.2.4 Gravure cylinder parameters

The parameters of the mechanically engraved gravure cylinder were predefined by preliminary printing experiments with the same ink using a printability tester IGT G1, as summarized in Appendix C.1 on page 170. Thereby, the suitable range of gravure cell volumes used for the later experiments was determined such that at the lower limit, ink transfer just ceased to be possible, and at the upper limit, the onset of an uncontrolled flooding of the substrate by the ink was just observed.

Four different screen rulings were selected, SR $= 60, 70, 95, 120$ L/cm. The cell volume was varied in eight steps from 0.2 to 5 ml/m^2 per screen ruling. In total, 128 different fields (4 velocities, 4 screen rulings, 8 cell volumes) span the 3-dimensional input parameter space.

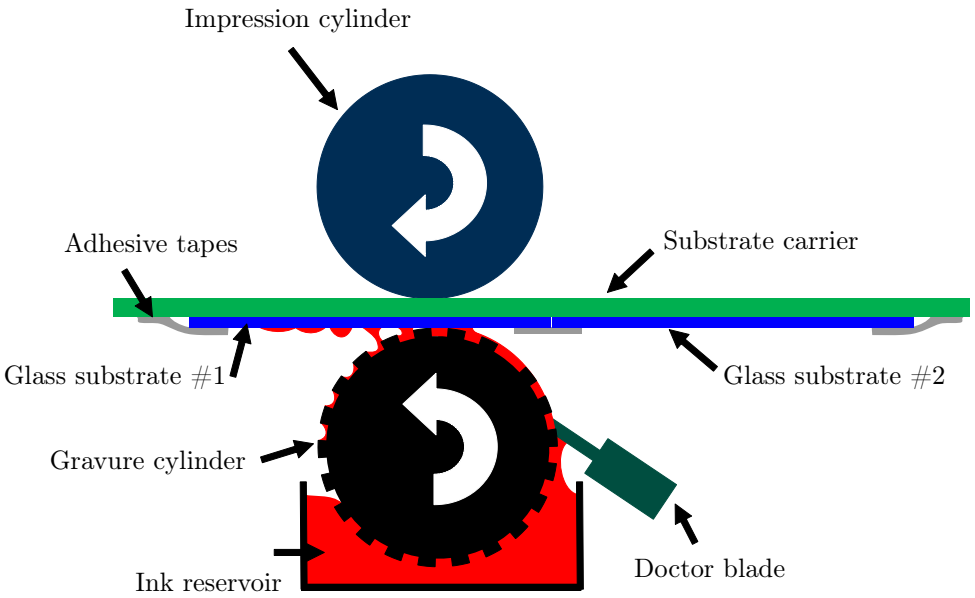

Figure 4.4: Sketch of the operation principle of the Prüfbau laboratory printing machine.

The cylinder was engraved with 32 fields of 30×30 mm^2, 3 mm spaced, using a stylus angle of $\alpha_{\mathrm{St}} = 140\,^\circ$ and a screen angle of $\alpha_{\mathrm{SR}} = 45\,^\circ$ by Krandick, Germany. After performing the complete set of printing experiments and because unexpected printing results have been found in

parts, especially for low cell volumes (details in Section 4.4.4 on page 119), I characterized the gravure cylinder parameters. For this, I adapted confocal microscopy with a Sensofar Plu Neox[3] and developed an analysis method published in [26]. Remarkably, this investigation revealed a tremendous deviation between manufacturer and measured values. The comparison of cell depths[4] is representatively illustrated in Figure 4.5 for a screen ruling of SR = 95 L/cm, reprinted with permission from [26].

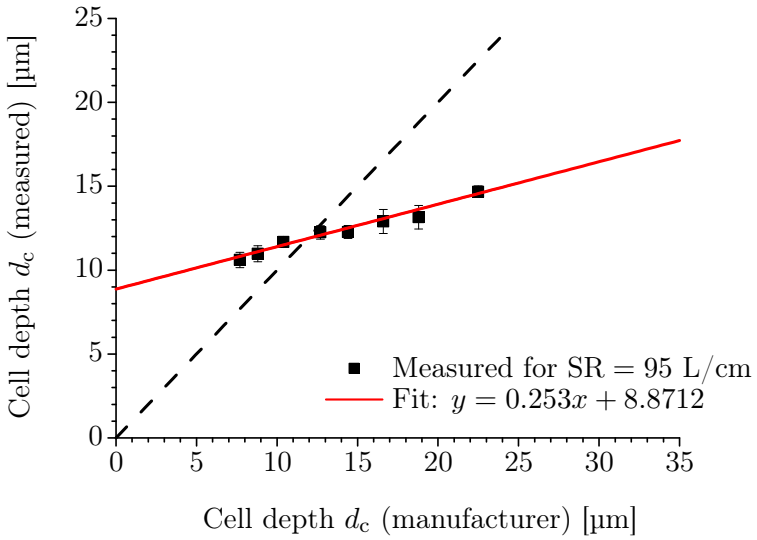

Figure 4.5: Measured cell depths of the fields with a screen ruling of SR = 95 L/cm compared to the given values from the manufacturer, reprinted with permission from [26]. Black dashed line shows the angle bisector line representing equal values. The linear regression is marked in red and illustrated the deviation.

In Figure 4.5, the red line represents the linear regression and it deviates by a considerable slope and offset from the dashed bisector line.[5] The cell volume is proportional to the cell depth cubed, thereby the strongest deviation between measured and expected values for the cell volume reached 647% [26]. This discrepancy motivates the discussion including the preliminary printing experiments with the IGT G1 summarized in Appendix C.1 in the following sections.

The 8 different cell volumes per screen ruling are arranged in ascending order in printing direction and the 4 screen rulings are arranged perpendicular to the printing direction. The measured gravure cylinder parameters are listed in Table 4.1, the maximum standard deviation of the measured values is 18%. The arrangement in the table corresponds to the designed pattern of the gravure cylinder illustrated in Figure 4.6.

[3] see Appendix A on page 143 for details

[4] these were the values communicated with the manufacturer

[5] On the contrary, the linear regression in Figure 4.5 enables to "normalize" between manufacturer and measured (received) gravure cylinder parameters for subsequent cylinder orders.

Table 4.1: Measured cell volumes V_c of the gravure cylinder used in the present study categorized by corresponding screen rulings SR.

SR [L/cm]	V_c **[ml/m^2]**							
120	0.96 ± 0.06	1.16 ± 0.08	1.23 ± 0.03	1.36 ± 0.15	1.42 ± 0.13	1.61 ± 0.12	1.70 ± 0.20	2.12 ± 0.11
95	1.34 ± 0.15	1.44 ± 0.16	1.69 ± 0.11	1.91 ± 0.14	1.90 ± 0.13	2.16 ± 0.27	2.23 ± 0.26	2.98 ± 0.21
70	1.49 ± 0.13	1.85 ± 0.16	2.49 ± 0.49	2.31 ± 0.31	2.59 ± 0.11	2.82 ± 0.26	2.99 ± 0.45	3.70 ± 0.53
60	1.49 ± 0.06	1.80 ± 0.08	2.13 ± 0.22	2.35 ± 0.15	2.73 ± 0.23	3.10 ± 0.23	3.53 ± 0.56	4.38 ± 0.47

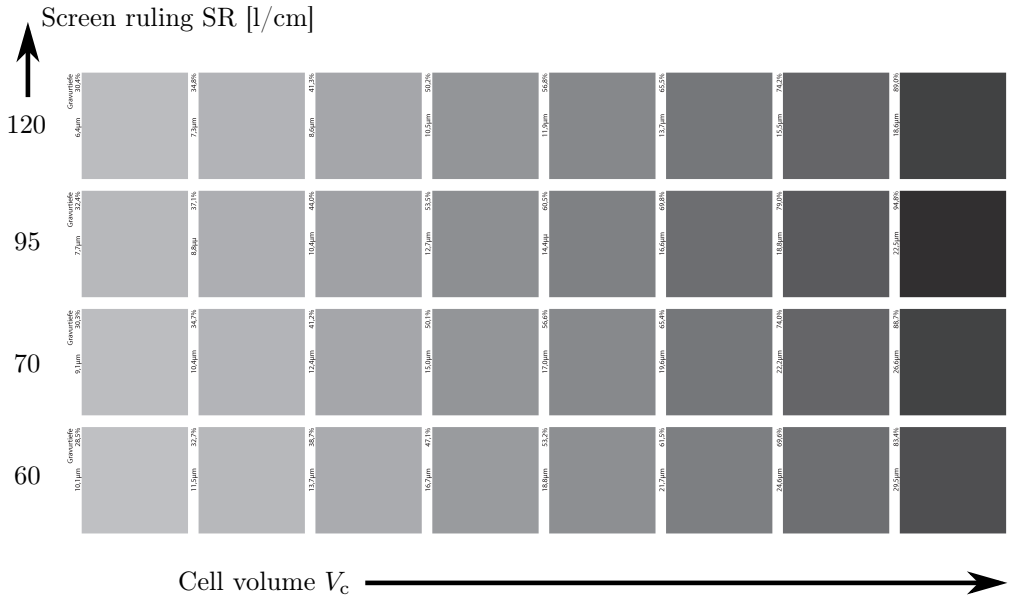

Figure 4.6: Designed pattern of the gravure cylinder with its 32 different fields. The gray values of the different fields are proportional to their desired cell volumes. The sketch is mirror-inverted, hence it shows the expected printing result. Thereby, fields on the right-hand side are printed at first. The arrangement of the fields in this sketch corresponds with the one in Table 4.1.

4.3 Important surface parameters of gravure printed layers

A key task of the current research is the understanding the formation of large-area, ultra-thin, homogeneous layers produced by gravure printing. *Large-area*, in the sense that the substrate sizes are in the decimeter range; *ultra-thin*, meaning processed with layers in the nanometer thickness range; and *homogeneous*, revealing minimal thickness variations across the processed layers.

In this section, I introduce the underlying quality parameters, especially for the meaning of *homogeneity* in the present context.

For the analysis of the printing results, I used the imaging color reflectometry (ICR) presented in Chapter 2. This provided laterally resolved thickness results in the nanometer thickness range of the entire area of the eight printed substrates, in total 1800 cm^2.

I determined five different surface parameters for each printed field: mean dry film thickness $\overline{h}$, relative root mean square (RMS) roughness S_{qr}, skewness S_{sk}, kurtosis S_{ku} and dominant isotropic wavelength λ_{iso}. Apart from the mean dry film thickness, the parameters in combination characterize the homogeneity of the layers, for which I consider the relative RMS roughness the be of highest importance.

The scope of the present investigation is the quality of the printed fields neglecting the characteristics of the edges. Different mechanisms might result in structures/defects such as rims or fingers at these edges which might be related to drying kinetics and contact line effects [53, 54, 110–113].

I therefore determined the surface parameters only for an inner part of each field in order to exclude edge effects and printing failures. Figure 4.7 shows an example of the surface area selected for parameter extraction.

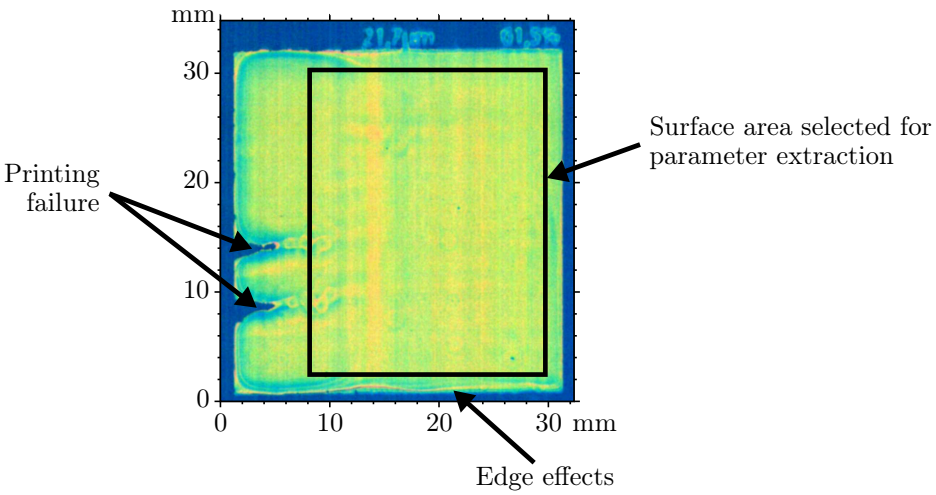

Figure 4.7: Contrast enhanced image of a representative printed field acquired by the modified flatbed scanner. The surface parameters are calculatedfor the area indicated by the black rectangle. Edge effects in the form of rims originating from drying kinetics or printing failure due to inappropriate contact between cylinder and substrate are thereby excluded from the surface analysis.

In the following, I introduce the surface parameters of interest and motivate their relevance for printed layers.

Mean dry film thickness

The mean dry film thickness is calculated by averaging over the laterally resolved discrete topography data $h(i,j)$ as

$$\overline{h} = \frac{1}{(i_\mathrm{m}+1)(j_\mathrm{m}+1)} \sum_{i=0}^{i_\mathrm{m}} \sum_{j=0}^{j_\mathrm{m}} h(i,j), \tag{4.1}$$

where $i \in [0, i_\mathrm{m}]$ corresponds to the image pixel resolution of $(i_\mathrm{m}+1) \times (j_\mathrm{m}+1)$. If not specified otherwise by additional indices, $\overline{h}$ and $h(i,j)$ describe the mean and local thickness of the top layer, respectively.

Relative RMS roughness

The lateral root mean square RMS roughness S_q is a scalar parameter of unit length ([m]) which is usually determined for surfaces represented by topography (height) data $z(i,j)$ (with its mean $\overline{z}$), such as acquired by profiling techniques. It is defined by, [240],

$$S_\mathrm{qz} = \sqrt{\frac{1}{(i_\mathrm{m}+1)(j_\mathrm{m}+1)} \sum_{i=0}^{i_\mathrm{m}} \sum_{j=0}^{j_\mathrm{m}} |\overline{z} - z(i,j)|^2}. \tag{4.2}$$

In this case, the surface is usually aligned parallel to the xy or ij plane before determining the roughness. For example, a perfectly planar surface in a xyz box of unity (side lengths of 1) which is misaligned by an angle of $\sim 6\,^\circ$ to the xy plane would exhibit an apparent roughness of $S_{\mathrm{qz}} = 0.1$ instead of the true value of $S_{\mathrm{qz}} = 0$ if aligned.

On the contrary, the imaging color reflectometry (ICR) determines the layer thickness relatively to a substrate, i.e. a wavy, curved or inclined substrate do not affect the thickness data of the thin film. It is important to note that, strictly speaking, the thickness data $h(i,j)$ does not represent an arbitrary topography. It possesses the constraint that the bottom surface of the film is located at $z = 0$. Then, $h(i,j)$ can be understood as "topography data" $z(i,j)$. However, since I am interested in the variation of $h(i,j)$, it does not need to be aligned before calculating the roughness. For the afore mentioned example of a perfect upper surface of $\sim 6\,^\circ$ inclination (to the bottom surface of the layer at $z = 0$), this means for the thickness $h(i,j)$ that it obeys a strong variation of 0.1 which would be the value of interest. Therefore, ICR systematically ensures that the RMS roughness values are not distorted by misalignment, curvatures or in-homogeneities of the substrate as is the case with other profiling techniques.

Following Equation 4.2, the RMS roughness S_{q} of the thickness data $h(i,j)$ is defined by, [240],

$$S_{\mathrm{q}} = \sqrt{\frac{1}{(i_{\mathrm{m}}+1)(j_{\mathrm{m}}+1)} \sum_{i=0}^{i_{\mathrm{m}}} \sum_{j=0}^{j_{\mathrm{m}}} \left|\overline{h} - h(i,j)\right|^2}. \tag{4.3}$$

S_{q} can also be understood as the standard deviation of the thickness $h(i,j)$ or the root of the second central moment (variance) [240]. It describes the deviation of the thickness from its mean[6], but it does not contain any information about the lateral distribution.

It is also important to note that the measured roughness depends on the spatial resolution of the measurement device. Each pixel represents the average thickness of a certain area. A decrease in resolution increases this area, which filters out therein containing inhomogeneities, possibly resulting in a reduced roughness. Thickness variations below the spatial resolution of the measurement device are accounted for by the RMS roughness value although strong roughness might be present in the nanometer range. For this reason, I compare roughnesses of different fields and printing runs based on data obtained with the same settings and the same hardware setup.

In gravure printing, varying process parameters usually result in different film thicknesses. To compare the different printing outcomes, I therefore normalize S_{q} by the mean of the layer thickness yielding the dimensionless relative RMS roughness

$$\begin{aligned} S_{\mathrm{qr}} &\equiv \frac{S_{\mathrm{q}}}{\overline{h}}, \\ \tilde{S}_{\mathrm{qr}} &\equiv S_{\mathrm{qr}} \cdot 100\%. \end{aligned} \tag{4.4}$$

The second definition $\tilde{S}_{\mathrm{qr}}$ in units of [%] is also known as the coefficient of variation. Stahl [237] and Michels et al. [179] used this as a key parameter to describe the homogeneity of gravure printed polymer layers in their studies. Throughout this thesis, I might denote the relative RMS roughness S_{qr} sometimes "roughness" only.

[6] assuming a Gaussian distribution around its mean, then, 65.7% of the data lie within this distribution [240]

Skewness and kurtosis

Whereas the RMS roughness is proportional to the second statistical central moment of the surface describing the variation of the data, I also applied the third and fourth normalized central moment as a measure. They are termed skewness and kurtosis in the literature and are dimensionless because they are normalized by the RMS roughness to the power of the order number.

The skewness is defined as [240]

$$S_{\mathrm{sk}} \equiv \frac{1}{{S_{\mathrm{q}}}^3} \frac{1}{(i_{\mathrm{m}}+1)(j_{\mathrm{m}}+1)} \sum_{i=0}^{i_{\mathrm{m}}} \sum_{j=0}^{j_{\mathrm{m}}} \left|\overline{h} - h(i,j)\right|^3 \quad \text{(skewness)}, \tag{4.5}$$

and represents the direction of the variation or its asymmetry to the mean.

Figure 4.8f shows different example profiles to illustrate the surface parameters. Skewness values are termed *negatively skewed* if more values are located above the mean, such as example profiles shown in Figure 4.8a, c, d, f, and *positively skewed* vice versa as depicted in Figure 4.8e. For a complete symmetric distribution of the values around the mean, the skewness is zero as illustrated in the periodic profile in Figure 4.8b.

The fourth moment, the kurtosis of a surface, is defined as [240]

$$S_{\mathrm{ku}} \equiv \frac{1}{{S_{\mathrm{q}}}^4} \frac{1}{(i_{\mathrm{m}}+1)(j_{\mathrm{m}}+1)} \sum_{i=0}^{i_{\mathrm{m}}} \sum_{j=0}^{j_{\mathrm{m}}} \left|\overline{h} - h(i,j)\right|^4 \quad \text{(kurtosis)} \tag{4.6}$$

and might be a measure of the "peakedness" of the distribution of the topography data compared to a Gaussian one [49, 50]. For a Gaussian distribution, finding values in the interval between h_1 and h_2 exhibits a probability $W(h_2, h_1)$ proportional to

$$W(h_2, h_1) \propto \int_{h_1}^{h_2} \exp\left(\frac{x-\overline{h}}{S_{\mathrm{q}}}\right)^2 \mathrm{d}x, \tag{4.7}$$

where $\overline{h}$ is the mean height and S_{q} the RMS roughness. For a height profile with a Gaussian distribution, such as illustrated in Figure 4.8a, the kurtosis is exactly $S_{\mathrm{ku}} = 3$. For real lateral extended height measurements of flat surfaces with small roughnesses below the resolution of the measurement device one can expects a kurtosis of $S_{\mathrm{ku}} \sim 3$ because of the thermal noise in the measurement system.

Regular patterns, such as the periodic height profile sketched in Figure 4.8b, show a kurtosis of $S_{\mathrm{ku}} < 3$. One can expect these values for surfaces of solution-processed layers which exhibit undulations of preferred wavelengths such as those originating from spinodal dewetting (see Section 3.6.2) or ribbing structures from printing nip instabilities (see Section 3.5).

A single valley in an otherwise flat topography of the dry film could evolve from defects on the substrate, impurities in the ink or thermal fluctuations as introduced in Section 3.6.3. Figure 4.8c sketches such example profile in which the thickness values are closely distributed around its mean. Therefore, the kurtosis of this type of topography is in the range $S_{\mathrm{ku}} > 3$, for the profile of Figure 4.8c it is $S_{\mathrm{ku}} = 9.27$.

A sample profile with even more deep trenches is illustrated in Figure 4.8d, which has a very high kurtosis value of $S_{\mathrm{ku}} = 31.98$.

In the late stages of a dewetting process, the fluid tend to form drop-like shapes minimizing surface area. This does not require complete dewetting of the substrate, it is also possible that drops

are formed on top of the liquid film as schematically shown in Figure 4.8e, [24]. In this case, the skewness is positive and the kurtosis is close to 3.

Finally, Figure 4.8f sketches the sum of all profiles from Figure 4.8a-e shifted back to ensure a mean height of 1. Skewness and kurtosis are comparable to a Gaussian distribution, but the RMS roughness is doubled. This elucidates that roughness, skewness and kurtosis are not necessarily connected and constitute independent surface parameters.

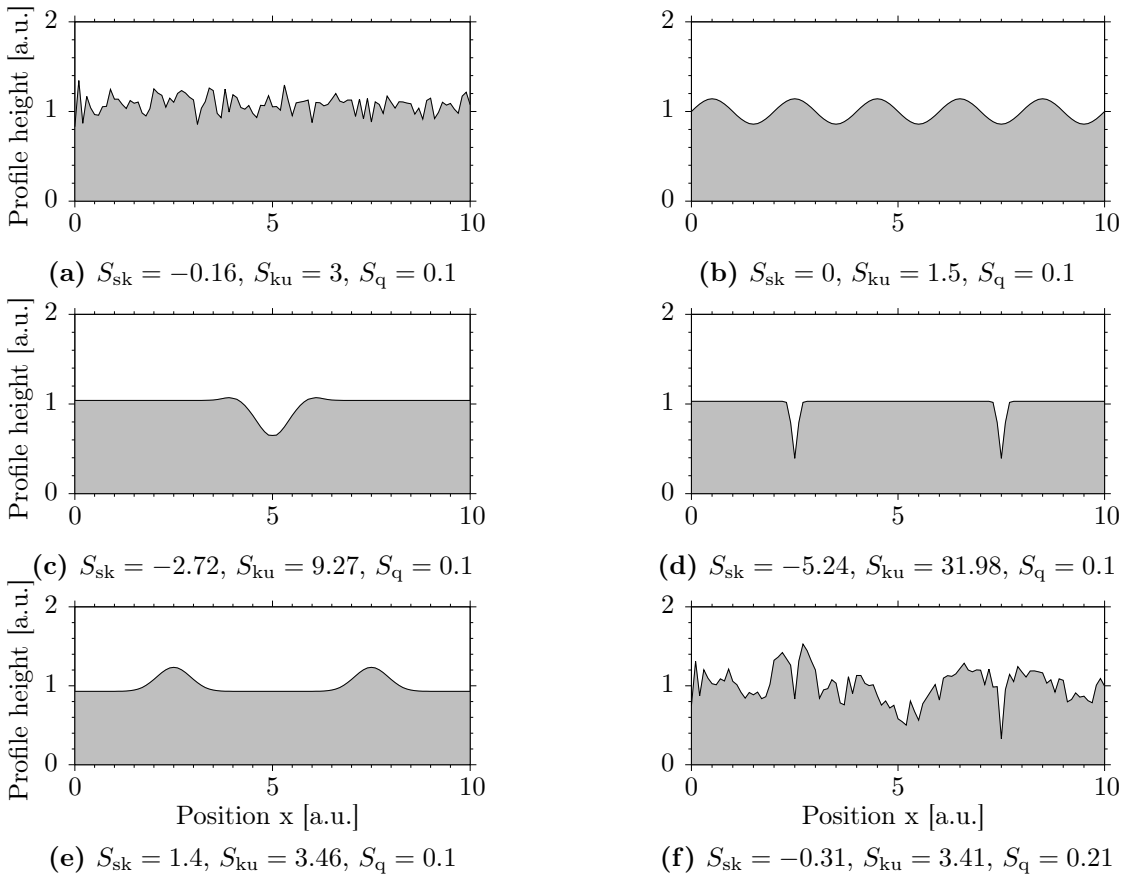

(a) $S_{\mathrm{sk}} = -0.16$, $S_{\mathrm{ku}} = 3$, $S_{\mathrm{q}} = 0.1$

(b) $S_{\mathrm{sk}} = 0$, $S_{\mathrm{ku}} = 1.5$, $S_{\mathrm{q}} = 0.1$

(c) $S_{\mathrm{sk}} = -2.72$, $S_{\mathrm{ku}} = 9.27$, $S_{\mathrm{q}} = 0.1$

(d) $S_{\mathrm{sk}} = -5.24$, $S_{\mathrm{ku}} = 31.98$, $S_{\mathrm{q}} = 0.1$

(e) $S_{\mathrm{sk}} = 1.4$, $S_{\mathrm{ku}} = 3.46$, $S_{\mathrm{q}} = 0.1$

(f) $S_{\mathrm{sk}} = -0.31$, $S_{\mathrm{ku}} = 3.41$, $S_{\mathrm{q}} = 0.21$

Figure 4.8: Example 2D height profiles to demonstrate values of the surface parameters **skewness** $S_{\mathbf{sk}}$ and **kurtosis** $S_{\mathbf{ku}}$. Plot (a) shows a Gaussian distributed profile, (b) a periodic undulation, (c) a possible dewetting process originated from a nucleation, (d) a flat surface with deep and narrow holes, (e) hemisphere formation on top of the surface and (f) the sum of all profiles from (a) - (e) shifted back to the mean height. The mean height is 1 for all profiles. The **RMS roughness** $S_{\mathbf{q}}$ is $S_{\mathrm{q}} = 0.1$ for (a) - (e) and $S_{\mathrm{q}} = 0.21$ for (f).

Michels et al. discuss the possibility of using the kurtosis as a measure for the anisotropy of gravure printed OLED layers, but they discarded it because of high noise present in their topography data [179].

The scalar standardized surface parameters introduced above do not contain any information of lateral length scales of possible undulations. I therefore introduce the isotropic dominant wavelength of surfaces in the following paragraph.

Isotropic dominant wavelength of surface undulations

A common method for describing lateral or spectral properties of surfaces is power spectral analysis, which makes it possible to determine periodicity and wavelength. I performed spectral analysis on my

measurements in the frequency domain by using a Fourier transformation. The obtained thickness data $h(i,j)$ with i,j as pixel position or $h(x_j,y_i)$ with x_j, y_i as spatial position is discretized in all dimensions. Therefore, the lateral 2D discrete Fourier transformation $\mathcal{H}$ of the thickness data is defined as [29, 62]

$$\mathcal{H}(\mu_q,\nu_p)=\frac{1}{XY}\sum_{j=0}^{j_\mathrm{m}}\sum_{i=0}^{i_\mathrm{m}}h(x_j,y_i)e^{-\mathrm{i}\,2\pi(\mu_q x_j+\nu_p y_i)}, \tag{4.8}$$

where X and Y are the spatial width and height of the initial image data, p and q are the spatial integers in the frequency domain and μ_q and ν_p the corresponding frequencies. All integers used in the description of Equation 4.8 are limited by the pixel resolution of the initial image[7] as follows

$$\begin{aligned}0\leq i,p\leq i_\mathrm{m},\\ 0\leq j,q\leq j_\mathrm{m}.\end{aligned} \tag{4.9}$$

The relationships of the centered spatial variables in both domains are as follows [233]

$$\begin{aligned}x_j&=(j+1-j_\mathrm{m}/2)\cdot\Delta x,\\ y_i&=(i+1-i_\mathrm{m}/2)\cdot\Delta y,\\ \mu_q&=(q+1-j_\mathrm{m}/2)/X,\\ \nu_p&=(p+1-i_\mathrm{m}/2)/Y,\end{aligned} \tag{4.10}$$

where Δx and Δy denote the spatial smallest distances between two adjacent lateral data points or pixels in x and y direction. The frequencies μ_q and ν_p denote the periods or cycles per unit length. Thus, the reciprocals describe the wavelength in the lateral dimensions with

$$\lambda_x=\frac{1}{\mu_q},\ \lambda_y=\frac{1}{\nu_p}. \tag{4.11}$$

The discrete Fourier transform determined using a mathematical computer software (such as MATLAB) is commonly implemented by the so-called fast Fourier transformation (FFT) which strongly reduces computational time [203, 259].

Since I am interested in the wavelength spectrum of the undulations appearing at the surface regardless of the phase, I determine the power spectral density $PSD(\mu_q,\nu_p)$ which is the square of the Fourier transform defined as [233]

$$PSD(\mu_q,\nu_p)\equiv|\mathcal{H}(\mu_q,\nu_p)|^2. \tag{4.12}$$

Figure 4.9a shows the thickness data h of a representative field[8] with its lateral dimensions in millimeter (centered for x_j, y_i). The corresponding 2D power spectral density surface plot is depicted in Figure 4.9b reduced to frequencies $|\mu_q,\nu_p|\leq 5\cdot 1/\mathrm{mm}$. Equation 4.12 and Figure 4.9b describe the power spectral density of the surface h. To compare the 128 printed fields according to their undulations, a scalar parameter per field needs to be formulated. One could find frequency positions of maxima directly within the PSD, or one could average the PSD in one dimension, for example in x, to result in a one-dimensional PSD_1D representing undulations in printing direction. Herein, the maximum would signify the dominant wavelength. For stripe-like printing defects such as commonly

[7] $(i_\mathrm{m}+1)\times(j_\mathrm{m}+1)$

[8] process parameters: printing velocity $v=1.25$ m/s, cell volume $V_\mathrm{c}=1.42$ ml/m^2 and screen ruling SR = 120 L/cm

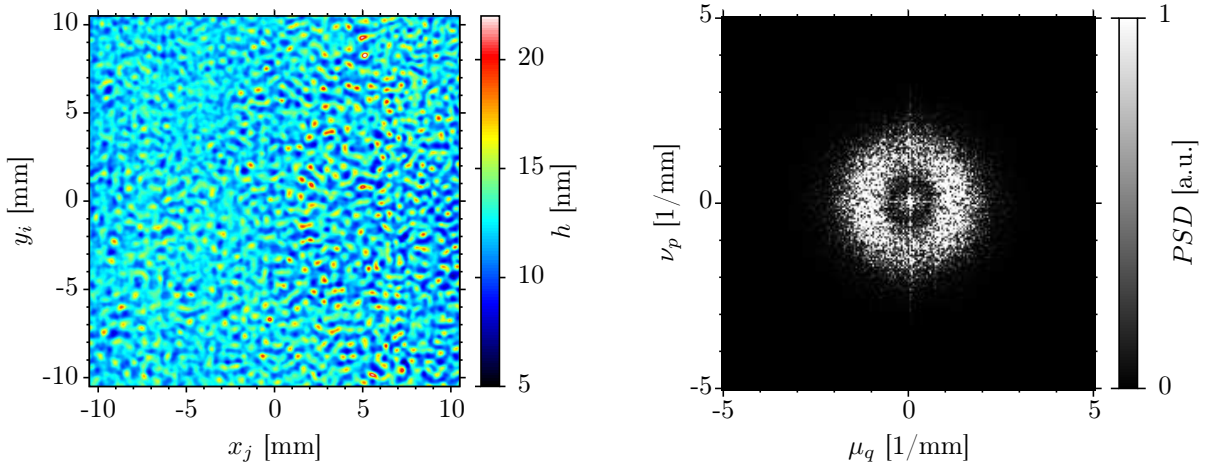

(a) Thickness data h in the spatial domain.

(b) Power spectral density PSD in the frequency domain.

Figure 4.9: Central area of the thickness data of a representative printed field in (a) and the corresponding power spectral density in (b). The frequencies are reduced to the central part of the maxima located within $|\mu_q, \nu_p| \leq 5 \cdot 1/\text{mm}$.

obtained for more viscous inks such as investigated by Michels et. al., Stahl or Hernandez-Sosa et al. [103, 179, 237], this procedure would be suitable.

But as representatively illustrated in Figure 4.9b and valid for most of the printing results discussed in the next section, the PSDs obey a circular symmetric shape. This indicates that the undulations follow a strongly isotropic distribution. Therefore, I change from the cartesian (μ_q, ν_p) to the polar (ϱ, φ) coordinate system in the frequency domain. The variables are now

$$\mu_q = \varrho \cos\varphi, \quad \nu_p = \varrho \sin\varphi, \tag{4.13}$$

with the radial frequency

$$\varrho = \sqrt{{\mu_q}^2 + {\nu_p}^2}, \tag{4.14}$$

and the radial wavelength

$$\lambda_\varrho = \frac{1}{\varrho}. \tag{4.15}$$

Strictly speaking, the mapping of the discrete values of the rectangular grid as described in Equation 4.14 is not an exact transformation, which may result in small errors that I assume to be negligible. I radially average the 2D power spectral density with

$$PSD_{1\text{D}}(\varrho) \equiv \frac{1}{2\pi\varrho} \sum_{\varphi} PSD(\varrho, \varphi). \tag{4.16}$$

I determine the maxima of the now wavelength dependent $PSD_{1\text{D}}(\lambda_\varrho)$ within the range from $\lambda_\varrho \in [0, 3]$ mm because this contains the main lateral undulations of interest. I define the argument for which $PSD_{1\text{D}}(\lambda_\varrho)$ takes its maximum value as the **isotropic dominant wavelength** of the surface undulations of the printed field with

$$\lambda_{\text{iso}} \equiv \underset{\lambda_\varrho \in [0,3]\ \text{mm}}{\arg\max} \left\{ PSD_{1\text{D}}(\lambda_\varrho) \right\}. \tag{4.17}$$

The radially averaged $PSD_{1D}(\lambda_\varrho)$ of Figure 4.9b is depicted in Figure 4.10.[9] The maximum wavelength is located at $\lambda_{iso} = 0.86$ mm. In this way, I determined the surface parameters of all printed

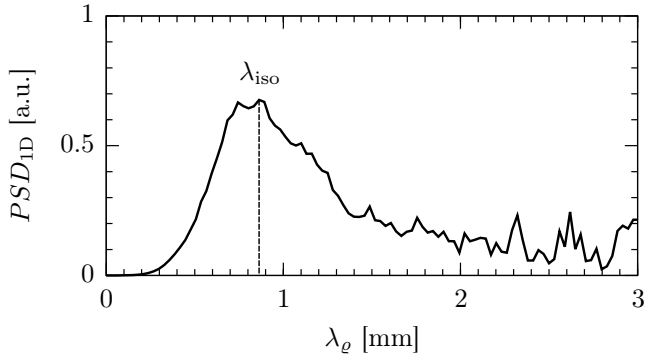

Figure 4.10: Radially averaged power spectral density PSD_{1D} of the 2D data depicted in Figure 4.9b and the topography shown in Figure 4.9a. The maximum value is located at the isotropic dominant wavelength $\lambda_{iso} = 0.86$ mm.

fields presented in the following section.

4.4 Results and discussion

The 32 different engraved fields on the gravure cylinder depicted in Figure 4.6 and summarized in Table 4.1 were printed with the four different velocities of the lab-scale printing unit from Prüfbau (Figure 4.3). The toluene-based ink solved with 3.5 wt-% spiro-MeOTAD dried within 9 s or less on the two consecutively mounted 150×150 mm^2 ITO-glass substrates after printing, as captured by the video camera. These drying times correspond to the drying constant C_{dry} of this solution which was obtained using a micro-balance. Thereby, the mass loss within a known time period was determined resulting in $C_{dry} = (441 \pm 13)$ nm/s under the same environmental laboratory conditions as for the printing experiments.

With the imaging color reflectometry ICR introduced in Chapter 2, I characterized all printed samples using the flatbed scanner setup. The resulting layer thicknesses of the different fields of the dry spiro-MeOTAD of all samples are depicted in Figure 4.11. Two consecutively mounted substrates per printing run are arranged horizontally, the samples for different printing velocities vertically (in Figure 4.11). Since the printing unit lacked the function of registered printing (alignment in printing direction), fields of different printing runs (different v_i's) can not be directly compared vertically in Figure 4.11. For some fields at the border of the substrates and in particular for the fields of sample #2 for velocity v_4 in Figure 4.11, we observe visible stripes within the fields originating from inappropriate contact of gravure cylinder and substrate. Additionally to these fields, I excluded those from the analysis which were undersized.

The ICR algorithm using the modified Epson flatbed scanner revealed two issues. Occasionally, scanned images of printed fields with a screen ruling of SR = 70 L/cm showed optical artifacts in form of rings, for example, the fields on sample #1 for v_3 in Figure 4.11. Possible origins of this

[9] I setup a MATLAB script for computing the radial averaged PSD_{1D}, it is presented in the Appendix C.3.2 on page 174. Nevertheless, I half-automatically determined the isotropic dominant wavelength using the software Mountains Map 5.1 from Digital Surf, France, after validation of the method with the MATLAB script.

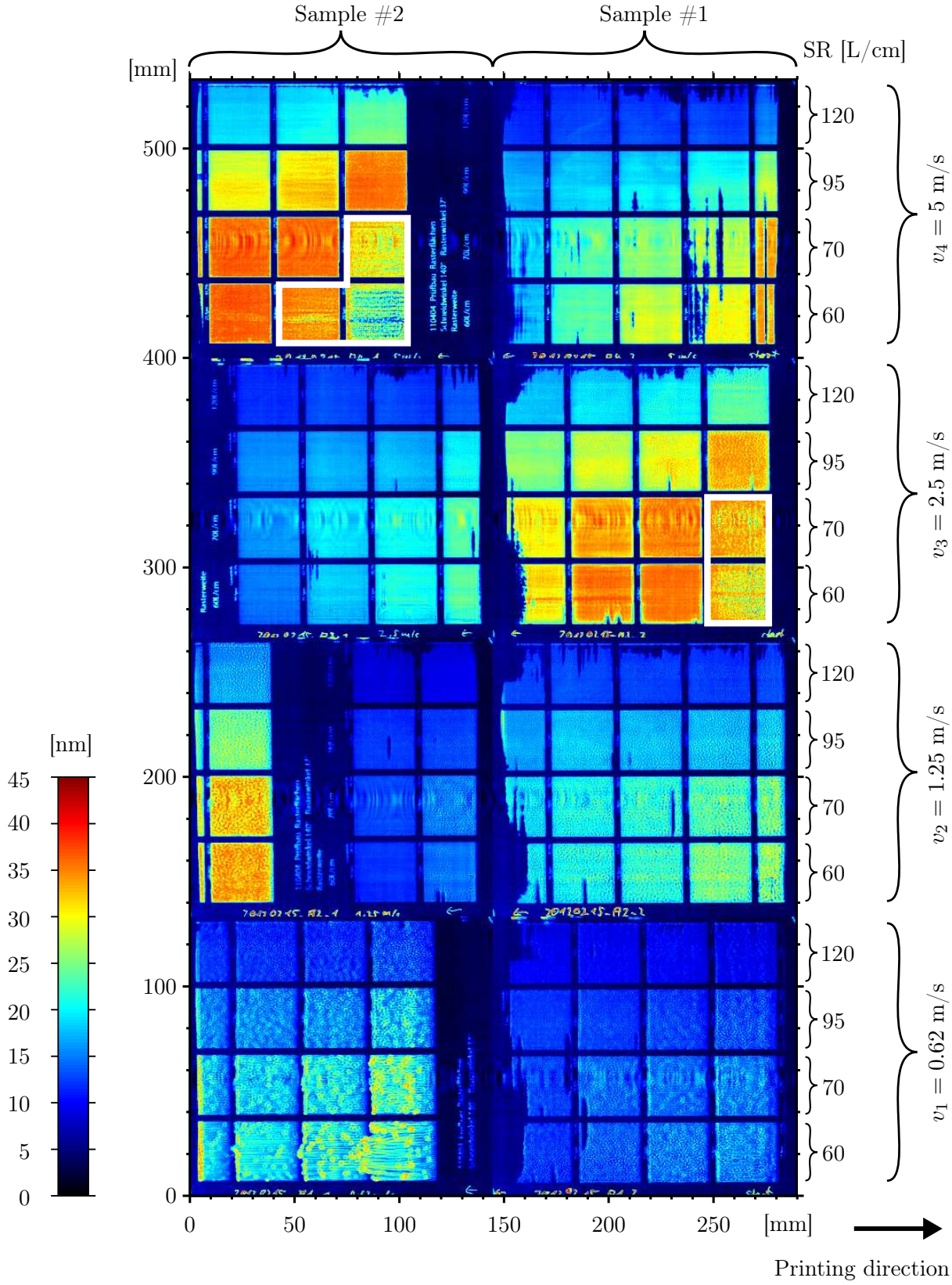

Figure 4.11: Topography of all 8 printed 150×150 mm^2 samples determined by imaging color reflectometry (ICR). Two samples arranged horizontally represent a single printing experiment with its desired printing velocity v_i. The 128 printed fields have dimensions of 30×30 mm^2 each, for some fields the printing step failed due to inappropriate contact of gravure cylinder and substrate. Issues resulting from the ICR method: optical artifacts in form of rings and failure of the thickness estimation of the framed fields in white.

phenomenon are discussed in Section 2.3.2 on page 32. The drawbacks of these rings were slightly increased roughness values and broadened wavelength spectra.

Second, the ICR algorithm estimated unreliable thickness values of fields with thicknesses above 45 nm. Those five fields framed with white lines in Figure 4.11 (sample #1 for v_3 and #2 for v_4) were excluded from the analysis at first. The failure of the thickness estimation was confirmed by counter-checking thicknesses of some fields above and below 45 nm using phase-shifting interferometry. I also repeated ICR measurements of layers > 45 nm with the microscope resulting in the same issue. The latter confirmed that this did not originate from the optical hardware setups. Because of this and based on the results of the sensitivity analysis of the ICR method in Section 2.6, I concluded that deviations in the refractive indices might had caused this problem.

4.4.1 Mean dry film thickness

Based on the thickness data shown in Figure 4.11, I determined the mean dry film thickness $\overline{h}$ of the organic semiconductor spiro-MeOTAD on the ITO coated glass substrates of the printed fields. In Figure 4.12, I relate the film thickness $\overline{h}$ to the cell volume V_c of the corresponding fields on the gravure cylinder for the different printing velocities v_i and all screen rulings SR. The thicknesses

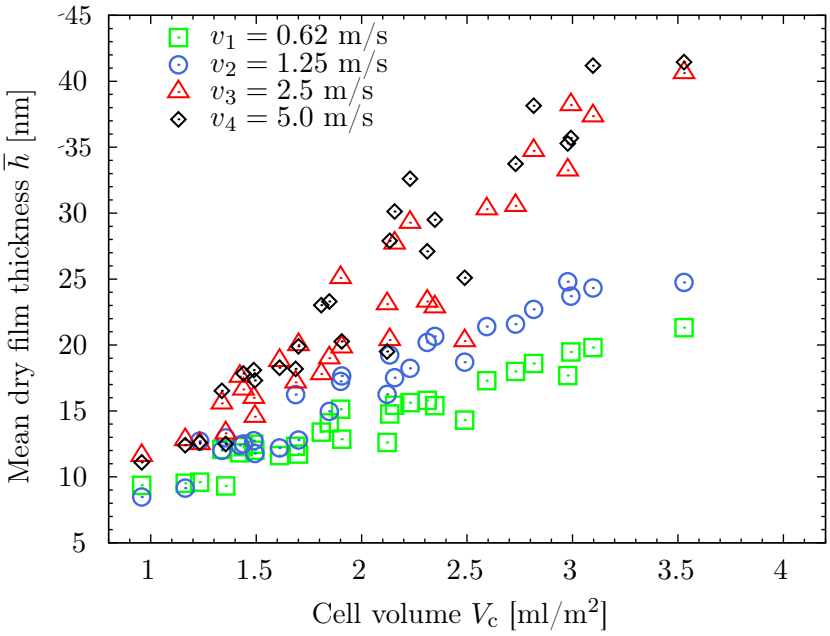

Figure 4.12: Mean dry film thickness $\overline{h}$ of all fields related to corresponding cell volumes V_c on the gravure cylinder for different printing velocities v_i and all screen rulings SR.

seem to increase for increasing cell volume as expected because the more fluid is provided in the cells the more is transferred to the substrate. Additionally, we can observe that the films become thicker for faster printing velocities. This dependency is the opposite of the one found in graphical gravure printing as for example investigated by Takahashi et al. and Elsayad et al. [65, 242] or as one can deduce from Figure 3.15a of the preliminary printing results in Section 3.7.1. This behavior is rather known from forward gravure or roll coating applications [16]. In the following sections, I recurringly elaborate on this parallelism.

In Figure 4.12, I omitted the dependency on screen ruling because usually[10] cell volume and printing velocity mainly affect the transferred film thickness. However, by distinguishing between different screen rulings, I found surprising dependencies which are depicted in Figure 4.13. To simplify the

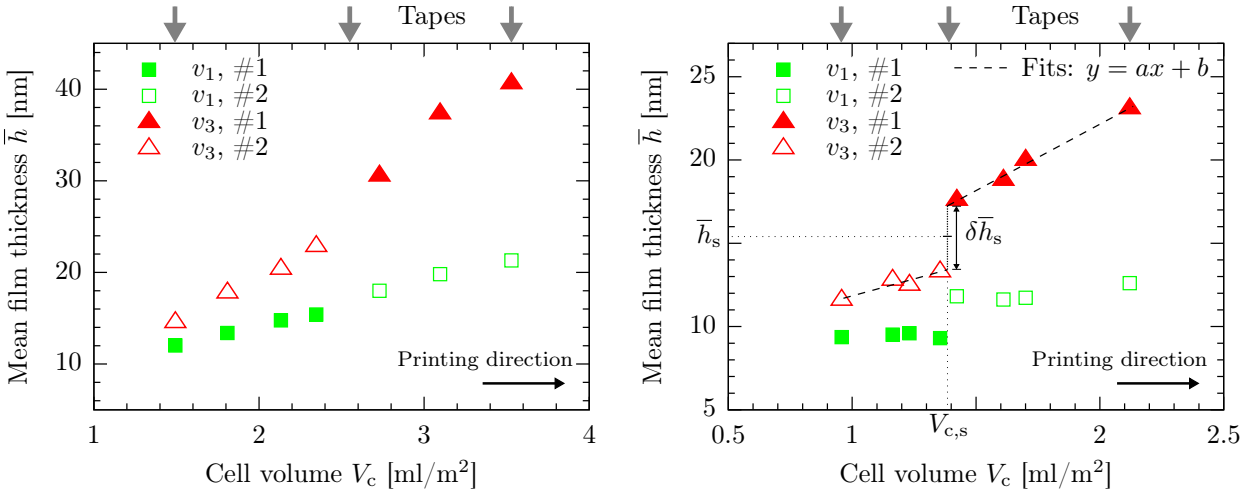

(a) SR = 60 L/cm. **(b)** SR = 120 L/cm.

Figure 4.13: Dry film thickness vs. cell volume for different velocities ($v_1 = 0.62$ m/s and $v_3 = 2.5$ m/s) and screen rulings (SR). Gray vertical arrows indicate the position of the adhesive tapes (width: 10 mm, thickness: 50 µm) for the fixation of the substrates related to the cell volume. Filled symbols indicate results of the substrates which were printed first (#1) and open symbols which were printed second (#2) in each run. In (b), the steps are qualitatively marked as $\delta\overline{h}_s$, which is the vertical difference in thickness of the two extrapolated linear fits for the two substrates at the mean x-position $V_{c,s}$ of the cell volume between the adjacent data points of the step. The relative step height $\delta\overline{h}_s/\overline{h}_s$ is summarized in the Figure 4.15 for all printing runs.

presentation, I separated the plots by different velocities and screen rulings and show only representative data sets. In Figure 4.13, film thickness is plotted against cell volume for different velocities and constant screen ruling. The printing direction from left to right coincides with the arrangement of the fields on the gravure cylinder from small to large cell volumes. The gray vertical arrows indicate the position, related to the cell volume, of the adhesive tapes (with width 10 mm and thickness 50 µm) which were used to mount the substrates on the carrier. The same type of symbols (open and filled) within each plot represent the same printing run with its specific printing velocity. Filled symbols indicate the data points of the substrates which were printed first (#1) and open symbols which were printed second (#2). Hence, the rightmost data point of the filled symbols in Figures 4.13 represent the initial printed field and the leftmost open symbol the last printed field of each run.

Because of the lacking registration of the printing unit, the position of the gravure fields in printing direction with respect to the substrate position differs in subsequent printing runs. Accordingly, the volume of the cells that hit a given position of the substrate is distinct in different printing runs, and at different printing velocities. Specifically the printing start can be located at any of the cylinder's cell volumes. By chance, for velocity v_1 and v_3, the transition from the first to the second substrate is located between the same fields but in opposite order. Therefore, the presentation of these printing velocities is combined in Figures 4.13a and 4.13b.

[10] in graphical gravure printing

From Figure 4.13 three remarkable features can be identified: First, the overall slopes of the $\overline{h}$-V_c curves[11] for the different data sets seem to depend on the screen rulings. To clarify this aspect, I performed linear regressions on all data sets for both substrates within a single printing run for constant velocity and different screen rulings. The resulting slopes a of the linear regression with $y = ax + b$ of all $\overline{h}$-V_c curves are shown in Figure 4.14. The slope expresses the change in dry film thickness in units of [nm] for changing cell volume in units of [ml/m^2]. For example, the maximum value of $a = 14.5$ nm/(ml/m^2) in Figure 4.14 at SR = 60 L/cm means that an increase of the cell volume by 1 ml/m^2 would result in a thickness increase of 14.5 nm. Figure 4.14 clearly shows that

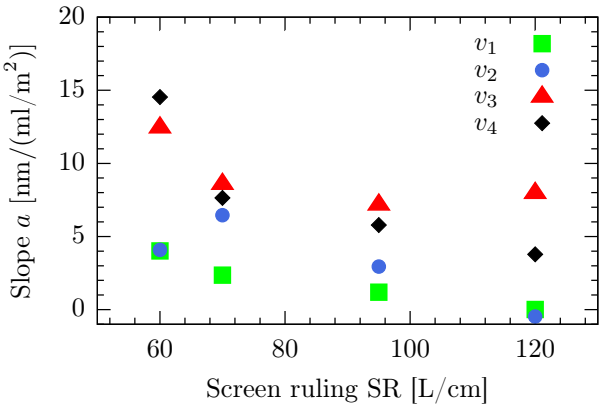

Figure 4.14: Different slopes $a = \mathrm{d}\overline{h}/\mathrm{d}V_c$ of the linear regressions of all $\overline{h}$-V_c curves for all printed fields within a single printing run in relation to cell volume V_c and for different printing velocities v_i.

increasing the dry film thickness of the printed layer by using larger cell volumes is most efficient for small screen rulings and high printing velocities, but almost without effect in the opposite case.

Second, Figure 4.13b reveals slopes close to zero, especially for $v = 0.62$ m/s. For both printed substrates in each run, this is also verified by values around zero in Figure 4.14. This means that although the cell volume increases the resulting film thickness stays constant. This is a surprising observation.

Third and most obvious, Figure 4.13b reveals discontinuous changes of the film thickness after the gravure cylinder passed the adhesive tapes, mainly depending on printing velocity and on the resulting cell volume at the step $V_{c,s}$ which coincides with the screen ruling in this case.

The proportionality of the cell volume at the step and the screen ruling mainly originates from the design of the gravure cylinder, as shown in Figure 4.6 and with values given in Table 4.1. Therein, it is obvious that at a given printing position (horizontal values in the table), the cell volumes always linearly increase for decreasing screen rulings (vertical values in the table). Because the tape is fixed along the printing width, the step occurs always for four fields with different screen ruling and almost constant relation of the cell volumes. It is important to note that this dependency is only valid for the analysis of the present layer steps.

In Figure 4.13b, these discontinuities in layer thicknesses are qualitatively marked as $\delta\overline{h}_s$. They denote the vertical difference in thickness of the extrapolated linear fits for the two substrates (dashed

[11] dry film thickness vs. cell volume of the gravure cylinder

lines in Figure 4.13b) at the mean x-position (in cell volume) between the adjacent data points of the step. I define the resulting relative step heights $\delta\overline{h}_{\mathrm{sr}}$ as

$$\delta\overline{h}_{\mathrm{sr}} \equiv \frac{\delta\overline{h}_{\mathrm{s}}}{\overline{h}_{\mathrm{s}}}, \tag{4.18}$$

where $\overline{h}_{\mathrm{s}}$ is the mean thickness (see Figure 4.13b). These values are summarized in Figure 4.15 for thickness steps of all printing runs.

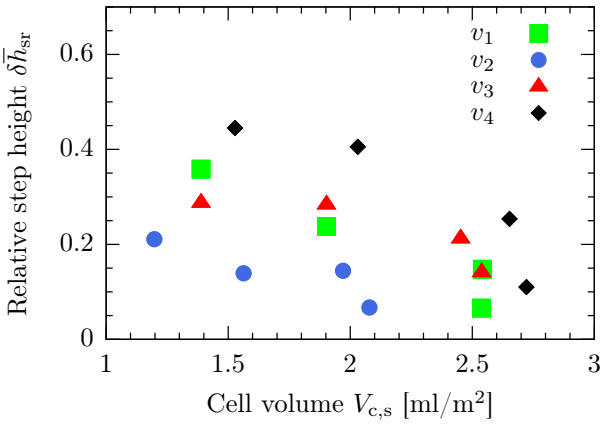

Figure 4.15: Relative step height $\delta\overline{h}_{\mathrm{sr}} = \delta\overline{h}_{\mathrm{s}}/\overline{h}_{\mathrm{s}}$ (compare Figure 4.13b) when passing an adhesive tape during printing, related to the corresponding cell volume at the step $V_{\mathrm{c,s}}$.

Thus, the relative step height $\delta\overline{h}_{\mathrm{sr}}$ increases for increasing printing velocity and cell volume at the step $V_{\mathrm{c,s}}$ (Figure 4.15). A maximum of almost $\delta\overline{h}_{\mathrm{sr}} = 0.45$ (a step height of 45 % of the initial layer thickness) is located at $V_{\mathrm{c,s}} = 1.5$ ml/m^2 for $v = 5$ m/s.

Without discussing possible driving mechanisms for this phenomenon here[12], I conclude that passing a physical step (adhesive tape) during printing affects the subsequent ink transfer behavior so that the final dry layer exhibits a step as well. This means that for the same printing, ink and cylinder parameters, the ink transfer after the step is different from that one without passing a step. Generally speaking, the fluid transfer from cylinder to substrate is influenced by former printing events or so to say by the *printing history* within each specific printing run. This might not necessarily be restricted to steps on the substrate but to any feature which affects the boundary condition of ink transfer hydrodynamics.

Nonlinear regression

After presenting different aspects and parameters concerning layer thickness, I applied a non-linear regression to detect a possible universal relation between the parameters. I describe the regression of the dry film thickness $\tilde{h}$ as a function of cell volume V_{c}, screen ruling SR and printing velocity v:

$$\tilde{h}(V_{\mathrm{c}}, v, \mathrm{SR}) = a\, {V_{\mathrm{c}}}^{b}\, \mathrm{SR}^{c}\, v^{d}, \tag{4.19}$$

where the constants a and the exponents b, c, d are the fit parameters. The difference between two consecutive substrates, i.e. the thickness step (see Figure 4.13), was left out. A polynomial fit of high orders might result in a fit better matching the experimental data, but I chose a power-law

[12] this is presented in the paragraph in Section 4.4.3 on page 112

function to obtain a scaling behavior dependent on a single exponent for the different parameters. For the regression, I used the multi-dimensional non-linear fitting algorithm `nlinfit(...)`[13] from the numerical computation software MATLAB which is implemented according to Demouchel et al. [63]. I obtained the following fitting constants based on Equation 4.19 and applied to the experimental data illustrated in Figure 4.12

$$\begin{aligned} a &= 7.50 \pm 54\% \\ b &= 0.96 \pm 9.3\% \\ c &= 0.02 \pm 494\% \\ d &= 0.29 \pm 10.7\%. \end{aligned} \tag{4.20}$$

The coefficient of determination of the regression was $R^2 = 0.91$. The errors of the fitting constants mark the confidence bounds of the regression which were set by default to 95%. The film thickness insignificantly depends on the screen ruling ($\sim \mathrm{SR}^{0.02}$). One the other hand, by rounding the other exponents, which possess errors below 11%, in Equation 4.20 to one decimal place within the bounds of confidence, the mean dry film thickness results in[14]

$$\boxed{\overline{h} \propto V_\mathrm{c}\, v^{0.3}}. \tag{4.21}$$

This relation −thickness is proportional to cell volume times velocity to the power of 0.3− summarizes the most dominant tendency of the total data set illustrated in the first Figure 4.11 of this section. As mentioned before, linear dependency on cell volume is expected but the positive proportionality to printing velocity is a surprising result and possibly a specific feature of the type of low viscous functional inks as discussed here.

In the next section, I present and discuss the transfer ratio and compare the results to gravure coating experiments from Benkreira et al. [16].

4.4.2 Transfer ratio

In graphical gravure printing, the quantity of transferred ink is usually specified in terms of the transfer ratio, which relates the transferred mean wet film thickness on the substrate to the cell volume of the gravure cylinder. From the known concentration of the organic material spiro-MeOTAD of $c_\mathrm{spiro} = 3.5$ wt-% dissolved in toluene and the mean dry film thickness $\overline{h}$, I estimated the transferred mean wet film thickness h_w, which was applied to the substrate. For that, I had to specify the mass densities of the ink solution and the dried layer. For the solution, I determined the density from the value of pure toluene ($\rho_\mathrm{tol} = 0.862$ g/cm^2 at 20°C, [126]) adding the mass of the organic compound without changing the total volume which resulted in $\rho_\mathrm{sol} = 0.9$ g/cm^3. The density of spiro-MeOTAD was determined by Ding et al. to $\rho_\mathrm{spiro} = 1.82$ g/cm^3 [57]. With this, I estimated the transferred mean wet film thickness of the ink solution h_w using

$$h_\mathrm{w} \approx \frac{\rho_\mathrm{spiro}}{\rho_\mathrm{sol}} \frac{100}{c_\mathrm{spiro}}\, \overline{h}. \tag{4.22}$$

[13] the MATLAB program can be found in the appendix on page 173

[14] supposing $\overline{h} \stackrel{!}{=} \tilde{h}$

Now, by relating the wet film thickness h_w to the empty total cell volume of the gravure cylinder V_c, which effectively also has units of length $[\mathrm{ml/m^2}] = [\mu\mathrm{m}]$, I determined the dimensionless transfer ratio defined as

$$A_\mathrm{TR} \equiv \frac{\overline{h}_\mathrm{w}}{V_\mathrm{c}} \approx \frac{\rho_\mathrm{spiro}}{\rho_\mathrm{sol}} \frac{100}{c_\mathrm{spiro}} \frac{\overline{h}}{V_\mathrm{c}} \propto \frac{\overline{h}}{V_\mathrm{c}} \tag{4.23}$$

per printed field. For the right term of Equation 4.23, I used Equation 4.22. Hence, all dependencies discovered for the dry film thickness in Section 4.4.1 should be normalized by the cell volume when dealing with the transfer ratio. However, it is worth taking up the point of the general scaling behavior of Equation 4.21 because then, Equation 4.23 reduces to

$$\boxed{A_\mathrm{TR} \propto v^{0.3}}. \tag{4.24}$$

Hence, for the present experiments and despite of the specific behavior of $\overline{h}$ related to its steps (as shown in Figure 4.13 to 4.15), the transfer ratio depends only on a single varying process parameter, the printing velocity. This important relation for the experimental data is depicted as black squares in Figure 4.16 which shows the transfer ratio averaged over screen ruling versus printing velocity. Regarding the transfer ratio, the regression formula presented in Equation 4.19 is well suited to

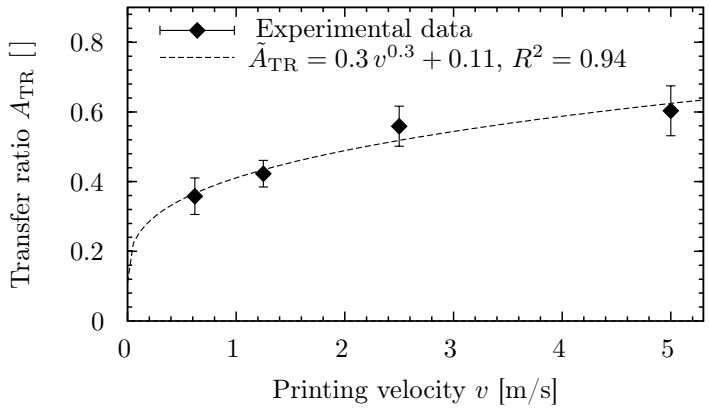

Figure 4.16: Deduced transfer ratio A_TR for different printing velocities (black squares) averaged over screen rulings with a power-law fit $\tilde{A}_\mathrm{TR}$ (dashed line).

acquire a power-law scaling behavior but it exhibits an inherent inconsistency in the limit of low printing velocities. Then, the thickness as well as the transfer ratio apparently approaches zero which contradicts the expectation. This is motivated by the following simple consideration:

We neglect gravity and consider a symmetric fluid meniscus between parallel plates at low relative separation velocity related to the center between the plates. Then, the surface tension has plenty of time to shape the fluid surface against the viscous friction. Because of the complete symmetric motion and the symmetric setup, the remaining fluid volume on both plates after meniscus splitting has to be equally distributed. Thereby, the transfer ratio would be $A_\mathrm{TR} = 0.5$ and not zero. For the gravure cell - substrate setup, although it is asymmetric, I would expect a value rather below 0.5 but also not approaching zero for decelerating velocities. This is also confirmed

by experiments of Sankaran et al. [222] and by numerical simulations of Lee et al. [6] who analyzed transfer ratios for very low separation velocities in gravure cell geometries.

I therefore extended the power-law regression by adding a constant b, which is negligible at sufficiently high velocities where the power-law is dominant

$$\tilde{A}_{\mathrm{TR}} = a\, v^{0.3} + b, \tag{4.25}$$

where a, b are the fitting constants and the exponent of the velocity v was taken from Equation 4.24.[15] The regression based on Equation 4.25 revealed a coefficient of determination of $R^2 = 0.94$ and is presented by the dashed line in Figure 4.16. The fitting constant b resulted in $b = 0.11 \pm 268\%$ which marks a minimal transfer ratio of the present gravure cell geometry at infinitesimal small velocity. Unfortunately, the error of b in the power-law fit is too large to give final evidence. This deficiency is due to the small number of different velocities and on the other hand, the resulting transfer ratios for different velocities are distributed in a very linear regime. However, the high coefficient of determination of $R^2 = 0.94$ of the fit in Figure 4.16 additionally proved that the transfer ratio and the dry film thickness is proportional to the velocity to the power of 0.3.

Transfer ratio: Comparison to gravure coating. In contrast to conventional graphical gravure printing which commonly operates with ink viscosities from $\eta = 50$ mPa·s to 200 mPa·s [136], forward gravure coating can operate with viscosities in the range of the present ink formulation of $\eta \sim 1$ mPa·s [16]. But this process might differ according to the distinct velocities of cylinder and substrate whose ratio is usually termed as *speed ratio* S. For values $S \neq 1$ the coating process is usually more robust to different types of instabilities [104]. However, Figure 4.17 compares the transfer ratio of the present study to results reconstructed from Benkreira et al. [16] (therein Figure 9) who investigated the transfer ratio (termed *dimensionless film thickness* in their study) in forward gravure coating with a speed ratio of $S = 1$.

Most studies on gravure coating investigate the reverse mode ($S < 0$) instead of the forward coating mode ($S > 0$). The publication of Benkreira et al. is the only one which could be compared to the present experiments directly.

Following Benkreira et al. [16], the x-coordinate is presented by the dimensionless capillary number Ca (recall Equation 3.15 for $\mathrm{Ca} = \eta v/\sigma$ where σ is the surface tension of the ink). Although Benkreira et al. used larger cell volumes with $V_c > 13$ ml/m^2 versus $V_c < 4.4$ ml/m^2 of the present study, the results presented in Figure 4.17 are in good agreement with each other. This underlines the analogy that, because of the low viscosity, the present process is strongly comparable to forward gravure coating.

[15] REMARK: Including this additive constant to Equation 4.19 resulted in a failure of the fitting algorithm by MATLAB.

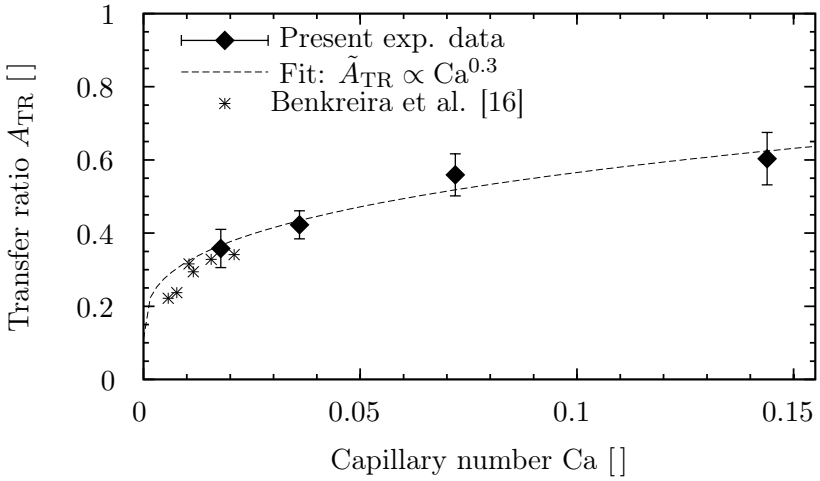

Figure 4.17: Transfer ratio A_{TR} vs. capillary number $Ca = \eta v/\sigma$. Comparison of the experimental data of the present study (black squares) to results of forward gravure coating experiments reconstructed from Benkreira et al. [16]. The fit $\tilde{A}_{TR}$ is based only on the present experimental data excluding values from Benkreira.

4.4.3 Explanatory model of ink transfer mechanisms

Summarizing the results of the printing experiments regarding dry film thickness and transfer ratio presented in the previous Sections 4.4.1 and 4.4.2, revealed three surprising features:

- Film thickness is proportional to printing velocity with $\overline{h} \propto v^{0.3}$ (Equation 4.21).
- Film thickness depends on printing history, i.e. exhibits a change in thickness after after passing an adhesive tape on the substrate (Figure 4.13b).
- For large screen rulings and slow printing velocities, the thicknesses per substrate are independent of cell volume (slope of the $\overline{h}$-V_c curves, compare Figure 4.14).

For these three aspects, I present possible explanations in the following paragraphs. The first one is related to the centrifugal force acting on the low viscous ink in the gravure cells. The second point is linked to the accumulation of excess ink at the inlet of the contact zone. In contrast, I associate the third point to a the cell emptying process more directed to a bounded outlet meniscus in the nip rather than directly to the substrate.

Effect of inertia forces on film thickness and transfer ratio

As mentioned above, the increase of layer thickness or transfer ratio for increasing velocity is more commonly known from gravure coating processes [16] rather than from graphical gravure printing. The main difference of the present ink formulation to color inks is the lower viscosity of $\eta = 0.8$ mPa·s versus $\eta = 50$ mPa·s to 200 mPa·s [136]. As confirmed in Section 3.7.1, for gravure printing of color inks, the decrease of transfer ratio for increasing velocity mainly originates from the reduced filling of the gravure cells during the doctor blade process instead of on the ink transfer itself. Based on the general definition of the transfer ratio (Equation 4.23), which relates the transferred volume to the empty volume of the gravure cell and not to the actual ink volume in the cell before transfer, this decreasing transfer ratio is a necessary consequence for color inks. Publications experimentally and

numerically investigating the transfer ratio of the emptying process in gravure printing often relate the transferred ink volume to the actual ink volume in the cells before ink transfer[16]. For this, the fill ratio is defined as $A_{\text{fill}} \equiv V_{\text{fill}}/V_{\text{c}}$, where V_{fill} is the actual ink volume in the gravure cell after the doctor blade process and before ink transfer. The effective transfer ratio relates the transferred wet film thickness to V_{fill} with

$$A_{\text{eff}} \equiv \overline{h}_{\text{w}}/V_{\text{fill}} = A_{\text{TR}}/A_{\text{fill}}. \tag{4.26}$$

This difference of the definitions has to be considered when comparing results from different pubications.

Unfortunately, the present experiments with the toluene-based ink did not allow any direct analysis of the doctor blade process. But the interpretation of the relative thickness steps (shown in Figure 4.13b) allows a direct inference on the fill ratio of the gravure cells provided by the doctor blade process, as presented in the paragraph on page 112.

Concentrating on the ink transfer mechanism between gravure cylinder and substrate, three main forces compete to dominate the process. They are based on surface tension, viscosity and printing velocity. Their magnitudes relative to each other can be estimated by comparing dimensionless numbers as introduced in Section 3.4 on page 72. They allow to estimate the relevance of different physical contributions to equations of motion. In the following, I motivate two dimensionless numbers for describing the driving mechanism for the enhanced ink transfer at higher velocities mentioned in the previous Sections 4.4.1 and 4.4.2:

(i) First, the fluid is subject to a volume force which is directed outwards in the accelerated, rotating reference frame of the ink in the gravure cell of the cylinder. This so-called centrifugal force is dependent on the velocity squared with $F_c = mv^2/R$, where m is the mass[17], R the radius of the cylinder (here, $R = 46$ mm) and v the tangential velocity which equals the printing velocity. The acceleration associated with this rotation is then given as $a_c = v^2/R$. Compared to the gravitational acceleration of $g = 9.81$ m/s^2, the radial acceleration on the fluid in the cell ranges from $a_c = 8.36$ m/s^2 to $a_c = 543.5$ m/s^2 for velocities from $v = 0.62$ m/s to 5 m/s. The dimensionless **Bond number** Bo relates the gravitational force to the surface tension force (Equation 3.13) as formulated in Equation 3.17. By associating not the gravitational force but the centrifugal force to the surface tension force, I define the modified Bond number Bo_c

$$\text{Bo}_c \equiv \frac{\rho L^2 a_c}{\sigma} = \frac{\rho L^2 v^2}{R\sigma} \mathrel{\widehat{=}} \frac{\text{centrifugal force}}{\text{surface tension}}. \tag{4.27}$$

Aside from a factor of L/R, this number equals the Weber number (We in Equation 3.16) which relates inertia without rotation to the surface tension.

Both Bond numbers are a measure to estimate the dominant force acting on the curvatures of the fluid surface in the system. Taking the dimension of the gravure cell as the characteristic length with $L = 1/\text{SR} \approx 142$ µm (with SR = 60 L/cm), and from known ink properties[18] and maximum printing velocity $v = 5$ m/s, the Bond number is of the order of $\text{Bo} \approx 6.4 \cdot 10^{-3}$ and Bo_c ranges from $\text{Bo}_c \approx 5.5 \cdot 10^{-3}$ to $\text{Bo}_c \approx 0.4$ for $v = 0.62$ m/s to 5 m/s. This difference of up to three orders motivates why gravity can be neglected in gravure printing applications, in

[16] [3, 6, 51, 61, 65, 82, 104, 114, 125, 159, 222, 242]
[17] here the mass of the fluid
[18] surface tension $\sigma = 27.8$ mN/m, density $\rho_{\text{sol}} = 0.9$ g/cm^3

contrast to inertial forces originating from cylinder rotation which may become significant at high velocities.

(ii) Second, the viscous dissipation acts as a counterpart to the body force and decelerates the resulting dynamics of the fluid at the surface as well as in the bulk. It would not affect the equilibrium state, as for example for a pendant drop which is deformed by gravity, but defines a characteristic time for reaching the equilibrium state. In the present case, the dynamics have to take place within the time the fluid is confined in the printing nip. This requires that the body force is of the order of or larger than the viscous force. A characteristic dimensionless number scaling the strength of centrifugal and viscous forces is the **Taylor number** Ta which is adopted from treating a fluid confined in the gap Δr between two concentrically rotating cylinders [243] with [261]

$$\mathrm{Ta} = \frac{\rho^2 {d_\mathrm{c}}^3 v^2}{R\eta^2} \mathrel{\widehat{=}} \frac{\text{centrifugal force}^2}{\text{viscous force}^2}, \tag{4.28}$$

where I replaced Δr by the depth d_c of the gravure cells.[19] For the present setup, a cell depth of $d_\mathrm{c} = 10$ µm and within the velocity range of $v = (0.62 \ldots 5)$ m/s, the Taylor number for a color ink with a viscosity of $\eta = 60$ mPa·s results in $\mathrm{Ta} = (0.02 \ldots 1.2) \cdot 10^{-4}$, and for the toluene-based ink with $\eta = 0.8$ mPa·s in $\mathrm{Ta} = 0.01 \ldots 0.7$. The difference of four orders in the Taylor number emphasizes that the additional body force in the rotating reference frame is negligible for processing color inks, while it is important for the dynamics in the nip region when using low viscous inks.

By relating the centrifugal force to the surface tension expressed by the Bond number Bo_c (i) and to the viscous force expressed by the Taylor number Ta (ii), the relevance of the centrifugal force in additionally dragging the fluid from the gravure cells to the substrate is reasonably emphasized.

Thickness step resulting from excess ink in the printing nip?

The thickness steps observed after passing the adhesives tapes[20] could be associated to accumulated excess ink at the inlet and/or the outlet of the nip, as illustrated in Figure 4.18.

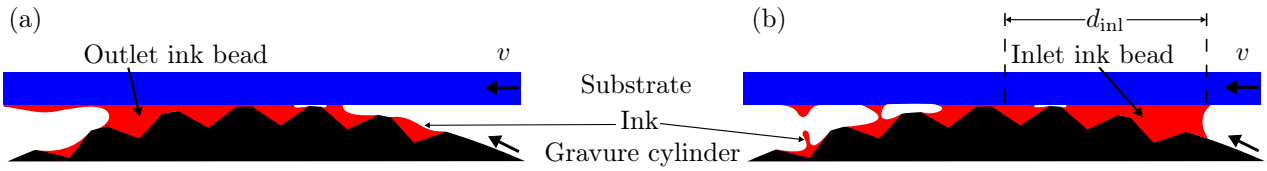

Figure 4.18: Contact zone of gravure cylinder and substrate. Schematic representation of the different types of excess ink that might have accumulated at the outlet of the contact zone (a) and the inlet (b) forming an ink bead. The bead might also be extended parallel to the rotation axis (directed into the image plane).

The question arising at this point is whether the outlet or the inlet bead is more dominantly influencing the transfer dynamics. The outlet ink bead could be accumulated by a net volume which is neither removed from the cylinder nor transferred to the substrate, it remains in the nip. The size

[19] The same number is obtained when replacing the gravitational by the centrifugal force in the so-called Galileo number.

[20] see Figures 4.13 and 4.15

of this bead has to scale with the widening of the last printed edge of a field. After the last row of cells of a field has deposited its content to the substrate, the bead would completely be squeezed on the substrate, smearing the border of the last field. I analyzed the widening of the last printed edges of the printed fields, denoted with X_{bord}, and found that apart from the fields printed with $v = 0.62$ m/s the tails did not exceed 1.5 mm, as representatively shown in the lower field of Figure 4.19. Additionally, the thickness of the smeared ink tails is far below the thickness of the layer directly deposited from the gravure cells indicating a very small outlet bead.

Furthermore, an outlet ink bead that obviously does not survives the transition from one field to another, but is completely vanishing within the width of the separation rim between adjacent fields, could not be responsible for the *printing history* motivated by the thickness layer steps. This is also confirmed by the first printed edges of the fields. Within the first one or two rows of printed gravure cells, the borders of the fields often exhibit separated single dots as representatively shown in the upper field of Figure 4.19. This also contradicts the existence of an considerable amount of

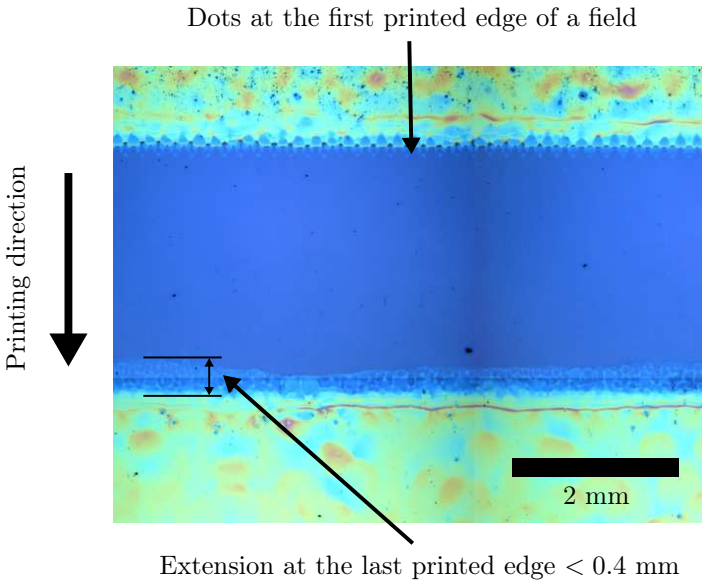

Figure 4.19: Representative microscope image of the border of two printed fields printed with $v_4 = 5$ m/s and SR = 70 L/cm. The lower field was printed first, the printing direction is from top to bottom. The extension of the last printed edge of the bottom field X_{bord} is widened below $X_{\text{bord}} < 0.4$ mm. Individual dots can be observed in the first two printed rows of gravure cells at the first printed edge of the top field.

ink volume at the outlet of the printing nip.

Given the absence of ink beads at the outlet of the nip, it is more likely that an inlet excess ink bead causes the observed behavior (as depicted in Figure 4.18b). An inlet bead can originate from ink present on the non-engraved areas or bridges between the cells of the cylinder. Apart from a small amount of ink present in the roughness of the chromium cylinder apart from the gravure cells, the extra ink cannot be transferred through the nip because of the close contact between cylinder surface and substrate. Consequently, this ink accumulates at the inlet of the contact zone and builds up an ink bead basically fed by a considerable wet layer on the bridges and the non-engraved regions on the cylinder. In preliminary experiments [25], I showed that this wetted layer can possess thicknesses of around 100 nm for a color ink with a viscosity of $\eta = 60$ mPa·s. For the present ink formulation, this should rather constitute a lower limit for the assumed wet layer thickness on the bridges. That is because the viscosity of the toluene-based ink is very low, with $\eta = 0.8$ mPa·s. Therefore, the ink

can more easily penetrate underneath the doctor blade during wiping and set up a receding meniscus at the back of the blade which additionally coats the non-engraved cylinder surface with ink.

The accumulation of ink from the non-engraved surface feeding the inlet bead can be estimated by geometrical considerations comparing the volumes. Assuming a bead extension in the direction of the rotational axis, the volume of the inlet ink bead must be proportional to the distance d_{inl} of the meniscus surface to the contact line (see Figure 4.18b). As an example, I estimated which distance d_{inl} a volume of a layer on the gravure cylinder would produce if it completely fills the inlet nip. Considering a cylinder surface with a residual ink layer of 100 nm thickness at a non-engraved region approaching only 10 mm through the nip, then, the inlet bead receives an ink volume which would solely build up a meniscus distance of $d_{\mathrm{inl}} = 0.65$ mm (compare Figure 4.18b).

As a result of this accumulated inlet bead, the gravure cells can acquire an additional amount of ink from the inlet ink meniscus. Furthermore, the bead could prevent an entrainment of air bubbles at the inlet nip which might be trapped when the substrate contacts the cell with negatively curved ink meniscus, as presented in Section 3.7.3. Consequently, based on the foregoing mechanisms promoting extra filling of the cells, more ink is transferred to the substrate.

According to this, when entering the positive step of the 50 µm thick and 10 mm wide tape, the inlet bead might be wiped off[21] so that the ink transfer is suddenly reduced and produces the thickness steps observed in Figure 4.13b.

Furthermore, Figure 4.15 illustrates that the relative step height depends on cell volume. A possible explanation is that the inlet bead might be sufficiently fed by the ink layer from the non-engraved areas. This ink bead might then be drained into the cells during printing of the fields. The amount of extra ink from the bead filling the gravure cells strongly depends on the fill ratio of the cells from the previous doctor blade process. In preliminary experiments using color inks with a viscosity of $\eta = 60$ mPa·s, I found that the fill ratio increases for increasing cell volumes [28]. Assuming similar behavior for the present low viscous ink, larger cells are less affected by the inlet bead because they already exhibit a high fill ratio, and the excess ink will not substantially change the filling level. For smaller cell volumes, the inlet ink bead substantially raises the fill ratio of the cells. Consequently, passing the edge of a tape, which provides additional space for the ink bead to settle in the corner between the edge of the tape and the substrate, yields step heights more pronounced for smaller cell volumes rather than for larger ones, as shown in Figure 4.15. Based on this explanation, the relative step height $\delta\overline{h}_{\mathrm{sr}}$ is a direct measure of the fill ratio A_{fill} provided by the doctor blade process with

$$A_{\mathrm{fill}} \propto 1 - \delta\overline{h}_{\mathrm{sr}}. \tag{4.29}$$

Film splitting rather than single cell transfer

An explanation for the layer thickness which is independent of the cell volume for higher screen rulings and slower velocities (Figure 4.14) is difficult to obtain using the present data. Nevertheless, important aspects can be deduced from the type of ink transfer mechanisms in the outlet zone of the nip as mentioned in Section 3.2 on page 64. In the previous paragraph, I estimated that the accumulation of excess ink at the outlet nip should be rather small. Nevertheless, it could drastically change the transfer process as discussed in the following.

Let us consider the two situations of single cell and film splitting depicted in the high-speed images of Kunz in Figure 3.3 on page 65 and illustrated in Figure 4.20.

[21] by geometrical considerations more easily than for the outlet bead

First, the amount of ink volume transferred by a single cell transfer, similar to Figure 3.3a and 4.20a, is usually dependent on the gravure cell volume. The bases of these filaments are located at the position of the single cells and on the corresponding opposite site on the substrate. They are moving with the cylinder surface velocity. In this case, the ink transfer is promoted by the ink filament separation and its participating ink volume. After separation, the ink provided by the gravure cell is partly transported by the substrate, with the rest remaining in the cell. There is no ink left behind in the nip.

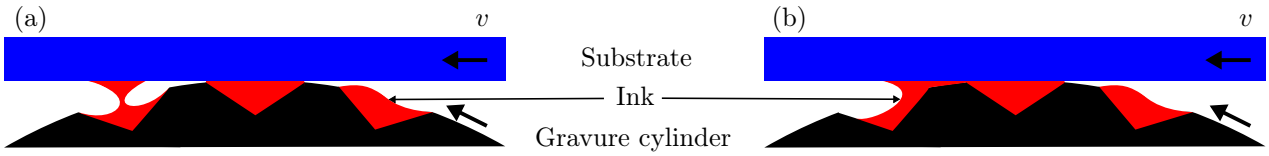

Figure 4.20: Sketch of two possible splitting scenarios. A single cell transfer mechanism in (a) as imaged by Kunz in Figure 3.3a. An outlet single-sided meniscus bounded to the contact zone representing a film splitting mechanism in (b) as imaged by Kunz in Figure 3.3b.

Second, for distinct process parameters, the outlet meniscus could be bounded to the wedge consisting of the contact line of the cylinder surface and the substrate as indicated in Figure 3.3b (red lines) on page 65 and 4.20b. In this case, the meniscus only shows a single-sided free fluid surface and I assume that it is extended along the contact line of the solid surfaces giving the onset for a film splitting transfer. The single-sided meniscus is bounded to the nip instead of the filament case and remains *static* in the wedge during printing of the fields. It is *static* in the sense that it is not moving instead to the solid surfaces it is bounded to. This film splitting mechanism might develop vortex ink flow in the wedge meniscus of the order of the printing velocity, possibly with stagnation points, as investigated for nip flows in gravure coating by Coyle et al. and Lecuyer et al. [47, 155]. Otherwise, for higher capillary numbers (higher velocity or viscosity), the ink might not undergo film splitting and tend to form separating filaments from single cell ink splitting. It is interesting to note that the exemplary numerical simulations presented in the Appendix D on page 177 exactly show a transition from single cell to film splitting transfer in Figure D.4 and D.5.

I now assume that the transfer mechanism is of the film splitting type with a *static* meniscus as illustrated in Figure 4.20. By including the effect of the gravure cells to this splitting scenario, the meniscus in the wedge might pin at the front falling edge of a passing gravure cell, as illustrated in Figure 4.21a. The ink surface starting at the pinned edge acts as a sort of spring resisting the cylinder movement. At a specific length of this pinned meniscus (denoted as pinning length), which mainly depends on surface tension, velocity and shape of the edge, the pinning might be suddenly abandoned and the contact lines recedes over the cylinder surface again.

If in this specific situation, the opening of the cell (large screen ruling, small cell volume) is smaller than the pinning length, the meniscus might touch the back edge of the cell before the front pinning is abandoned as shown in Figure 4.21a. This might result in ink volume provided for the ink transfer to the substrate which is less dependent on the actual cell volume of the gravure cells instead to the situation illustrated in Figure 4.21b. Here, the large cell opening (small screen ruling, large cell volume) might exceed the pinning length and the receding meniscus moves down the wall of the cell and drains the ink from the cell to the nip until the meniscus reaches the back raising edge. This ink volume, and with it the film thickness, are then more dependent on the cell volume and on the inverse of the screen ruling of the gravure cell as shown in Figure 4.15 on page 106.

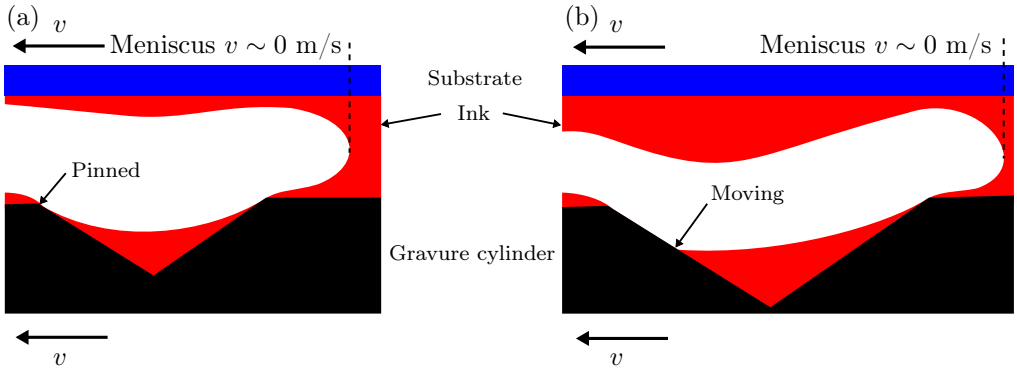

Figure 4.21: Sketch of possible ink splitting menisci between substrate and gravure cylinder bounded to the nip. The menisci between the solid moving surfaces are assumed to be at rest ($v \sim 0$ m/s). For small gravure cells (a), the ink is pinned at both edges of the gravure cell. For larger cells (b), the pinning at the front edge is abandoned so that the ink contact line can recede down the cell wall.

Aside from missing further experimental indicators confirming this hypothesis, I assume that this explanatory model underlies the observed behavior in Figure 4.14. Therein, large screen rulings and slow printing velocities reveal layer thicknesses that are independent of cell volume.

4.4.4 Relative RMS roughness

Although the relative RMS roughness S_{qr} (RMS roughness S_q devided by the mean thickness value $\overline{h}$, introduced in Equation 4.4 on page 96) does not express information about lateral structures, it is a key quantity for characterizing the homogeneity of printed layers.

Figure 4.22 depicts the relative RMS roughness S_{qr} of all printed fields dependent on the cell volume V_c for different printing velocities and all screen rulings. From Figure 4.22 it is obvious that

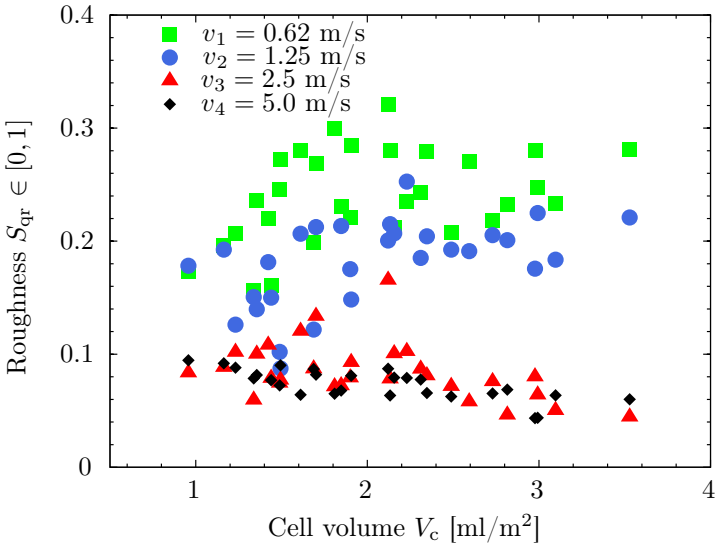

Figure 4.22: Relative RMS roughness S_{qr} of the fields related to the to gravure cell volume V_c for all screen rulings and different printing velocities v_i.

S_{qr} is minimized for fast velocities and high cell volumes.

Nevertheless, a clear dependency is difficult to determine from Figure 4.22. Therefore, in Figure 4.23, I present the roughnesses of representative fields separated for two screen rulings and two velocities[22].

In Figure 4.23 (and C.5) we can observe different slopes $a = \mathrm{d}S_{qr}/\mathrm{d}V_c$ of the linear regressions for different velocities and screen rulings. That implies by changing the cell volume we can either improve or reduce the relative RMS roughness of the fields depending on the screen ruling and the corresponding slope a. I determined the slopes a of all corresponding regression lines of the S_{qr}-V_c curves, the results are illustrated in Figure 4.24. For negative values, i.e. negative slopes a, in Figure 4.24, layer homogeneity is improved[23] by increasing cell volume while remaining the screen ruling constant. This means that for velocity $v_4 = 5.0$ m/s an increase of cell volume would reduce the roughness of the fields for all screen rulings. On the contrary, for positive values in Figure 4.24, for example for $v_3 = 2.5$ m/s, fields printed with screen rulings above SR = 95 L/cm start to become more inhomogeneous for increasing cell volume. This marks an important property which was not evident from Figure 4.22.

Comparing the velocity dependence of the roughness according to the screen ruling averaged over the cell volumes[24] resulted in Figure 4.25. As indicated before, Figure 4.25 proves that the roughness is minimized for higher velocities. Subdividing into screen ruling (SR), the lowest roughness is

[22] plots for remaining screen rulings and velocities show similar behavior and are depicted in the appendix in Figure C.5 on page 173

[23] equals reducing S_{qr}

[24] omitting the error bars for ease of presentation

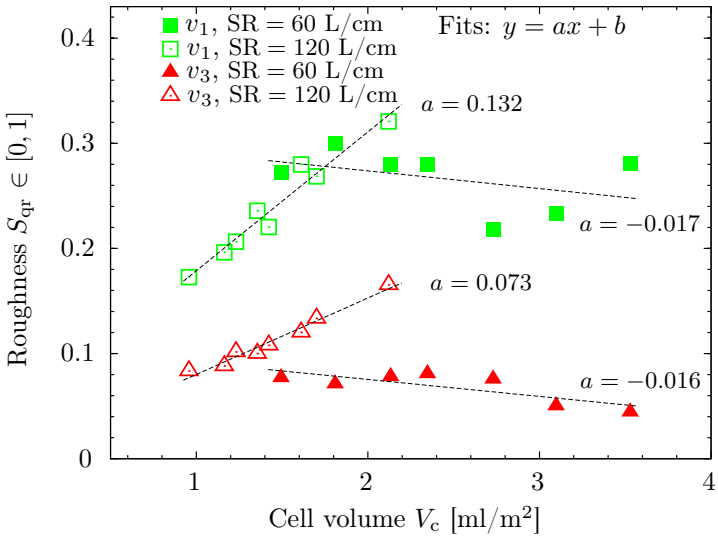

Figure 4.23: Relative RMS roughness S_{qr} of different fields (data points) related to gravure cell volume V_c for screen rulings of SR = 60 L/cm, SR = 120 L/cm and printing velocities $v_1 = 0.62$ m/s, $v_3 = 2.5$ m/s. The slopes of the regression lines a of all S_{qr} - V_c curves are summarized in Figure 4.24.

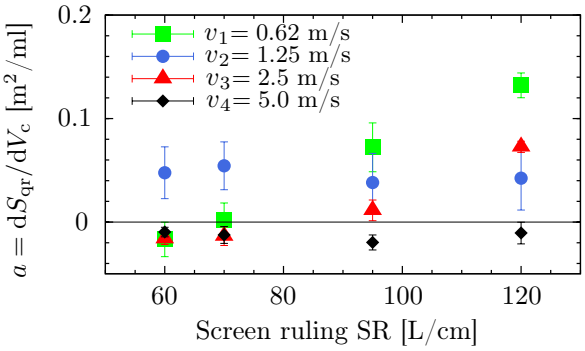

Figure 4.24: Slope of the regression lines of the S_{qr} - V_c curves of Figure 4.23 and C.5 vs. screen ruling. Positive values indicate increasing roughness S_{qr} for increasing cell volume V_c and negative vice versa.

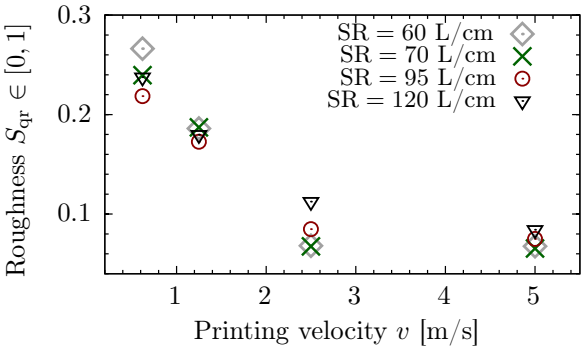

Figure 4.25: Relative RMS roughness S_{qr} vs. printing velocity v for different screen rulings (SR) and averaged over corresponding cell volumes V_c.

observed for fields printed with SR = 60 L/cm and SR = 70 L/cm at velocities of $v_3 = 2.5$ m/s and $v_4 = 5.0$ m/s. In Figure 4.25, choosing for example the fields represented by the black triangle for SR = 120 L/cm and $v_3 = 2.5$ m/s, we would reduce the relative layer roughness by reducing the cell volume. This correlation clearly results from Figure 4.23 and 4.24.

Nonlinear regression

Using the same approach to find an overall connection of the main input parameters as in Section 4.4.1 on page 106, I applied the following fitting function to the experimental data

$$\tilde{S}_{qr} = a\, V_c{}^b\, SR^c\, v^d, \tag{4.30}$$

where a, b, c and d are the fitting constants. With a coefficient of determination of $R^2 = 0.81$, MATLAB resulted the following constants

$$\begin{aligned} a &= 0.06 \pm 91\% \\ b &= 0.28 \pm 55\% \\ c &= 0.21 \pm 90\% \\ d &= -0.61 \pm 11\%. \end{aligned} \tag{4.31}$$

With an error of 11%, the dependency between relative roughness S_{qr} and printing velocity v is given by[25]

$$\boxed{S_{\mathrm{qr}} \propto v^{-0.6}}. \tag{4.32}$$

This is in agreement with the data points shown in Figure 4.25. The connection between S_{qr} and the other variables should rather gained from Figure 4.24 than from Equation 4.30 and 4.31.

Preliminary process window for minimal layer roughness

In this paragraph, I draw a preliminary process window for the present system minimizing the relative RMS roughness S_{qr}.

Recalling previous results, Figure 4.22 shows minimal layer roughness for higher printing velocities and higher cell volumes. The specific gradients of $S_{\mathrm{qr}}(V_{\mathrm{c}})$ dependent on the screen ruling are illustrated in Figure 4.24, stating that larger cell volume at high velocities improve layer quality for small screen rulings. From Figure 4.25 and Equation 4.32 it follows that layer roughness is minimized for faster printing velocities.

Before combining these results to a descriptive process window, I discuss the following two aspects.

- As mentioned in Section 4.2.4 on pages 92 ff. (and Figure 4.5), the predefined cell volume range of the gravure cylinder, which was set by preliminary printing experiments, did not coincide with the values specified by the manufacturer. The measured minimal cell volume was 0.96 ml/m^2 instead of 0.2 ml/m^2 as intended to be. This specifically prevents the transition from a closed printed layer to a dot-like pattern, which finally must occur in the limit of sufficiently small cell volumes. Because of this limitation, I incorporated preliminary printing results from experiments that I performed with a printability tester IGT G1 as summarized in Appendix C.1 and published in [27]. These experiments provided the opportunity to employ gravure cylinders with much smaller cell volumes compared to the cylinders of the gravure printing unit from Prüfbau. Printing experiments were performed with the same inks and substrates. The IGT gravure cylinder parameters of the printed fields possessed a screen ruling of SR = 70 L/cm and cell volumes of $V_{\mathrm{c}} = (0.25, 0.84, 1.5)$ ml/m^2. The printing velocity was $v = 1$ m/s. According to Table C.1 on page 172, the resulting dry film thicknesses were $h = (5.7, 12.0, 14.8)$ nm and their relative RMS roughnesses $S_{\mathrm{qr}} = (0.30, 0.10, 0.23)$ (marked as blue squares in Figure 4.27). As expected for the lowest cell volume, the field shows a dot-like pattern as determined with phase-shifting interferometry (PSI) and illustrated as color-coded topography in Figure 4.26. This originated from ink transferred by single gravure cells and which dried before the droplets could coalesce.

[25] rounding the exponent d to one decimal place within the bounds of confidence

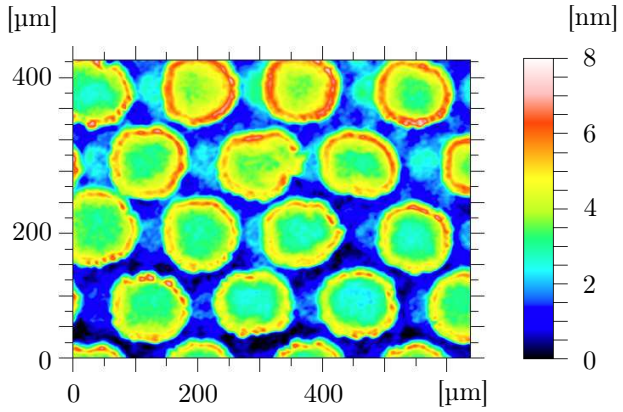

Figure 4.26: Topography of a printed field (spiro-MeOTAD on ITO coated glass) from preliminary experiments (summarized in Appendix C.1 and published in [27]) using an IGT G1 with a cell volume of $V_c = 0.25$ ml/m^2, a screen ruling of SR = 70 L/cm and a printing velocity of $v = 1$ m/s, measured with PSI.

- The imaging color reflectometry (ICR) was not suitable to measure layers printed at high cell volume exceeding a thicknesses $\overline{h} > 45$ nm because of a failure of the algorithm as discussed before (at beginning of this chapter on page 101). At this upper limit the layers seem to become inhomogeneous again. Therefore, I measured these "missing" fields exemplary for the velocity $v = 2.5$ m/s with the phase-shifting interferometry (PSI) on a much smaller lateral scale (marked as red circles in Figure 4.27 and the following figures of this type). To compare the roughness values between the two measurement methods (PSI and ICR), I laterally averaged the thickness data to match the same lateral resolution as used with ICR for the other layers.

Including the latter aspects, I combined the resulting dependencies in a representative process window for S_{qr} versus V_c as illustrated in Figure 4.27. Region (II) and (III) represent the cell volume range of the present printed fields and (III) only, the range which was not measurable with ICR but with PSI. (I) and (IV) mark regions which were not in the scope of the underlying experiments with the Prüfbau printing tool. Figure 4.27 exemplary shows two different curves for middle velocities and the lower two screen rulings. The roughness of preliminary experiments using the IGT G1 are marked as blue squares on the left-hand side. The additional measurements with PSI of the printed fields with highest cell volume are marked as red circles on the right-hand side of Figure 4.27. Red solid lines show trend curves within the present data set shown in Figure 4.22 and dashed lines the expected behavior.

Beginning with the cell volume from the left, the very high roughness of the upper curve (most left blue square) is the value of the dot-like field shown in Figure 4.26. I expect this behavior for any gravure printing experiment if the cell volumes are small enough. The next blue square marks the first important minimum of the roughness $S_{qr,1}^{m}$. It represents a field for which the ink was transferred with separated drops from the cells and during evaporation of the solvent, the drops coalesce, formed a homogeneous layer and reached the solid phase before undergo any type of dewetting scenario [27]. In the first part of region (II), layer roughness increased when the cell volume was further enhanced. This corresponds to the result that has been discussed in Figure 4.24, where the roughness decreases or increases according to the slopes in the S_{qr}-V_c diagram. Finally, the roughness decreases again and reaches a second local minimum ($S_{qr,2}^{m}$) or further increases. This second minimum is a very surprising observation. The two additional experiments (red circles) clearly confirm the increasing

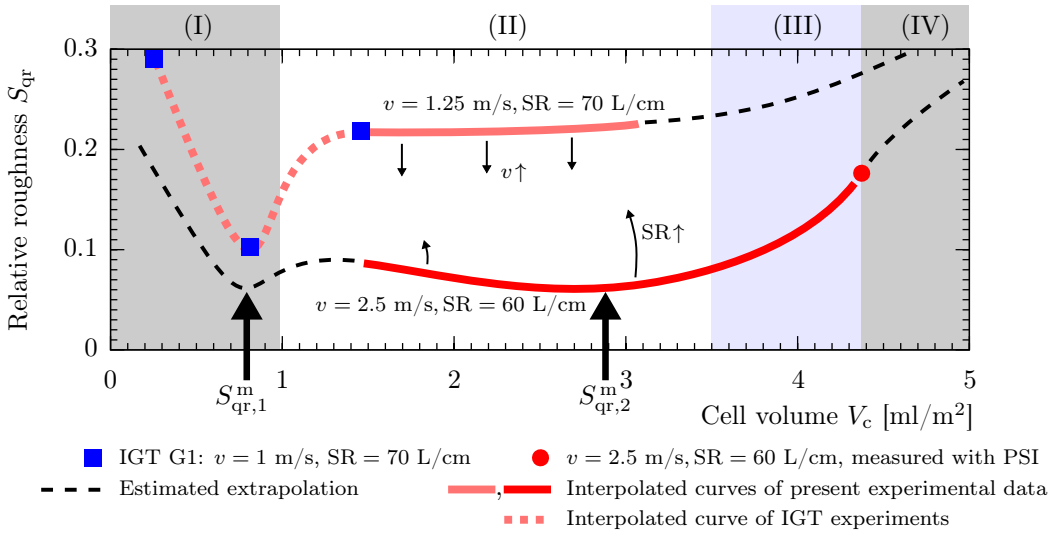

Figure 4.27: Descriptive process window for the relative RMS roughness S_{qr} of printed fields versus cell volume V_c. Region (II) and (III) represent the cell volume range of the present printed fields. Large-area thickness determination with imaging color reflectometry (ICR) marks region (II) and with phase-shifting interferometry (PSI) region (III) including single measurements (red circles). (I) and (IV) marks regions which were not in the scope of the underlying experiments with the Prüfbau printing tool. Results of preliminary experiments with an IGT G1 printing tool (summarized in Table C.1) using the same inks and substrates and with $v = 1$ m/s, SR = 70 L/cm are shown as blue solid squares with a red dotted trend curve. Red solid lines show trend curves within the present data set shown in Figure 4.22 for $v_3 = 2.5$ m/s, SR = 60 L/cm and $v_2 = 1.25$ m/s, SR = 70 L/cm. The black dashed lines illustrate assumptions of an extrapolated dependency. Possible local minima (one for the combined upper and two for the combined lower curve) of S_{qr} are denoted with $S^{m}_{qr,1}$ and $S^{m}_{qr,2}$. The black arrows at the red solid trend curves illustrate the direction of change for increasing velocity $v\uparrow$ ($S_{qr} \propto v^{-0.6}$) or screen ruling SR$\uparrow$.

roughness for higher cell volume (and higher layer thickness). The black arrows at the red solid trend curves illustrate the direction of change for increasing velocity $v\uparrow$ ($S_{qr} \propto v^{-0.6}$) or screen ruling SR$\uparrow$.

This descriptive process window ignores lateral distributions and length scales contributing to the roughness. The advantage of the large-area measurements using ICR is that the thickness data allows us to gain and analyze laterally resolved information. From this additional information, I could relate possible driving mechanisms to the behavior observed and summarized in Figure 4.27.

Therefore, I consider additional statistical parameters and discuss the dominant lateral wavelengths determined from the thickness maps in the following sections.

4.4.5 Skewness and kurtosis

The skewness S_{sk} which is defined in Equation 4.5 on page 97 and which indicates the distribution of values related to the mean ($S_{sk} > 0$ more values below the mean, $S_{sk} < 0$ more values above the mean, [240]) is depicted in Figure 4.28a. To simplify the presentation, I averaged over adjacent data points. The error bars in x and y resulted from this averaging step. In Figure 4.28a, higher velocities yield lower skewness values, whereas for all velocities a common maximum skewness is located between a cell volume from $V_c = 1.7$ ml/m^2 to 2.0 ml/m^2. These maxima belong to surfaces with more sharp and high peaks. Apart from the lowest velocity v_1, I found that the skewness changes from positive to negative values for specific cell volumes. This transition indicates a basic change from a topography dominated by sharp peaks to a one dominated by spare or deep holes (compare

examples on page 98). The skewness close to zero represents symmetric and possibly regular surface patterns. Best layer homogeneity (lowest S_{qr}) correlates with a skewness approaching high negative values.

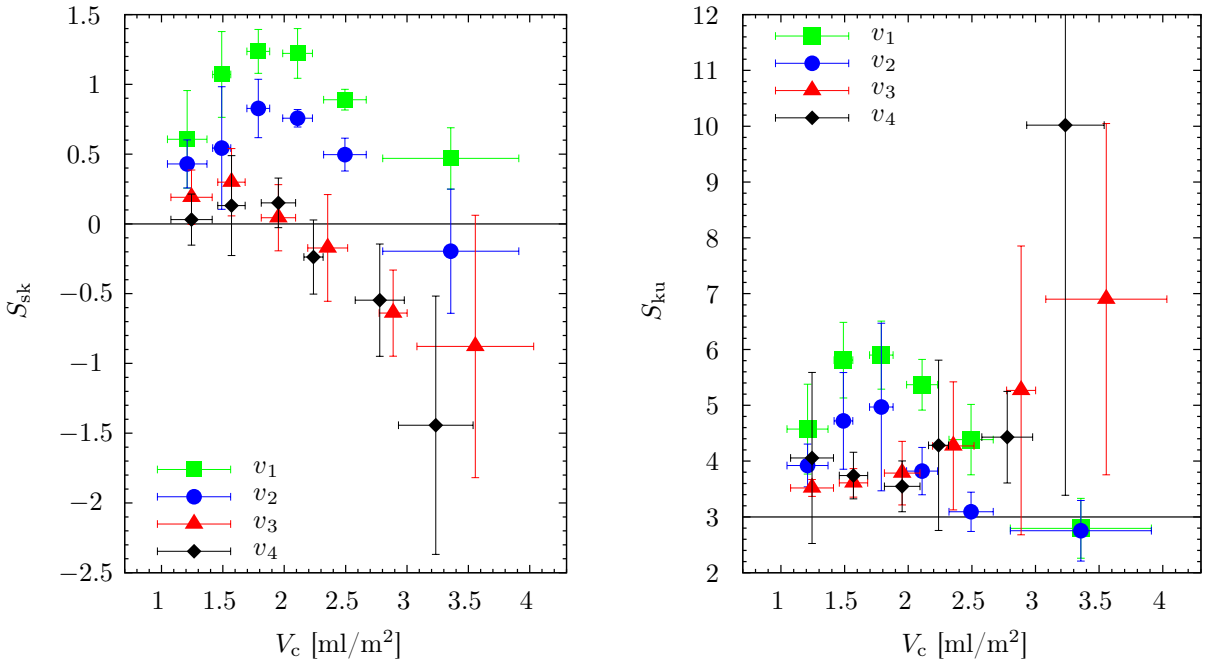

(a) Skewness. **(b)** Kurtosis.

Figure 4.28: Third order (skewness S_{sk}) and fourth order (kurtosis S_{ku}) statistical surface parameters of the printed fields in relation to the gravure cell volume V_c for all screen rulings and different printing velocities v_i.

The kurtosis S_{ku} of a surface as defined in Equation 4.6 on page 97 corresponds to height value distributions more flat if $S_{ku} < 3$ or with heavier tails and higher peaks if $S_{ku} > 3$ than the normal (Gaussian) distribution [50]. The kurtosis values versus cell volumes of the different printed fields of the organic semiconductor are shown in Figure 4.28b using the same averaging step as before. For the lower velocities $v_1 = 0.62$ m/s and $v_2 = 1.25$ m/s, we observe a similar functional behavior as for the skewness, a common maxima arose between cell volumes of $V_c = 1.7$ ml/m^2 and 2 ml/m^2. But for $v_3 = 2.5$ m/s and $v_4 = 5.0$ m/s, the dependency radically changes for higher cell volumes. Here, the kurtosis monotonically increases and approaches high values which additionally are strongly error prone. These high kurtosis values correlate to low roughness values S_{qr} of the printed fields.

The fields printed with velocity v_2 and highest cell volumes show the most regular patterns because skewness is close to zero and kurtosis below 3.

Combining the observations of skewness S_{sk} (Figure 4.28a), kurtosis S_{ku} (Figure 4.28b) and relative roughness S_{qr} (Figure 4.22), I assign the best film homogeneity for lowest skewness and highest kurtosis values. These in turn occur for high cell volumes and high printing velocities.

A nonlinear regression with a power-law model as used before in Equation 4.19 and 4.30, gave coefficients of determination of $R^2 = 0.34$ for the skewness and $R^2 = -0.13$ for the kurtosis with high errors and is therefore not further discussed.

Figure 4.29 representatively illustrates the dependency of skewness and kurtosis to cell volume and velocity (black arrows indicating the change for increasing velocity $v\uparrow$) for $v_2 = 1.25$ m/s and

SR = 70 L/cm. Additionally, I included the results of the preliminary printing experiments with the printing tool IGT G1 for v = 1 m/s and SR = 70 L/cm (blue symbols) summarized in Table C.1 on page 172. The latter shows a continuous extension to lower cell volumes which may confirm that the different experiments on different tools are comparable. The skewness value at $V_c = 0.84$ ml/m^2 for the IGT printing result exhibits a minimum which coincides with its minimum for the relative roughness in Figure 4.27.

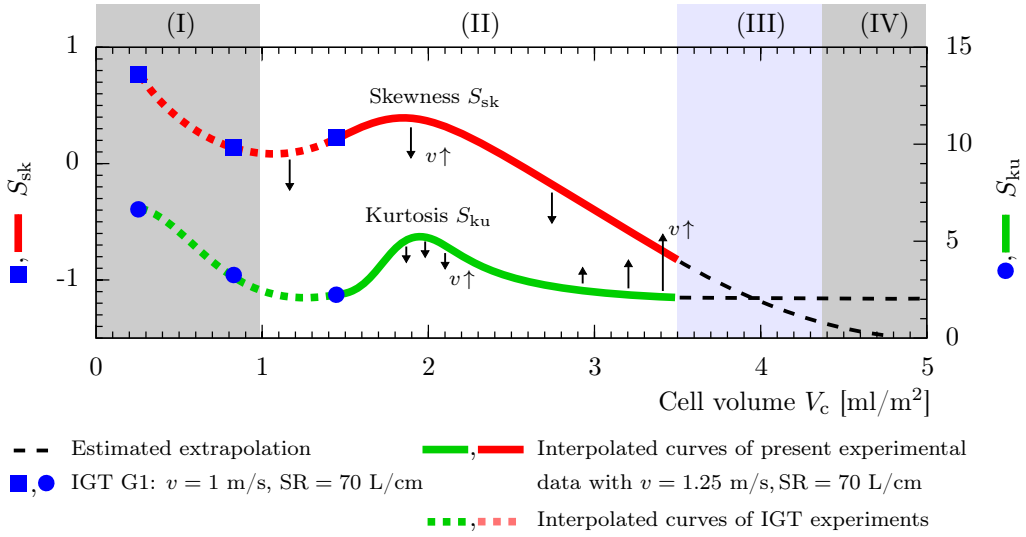

Figure 4.29: Trend charts of skewness S_{sk} and kurtosis S_{ku} versus cell volume including preliminary experiments. Region (II) and (III) represent the cell volume range of the present printed fields. Large-area thickness determination with imaging color reflectometry (ICR) marks region (II) and with phase-shifting interferometry (PSI) region (III). (I) and (IV) marks regions which were not in the scope of the underlying experiments with the Prüfbau printing tool. Results of preliminary experiments with an IGT G1 printing tool (summarized in Table C.1) using the same inks and substrates and with v = 1 m/s, SR = 70 L/cm are shown as blue solid squares (skewness) and circles (kurtosis) with red and green dotted trend curves. Red solid lines show trend curves within the present data for v = 1.25 m/s, SR = 70 L/cm. The black dashed lines illustrate assumptions of an extrapolated dependency. The black arrows at the red solid trend curves illustrate the direction of change for increasing velocity.

4.4.6 Dominant isotropic wavelength of surface undulations

Performing the 2-dimensional fast Fourier transformation (FFT) of the thickness data per field followed by radial averaging in the frequency domain and inverting as described in Section 4.3 on page 98 ff., results in the radial (isotropic) wavelength spectrum PSD_{1D} for the radial wavelength λ_ϱ. The maximum of this spectrum for $\lambda_\varrho < 3$ mm is denoted as the dominant isotropic wavelength λ_{iso}.

Figure 4.30 shows all acquired dominant isotropic wavelengths λ_{iso} of the printed fields related to cell volume and separated by printing velocity. From Figure 4.30, I deduce two main aspects:

First, the higher the cell volume (or equivalently the layer thickness), the higher the dominant wavelength. Second, the wavelength scales anti-proportional to the printing velocity. Higher velocities resulted in smaller wavelength.

Surprisingly, several spectral PSD_{1D} showed a second local maximum, denoted with λ_{iso}^{2nd}. Figure 4.32 representatively illustrates the change of the radial spectra for fields printed with the same screen ruling of SR = 95 L/cm and cell volume of $V_c = 2.16$ ml/m^2 for different printing velocities v_i. The corresponding thickness maps are shown in Figure 4.31. The mean layer thickness increased

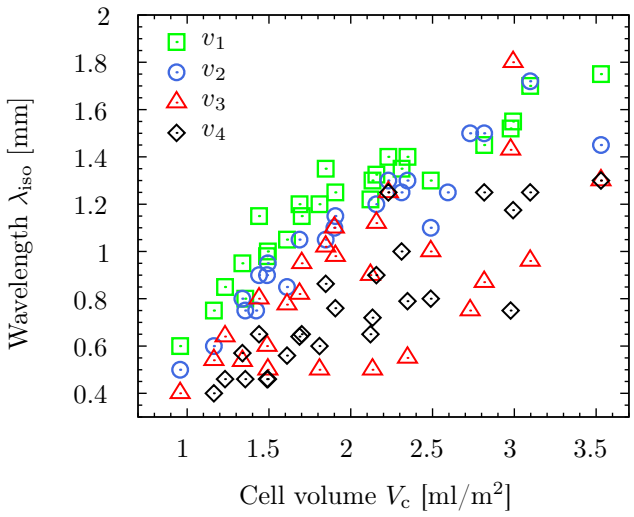

Figure 4.30: Dominant isotropic wavelength λ_{iso} of the surfaces of the printed fields related to gravure cell volume V_c, for all screen rulings and different printing velocities v_i.

from $\overline{h} = 15.4$ nm to $\overline{h} = 30.1$ nm and the relative RMS roughness was reduced from $S_{qr} = 0.21$ to $S_{qr} = 0.08$. Skewness was also reduced for higher printing velocities, as captioned in Figure 4.32. The values of the radial power spectral density PSD_{1D} in arbitrary units (a.u.) can be compared within the sub-figures of Figure 4.32. The latter reveals first an increase from v_1 to v_2, then a reduction of the amplitudes of the wavelength for $v \geq v_2$ which coincides with a strong reduction of the relative roughness S_{qr}. Apart from the lowest printing velocity $v_1 = 0.62$ m/s, second maxima λ_{iso}^{2nd} in the wavelength spectrum can be clearly observed which approximately occurred at half the wavelength of the first maximum λ_{iso} as verified in Figure 4.33. All second-order maxima emerged in the wavelength spectra of the fields are shown in Figure 4.33. Motivated by the broadened distributions of the wavelengths λ_ϱ in Figure 4.30 and by the Saffman-Taylor model for ribbing instabilities introduced in Equation 3.18 on page 74, I plotted the wavelengths against $\overline{h}/\sqrt{v}$ in Figure 4.33. The coefficients of determination above $R^2 = 0.79$ of the linear regressions of the wavelength reveal a good correlation between the experiments and the $\overline{h}/\sqrt{v}$ proportionality. The slopes of the regressions for λ_{iso} and λ_{iso}^{2nd} applied in Figure 4.33 approximately deviate by a factor of 2. This explicitly reveals that the λ_{iso}^{2nd} is half the dominant isotropic wavelength λ_{iso}.

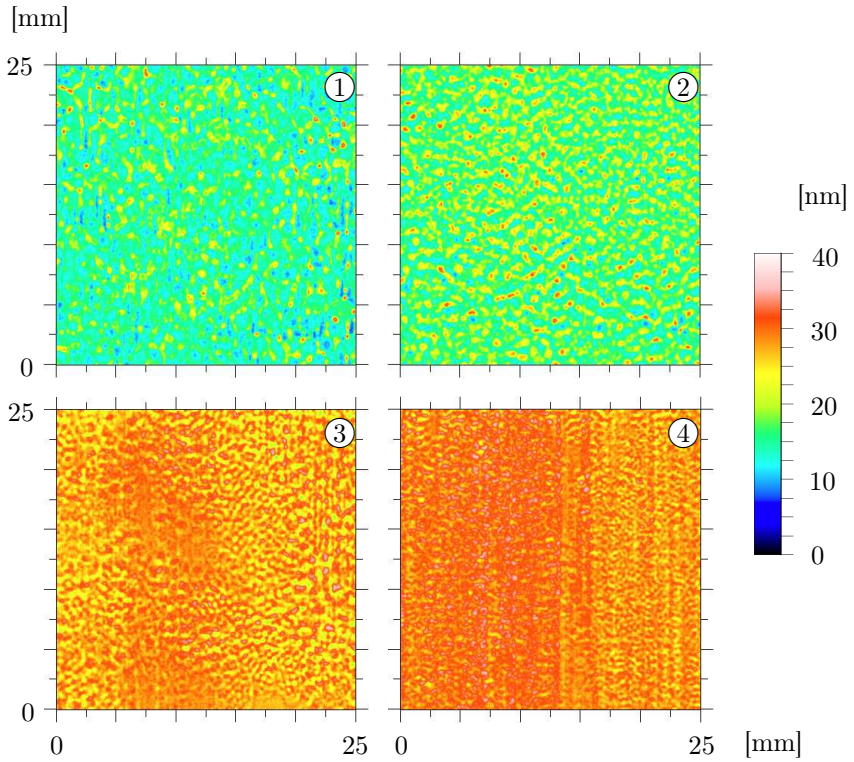

Figure 4.31: Thickness maps h of fields printed with a screen ruling of SR = 95 L/cm and a cell volume of $V_c = 2.16$ ml/m^2 for different printing velocities v_i ① - ④ . Spectra and thickness parameters are shown Figure 4.32.

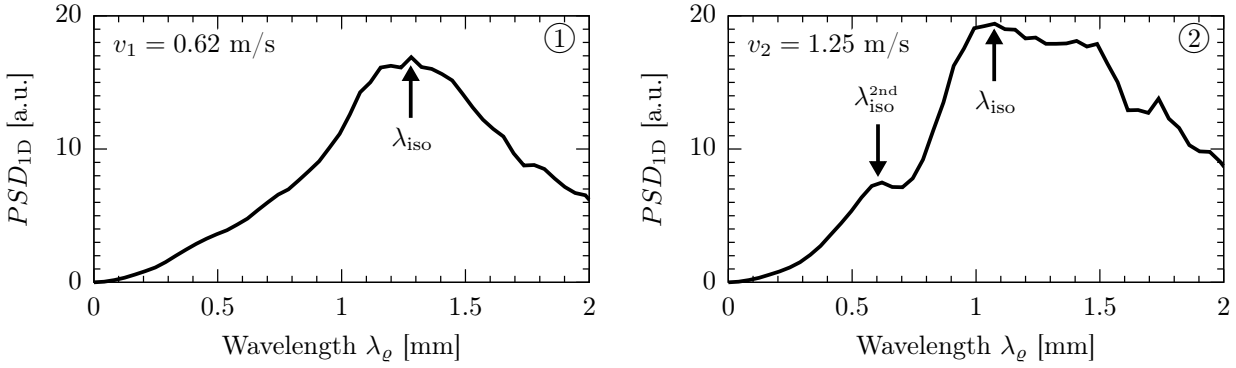

(a) $\overline{h} = 15.4$ nm, $S_{qr} = 0.21$, $S_{sk} = 0.99$, $S_{ku} = 5.02$ **(b)** $\overline{h} = 17.5$ nm, $S_{qr} = 0.20$, $S_{sk} = 0.78$, $S_{ku} = 3.73$

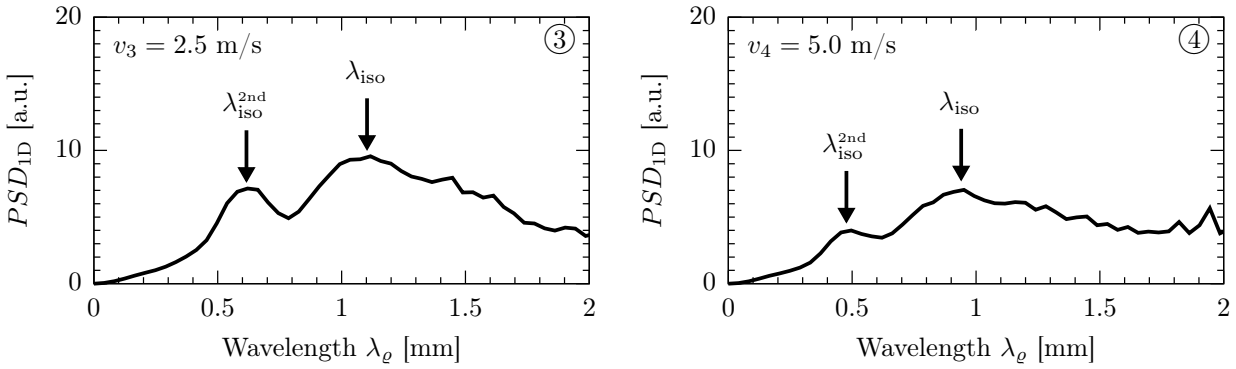

(c) $\overline{h} = 27.7$ nm, $S_{qr} = 0.10$, $S_{sk} = -0.2$, $S_{ku} = 3.09$ **(d)** $\overline{h} = 30.1$ nm, $S_{qr} = 0.08$, $S_{sk} = 0.08$, $S_{ku} = 4.93$

Figure 4.32: Radial power spectral density PSD_{1D} of fields (shown in Figure 4.31) printed using a screen ruling of SR = 95 L/cm and a cell volume of $V_c = 2.16$ ml/m^2 for different printing velocities v_i, with mean dry film thickness $\overline{h}$, relative RMS roughness S_{qr}, skewness S_{sk} and kurtosis S_{ku}.

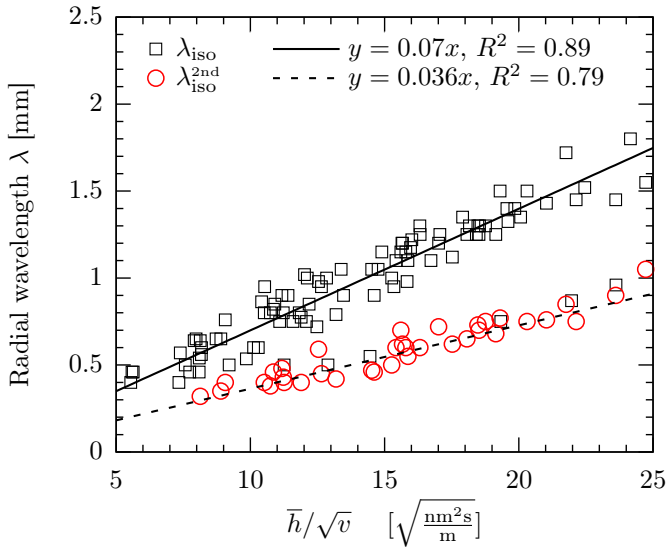

Figure 4.33: First λ_{iso} and second λ_{iso}^{2nd} isotropic wavelength of surface undulations of printed fields related to $\overline{h}/\sqrt{v}$, where $\overline{h}$ is the mean dry film thickness and v the printing velocity.

Nonlinear regression

To find an overall scaling behavior of the wavelength λ_{iso}, I performed a nonlinear regression using the input parameters dry film thickness $\overline{h}$, screen ruling SR and printing velocity v. I chose this approach rather than using the cell volume V_{c} instead of $\overline{h}$ in order to compare the results to the physical models of instability and to the data shown in Figure 4.33. Nevertheless, by using the previously determined proportionality of Equation 4.21, i.e. $\overline{h} \propto V_{\text{c}}\, v^{0.3}$, I can infer the dependency between λ_{iso} and V_{c}.

The regression formula handled by the MATLAB program `nlinfit(...)`[26] was as follows

$$\tilde{\lambda}_{\text{iso}} = a\, \overline{h}^{\,b}\, \text{SR}^{c}\, v^{d}. \tag{4.33}$$

The coefficient of determination resulted in

$$R^2 = 0.9 \tag{4.34}$$

and the regression constants in

$$\begin{aligned} a &= 0.1 \pm 76\% \\ b &= 0.95 \pm 12\% \\ c &= -0.04 \pm 279\% \\ d &= -0.46 \pm 13\%. \end{aligned} \tag{4.35}$$

From this regression, the statement that experimental data of the dominant wavelength λ_{iso} does not depend on the screen ruling is confirmed by the low and error prone exponent of $c = -0.04 \pm 279\%$. The proportionality of λ_{iso} to the thickness $\overline{h}$ and the velocity v with $\lambda_{\text{iso}} \propto \overline{h}/\sqrt{v}$ is also proven by the exponents $b = 0.95 \approx 1$ and $d = -0.46 \approx -0.5$ which possess errors below 13%, as illustrated in Figure 4.33 and predicted by the physical model in Equation 3.18 on page 74. The leading dependence of λ_{iso} deduced from the nonlinear regression is therefore[27]

$$\boxed{\lambda_{\text{iso}} \propto \overline{h}\, v^{-0.5}}. \tag{4.36}$$

This coincidence between theory and current experiments is a remarkable result. Using Equation 4.21, this relation yields

$$\boxed{\lambda_{\text{iso}} \propto V_{\text{c}}\, v^{-0.2}}. \tag{4.37}$$

Wavelengths in the limit of small cell volumes

The wavelength of surface undulations evolving for cell volumes in the range of $V_{\text{c}} = (1, \ldots, 3.5)$ ml/m^2 are depicted in Figure 4.30. Extending this range, especially to smaller volumes, is achieved by again including the results of the preliminary experiments of the IGT G1 tool summarized in Table C.1. Figure 4.34 illustrates these results in combination with trend curves of two printing runs with $v_2 = 1.25$ m/s, SR = 70 L/cm and $v_3 = 2.5$ m/s, SR = 60 L/cm. We can observe a consistent transition of the different experiments (most right blue square lies on the red solid trend curve). Starting with the smallest cell volume in region (I), the wavelengths only obey values of ~ 0.143 mm. This

[26] see Appendix C.3.1 on page 173

[27] rounding the exponents to one decimal place within the bounds of confidence

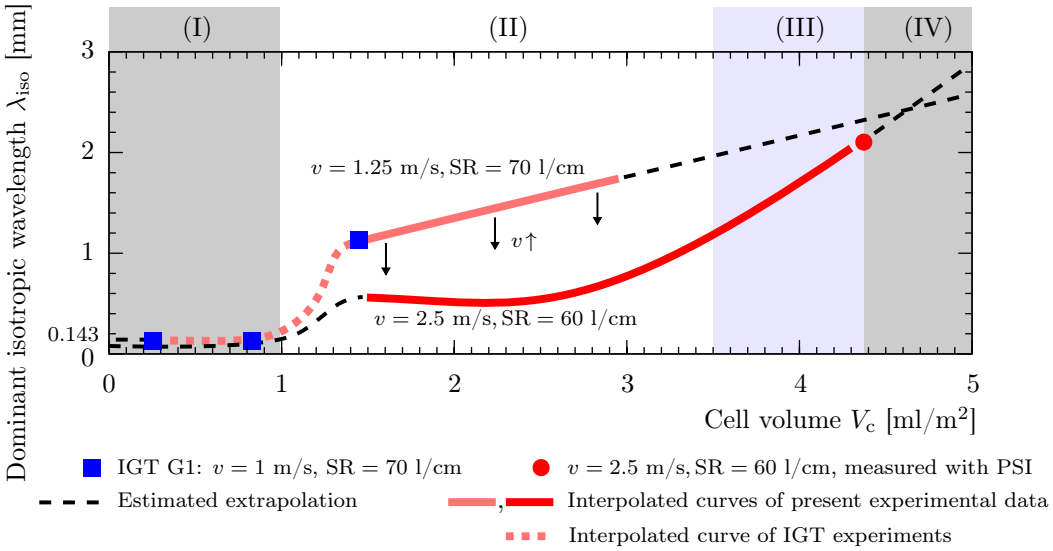

Figure 4.34: Trend charts of dominant isotropic wavelength λ_{iso} versus cell volume including preliminary experiments. Region (II) and (III) represent the cell volume range of the present printed fields. Large-area thickness determination with imaging color reflectometry (ICR) marks region (II) and with phase-shifting interferometry (PSI) region (III) including single measurements (red circles). (I) and (IV) marks regions which were not in the scope of the underlying experiments with the Prüfbau printing tool. Results of preliminary experiments with an IGT G1 printing tool (summarized in Table C.1) using the same inks and substrates and with $v = 1$ m/s, SR = 70 L/cm are shown as blue solid squares with a red dotted trend curve. Red solid lines show trend curves within the present data for $v_3 = 2.5$ m/s, SR = 60 L/cm and $v_2 = 1.25$ m/s, SR = 70 L/cm. The black dashed lines illustrate assumptions of an extrapolated dependency. The black arrows at the red solid trend curves illustrate the direction of change for increasing velocity $v\uparrow$ ($\lambda_{iso} \propto V_c v^{-0.2}$).

originates from the fact that the surface of the smallest cell volume consists of dried transferred single drops as illustrated in Figure 4.26 on page 120. Therefore, the wavelength of this field results in the inverse of the corresponding cell volume $\lambda_{iso} \approx 1/\text{SR} = 1/70$ L/cm ≈ 0.143 mm. For the printed field with a cell volume of $V_c = 0.84$ ml/m^2 (middle blue square) in Figure 4.30, the transferred drops coalesce before solidification and resulted in a very homogeneous layer (compare local minimum of roughness values in Figure 4.27). The remaining wavelength of the gravure pattern in the printed field almost leveled out and obeyed a very small measurable amplitude.

4.4.7 Physical mechanisms affecting the surface undulations

Leveling vs. drying time

Since gravure printing is a solution-based process, the transferred ink is subject to thin film dynamics before reaching the solid phase by evaporation of the solvent as introduced in Section 3.6. The time window in which the ink can undergo a surface leveling and accomplish fluid flow is therefore limited by the drying time t_d. In the present case, I assume that the thickness reduction of toluene-based ink under laboratory conditions without special heating or drying techniques can be described by

$$t_d = C_{dry} \overline{h}_w \tag{4.38}$$

for a mean wet film of thickness $\overline{h}_\mathrm{w}$, defined in Equation 4.22 on page 107. C_dry denotes the drying constant with a value of $C_\mathrm{dry} = 441$ nm/s[28]. This approach is very simplified and usually applicable for one-component fluids. For the present binary solution, the real drying time would be longer due to the concentration-related lowering of the vapor pressure of the printing solution as compared to the pure solvent. But according to the film dynamics during the late stage of drying, the ink is either comparable to a solid phase or in a highly viscous regime also suppressing the film dynamics. Therefore, the drying time in Equation 4.38 can be defined as an upper limit for the wet film dynamics on the substrate.

From the two types of thin film dynamics −spinodal dewetting and film leveling −introduced in Section 3.6, spinodal dewetting can be ruled out as playing a dominant role in the present experiments. This is because the driving van der Waals forces become important for wet film thicknesses far below $\overline{h}_\mathrm{w} \ll 100$ nm [121, 258], but all present wet films start with thicknesses above $\overline{h}_\mathrm{w} \sim 500$ nm.

Using Equations 3.25 and 3.26, I estimated the spinodal dewetting time t_spin, which is the time the thin film needs to evolve the spinodal pattern, and the spinodal wavelength λ_spin. For this, I calculated the Hamaker constant A_H via the Lifshitz theory following [8, 120] using the refractive indices of ITO $n_\mathrm{ITO} = 2$ and toluene $n_\mathrm{tol} = 1.5$ and the dielectric constants of $\epsilon_\mathrm{ITO} = 9.0$ and $\epsilon_\mathrm{tol} = 2.38$, from [8, 27, 71, 214]. Apart from the present values of viscosity ($\eta = 0.8$ mPa·s) and surface tension ($\sigma = 27.8$ mN/m), I chose a wet film thickness of $\overline{h}_\mathrm{w} = 1$ µm. With this, the spinodal wavelength resulted in a reasonable range of $\lambda_\mathrm{spin} = 1$ mm, but the time for its evolution was $t_\mathrm{spin} > 10^5$ s which excludes this type of dynamics.

In the following, I compare the leveling time t_lev formulated in Equation 3.22[29] to the drying time of the present layers. I chose to use the cell volume V_c as the dependent variable, for which the different wavelengths are shown in Figure 4.30 and the resulting dry film thicknesses in Figure 4.12. Using Equation 4.22, I calculated the wet film thickness $\overline{h}_\mathrm{w}$ which was required for the determination of t_lev and t_d.

The leveling and drying times associated to the printed fields are illustrated in Figure 4.35. The black open circles depict the leveling times which are longer than the corresponding drying times marked as red crosses, and the black filled circles are leveling times shorter than the drying times. The latter therefore represents fields which might have had enough time to evolve homogeneous surfaces before solidification. The velocities $v_3 = 2.5$ m/s, $v_4 = 5$ m/s and the screen ruling SR = 60 L/cm belong to these printing experiments of the fastest leveling times (filled circles in Figure 4.35) and are in very good agreement with the minimal relative roughnesses S_qr illustrated in Figure 4.22 and 4.23.

For this reason one may conclude, that, in the case of drying times larger than leveling times, surface roughness is usually small, and that this is due to the effect of surface tension in the liquid film.

I define the quotient of the corresponding leveling and drying times as a dimensionless measure for leveling, denoted as normalized leveling time

$$T_\mathrm{lev} \equiv \frac{t_\mathrm{lev}}{t_\mathrm{d}} \propto \left(\frac{\lambda_\mathrm{iso}}{\overline{h}}\right)^4, \tag{4.39}$$

[28] determined under ambient laboratory conditions using a micro-balance
[29] using the parameters of the present experiments mentioned above

where values around or below 1 promote fast leveling of undulations. For the right hand side of Equation 4.39, I used Equations 4.38, 4.22 and 3.21. The minimum normalized leveling times are shown in Figure 4.36. The horizontal line at 1 marks the position of equal leveling and drying time.

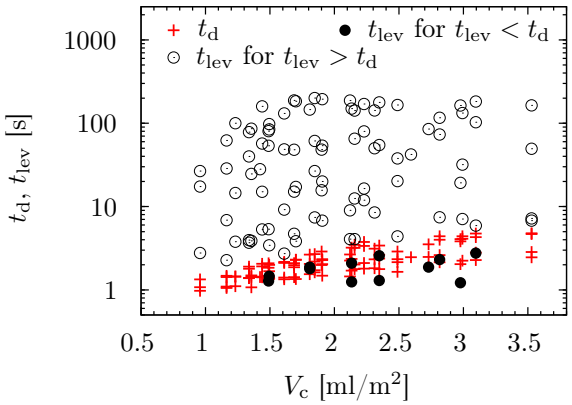

Figure 4.35: Calculated leveling t_{lev} and drying t_d times versus cell volume of the printed fields. t_{lev} and t_d were determined using Equations 3.21 and 4.38. t_{lev} for $t_{lev} > t_d$ is shown as black open circles and t_{lev} for $t_{lev} < t_d$ as black filled circles. Drying times t_d are shown for each field as red crosses.

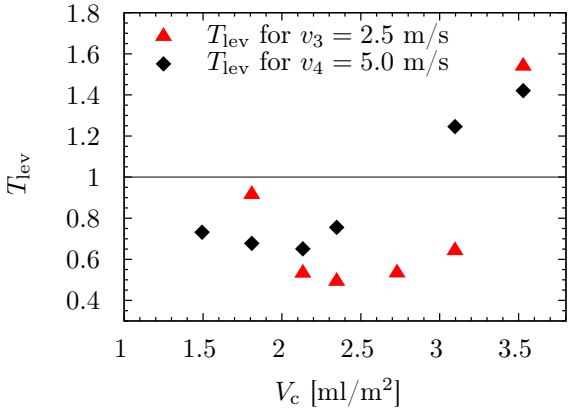

Figure 4.36: Fastest normalized leveling times versus cell volume. For velocities v_3 (red triangles) and v_4 (black squares) with screen ruling of SR = 60 L/cm, distinct minima are located at $V_c = 2.1$ ml/m^2 and $V_c = 2.35$ ml/m^2 .

Experiments of both printing runs with v_3 and v_4 show distinct broadened minima, at $V_c = 2.1$ ml/m^2 and $V_c = 2.35$ ml/m^2.

Trend charts of the representative normalized leveling times with corresponding printing parameters of $v = 2.5$ m/s, SR = 60 L/cm and $v_2 = 1.25$ m/s, SR = 70 L/cm, including the results of the preliminary experiments on the IGT G1 (summarized in Table C.1 on page 172), are shown in Figure 4.37. This extends the quantitative dependency and supports the qualitative extrapolation of the curves. In Figure 4.37, the blue squares represent the normalized leveling times of the IGT printing experiments with parameters $v = 1$ m/s, SR = 70 L/cm and cell volumes $V_c = (0.25, 0.84, 1.5)$ ml/m^2 summarized in Table C.1. The transition between the two different experiments (red dotted line and red solid upper line) differ by a factor of 4. Nevertheless, the minimum normalized leveling time in region (I) corresponds to its minimum roughness value $S^{m}_{qr,1}$ as shown in Figure 4.27. This mainly originates from the small wavelength of ~ 0.143 mm for this field which minimizes the leveling time (Equation 3.22). The corresponding lines in region (I) are not continued to smaller cell volumes because here, single droplets and not a closed wet film were present after printing, which is against the precondition for applying the present model of leveling dynamics.

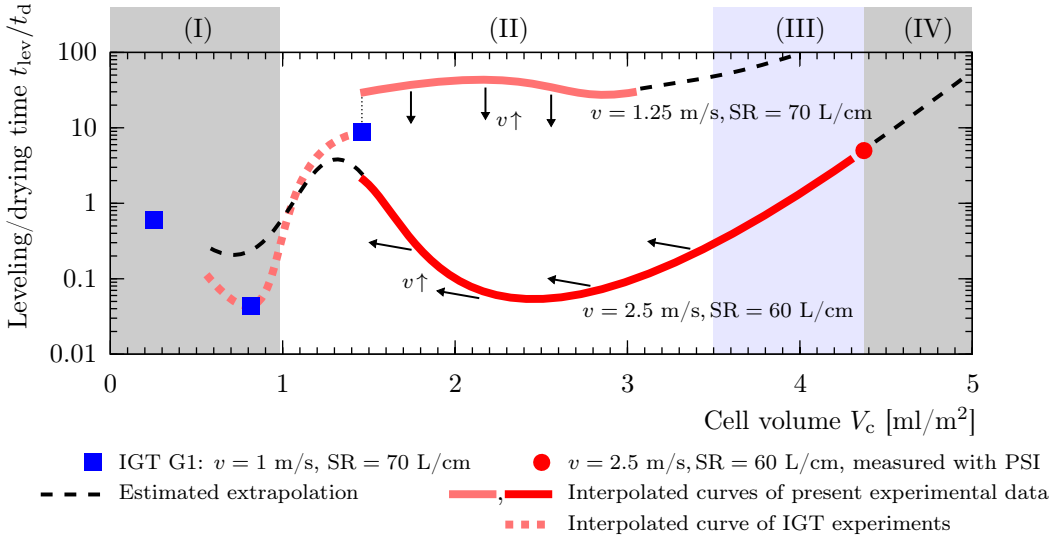

Figure 4.37: Trend charts of the normalized leveling time versus cell volume including preliminary IGT experiments. Region (II) and (III) represent the cell volume range of the present printed fields. Large-area thickness determination with imaging color reflectometry (ICR) marks region (II) and with phase-shifting interferometry (PSI) region (III) including single measurements (red circles). (I) and (IV) marks regions which were not in the scope of the underlying experiments with the Prüfbau printing tool. Results of preliminary experiments with an IGT G1 printing tool (summarized in Table C.1) using the same inks and substrates and with $v = 1$ m/s, SR = 70 L/cm are shown as blue solid squares with a red dotted trend curve. Red solid lines show trend curves within the present data for $v = 2.5$ m/s, SR = 60 L/cm and $v = 1.25$ m/s, SR = 70 L/cm. The black dashed lines illustrate assumptions of an extrapolated dependency. The black arrows at the red solid trend curves indicate the direction of change for increasing velocity $v\uparrow$.

Origins of the wavelengths

The proportionality of the wavelength $\lambda_{iso} \propto \overline{h}/\sqrt{v}$ determined by the regression of the experimental data in Equation 4.36 remarkably coincides with the physical model by Saffman and Taylor (Equation 3.18). The question is, how do the absolute values agree?

In Equation 3.18, the nip height h_{nip} or by additionally using Equation 3.19 the nip distance X_{nip} remains the only unknown quantity, see Figure 3.10 on page 75 for geometric explanation. Consequently, I could rearrange theses equations and calculate the "theoretical" nip position from the experimental data, which is shown as black squares for representative fields[30] in Figure 4.38.

On the other hand, I could estimate an upper limit of the meniscus position X_{nip} from the present printing experiments based on the extension (smearing) of the borders X_{bord} of the printed fields as illustrated in Figure 4.19 on page 113. This can be assumed to define an upper limit of the meniscus position, because the ink of the meniscus at the outlet nip empties itself after the last gravure cell passed the nip. Then, the distance of the meniscus position which defines the ink volume in the nip would be proportional to the tails on the substrates at a printed outlet edge.

For the same fields for which I calculated the "theoretical" nip position, I measured the border extension X_{bord} as shown in Figure 4.38.

In Figure 4.38, the different curves for the 'theoretical" nip position X_{nip} and the extension of the fields X_{bord} principally agree with each other apart from a scaling factor of 5.6 ± 0.4. According

[30] with distinct wavelengths λ_{iso} of $(0.69, 0.82, 0.9, 0.76)$ mm, printing velocity $v = 5$ m/s, screen rulings $(120, 95, 70, 60)$ L/cm and cell volumes V_c of $(1.4, 1.9, 2.6, 2.7)$ ml/m^2

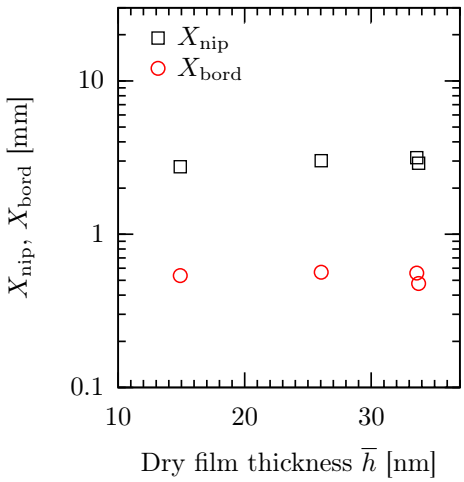

Figure 4.38: Comparison of the calculated nip position X_{nip} using Equation 3.18 and 3.19 based on measured wavelengths λ_{iso} and the border extension of the printed fields X_{bord}. Principally, the curves agree apart from a scaling factor of 5.6 ± 0.4.

to the approximate linear dependence between λ_{iso} and h_{nip} or X_{nip} in Equation 3.18, this involves the same factor of the ribbing wavelength between experiment and theory.

However, it is important to mention several aspects. The viscous fingering model was derived in the absence of any predefined structured surface as in case of the present gravure cylinders. The linear perturbation analysis resulting the Saffman-Taylor wavelength neglects any non-linear time evolution of the wavelength. Maher and Amar et al. investigated the non-linear time evolution of similar ribbing scenarios and found strongly increasing wavelengths in time [7, 168, 250]. Furthermore, the spectra of the fields showed smaller wavelengths at roughly half the value of the dominant one (see Figure 4.33), which possibly indicate that the initial wavelength originated from the nip was smaller, too.

This also supports the perspective that the underlying dynamics might be strongly non-linear and could therefore explain the deviation by the foregoing, identified factor of ~ 5. Based on the present experiments and the verified proportionality of the wavelength, film thickness and printing velocity (according to Equation 4.36), they follow the model of Saffman-Taylor in the first approximation.

Instead of using the model deduced directly from the Saffman-Taylor, I also compare the experiments to ribbing instabilities found in (un-structured) roll coating applications [34, 38]. Carvalho introduced a 3-dimensional stability analysis for the fluid flow at the nip region of two rotating rollers [34]. Apart from the missing gravure cell pattern on the roller, a gap of $2H_0$ is usually set between application roller and substrate in roll coating operations.

I associate half this gap to the wet film thickness $H_0 \approx \overline{h}_{\mathrm{w}}$ (with $\overline{h}_{\mathrm{w}}$ from Equation 4.22). Figure 4.39 compares the mean normalized wavelengths $\lambda_{\mathrm{iso}}/\overline{h}_{\mathrm{w}}$ per Capillary number Ca ($\sim v$) of all printed fields to results reconstructed from Carvalho et al. [34], therein Figure 20a. They investigated the "dimensionless" wavelength λ/H_0 of the ribbing in roll coating. In the log-log plot of Figure 4.39, the measured normalized wavelengths $\lambda_{\mathrm{iso}}/\overline{h}_{\mathrm{w}}$ of the fields are in good agreement with the ones from Carvalho. Because of the different slopes of the curves, the wavelengths would strongly deviate from each other for a different range of Capillary numbers. But in the present range, I conclude that the printing process of the low viscous ink formulation is comparable to roll

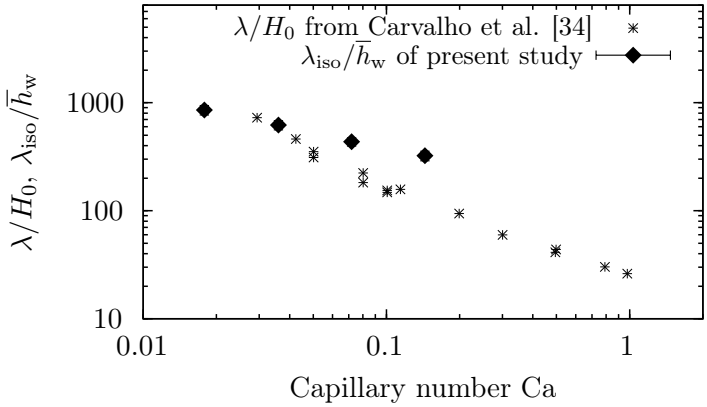

Figure 4.39: Normalized dimensionless wavelengths λ/H_0 and $\lambda_{iso}/\overline{h}_w$ of surface undulations of roll coated layers processed and analyzed by Carvalho et al. (reconstructed from [34]) and of the present printed fields, related to the Capillary number $Ca = \eta v/\sigma$.

coating processes. This analogy also confirms why the gravure cell pattern is less important for the development of the layer undulations.

4.5 Process window for gravure printed ultra-thin, homogeneous layers

In this section, I combine the previous results and outline the underlying process parameters which produce the most homogeneous layers. The varying input parameters of cell volume V_c, screen ruling SR and printing velocity v are closely related to the surface parameters of the printed fields as presented in Section 4.4. For "optimal" process parameters (v_3 = 2.5 m/s, v_4 = 2.5 m/s and SR = 60 L/cm), the relative RMS roughness as the leading parameter for layer homogeneity exhibits two minima, $S_{qr,1}^{m}$ denoted as *Type I* and $S_{qr,2}^{m}$ as *Type II*. For specific cell volumes they are shown in Figure 4.40 (and Figure 4.27).

I compare these minima of the roughness values to the trend charts (interpolation and extrapolation curves) of the other surface parameters for the "optimal" printing parameters v_3 = 2.5 m/s, and SR = 60 L/cm. It is important to note that the existence of the minima is not covered by the power-law regression functions applied in the previous section which only state a general scaling behavior.

The trend charts of the isotropic dominant wavelength λ_{iso} and the resulting normalized leveling time T_{lev} in Figure 4.40 have been already illustrated in Figure 4.34 and 4.37. The trend plots for the dry and wet film thickness, skewness and kurtosis are obtained by combining the present and preliminary experiments similarly as applied in the previous sections.

The combined trend charts of roughness S_{qr}, dry film thickness $\overline{h}$, wet film thickness $\overline{h}_w$, isotropic dominant wavelength λ_{iso}, skewness S_{sk}, kurtosis S_{ku} and normalized leveling time T_{lev} are shown in Figure 4.40. The black arrows indicate the direction of change of the trend lines for increasing velocity $v\uparrow$ and screen ruling SR$\uparrow$. The detailed dependence, especially of the roughness on screen ruling, should be better deduced from the results presented in Figure 4.24 on page 118. The gray colored regions mark the two minima of the roughness and the corresponding cell volume ranges of the other parameters. In contrast, the orange colored region marks the local maximum of the relative roughness.

According to the wet film dynamics and the results presented in the previous section, the layer surfaces evolve in the following way for increasing cell volume:

Starting with the smallest cell volume, the surfaces of the printed fields show wavelengths originating from the screening of the gravure cylinder because only single drops are transferred. For slightly larger cell volumes, the drops just coalesce with a very fast leveling because of the small surface wavelengths (inverse of the screen ruling). This marks the first minimum *Type I* ($S_{qr,1}^{m}$) of the roughness in Figure 4.40a. The layer becomes more inhomogeneous with further increasing cell volume and, depending on the process parameters (here v_3 = 2.5 m/s, SR = 60 L/cm and $V_c \approx 2.9$ ml/m^2), the wavelength and the wet film thickness exhibit values which minimizes the normalized leveling time yielding the second minimum *Type II* ($S_{qr,2}^{m}$) of the roughness.

It is important to note that this explanation strongly involves that the minimum *Type I* evolves mainly from a single cell transfer or from a transition between single cell and film splitting transfer. Both have in common that the resulting layer undulations directly after the nip are dominated by the screen pattern of the gravure cylinder. On the contrary, the minimum *Type II* is based on film splitting transfer where the dominant layer undulations originated from hydrodynamic nip instabili-

ties (viscous fingering).

From the charts illustrated in Figure 4.40, the most dominant common preconditions for the occurrence of a local minimum of the relative roughness of the printed fields according to cell volume are the existence of

a local minimum of the normalized leveling time T_{lev} and

a local minimum (high negative value) of the skewness S_{sk}.

A minimum of T_{lev} involves a minimum of the quotient $\lambda_{\mathrm{iso}}/\overline{h}$ according to V_{c}. For this aspect it is important to note that the layer thickness might deviate from the simplified line shown in Figure 4.40b and stays constant for varying cell volume as analyzed in Section 4.4.1 in Figure 4.13. The charts of λ_{iso} and T_{lev} in Figure 4.40c and 4.40e also reveal that the normalized leveling time might be a more suitable control parameter when looking for local minima than the wavelength. This is because the minima of λ_{iso} might be broadened and more difficult to determine.

A distinct feature which only occurred for the second roughness minimum at higher cell volumes is a maximum of the kurtosis shown in Figure 4.40d. The peak height is quite large and coincides with a deep minimum (in the negative) of the skewness. This might also imply that it is a required feature for homogeneity. Following the example profile in Figure 4.8d on page 98, this combination of low skewness (high negative value) and high kurtosis (> 3) could characterize a rather homogeneous layer with only a few small and deep holes. These could belong to dewetted holes originating from impurities on the substrate or within the ink. Assuming that the rate of impurities is not changing while varying the present input parameters (V_{c}, SR, v) would mean that this situation represents the most homogeneous layer accessible. This feature opens additional possibilities not only when looking for the most homogeneous film but also for investigating the "quality and purity" of the process. It is important to note that theoretically, the best layer (a perfect plane) would possess $S_{\mathrm{sk}} = S_{\mathrm{ku}} = 0$ and the best real layer (with small random noise in the thickness data) $S_{\mathrm{sk}} = 0$ and $S_{\mathrm{ku}} = 3$.

The local maximum of the relative roughness of this type of printed fields is marked in orange in Figure 4.40a and exhibits the opposite dependency as for the minima of S_{qr}, namely

a local maximum of the normalized leveling time T_{lev} and

a local maximum of the skewness S_{sk} (in the positive).

This maximum also involves small kurtosis values (Figure 4.40d) indicating drop-like surface formation as shown in the profile in Figure 4.8e on page 98. This coincides with an advanced dewetting process which might take place before solidification of the wet film.

In Figure 4.40a, the layer roughness increases for increasing cell volume above $V_{\mathrm{c}} > 3.4$ ml/m^2. This mainly originates from the growing wavelength and the resulting longer leveling times. But according to the non-linear regressions (summarized as boxed equations in Figure 4.40), I expect the leveling time to become independent of the cell volume. This is because both film thickness and wavelength linearly depend on cell volume. A possible contribution which is neither covered by the measurements nor by the adapted physical models are the amplitudes of the undulations which are initially imposed on the liquid layer after ink transfer. These could strongly influence the previously motivated process window.

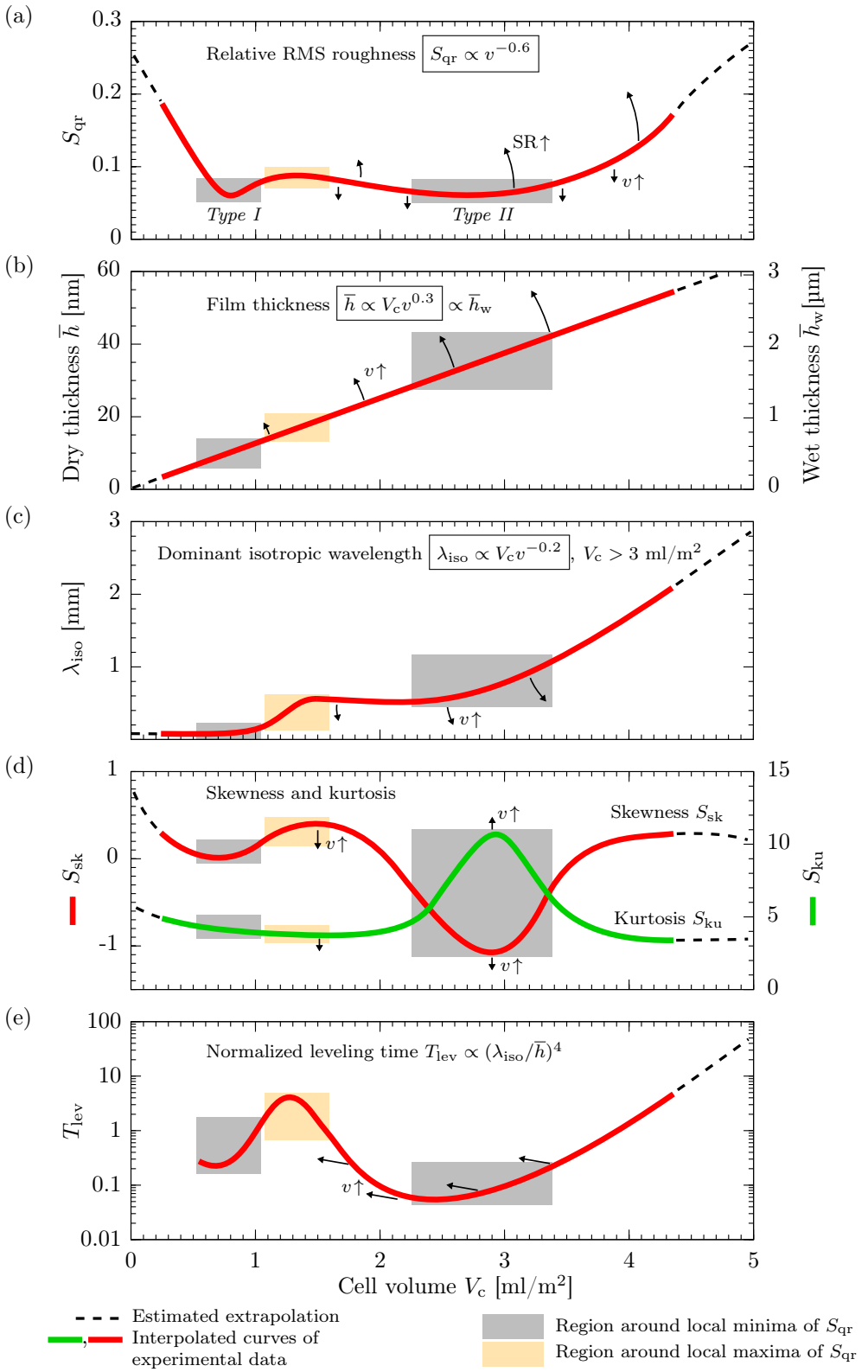

Figure 4.40: Combined trend charts (interpolated and extrapolated curves) of S_{qr}, $\overline{h}$, $\overline{h}_w$, λ_{iso}, S_{sk}, S_{ku} and T_{lev} for fields printed with printing velocity $v_3 = 2.5$ m/s and screen ruling SR = 60 L/cm. For S_{qr}, two different regions of minima (gray boxes, *Type I* and *Type II*) and one distinct region of a maximum (orange box) occurred. Red solid lines show trend curves within the present data set. The black dashed lines illustrate assumptions of an extrapolated dependency. The black arrows at the red solid trend curves illustrate the direction of change for increasing velocity v↑ or screen ruling SR↑. The boxed equations summarize the results of the nonlinear regression performed in the previous chapter.

4.5.1 Transferability of the process window

The thickness distributions of the present, gravure printed layers were verified by the theoretical models for hydrodynamic nip instabilities and thin film dynamics resulting in stable process windows for homogeneous layers. A transfer of the model to a second set of experiments in order to validate the obtained process windows was not performed. Instead, I briefly compare the process windows with the two types of minima (*Type I* and *II* in Figure 4.40) to the results of the afore mentioned authors Michels et al. [179], Stahl [237] and Hernandez-Sosa et al. [103] on page 86. In Figure 4.1 on page 89, the experiments are summarized in respect to the capillary number Ca showing the wide range of corresponding parameters used.

However, it was not possible to directly integrate their results into the trend charts of Figure 4.40 because of other missing values. Categorizing their results to either type of roughness minimum, I could clearly assign their "optimal" layers to one of them:

Michels et al.: They faced stripe-like undulations in the millimeter range in printing direction which they minimized by a neural-network approach. This means that they performed their layer optimization reaching the *Type II* of minimal layer roughness.

Stahl: He identified his most homogeneous layers for varying viscosity bounded by gravure cell patterns for high viscosities and with stripe-like undulations for low viscosities. Apart from the scaling of the corresponding values, this situation clearly matches the case of the single cell minimum of *Type I*.

Hernandez-Soza et al.: They obtained oriented stripes in printing direction in the millimeter range for varying viscosities and evaporation times. This marks clearly the leveling *Type II* minimum for their "best" layers.

4.5.2 Short, practical guideline to produce large-area ultra-thin films

In the following, I formulate a brief practical guideline which might help to process homogeneous, large-area gravure printed thin layers for given ink formulations. This should be seen as a guideline rather than a rule.

A precondition is that the desired ink on the substrate obeys contact angles not exceeding $\sim 40\,^\circ$ and falling below $\sim 5\,^\circ$. Possible pre-treatments could improve either way. Test prints with as much different engravings as available should be performed using the full range of velocities of the tool. From concentration of the solute, the desired dry film thickness and the test prints, check which of the two minima discussed above should be approached, the screen ruling *Type I* or the nip leveling *Type II*. The latter might be useful to reach thicker layer thicknesses, whereas the *Type I* might possess a wider range.

An important criterium is which sort of undulation the test layers show. If the pattern is directed stripe-like in printing direction, one might have a more viscous ink, which could be suitable for the leveling *Type II* to achieve a homogeneous layer. If a velocity increase and a screen ruling decrease at constant cell volume are not reducing the amplitudes of the stripes, an extension of the drying time might be considered.

If the pattern in the printing result is isotropic in the millimeter range, the ink might tend to fast dynamics reducing possible process windows for leveling. For the latter and as well as for undulations copying the structure of the gravure pattern, the *Type I* of the minima should be focussed to achieve

more homogeneous layers. If the viscosity might be an input parameter possible to change, then the relation presented in this thesis might me checked with replacing the velocity with the viscosity $v \to \eta$.

4.5.3 Remark on *isotropic* vs. *directed* viscous fingering

It is worth taking up an important point of the present type of undulations. All ribbing structures originating from the nip experimentally or numerically discussed in the literature, either for gravure printing (for graphical and for other applications) or for gravure/roll coating, are *directed* in printing/coating direction. The feature of the dominant isotropy of the present printing experiments has not been reported before.

Seen from this angle, it is even more surprising that the present *isotropic* undulations coincide with the theoretical model of *directed* viscous fingering that accurate. The loss of orientation of the undulations might be a special feature of the present low viscous ink, structure of the gravure cylinder and its thin film dynamics which has not been processed and analyzed in this detail before. This feature of isotropy has not been reported for gravure coating experiments using these low viscosities before and is therefore a surprising observation.

4.6 Summary

A low viscous ink solution based on the small molecule spiro-MeOTAD, which might be used in OLEDs or OPVs, dissolved in toluene was processed on ITO glass using a laboratory gravure printing unit from Prüfbau. The functional ink solution served as model ink to analyze, improve and understand the application of this printing technique for organic electronics in respect to their high requirements, in the present context: sub-100 nm thicknesses with minimal thickness variations.

The viscosity of the toluene-based ink was two orders below the values commonly used in gravure printing. I printed fields, each 30×30 mm^2 in size, on two consecutively mounted 150×150 mm^2 ITO-coated glass substrates with varying process parameters: velocity, cell volume and screen ruling. These three input parameters are easily accessible and adjustable for any kind of printing tool. Applying the proposed large-area characterization method ICR laterally resolved the thicknesses of the 128 printed fields (on total 1150 cm^2) ranging between 10 to 70 nm. I determined several surface parameters, such as relative RMS roughness, skewness, kurtosis and the isotropic dominant wavelength of the surfaces undulations. These determined surface parameters were referred to the physical models of fluid and thin film dynamics with respect to the underlying input process parameters.

I found a surprising feature when printing over topography. A step on the substrate influenced the mean thicknesses of the printed fields behind this step. I presented an explanatory model that gives insights into the possibly underlying ink transfer mechanisms assigning the process a dependence on its *printing history* per run.

The wavelengths of undulations could be assigned to Saffman-Taylor instabilities originating from the ink splitting process in the nip. By a scaling factor of ~ 5, I found a very good agreement of the wavelength between experiments and theory. For the first time, it was shown that the viscous fingering in gravure printing of low viscous inks can be well described by the model of Saffman-Taylor.

The spectral analysis revealed an additional feature. Some fields showed isotropic wavelengths at half the main wavelength which has not been reported in the literature before.

Except for the surface parameters skewness and kurtosis, non-linear regressions of the experimental data revealed scaling laws for the dry film thickness, roughness and wavelength in respect to velocity and cell volume.

Two distinct minima of the relative layer roughness were identified involving different underlying ink transfer mechanisms, i.e. single cell transfer and film splitting transfer. Other surface parameters revealed specific characteristics at these roughness minima and allowed to present a combined process window. Based on physical models of thin film dynamics, a normalized leveling time was defined which agreed well with the most homogeneous layers. These were obtained with a relative roughness of $S_{\mathrm{qr}} \approx 0.04$ ($\tilde{S}_{\mathrm{qr}} \approx 4\%$) for printing velocities of $v = (2.5, 5)$ m/s, screen rulings of $\mathrm{SR} = (60, 70)$ L/cm, and cell volumes around $V_{\mathrm{c}} \approx 3$ ml/m^2.

Results of previous studies on gravure printing thin homogeneous layers could be clearly categorized by the two types of minima.

4.7 Outlook

4.7.1 Understanding the gravure printing process

The present gravure printing experiments with their detailed analysis revealed new insights into the underlying physical mechanisms of printing low viscous inks. They also showed limiting aspects. The arrangement of the fields should be reconsidered when designing a gravure cylinder for test purposes, mainly because of the assigned *printing history*. In the present experiments, fields with high cell volumes were always consecutively printed before the ones with smaller cell volumes. To identify the effect of this sequence, one should also arrange fields in the opposite order on the cylinder.

The feature arising from the present experiments that topography on the substrate influence subsequent printing behavior could be extended to a "measurement" method for the ink transfer ratio as indicated by Equation 4.29 with $A_{\mathrm{fill}} \propto 1 - \delta\overline{h}_{\mathrm{sr}}$. By variation of the step height and step length of a well-defined topography on the substrate, one could obtain a test substrate which might be used to exactly characterize the underlying ink transfer mechanisms. In this case, step heights and lengths might be matched to the parameters of the fluid and the cylinder.

Combining an optimized gravure cell arrangement with an optimized substrate topography and an improved layer analysis, especially at the edges of printed fields, one could strongly receive further insight into the physics of gravure printing. As presented in Section 4.4.3 only for a few fields, measuring the exact form of the front and back edges of all fields and correlate chosen parameters (length, thickness wavelength of the smeared tails) to the other ones might more precisely define the stable process windows.

4.7.2 New ways to obtain homogeneous layers

The evaporation rate of the ink which defined the drying constant t_d was assumed to be constant in the present experiments. Taking this into account, especially for the sub-process of the fluid dynamics on the substrate could reveal a further promising control parameter for homogeneous layers. The latter could be either changed by the choice of solvent or by controlling the environment by using drying units or a controlled environmental atmosphere.

There might be also a very interesting possibility to obtain homogeneous layers by switching between the proposed two different types of minima of the layer roughnesses. Equation 4.39 reveals that the normalized leveling time is $T_{lev} \propto (\lambda_{iso}/\overline{h})^4$. I assume that the printing result exhibits strong undulations in the millimeter range and one has to match a desired thickness and can not strongly change $\overline{h}$. Now, the idea is two modify the gravure cell pattern so that when leaving the printing nip the shorter wavelength of the screen dominates the viscous fingering wavelength. Thereby one could obtain homogeneous layers by faster leveling with the screen-like minimum *Type I* of the roughness.

This could be achieved by introducing a superlattice into the primary gravure cell pattern to result in a second effective cell. This effective cell might be obtained without strongly changing the initial single cell shape and screen ruling SR_1. One might integrate a second short "screen ruling" SR_2 which exhibits a period $1/SR_2$ possible a factor of 2 or 3 above the original one $1/SR_1$ but below the wavelength of the layer undulation when printing only with SR_1. A possible gravure cell pattern is shown in Figure 4.41. At the outlet of the printing nip, the creation of a continuous meniscus

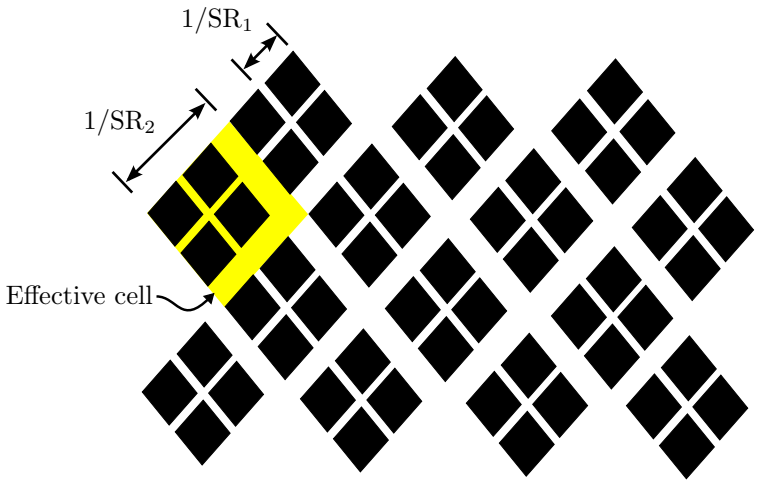

Figure 4.41: Proposed gravure cell pattern to switch between film splitting transfer to an effective cell transfer.

along the printing width might be suppressed in this way, so that the ink transfer is changed from film splitting to an effective single cell splitting.

Chapter 5

Conclusion

In the present study, I investigated three topics. First, I developed a characterization method for large-area, ultra-thin films. Second, I introduced relevant physics of gravure printing and investigated some general aspects of the process by performing experiments with color inks. Third, I applied the gravure printing technique to low viscous ink formulations used in organic electronics on large substrates. These were fully characterized by the developed measurement method and thoroughly analyzed with respect to minimal layer roughness.

The characterization technique for layer thicknesses in the nanometer range on a large lateral scale presented in Chapter 2 is based on optical thin film interference at the interfaces of the sample. The only hardware requirement is that the incident light angle and the observation angle of the optical setup is equal and close to the normal of the sample surface. I enabled an optical microscope and a modified flatbed scanner to obtain the image data of large-area thin film samples. Comparing contrast values and implementing a theoretical optical model, I estimated the most probable thickness for each pixel to obtain an overall thickness map of the top layer of a thin film stack. The proposed method was evaluated and validated by analyzing and comparing thicknesses of different test samples to the ones determined by reference methods. A detailed sensitivity analysis related to selected variables was performed revealing the predominant perturbation terms. Both setups showed reliable thickness determination of the test samples matching the results of corresponding reference methods. The high quality optical system of the microscope gave slightly better results than the modified scanner, but the scanner acquired the test samples within half a minute, a factor of 30 faster than the microscope. The scanner occasionally produced images with artifacts of bright rings whose origins remained unresolved.

In Chapter 3, I introduced the relevant physics associated to the gravure printing process. Thereby, the complexity of gravure printing was reduced by descriptively separating the process into different phases. In anticipation of the application of low viscous inks for large-area electronic applications, I focussed the introduction on printing nip instabilities related to viscous fingering and on thin film dynamics on the substrate related to leveling and dewetting. Results of preliminary printing experiments with color inks revealed a new method for gaining insights into sub-process of gravure printing. The combination of the easily removable printing plate of the test device, the usage of non-evaporating inks, transparent substrates and an optical profilometer enabled these new types of measurement setups. For the first time, air bubbles trapped in the apex of gravure cells, theoretically not surprising, but experimentally not reported before, were verified. Additionally, the dependence

of the air voids originating from the first gravure cell – substrate contact were presented which correlated with the filling of the gravure cell after doctoring. First numerical simulations of a complete 2D gravure printing setup are shown in the appendix.

In the main investigation of the thesis, in Chapter 4, I present direct gravure printing experiments of ultra-thin, small molecule based ink formulations on glass with thicknesses ranging from 10 to 70 nm. The viscosity of the toluene-based ink was two orders below common values used in gravure printing. I chose a gravure cylinder with 32 different 30×30 mm^2 engraved fields to span a wide parameter space.

By applying the thickness measurement method introduced in Chapter 2, I was able to determine nanometer thickness maps of all printed 150×150 mm^2 substrates, with a total area of 1800 cm^2 (analyzed printed fields 1150 cm^2). Apart from the mean layer thicknesses, I analyzed the relative RMS roughness, skewness, kurtosis and the isotropic dominant wavelength of the surfaces of the printed fields.

I found a surprising feature when printing over topography steps on the substrate. They influenced the mean thicknesses of the printed fields behind these steps. I presented an explanatory model that gives insights into the underlying ink transfer mechanisms revealing that the ink transfer is dependent on its *printing history*, i.e. what the ink experienced before.

The wavelengths of undulations could be assigned to Saffman-Taylor instabilities originating from the ink splitting process in the nip. By a scaling factor of ~ 5, I found a very good agreement of the wavelength between experiments and theory. For the first time, it was shown that the viscous fingering in gravure printing of low viscous inks can be well described by the model of Saffman-Taylor. The spectral analysis revealed an additional feature. Some fields showed isotropic wavelengths at half of the main wavelength which has not been reported in the literature before.

Except for the surface parameters skewness and kurtosis, non-linear regressions of the experimental data revealed scaling laws for the dry film thickness, roughness and wavelength in respect to velocity and cell volume.

Two distinct minima of the relative layer roughnesses were identified involving different underlying ink transfer mechanisms, i.e. single cell transfer and film splitting transfer. Other surface parameters revealed specific characteristics at these roughness minima and allowed to present a combined process window. Based on physical models of thin film dynamics, a normalized leveling time was defined which agreed well with the most homogeneous layers.

Results of previous studies on gravure printing thin homogeneous layers could be clearly categorized by the two types of minima.

Appendix A

Optical profilometry

Throughout the thesis, several measurements were performed using the optical profilometer Plu Neox from Sensorfar, Spain. This tool combines confocal microscopy, white-light and phase-shifting interferometry in a single tool [17, 201]. In the following, I briefly describe the operational principles of these methods and how they are implemented in the tool.

A.1 Confocal microscopy

Confocal microscopy usually enables pin-hole like apertures in front of the bright field illumination and the photo detector to strongly reduce the depth of focus (DoF) of the optical system [10]. It is important that both apertures a "confocally" projected onto the sample surface. With this, the detector only determines considerable intensities when the sample surface is exactly positioned in the focal plane of the optical system. The sample is laterally and vertically scanned by the optical sensor [10]. From each vertical resolved data set per lateral pixel the brightest detected signal is correlated to the corresponding z-position. Thereby, a laterally resolved height map is reconstructed.

Contrary to common confocal profilers, the Sensofar Plu Neox performs the lateral scanning without mechanical movement [17]. This is achieved by implementing a reflective micro display in the optical path. The optical setup is illustrated in Figure A.1, [17, 26].

An LED illuminates the reflective micro display through a beam splitter. The reduced DoF is achieved by subsequently switching only single pixels of the micro display on the illumination side. At the same time, the reduced aperture on the detector side is obtained by analyzing only intensities from the corresponding single detector pixel of the camera chip. Therewith, the "confocal" small apertures in front of the illumination and the detector are ensured. The system allows acquiring topographic measurements within less than ten seconds while resolving height differences of below 10 nm nanometers [201].

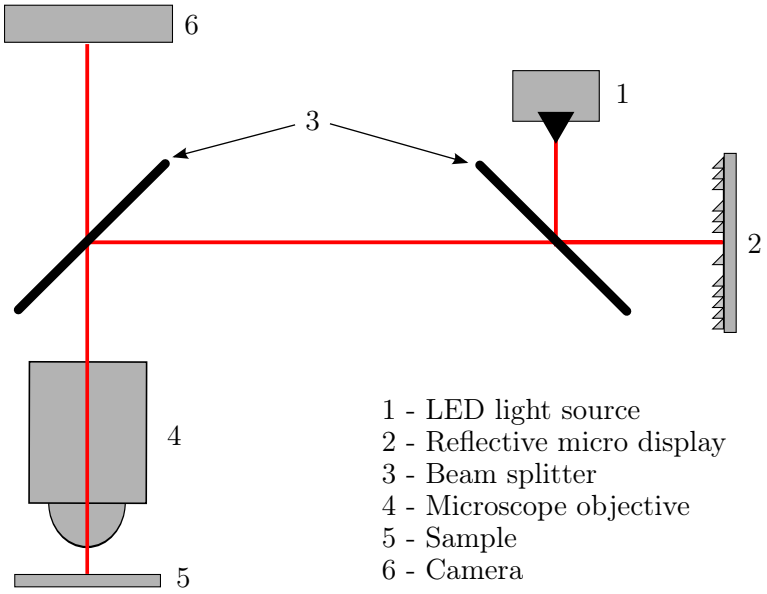

Figure A.1: Sketch of the optical path (red lines) and the setup of the confocal microscopy mode of the Sensofar Plu Neox, reprinted with permission from [26].

A.2 Interferometric surface profilometry

Sample surfaces which reflect a considerable amount of light might be analyzed by interferometric microscopy. A principle setup following the arrangement of the Sensofar Plu Neox [17] is shown in Figure A.2. The reflective micro display is completely switch "on", meaning it acts as a mirror, while operating in the interferometric modes.

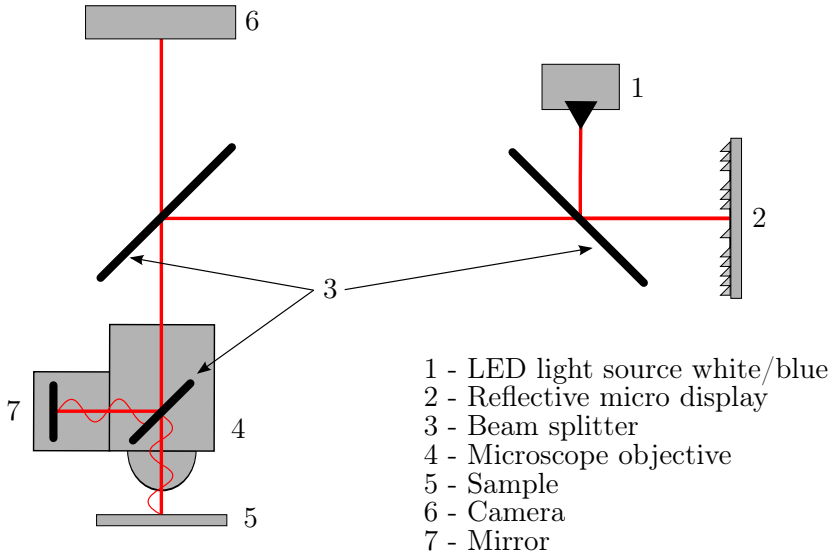

Figure A.2: Sketch of the optical path (red lines) and the setup of the interferometric modes of the Sensofar Plu Neox. A white LED is used for the VSI and a blue LED for the PSI mode, following [17].

The main modification compared to the confocal mode shown in Figure A.1 is the change to a different type of objectives. They additionally exhibit reference mirrors as illustrated in Figure A.2. This provides a reference beam which optically interferes with the light reflected from the sample surface during vertical scanning of the sample. Depending on the height distribution the two beams

constructively or destructively interfere producing distinct fringe patterns on the image sensor of the microscope which correlate to the sample surface.

Depending on the light source used, the method is denoted as white-light interferometry, also known as vertical scanning interferometry (VSI), or phase-shifting interferometry (PSI). As indicated by the first method, this requires a white-light source, whereas the second method uses monochromatic light.

A.2.1 Phase-shifting interferometry (PSI)

In phase-shifting interferometry, usually the sample is imaged under 4 different phase angles (z-positions) [77]. Originating from the extended coherent length of the monochromatic light, the difficulty in reconstructing the surface map from the interference intensities is the occurrence of equal fringe patterns at multiples of the wavelength distance. This means that for height variations above half the wavelength of the light, the resulting thickness map would contain unrealistic steps or inverted structures. Therefore, so-called "unwrapping" techniques are applied to add or subtract 2π to or from the phase per lateral image pixel [77, 147]. This procedure tends to often fail using the Plu Neox. Therefore, this method is well suited for layer thickness variations below 100 nm with a resolution of < 1 nm [201].

A.2.2 White-light interferometry (VSI)

The white-light used in VSI provides a much shorter coherent length which result in an enveloping Gauss distribution around the peak intensity of the interference patterns [92, 93]. This usually prevents the reconstruction algorithm from producing inverted topographies. This method is therefore suitable to profile surfaces which obey height variations > 1µm with a resolution of < 5 nm [201].

Appendix B

Imaging color reflectometry

B.1 Sensitivity/error analysis: Results for all SiO_2 layers

The following graphs complement the plots discussed in Section 2.6. They show the estimated thicknesses of all fields of the SiO_2 on the Si wafer imaged by the microscope with small variations added to selected variables. For details see Section 2.6 on pages 43 ff..

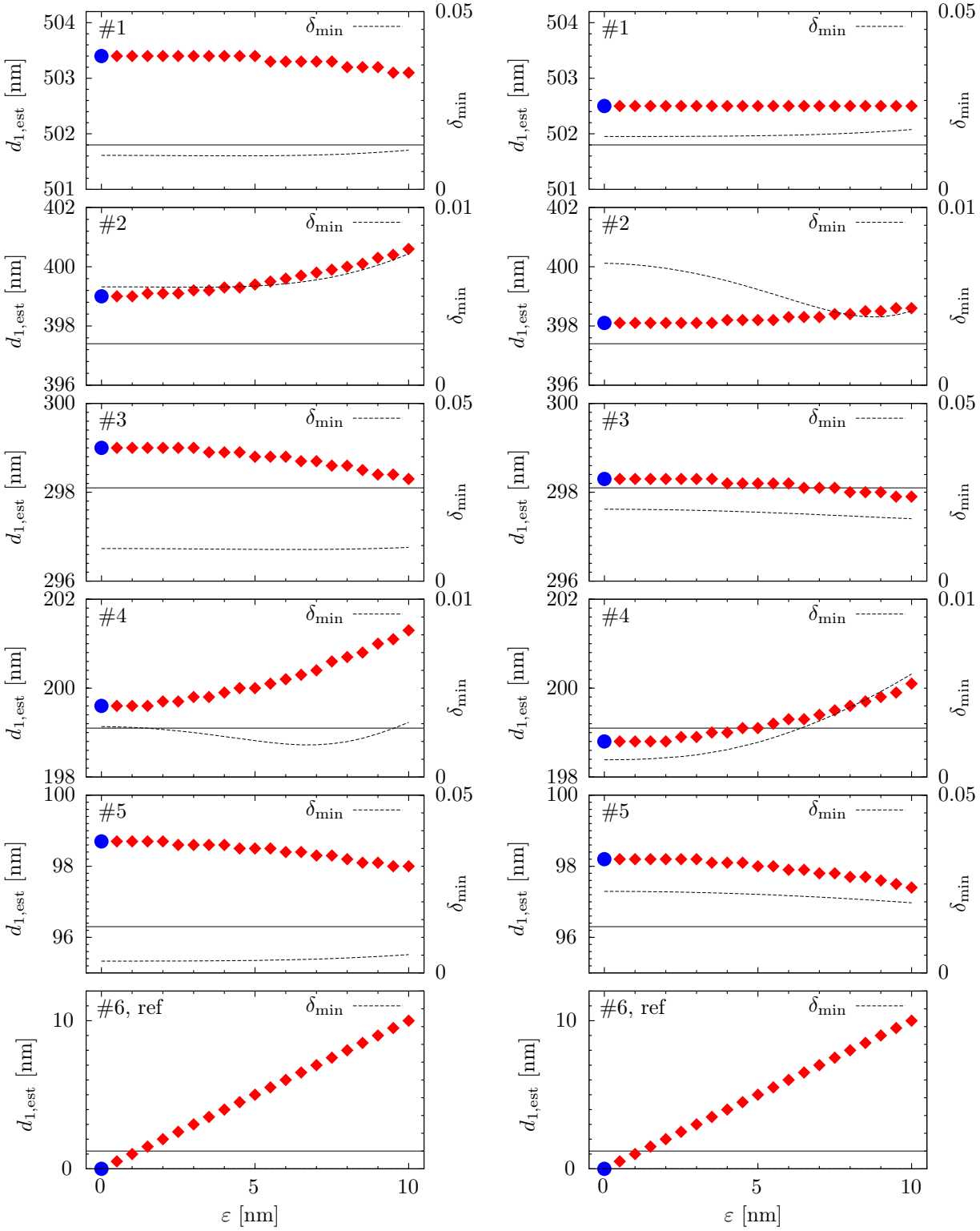

(a) Leica microscope, variation of reference thickness of field #6 from $d_{1,\text{ref}} = 0$ nm.

(b) Epson flatbed scanner, variation of reference thickness of field #6 from $d_{1,\text{ref}} = 0$ nm.

Figure B.1: Estimated thicknesses of all SiO_2 layers (apart from reference field #6) on Si wafer based on analyzed images of the two different hardware setups according to a variation of the reference thickness $d_{1,\text{ref}}$ by $\varepsilon = 0 \ldots 10$ nm. Blue circles depict thickness values for $d_{1,\text{ref}} = 0$ nm. Grey triangles show results using $d_{1,r}^{\text{narrow}}$ with simultaneous failure of the algorithm for $d_{1,r}^{\text{wide}}$. The black horizontal lines show the manufacturer thickness values for the different fields. Residuals $\delta_{\min}$ in contrast space are depicted as dashed curves.

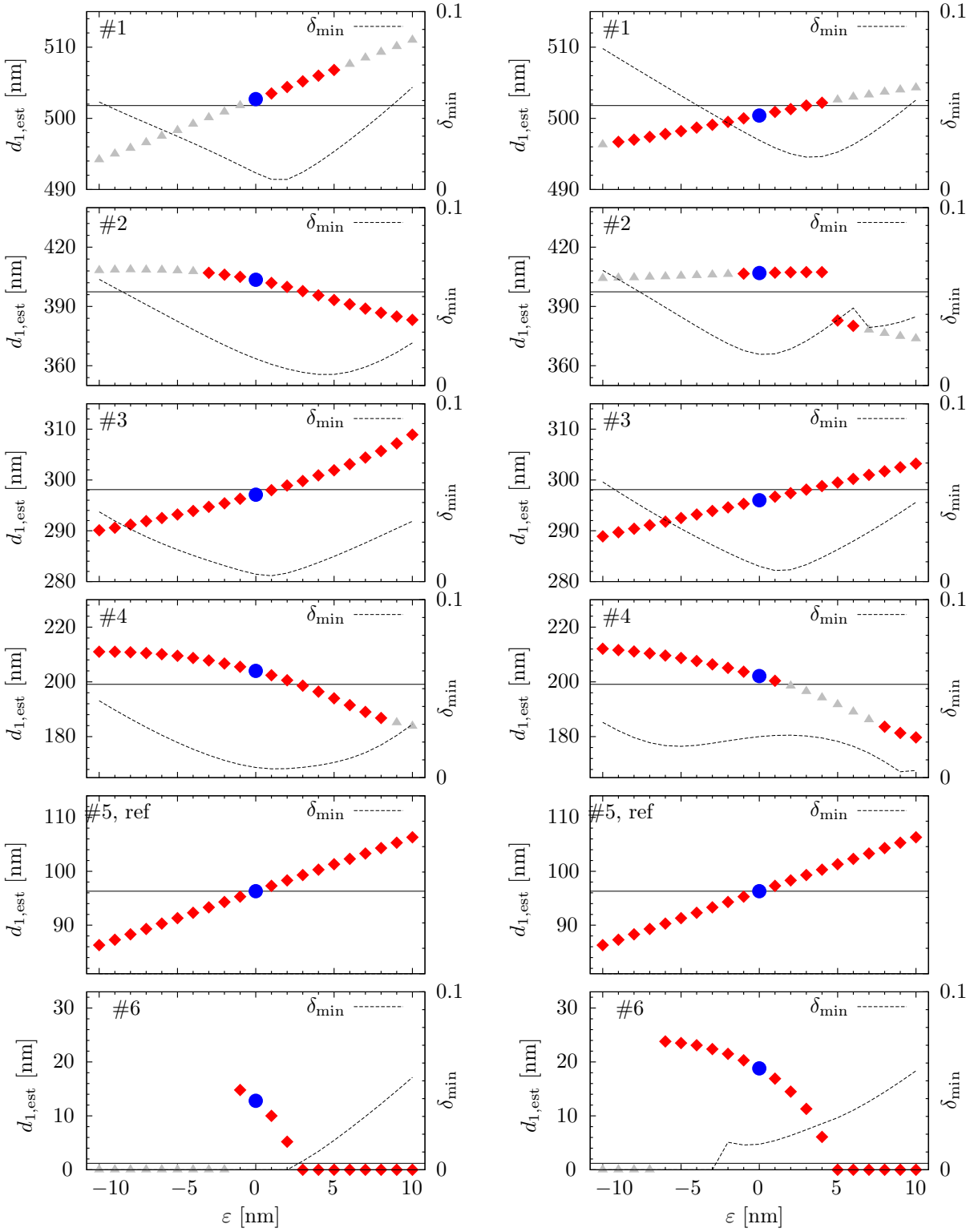

(a) Leica microscope, variation of reference thickness of field #5 from $d_{1,\mathrm{ref}} = 100$ nm.

(b) Epson flatbed scanner, variation of reference thickness of field #5 from $d_{1,\mathrm{ref}} = 100$ nm.

Figure B.2: Estimated thicknesses of all SiO_2 layers (apart from reference field #5) on Si wafer based on analyzed images of the two different hardware setups according to a variation of the reference thickness $d_{1,\mathrm{ref}} = 100$ nm by $\varepsilon = \pm 10$ nm. Blue circles depict thickness values for $d_{1,\mathrm{ref}} = 0$ nm. Grey triangles show results using $d_{1,r}^{\mathrm{narrow}}$ with simultaneous failure of the algorithm for $d_{1,r}^{\mathrm{wide}}$. The black horizontal lines show the manufacturer thickness values for the different fields. Residuals $\delta_{\min}$ in contrast space are depicted as dashed curves.

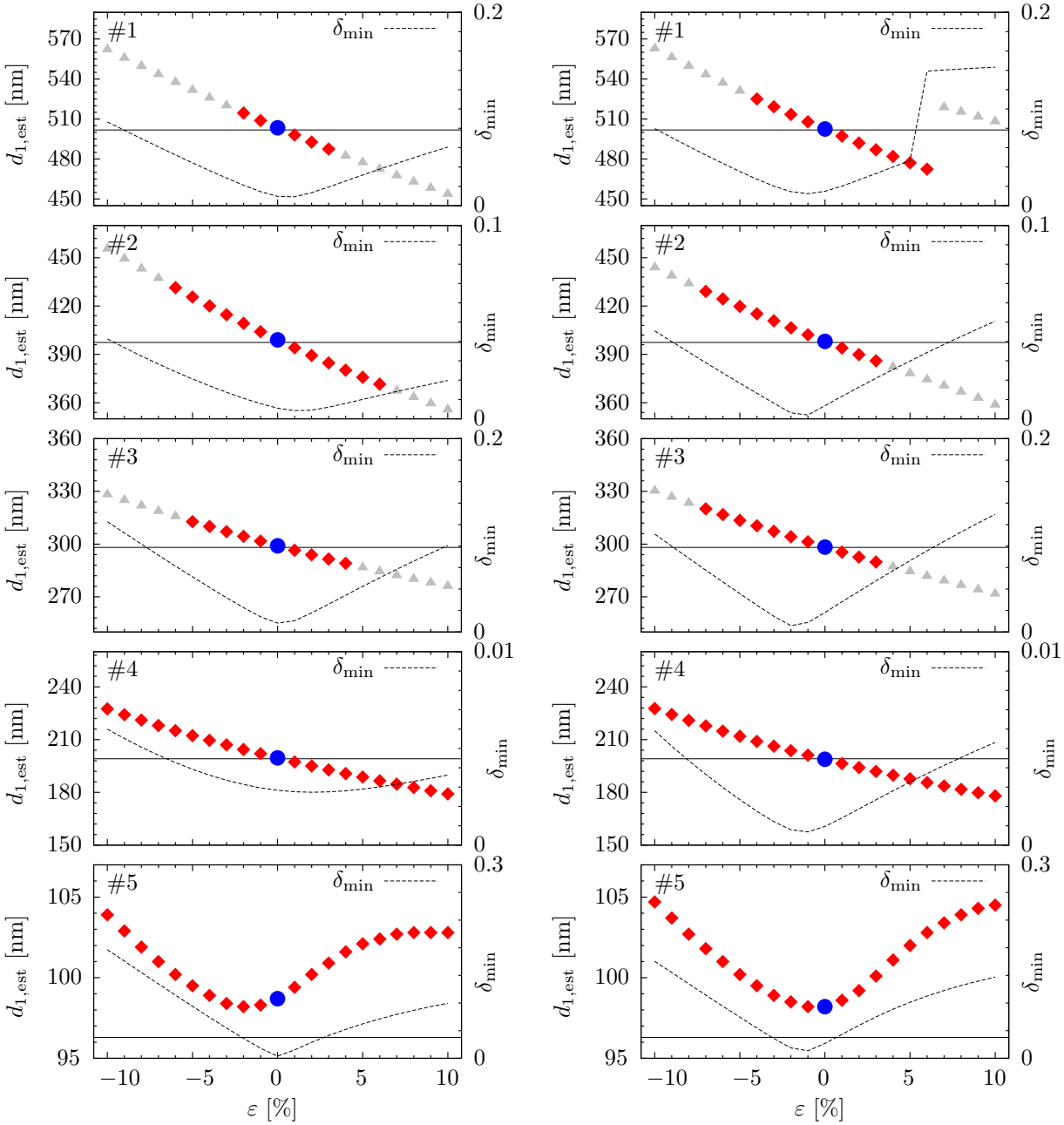

(a) Leica microscope, variation of the refractive indices of SiO_2.

(b) Epson flatbed scanner, variation of the refractive indices of SiO_2.

Figure B.3: Estimated thicknesses of all SiO_2 layers (apart from reference field #6) on Si wafer based on analyzed images of the two different hardware setups according to a variation of the refractive indices of SiO_2 with up to $\varepsilon = \pm 10$ %. Blue circles depict thickness values for $\varepsilon = 0$ %. Grey triangles show results using $d_{1,r}^{\text{narrow}}$ with simultaneous failure of the algorithm for $d_{1,r}^{\text{wide}}$. The black horizontal lines show the manufacturer thickness values for the different fields. Residuals $\delta_{\min}$ in contrast space are depicted as dashed curves.

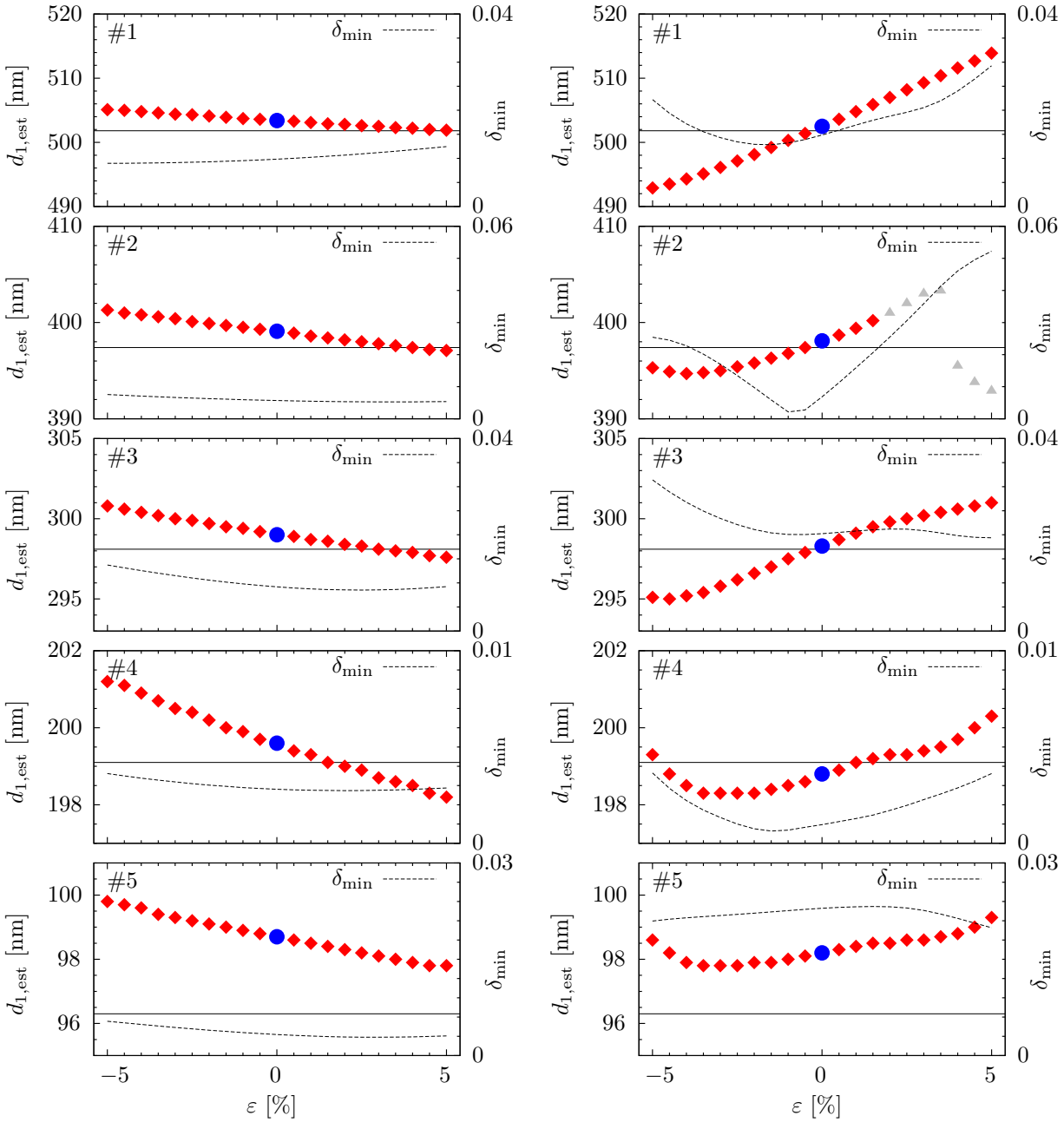

(a) Leica microscope, induced wavelength shift of the spectrum of the light source.

(b) Epson flatbed scanner, induced wavelength shift of the spectrum of the light source.

Figure B.4: Estimated thicknesses of all SiO_2 layers (apart from reference field #6) on Si wafer based on analyzed images of the two different hardware setups according to a wavelength shift of the spectrum of the light source $L(\lambda)$ by $\varepsilon = \pm 5\%$ (± 20 nm). Blue circles depict thickness values for $\varepsilon = 0$ %. Grey triangles show results using $d_{1,r}^{\mathrm{narrow}}$ with simultaneous failure of the algorithm for $d_{1,r}^{\mathrm{wide}}$. The black horizontal lines show the manufacturer thickness values for the different fields. Residuals $\delta_{\min}$ in contrast space are depicted as dashed curves.

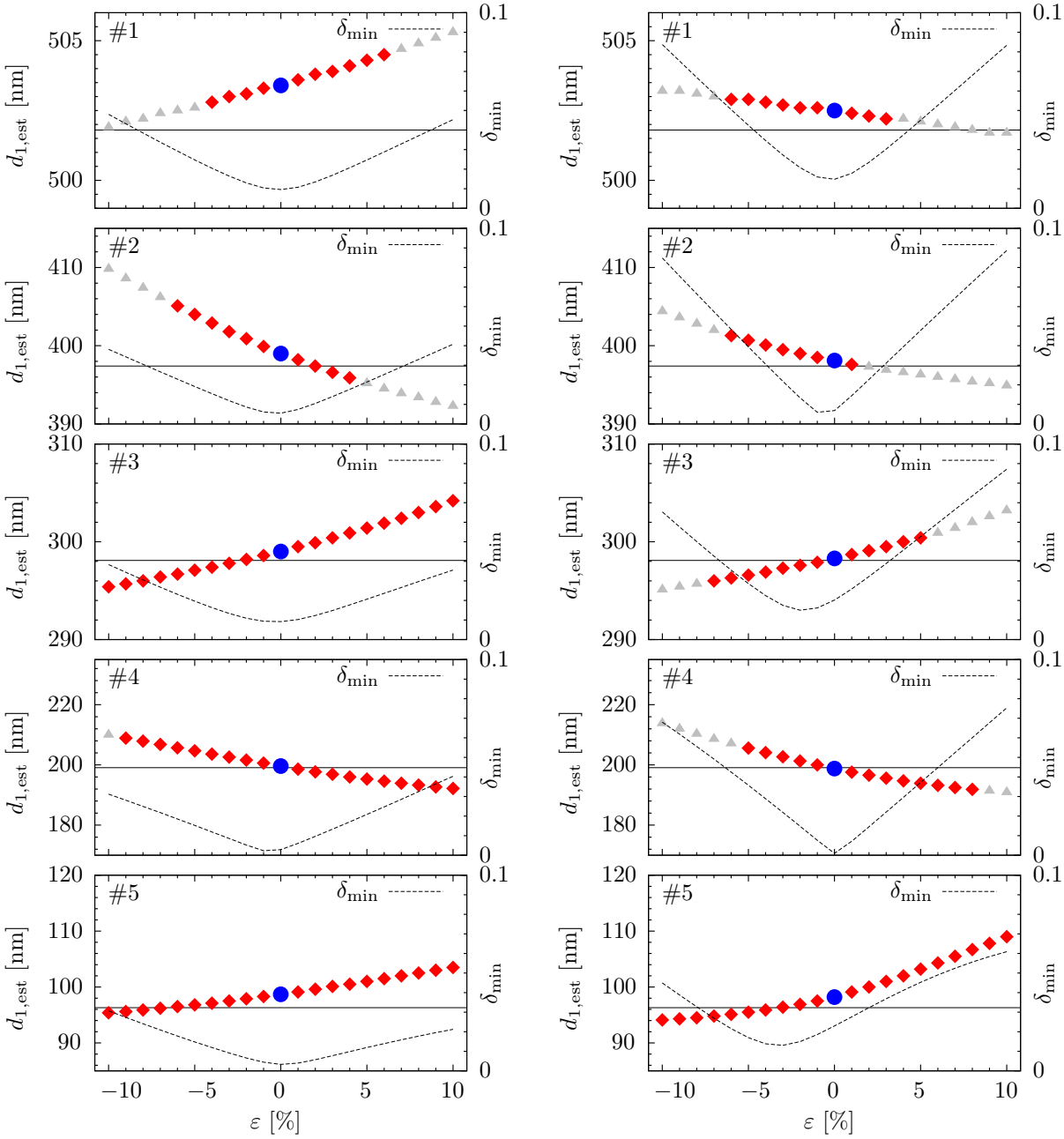

(a) Leica microscope, variation of measured $\mathcal{RGB}$ values (apart from reference $\mathcal{RGB}$ values).

(b) Epson flatbed scanner, variation of measured $\mathcal{RGB}$ values (apart from reference $\mathcal{RGB}$ values).

Figure B.5: Estimated thicknesses of all SiO_2 layers (apart from reference field #6) on Si wafer based on analyzed images of the two different hardware setups according to a variation of the measured $\mathcal{RGB}$ values of the layers by $\varepsilon = \pm 10\%$ apart from reference $\mathcal{RGB}$ values (field #6). Blue circles depict thickness values for $\varepsilon = 0$ %. Grey triangles show results using $d_{1,r}^{\text{narrow}}$ with simultaneous failure of the algorithm for $d_{1,r}^{\text{wide}}$. The black horizontal lines show the manufacturer thickness values for the different fields. Residuals $\delta_{\min}$ in contrast space are depicted as dashed curves.

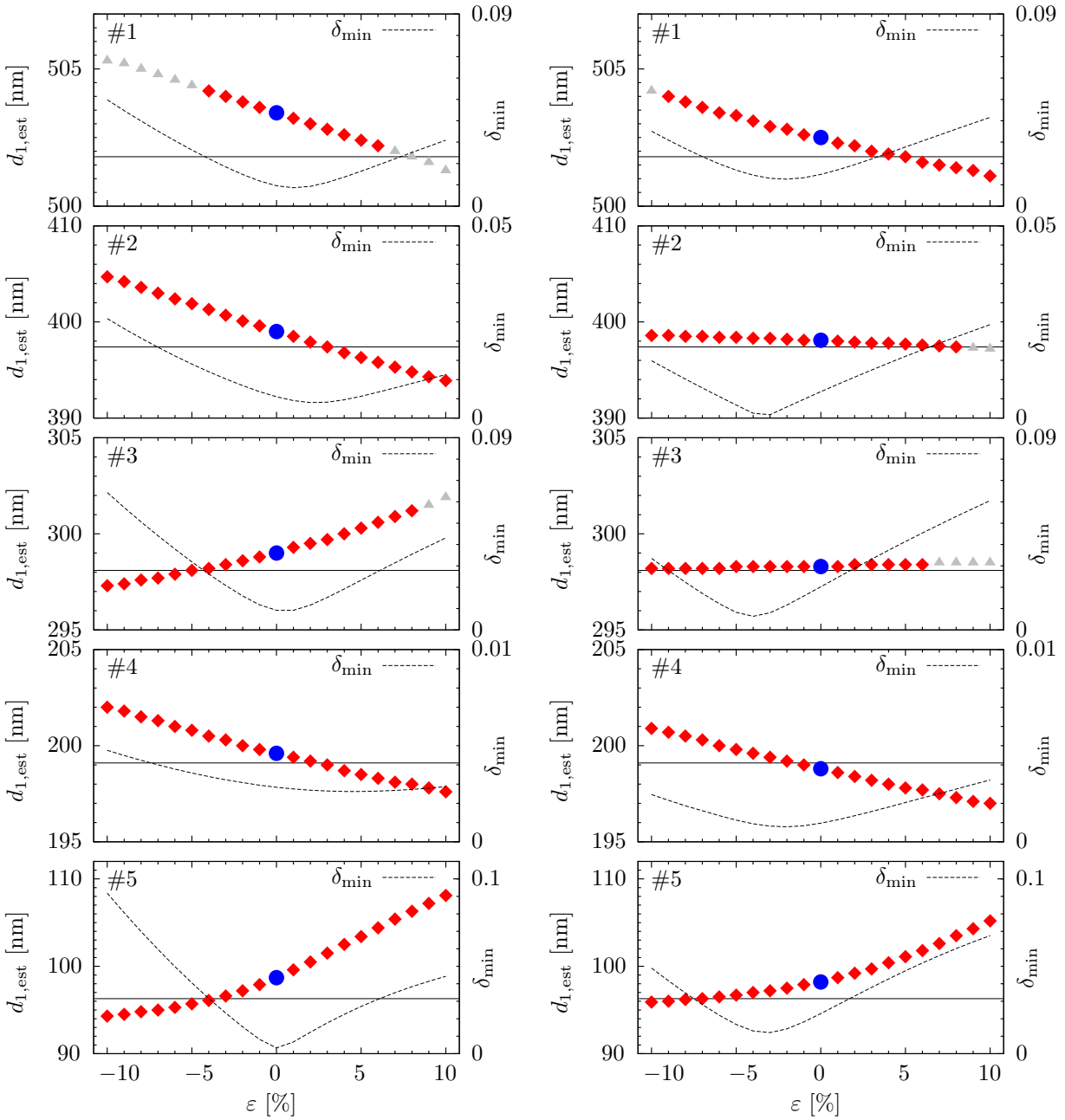

(a) Leica microscope, offset added to all measured $\mathcal{RGB}$ values.

(b) Epson flatbed scanner, offset added to all measured $\mathcal{RGB}$ values.

Figure B.6: Estimated thicknesses of all SiO_2 layers (apart from reference field #6) on Si wafer based on analyzed images of the two different hardware setups according to an offset added to all measured $\mathcal{RGB}$ values of $\varepsilon = \pm 10\%$. Blue circles depict thickness values for $\varepsilon = 0$ %. Grey triangles show results using $d_{1,r}^{\mathrm{narrow}}$ with simultaneous failure of the algorithm for $d_{1,r}^{\mathrm{wide}}$. The black horizontal lines show the manufacturer thickness values for the different fields. Residuals δ_{min} in contrast space are depicted as dashed curves.

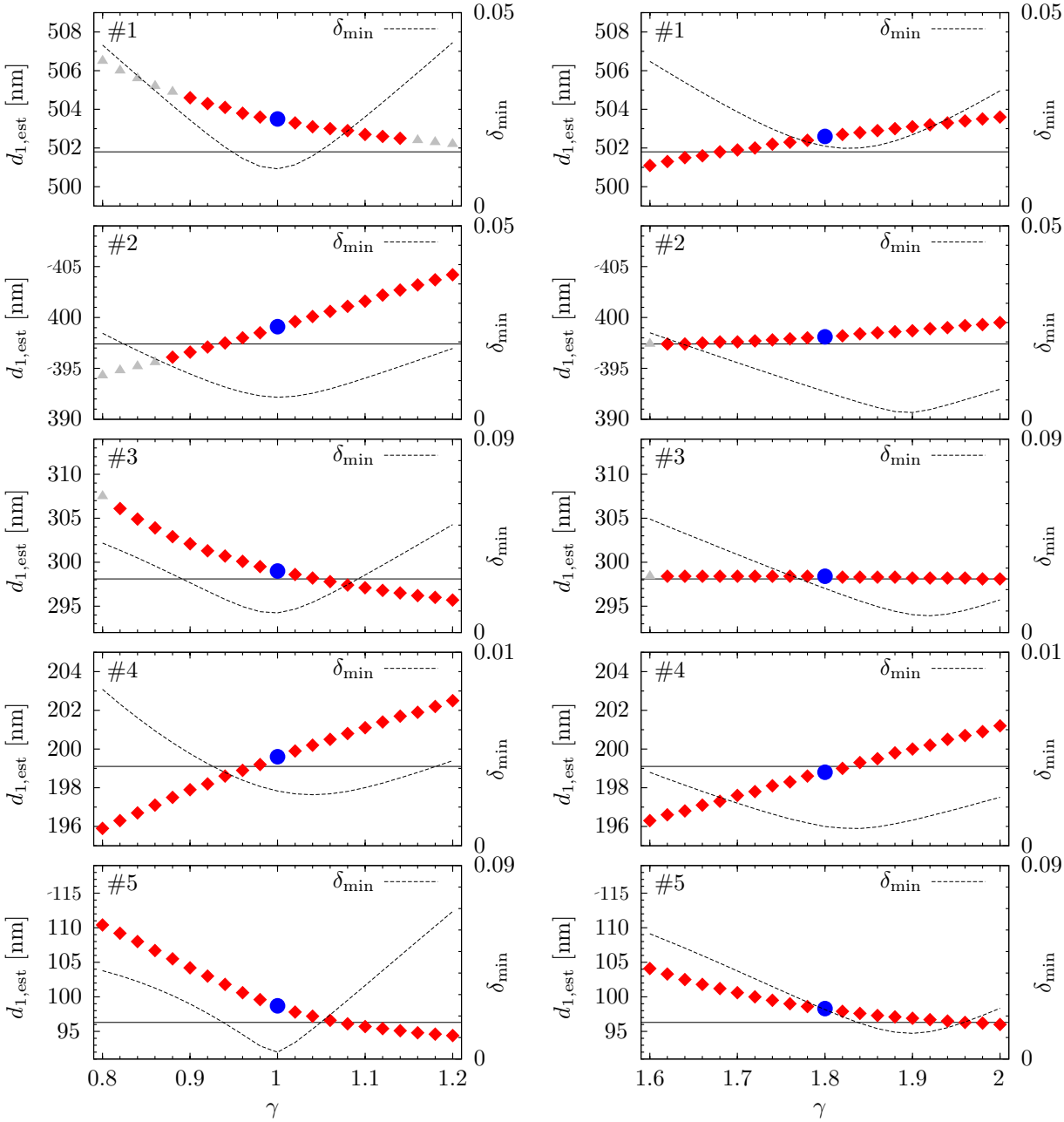

(a) Leica microscope, variation of $\gamma = 1.0 \pm 0.2$.

(b) Epson flatbed scanner, variation of $\gamma = 1.8 \pm 0.2$.

Figure B.7: Estimated thicknesses of all SiO_2 layers (apart from reference field #6) on Si wafer based on analyzed images of the two different hardware setups according to a variation of the γ image encoding/correction. $\mathcal{RGB}$ values of images required for spectral characterization of the hardware and the image of the sample were gamma corrected to the power of γ. Blue circles depict thickness values for $\gamma = 1.0$ and $\gamma = 1.8$, respectively. Grey triangles show results using $d_{1,r}^{\text{narrow}}$ with simultaneous failure of the algorithm for $d_{1,r}^{\text{wide}}$. The black horizontal lines show the manufacturer thickness values for the different fields. Residuals $\delta_{\min}$ in contrast space are depicted as dashed curves.

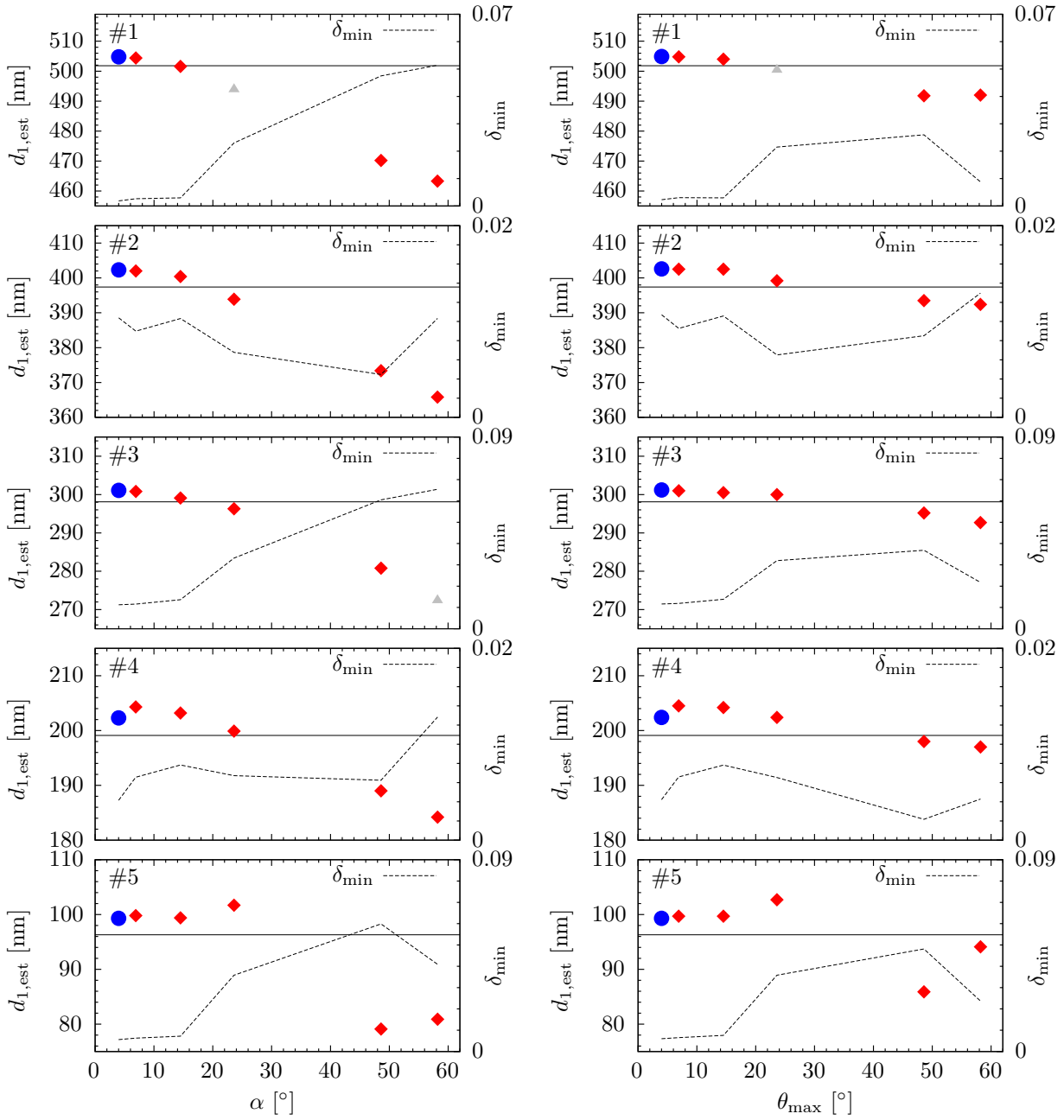

(a) Microscope: Different objective with α were used. Estimation algorithm assumed normal incidence and detection $\theta = 0\,^\circ$ (based on Equation 2.21).

(b) Microscope: Estimation algorithm assumed integration over the angle of incidence (circular aperture) from $0\,^\circ$ to $\theta_{\max} = \alpha$ (based on Equation 2.40).

Figure B.8: Estimated thicknesses of all SiO_2 layers (apart from reference field #6) on Si wafer based on analyzed microscope images with different objectives and numerical apertures (different physical opening angles 2α, blue circle for 2.5x objective, red squares others). Grey triangles show the result using $d_{1,r}^{\mathrm{narrow}}$ with simultaneous failure of the algorithm for $d_{1,r}^{\mathrm{wide}}$. The black horizontal lines show the manufacturer thickness values for the different fields. Residuals $\delta_{\min}$ in contrast space are depicted as dashed curves.

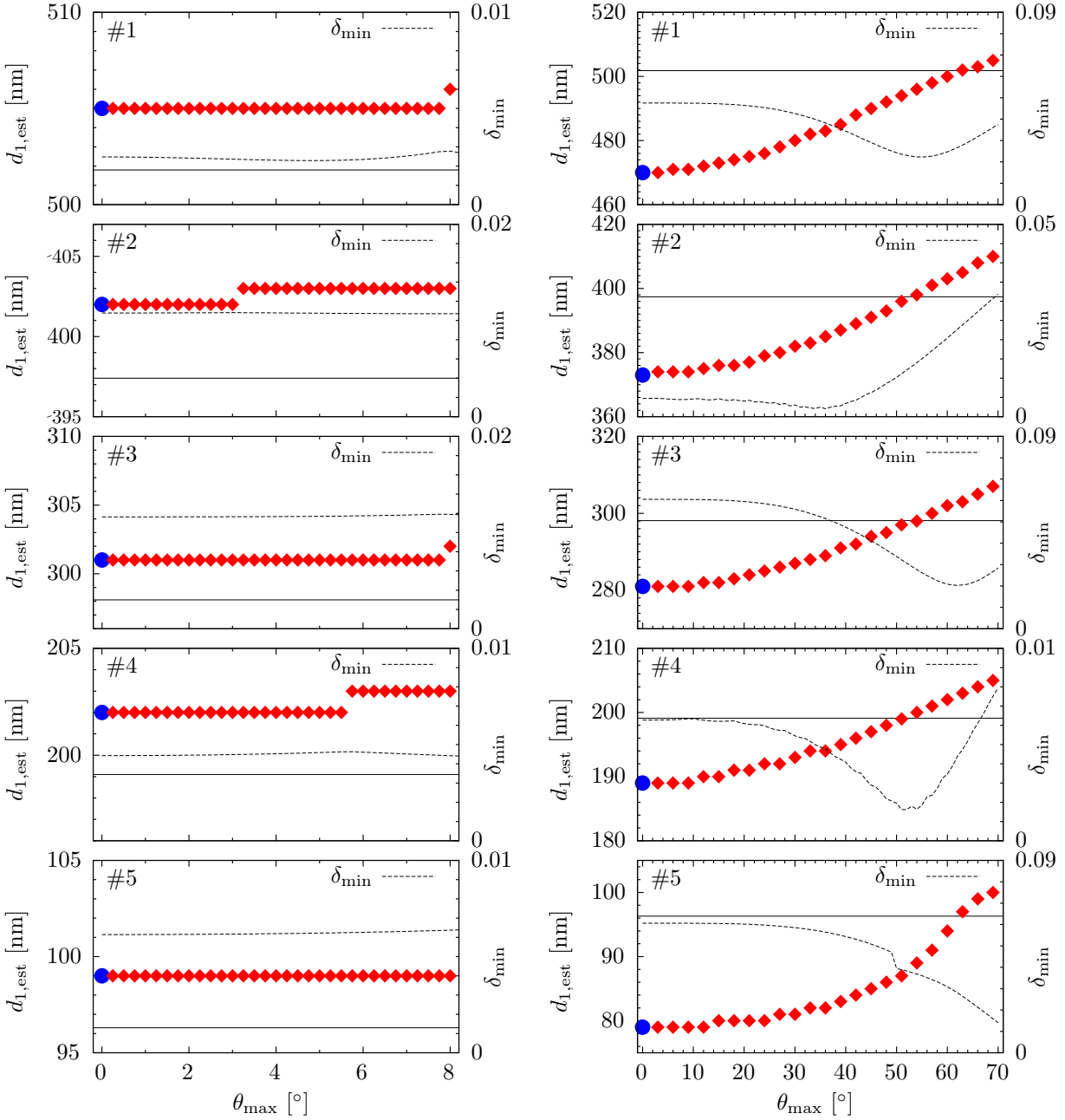

(a) Microscope: 2.5x objective with NA = 0.07 ($\alpha = 4.0\,°$) were used. Estimation algorithm integrated over angle of incidence θ.

(b) Microscope: 50x objective with NA = 0.75 ($\alpha = 48.6\,°$) were used. Estimation algorithm integrated over angle of incidence θ.

Figure B.9: Estimated thicknesses of all SiO_2 layers (apart from reference field #6) on Si wafer based on analyzed microscope images captured with 2.5x and 50x objectives. Estimation algorithm integrated over the incident angle θ from $0\,°$ to $\theta_{\max}$ (according to Equation 2.40). Grey triangles show the result using $d_{1,r}^{\mathrm{narrow}}$ with simultaneous failure of the algorithm for $d_{1,r}^{\mathrm{wide}}$. The black horizontal lines show the manufacturer thickness values for the different fields. Residuals $\delta_{\min}$ in contrast space are depicted as dashed curves.

B.2 MATLAB program to control the Minolta spectrophotometer CS1000A

Controlling of the Minolta spectrophotometer CS1000A is performed by running the following m-file[1].

writeSpec.m

```
function [ output_args ] = writeSpec( folder, name, IntegrationTime, plotOnOff )
%   writes a csv file in the folder with nm and intensity and if
%   needed plots the result for plotOnOff=1
%   e.g. writeSpec( 'LeitzLampFilt', 'specCS1000A_INT_0.3_Filt_300nm.dat',
%   0.3, 1 );

lambdaVec= (380:1:780);
[spec err] = MeasureCS1000A(IntegrationTime);
result = [lambdaVec' spec'];
csvwrite([folder '/' name],result);

if plotOnOff ≥ 1
    plot(result(:,1),result(:,2));
end

end
```

The second code is the core program to communicate over a RS232 computer interface with the CS1000 and acquire the spectrum.

The following MATLAB program[2] was provided by Philipp Urban and Ingmar Lissner from the color group of the Institute of Printing Science and Technology of the Technische Universität Darmstadt.

MeasureCS1000A.m

```
% SPEC                  The measured spectrum
% error                 error=0 -> no error, error=1 -> measurement error
%
% IntegrationTime       Time the CS1000A is supposed to measure. If = 0,
%                       the integration time is automatically determined by
%                       the device
function [SPEC error] = MeasureCS1000A(IntegrationTime)

error = 0;  % 0 = no error during measurement, 1 = some error occured

% Initialize serial port
s = serial('COM17');%('COM2');
fopen(s);
s.BaudRate = 9600;
s.RequestToSend = 'off';
s.DataTerminalReady = 'off';
s.RequestToSend = 'on';
fprintf(s, 'RMT,1');
```

[1] replace "≥" with ">="

[2] replace "¬" with "∼"

```
% Wait for device response
while ¬s.BytesAvailable
    disp([TimeStamp() '  Waiting for device response...']);
    pause(1);
end
Response = fread(s, s.BytesAvailable);
ResponseS = char(Response');
if (¬strcmp(ResponseS(1:2),'OK'))
    % Device error
    SPEC = 0; error = 1;
    disp([TimeStamp() '  ' strcat('Cannot enter remote mode. Error Code: ', ...
        ResponseS)]);
    pause(2);
    fprintf(s,'RMT,0');
    fclose(s);  % Close the COM port
    return;
end

if (IntegrationTime)
    % Device answered. Set the integration time.
    fprintf(s, ['MMS,3,' num2str(IntegrationTime)]); % Set the integration time
    while ¬s.BytesAvailable
        pause(1);
    end
    Response = fread(s, s.BytesAvailable);
    ResponseS = char(Response');
    if (¬strcmp(ResponseS(1:2),'OK'))
        % Device error
        SPEC = 0; error = 1;
        disp([TimeStamp() '  ' strcat('Measurement problem (when setting custom ...
            integration time). Error Code: ', ResponseS)]);
        pause(2);
        fprintf(s,'RMT,0');
        fclose(s);  % Close the COM port
        return;
    end
    % Start measurement.
    fprintf(s, 'MES,1'); % Trigger measurement
    while ¬s.BytesAvailable
        pause(1);
    end
    Response = fread(s, s.BytesAvailable);
    ResponseS = char(Response');
    if (¬strcmp(ResponseS(1:2),'OK'))
        % Device error
        SPEC = 0; error = 1;
        disp([TimeStamp() '  ' strcat('Measurement problem (when starting ...
            measurement). Error Code: ', ResponseS)]);
        pause(2);
        fprintf(s,'RMT,0');
        fclose(s);  % Close the COM port
        return;
    end
else
    % Device answered.
    fprintf(s, 'MMS,0'); % Set the integration time to auto
```

```
    while ¬s.BytesAvailable
        pause(1);
    end
    Response = fread(s, s.BytesAvailable);
    ResponseS = char(Response');
    if (¬strcmp(ResponseS(1:2),'OK'))
        % Device error
        SPEC = 0; error = 1;
        disp([TimeStamp() '  ' strcat('Measurement problem (when setting automatic ...
            integration time). Error Code: ', ResponseS)]);
        pause(2);
        fprintf(s,'RMT,0');
        fclose(s);  % Close the COM port
        return;
    end
    % Start measurement (read the integration time).
    fprintf(s, 'MES,1'); % Trigger measurement
    while ¬s.BytesAvailable
        pause(1);
    end
    Response = fread(s, s.BytesAvailable);
    ResponseS = char(Response');
    if (¬strcmp(ResponseS(1:2),'OK'))
        % Device error
        SPEC = 0; error = 1;
        disp([TimeStamp() '  ' strcat('Measurement problem (when starting ...
            measurement). Error Code: ', ResponseS)]);
        pause(2);
        fprintf(s,'RMT,0');
        fclose(s);  % Close the COM port
        return;
    end
    IntegrationTime = str2double(ResponseS(4:4+6));
end
while ¬s.BytesAvailable
    pause(1);
end
Response = fread(s, s.BytesAvailable);
ResponseS = char(Response');
if (¬strcmp(ResponseS(1:2),'OK'))
    % Device error
    SPEC = 0; error = 1;
    disp([TimeStamp() '  ' strcat('Measurement problem (when requesting device ...
        response). Error Code: ', ResponseS)]);
    pause(2);
    fprintf(s,'RMT,0');
    fclose(s);  % Close the COM port
    return;
end

% Device answered. Start measurement (read the BDR).
fprintf(s,'BDR,0,0,1');
while ¬s.BytesAvailable
    pause(1);
end
Response = fread(s, s.BytesAvailable);
```

```
ResponseS = char(Response');
if (¬strcmp(ResponseS(1:2),'OK'))
    % Device error
    SPEC = 0; error = 1;
    disp([TimeStamp() '  ' strcat('Problem in reading measurement data. Error Code: ...
        ', ResponseS)]);
    pause(2);
    fprintf(s,'RMT,0');
    fclose(s);  % Close the COM port
    return;
end
BDR.MeasurementMode = ResponseS(4);
BDR.IntegrationTime = ResponseS(6:6+5);
BDR.LensType = ResponseS(13);
BDR.UnderFlag = ResponseS(15);
BDR.data = [];
%fprintf(s,'&');
for I = 1:7
    fprintf(s,'&');
    while ¬s.BytesAvailable
        pause(0.5);
    end
    BDR.data = [BDR.data;fread(s, s.BytesAvailable/4,'float32')];
end
pause(2);
fprintf(s,'RMT,0');
fclose(s);
SPEC = BDR.data';


% Generate timestamp
function TS = TimeStamp()
datetime = clock;
datetimestr = [num2str(datetime(1)) '/' ...
               num2str(datetime(2), '%.2d') '/' ...
               num2str(datetime(3), '%.2d') ' ' ...
               num2str(datetime(4), '%.2d') ':' ...
               num2str(datetime(5), '%.2d') ':' ...
               num2str(round(datetime(6)), '%.2d')];
TS = ['[' datetimestr ']'];
```

B.3 MATLAB program for ICR thickness determination

The MATLAB (Version R2012a) program presented here consists of 14 m-files. With these codes a thickness map based on a reference image and a sample image is computed. For successful computation, different data files are required which are not listedin this section. These include the refractive indices of the materials, the spectrum of the light source, the $\mathcal{RGB}$ filter functions, the input reference image and the image of the sample. The main script is `run_theoSpectrum.m`, this should be started to evaluate the thickness data. The underlying folder and file structure is the following:

`run_theoSpectrum.m`

`LSmethodOnPic.m`

`addPath_mFunctions.m`

/DeviceFilter/Leica_Filter.dat

/Materials/Si(100).dat

/Materials/SiO2_(therm).dat

/m-functions/abelesL.m

/m-functions/contrastVal.m

/m-functions/convertIK.m

/m-functions/extractSpectrumMinMax.m

/m-functions/gammacorrection.m

/m-functions/intensity.m

/m-functions/matProd2x2xn.m

/m-functions/path_difference.m

/m-functions/reflectionL.m

/m-functions/TotalReflectionL.m

/m-functions/transmissionL.m

/Pictures/Leica_2.5x_Wafer_20x18=360pics_800x630.tif

/Pictures(Leica_2.5x_Wafer_20x18=360pics_ref_outfoc_800x630.tif

/Spectra/CS1000A_LeicaBF.dat

I included the main m-file[3] first followed by the remaining 13 ones in the same order they are listed above.

run_theoSpectrum.m

```
function [] = theoSpectrumFilt(extName)


% To run the alogorithm in MATLAB just press F5 using this script


tic
%Geeneral definitions————————————————————————————
    addPath_mFunctions;
    n_ini = 1.0029; %refractive index of surrounding medium, here air

%Directories of and for files:
    directoryOfSpectra    = 'Spectra/';
    directoryOfDevFilters = 'DeviceFilters/';
    directoryOfMaterials  = 'Materials/';
    pictureFolder         = 'Pictures\';
%Wavelengths: lower and upper wavelength limit for all calculations
    lambda_1 = 380e-9; %lower limit in m
    lambda_2 = 780e-9 ; %upper limit in m

    lambda = lambda_1:1*10^(-9):lambda_2; %list of wavelength in m
    △_lambda = length(lambda); %number of wavelengths used
```

[3] replace "△" with "delta"

```
%load refractive indices of all materials within limits defined by
%lambda_[1,2] and convert to n+i*k:----------------------
% form of the csv-files: columns 401x3: [wavelength in [nm], n, k] and in the
% rows the wavelength is running in steps of 1 nm
    Si100 = convertIK(extractSpectrumMinMax(csvread([directoryOfMaterials ...
        'Si(100).dat'])));
    SiO2 = convertIK(extractSpectrumMinMax(csvread([directoryOfMaterials ...
        'SiO2_(therm).dat'])));
    %  ...
%-------------------------------------------------------------------------

%Specific definitions for names and files-----------------------------------
    %Defintions for files to search and to write:
        %Device: Leica microscope
            deviceName = 'Leica';

        %Loading device filter:
            %NOTE: If the filter curves were determined using images of
            % narrow band filters, a requirement would be that any gamma
            % encoding of the images had been corrected, on total gamma = 1.
            % form of the csv-files 401x3: columns: [R_filt_value, G_filt_value,
            %B_filt_value] and  the rows count the wavelength from 380 to
            %780 nm. NOTE: There is no entry for the wavelength in the
            %file!
            deviceFilter = (csvread([directoryOfDevFilters deviceName ...
                '_Filter.dat'])');

        %Illumination
            %Load illumination spectrum
            % form of the csv-files 401x2: columns: [wavelength in [nm], intensity]

            deviceLight = extractSpectrumMinMax(csvread([directoryOfSpectra ...
                'CS1000A_LeicaBF.dat']));

    %Number of layers in the system, without substrate
        NrOfL = 1;
    %Choose the layer setup, up to 5 layers are implemented yet, all must be defined:
        n5 = SiO2;
        n4 = SiO2;
        n3 = SiO2;
        n2 = SiO2;
        n1 = Si100;
    %Choose susbtrate:
        n_ex = Si100;
        extName = [deviceName 'Si100'];

    %Unknown layer: Here, the unknown one is always layer number 5, the top.
        %Specify the thickness range within the algorithm search for the
        %match in [m]
            d5_min = 0e-9;
            d5_max = 600e-9;
        %Specify the thickness of the reference thickness (picture or values)
            d5_ref = 0e-9;
        %Specify the thickness step resolution
            d_nmStep = 1e-9;
```

```
    %Thicknesses of other known layers. If layers are not used, the thickness must ...
        be set to "0".
        d(4) = 0e-9;
        d(3) = 0e-6;
        d(2) = 0;
        d(1) = 0;
    %Thickness of the substrate
        d_ex = 700e-6;

    %Here, you choose whether the algorithm takes backside reflections into
    %account:
    % with set (1) or off (0), without the calculations are faster
        backSideOn = 0;


%-------------------------------------------------------------------------

%Controlling for other functions.-----------------------------------------

    %Definition for the function LSmethodOnPic(...)
    control_LSmethodOnPic = 1; %controls if the algorithm is executed on
    %the images with LSmethodOnPic(...) or if just the theoretical values
    %are computed and plotted
%-------------------------------------------------------------------------


%%-------Here starts the loop only for the theoretical values-------------
%#########################################################################%

%Definitions and initialization of variables------------------------------
%lambda = lambda_1:1*10^(-9):lambda_2; %the spectrum
%Δ_lambda = length(lambda); %number of wavelengths in the list
d5 = d5_min:d_nmStep:d5_max; %list of all possible thicknesses
Δ_d5 = length(d5);  %number of thicknesses in the list

I_RGB  = zeros(Δ_d5,3); %initialize theoretical image data
I_RGBr = zeros(Δ_d5,3); %initialize theoretical reference image data

spec = zeros(Δ_d5,Δ_lambda); %initialize theoretical expected total reflected ...
    spectrum per wavelength
specRef = zeros(Δ_d5,Δ_lambda); %initialize theoretical expected total reflected ...
    spectrum per wavelength of reference
%-------------------------------------------------------------------------

%Main loop to determine the theoretical values for reflected spectra.-------

%For the reference the spectrum is calculated just for one thickness:
%d5_ref:
    if backSideOn == 1
        specRefTR = TotalReflectionL(lambda',d(1),d(2),d(3),d(4),d5_ref, ...
            n1,n2,n3,n4,n5,n_ini,n_ex,d_ex,NrOfL) .* deviceLight(:,2);
    else
        specRefR = reflectionL(lambda',d(1),d(2),d(3),d(4),d5_ref,n1,n2, ...
            n3,n4,n5,n_ini,n_ex) .* deviceLight(:,2);
    end
```

```
%The spectrum for varying thickness (layer 5) is computed by performing a
%loop from q to △_d5:
    for id1 = 1:△_d5
        %In TotalRef... the backside reflections are included
        if backSideOn == 1
            spec(id1,:) = TotalReflectionL(lambda',d(1),d(2),d(3),d(4), ...
                d5_min + (id1-1) * d_nmStep,n1,n2,n3,n4,n5,n_ini,n_ex,d_ex,NrOfL) ...
                    .*deviceLight(:,2);
            specRef(id1,:) = specRefTR;
        else
            spec(id1,:) = reflectionL(lambda',d(1),d(2),d(3),d(4),d5_min + ...
                (id1-1) * d_nmStep,n1,n2,n3,n4,n5,n_ini,n_ex) .* deviceLight(:,2);
            specRef(id1,:) = specRefR;
        end

        for i2 = 1:3
            %Here, intensity values are computed from the spectra
            I_RGB(id1,i2) = intensity(spec(id1,:),deviceFilter(i2,:));
            I_RGBr(id1,i2) = intensity(specRef(id1,:),deviceFilter(i2,:));
        end
    end

%Finally, contrast values from the intensities are determined:
    I_RGBc = contrastVal(I_RGB,I_RGBr);

%%------End of loop for the theoretical values----------------
%##########################################################################%

%Output and plotting of theoretical values-------------------------------

%Plot RGB contrast values in 3D:
    figure(1)
    clf reset
    plot3(I_RGBc(:,1),I_RGBc(:,2),I_RGBc(:,3),'o','MarkerSize',3);
    xlabel('c_R');
    ylabel('c_G');
    zlabel('c_B');
    title('RGB contrast values for thickness in 3D');
    grid on

%Plot RGB intensity values for thickness in 2D:
    figure(2)
    clf reset
    hold on
    xlabel('Thickness d_{q} in [nm]');
    ylabel('Intensity');
    title('RGB vs. thickness');
    plot(d5,I_RGB(:,1),'Color','red');
    plot(d5,I_RGB(:,2),'Color','green');
    plot(d5,I_RGB(:,3),'Color','blue');
    title('RGB intensity values for thickness in 2D');
    hold off

%Plot RGB intensity values for thickness in 2D:
    figure(3)
    clf reset
```

```
    hold on
    xlabel('Thickness d_{q} in [nm]');
    ylabel('Contrast values [-1 1]');
    title('RGB contrast vs. thickness');
    plot(d5,I_RGBc(:,1),'Color','red');
    plot(d5,I_RGBc(:,2),'Color','green');
    plot(d5,I_RGBc(:,3),'Color','blue');
    title('RGB contrast values for thickness in 2D');
    hold off

%Plot of distance relations
%Determine the Euclidian distance dd of the nanometer steps in thickness in
% the contrast 3D space:
    I_RGBc_1rowShift = circshift(I_RGBc,1);
    X = I_RGBc-I_RGBc_1rowShift;
    dd = sqrt(sum((X.^2)')')./(d_nmStep*1e9);
    dd(1) = mean(dd); %First entry is the mean

    %for plotting with Gnuplot I need the lambdas in first column
        I_RGB_lambda = zeros(length(d5),4);
        I_RBG_lambda(:,1)=d5';
        I_RBG_lambda(:,2:4)=I_RGBc;
        csvwrite([pictureFolder extName '_d5_list.csv'],I_RBG_lambda);
        csvwrite([pictureFolder extName '_dd5_list.csv'],dd);
%-------------------------------------------------------------------------
% Running of other function on pictures or on reference wafer values------
    if control_LSmethodOnPic == 1
        LSmethodOnPic(extName, pictureFolder, d5, I_RGBc)
    end
%-------------------------------------------------------------------------

rmpath([pwd '\m-functions']);
toc
```

LSmethodOnPic.m

```
function [] = LSmethodOnPic(extName, pictureFolder, d5, I_RGBc)
tic

% Define image and reference image names
        gamma = 1.0; %This gamma corrects for the following images, BUT does not
        % correct for possible images of the RGB filter determination of
        % the sensor
        %
        pictureName = 'Leica_2.5x_Wafer_20x18=360pics_800x630.tif';
        %The reference image of the Leica was acquired by focusing the
        %bare silicon and stitched the same number of images as for the "real" image
        % pixel resolution of both images MUST be the same,
        % format of images, preferable TIF
        refPictureName = 'Leica_2.5x_Wafer_20x18=360pics_ref_outfoc_800x630.tif';

%Get definitions for this run from running theoSpectrumFilt.m

%Load, gamma correct and resize images if necessary
    controlResize = 0;
```

```
    pixelX =800;
    if controlResize == 1
        RGBs = imresize(double(gammacorrection(imread([pictureFolder ...
            pictureName]),gamma)), [pixelX NaN],'bilinear');
        RGBsRef = imresize(double(gammacorrection(imread([pictureFolder ...
            refPictureName]),gamma)), [pixelX NaN],'bilinear');
    else
    RGBs = double(gammacorrection(imread([pictureFolder pictureName]),gamma));
    RGBsRef = double(gammacorrection(imread([pictureFolder refPictureName]),gamma));
    end

minD1 = min(d5)/10^(-9); % minimum of the thickness d5 in [nm]

% Determined contrast values using image and reference image
IM_RGBc = contrastVal(RGBs,RGBsRef);

%Main loop: LS search algorithm with MATLABs dsearchn():----------------------
%########################################################################%

%k = dsearchn(X,XI) returns the indices k of the closest points in X for
%each point in XI. X is an m-by-n matrix representing m points in
%n-dimensional space. XI is a p-by-n matrix, representing p points in n-dimensional ...
    space.
%With large X and small XI, this approach is faster and uses much less memory.
%The output k is a column vector of length p:
%XI created from the IM_RGBc:
    [m, n, o] = size(IM_RGBc);
    XI = reshape(IM_RGBc,m*n,o);
    tri = delaunayn(I_RGBc);
    [dsearchTemp, c_dist_mins] = dsearchn(I_RGBc,tri,XI);

    k = (dsearchTemp+ minD1 - 1).*(d5(2)-d5(1))*1e+9;
    dDet = reshape(k,m,n);  % final thickness map
    c_dist_min_map = reshape(c_dist_mins,m,n);  % map of distances in contrast space
    mean_dist_c = mean(mean(c_dist_min_map)); % mean of distances in contrast space

%-------------------------------------------------------------------------------

%Plotting and writing of results in the picture folder-----------------------
%Plot thickness surface plot
    figure(5)
    clf reset
    hold on
    [X] = dDet;
    surf(X,'linestyle', 'none')
    xlabel('x [pixel]');
    ylabel('y [pixel]');
    zlabel('z [nm]');
    title('Thickness of top layer in 3D');
    grid on
    hold off

%Plot 3D-plot again and the contrast values of all pixels additionally
    figure(6)
    clf reset
    hold on
```

```
    plot3(IM_RGBc(:,:,1),IM_RGBc(:,:,2),IM_RGBc(:,:,3),'.','MarkerSize',0.5);
    plot3(I_RGBc(:,1),I_RGBc(:,2),I_RGBc(:,3),'-rs','MarkerSize',3,'LineWidth',2);
    xlabel('c_R');
    ylabel('c_G');
    zlabel('c_B');
    title('RGB contrast values with data contrast point of image in 3D');
    hold off

%Write the results in the same folder of the pictures
    csvwrite([pictureFolder pictureName  extName '_mean_dist_c.csv'],mean_dist_c);
    csvwrite([pictureFolder pictureName  extName '_thickness.csv'],dDet);
    csvwrite([pictureFolder pictureName  extName ...
        '_c_dist_min_map.csv'],c_dist_min_map);

toc
```

addPath_Functions.m

```
function [ output_args ] = addPath_mFunctions()
%adds the specified path of other m-functions
mFunctionsFolder = 'm-functions';
mFilePath = [pwd '\' mFunctionsFolder];
path(path,mFilePath);
```

/m-functions/abelesL.m

```
function M = abelesL(lambda,d1,d2,d3,d4,d5,n1,n2,n3,n4,n5)
% abeles-matrix for a single layer
pd_1 = path_difference(lambda,d1,n1).';
pd_2 = path_difference(lambda,d2,n2).';
pd_3 = path_difference(lambda,d3,n3).';
pd_4 = path_difference(lambda,d4,n4).';
pd_5 = path_difference(lambda,d5,n5).';

%initialize M_...
M_1 = zeros(2,2,length(lambda));
M_2 = zeros(2,2,length(lambda));
M_3 = zeros(2,2,length(lambda));
M_4 = zeros(2,2,length(lambda));
M_5 = zeros(2,2,length(lambda));

n1 = n1.';
n2 = n2.';
n3 = n3.';
n4 = n4.';
n5 = n5.';

%determine first column entries of Abeles matrices

M_1(1:2,1,:) = [cos(pd_1);1i.*n1.*sin(pd_1)];
M_1(1:2,2,:) = [(1i./n1).*sin(pd_1);cos(pd_1)];

M_2(1:2,1,:) = [cos(pd_2);1i.*n2.*sin(pd_2)];
```

```
M_2(1:2,2,:) = [(1i./n2).*sin(pd_2);cos(pd_2)];

M_3(1:2,1,:) = [cos(pd_3);1i.*n3.*sin(pd_3)];
M_3(1:2,2,:) = [(1i./n3).*sin(pd_3);cos(pd_3)];

M_4(1:2,1,:) = [cos(pd_4);1i.*n4.*sin(pd_4)];
M_4(1:2,2,:) = [(1i./n4).*sin(pd_4);cos(pd_4)];

M_5(1:2,1,:) = [cos(pd_5);1i.*n5.*sin(pd_5)];
M_5(1:2,2,:) = [(1i./n5).*sin(pd_5);cos(pd_5)];

M = matProd2x2xn(M_5,matProd2x2xn(M_4,matProd2x2xn(M_3,matProd2x2xn(M_2,M_1))));
```

/m-functions/contrastVal.m

```
function [ contrast ] = contrastVal( vec, vecRef )
%calculate the contrast of values (vector) with a reference values
contrast = (vec-vecRef)./(vec+vecRef);
```

/m-functions/convertIK.m

```
function [ listOut ] = convertIK( listAll )
%convert the data from materials with wavelength, n, k to n+i*k

listOut = listAll(:,2) - listAll(:,3)*sqrt(-1);
```

/m-functions/extractSpectrumMinMax.m

```
function [ listMinMax ] = extractSpectrumMinMax( listAll )
%extract a spectrum with nx1 list with the values from minV to maxV
minV = 380;
maxV = 780;
i=1;
for i2 = 1:length(listAll(:,1))
    if ((listAll(i2,1) ≥ minV) & (listAll(i2,1) ≤ maxV))
            listMinMax(i,:) = listAll(i2,:);
            i = i+1;
    end
end
```

/m-functions/gammacorrection.m

```
function Correction = gammacorrection(Image,GammaValue)

Correction = imadjust(Image,[],[],GammaValue);
```

/m-functions/intensity.m

```
function I = intensity(reflectance,filter)
```

```
I=dot(reflectance,filter);
```

/m-functions/matProd2x2xn.m

```
function M2M1 = matProd2x2xn(M2,M1)
%MATPROD2X2XN 2x2 matrix multiplication for the first 2 dimensions
%initialize
M2M1 = zeros(size(M1));

%2x2 matrix multiplication
for i = 1:2
    for j = 1:2
        M2M1(i,j,:) = M2(i,1,:).*M1(1,j,:) + M2(i,2,:).*M1(2,j,:);
    end
end
```

/m-functions/path_difference.m

```
function d = path_difference(lambda,d,n)
% function to evaluate the path difference for a given wavelength lambda, a
% thickness d and the index of refraction n(lambda)
d = 2*pi*d.*n./lambda;
```

/m-functions/reflectionL.m

```
function R_tf = reflectionL(lambda,d1,d2,d3,d4,d5,n1,n2,n3,n4,n5,n_ini,n_ex)
% returns the reflectance of up to 5 thin layers
M = abelesL(lambda,d1,d2,d3,d4,d5,n1,n2,n3,n4,n5);

%reflection of thin films
r_tf = (n_ini.*squeeze(M(1,1,:)) - n_ex.*squeeze(M(2,2,:)) + ...
    n_ini.*n_ex.*squeeze(M(1,2,:)) - squeeze(M(2,1,:))./(n_ini.*squeeze(M(1,1,:)) + ...
    n_ex.*squeeze(M(2,2,:)) + n_ini.*n_ex.*squeeze(M(1,2,:))+squeeze(M(2,1,:)));
R_tf = abs(r_tf).^2;
```

/m-functions/TotalReflectionL.m

```
function R_total = TotalReflectionL( ...
    lambda,d1,d2,d3,d4,d5,n1,n2,n3,n4,n5,n_ini,n_ex,d_ex,NrOfL)
%Returns the total reflection including backside reflection

NrOfLayers = NrOfL +1; %to allow zero layers
n = [n_ini,n5,n4,n3,n2,n1];

beta = -abs(imag(2*pi*d_ex.*n_ex./lambda));

R_F = reflectionL(lambda,d1,d2,d3,d4,d5,n1,n2,n3,n4,n5,n_ini,n_ex);
R_FR = reflectionL(lambda,d5,d4,d3,d2,d1,n5,n4,n3,n2,n1,n_ex,n_ini);
T_F = transmissionL(lambda,d1,d2,d3,d4,d5,n1,n2,n3,n4,n5,n_ini,n_ex);
T_FR = transmissionL(lambda,d5,d4,d3,d2,d1,n5,n4,n3,n2,n1,n_ex,n_ini);
```

```
R_B = reflectionL(lambda,0,0,0,0,0,n1,n2,n3,n4,n5,n_ex,n_ini);

R_total = R_F + T_F.*T_FR.*R_B.*exp(4.*beta)./(1-R_FR.*R_B.*exp(4.*beta));
```

/m-functions/transmissionL.m

```
function T_tf = transmissionL(lambda,d1,d2,d3,d4,d5,n1,n2,n3,n4,n5,n_ini,n_ex)
% returns the transmission of up to 5 thin layers
M = abelesL(lambda,d1,d2,d3,d4,d5,n1,n2,n3,n4,n5);

%transmission of thin films
t_tf = 2.*n_ini./(n_ini.*squeeze(M(1,1,:)) + n_ex.*squeeze(M(2,2,:)) + ...
    n_ini.*n_ex.*squeeze(M(1,2,:)) + squeeze(M(2,1,:)));
T_tf = real(n_ex)./real(n_ini).*abs(t_tf).^2;
```

Appendix C

Printing experiments

C.1 Preliminary printing experiments on an IGT G1 with organic semiconductor

Preliminary printing experiments[1] using the given ink formulation with a concentration of $c_{\mathrm{spiro}} = 2, \ldots, 4$ wt.-% spiro-MeOTAD dissolved in toluene on ITO coated glass were performed on a test print device G1 from IGT, Netherlands, depicted in Figure C.1. The tool processes substrate widths

Figure C.1: IGT G1 test print device for gravure printing used for preliminary studies.

of 5 cm. In order to print on rigid glass substrates without breakage, the tool was modified to ensure exact planar guidance of the substrate carrier guidance through the gap between gravure cylinder and impression roller. Before printing, ink is applied with a pipette in front of doctor blade. Without extra cylinder rotation, the ink is directly scraped by the doctor blade and then transferred to the substrate. Figure C.2 illustrates a sketch of the operation principle. The printing velocity was $v = 1$ m/s and a standard mechanically engraved gravure cylinder from IGT (art.no: 402.153) was used. This cylinder possessed 10 different engraved fields of 33.5×15 mm^2, each with a screen ruling of SR = 70 L/cm, a screen angle of $\alpha_{\mathrm{SR}} = 53\,^\circ$ and engraved with a stylus angle of $\alpha_{\mathrm{St}} = 140\,^\circ$. Cell depths ranged from 11, 14, 17, 20, 24, 26, 29, 30, 31 and 33 µm. Using the measurement technique presented in [26], I determined the cell volumes of the 10 fields to (0.25 ± 0.01), (0.84 ± 0.02), (1.50 ± 0.03), (2.40 ± 0.05), (3.65 ± 0.02), (4.56 ± 0.06), (5.91 ± 0.06), (6.86 ± 0.03), (7.60 ± 0.01) and (8.52 ± 0.05) ml/m^2.

I compared the measurements of the cell depths d_{c} with the manufacturer values as shown in Figure C.3 [26]. The dashed line represents the angle bisector for equal values. According to Figure C.3,

[1] which is partly published in [27]

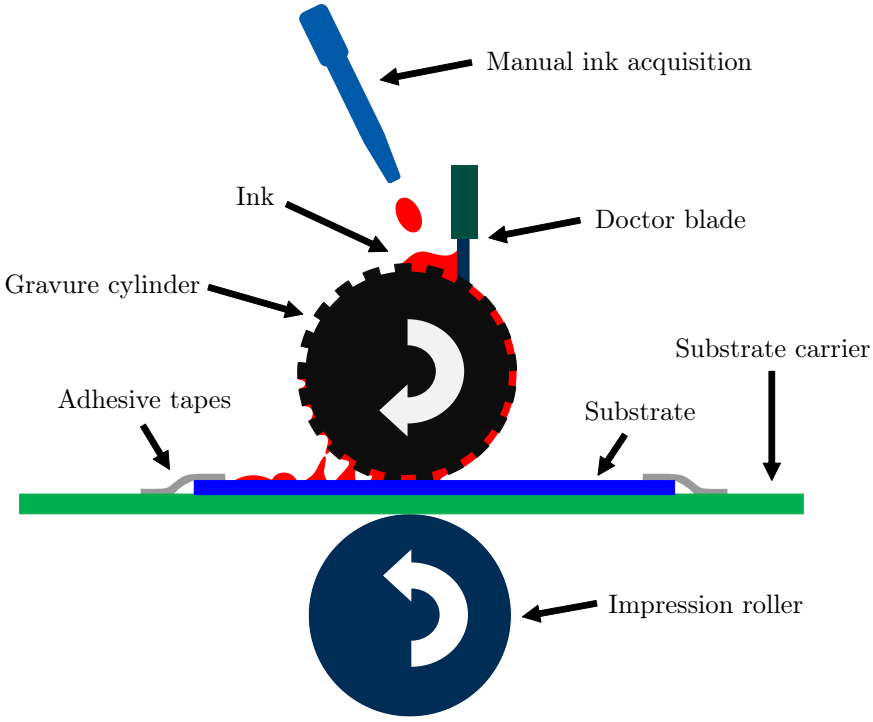

Figure C.2: Sketch of the operation principle of the test print device IGT G1.

the agreement between measured and given cell depth is very good contrary to the measured values of the cylinder manufactured by Krandick for the Prüfbau machine in Figure 4.5 on page 93.

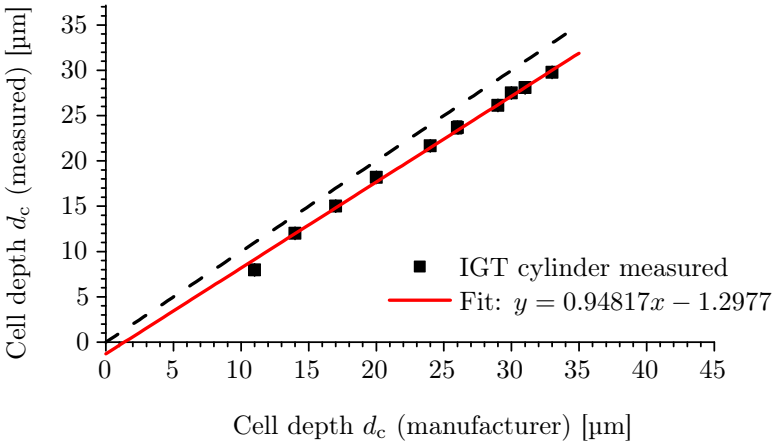

Figure C.3: Measured cell depths compared to given values from the manufacturer IGT of a standard gravure cylinder (art.no 402.153), reprinted with permission from [26]. The dashed line represents the angle bisector for perfect agreement.

The printing results were very reproducible, Figure C.4a shows a combined microscope image of the relevant (for the discussion in Chapter 4) first three fields of a representative printed sample. The grids visible in C.4 result from the stitching procedure of the single microscope images. The fields are denoted according to their nominal cell depth in micrometer F11, F14 and F17. Figure C.4b illustrates a color-coded thickness map based on the microscope image and determined with the ICR method presented in Chapter 2. The field F11 of Figure C.4 are barely visible and measurable. This is because the layer consist of single transferred and dried ink drops from separated gravure

cells, as measured with phase-shifting interferometry and depicted in Figure 4.26 on page 120. The

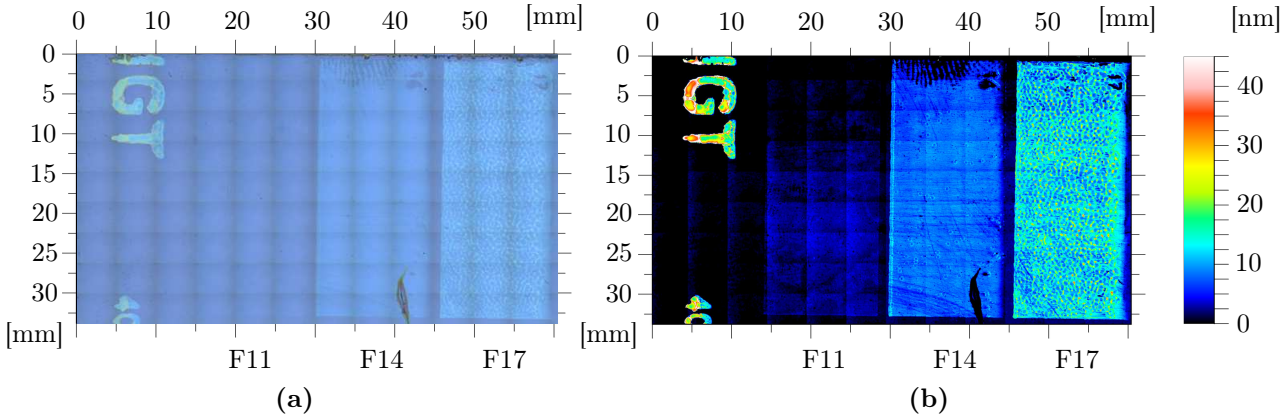

Figure C.4: Combined microscope image of a representative printing result (spiro-MeOTAD on ITO coated glass) on the IGT G1 test device for gravure printing in (a). Color-coded thickness map determined with ICR in (b). Field are labeled according to their nominal cell depth F11, F14, F17. Printing direction was from right to left.

corresponding surface parameters of mean dry film thickness $\overline{h}$, relative RMS roughness S_{qr}, skewness S_{sk}, kurtosis S_{ku} and isotropic dominant wavelength λ_{iso} were determined according to Section 4.3 and are summarized in Table C.1.

Table C.1: Determined surface parameters including the cell volume of the three fields F11, F14, F17 of the thickness data shown in Figure C.4b. Cell volume V_{c}, mean dry film thickness $\overline{h}$, relative RMS roughness S_{qr}, skewness S_{sk}, kurtosis S_{ku} and isotropic dominant wavelength λ_{iso}.

Field	V_{c} [ml/m^2]	$\overline{h}$ [nm]	S_{qr}	S_{sk}	S_{ku}	λ_{iso} [mm]
F11	0.25 ± 0.01	5.7	0.30	0.85	6.42	0.143
F14	0.84 ± 0.02	12.0	0.10	0.07	3.07	0.73
F17	1.50 ± 0.03	14.8	0.23	0.23	2.56	1.17

From the results of these preliminary printing experiments, I defined the parameters of the gravure cylinder for the experiments on the Prüfbau machine discussed in Chapter 4 on pages 85 ff..

C.2 Printing experiments with Prüfbau printing unit, additional figures

C.2.1 Relative RMS roughness S_{qr} vs. cell volume V_c

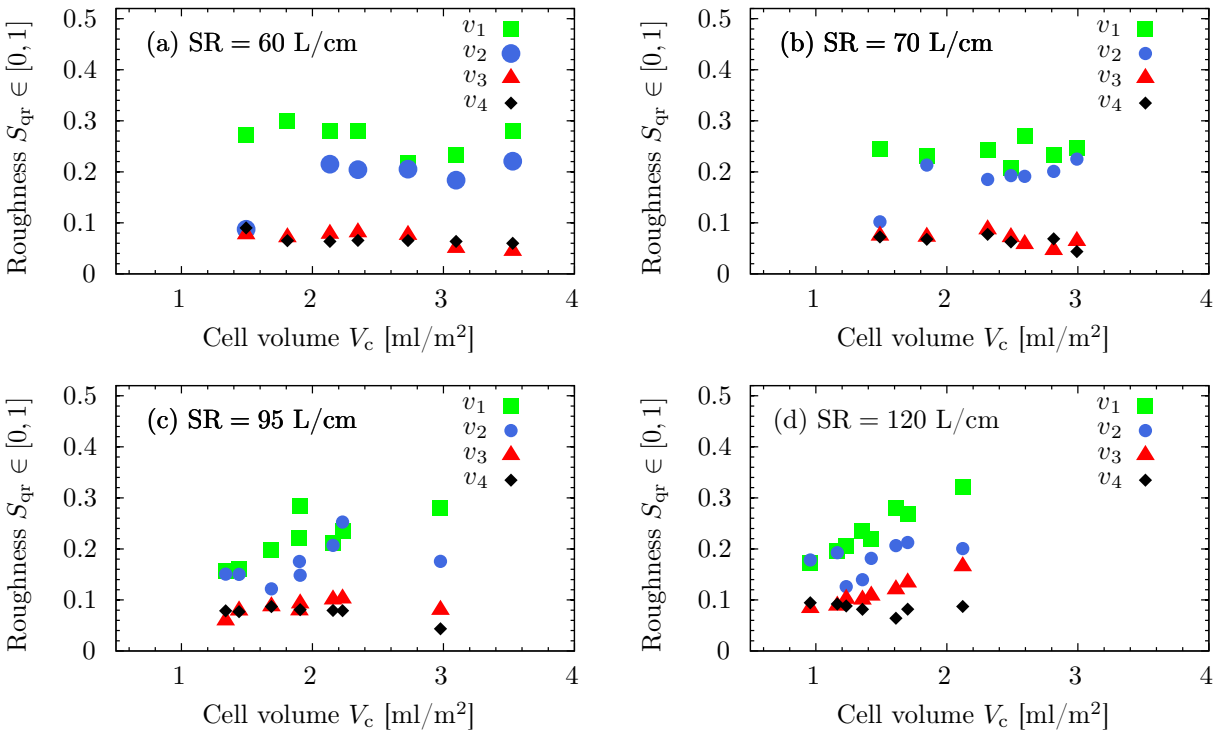

Figure C.5: Relative RMS roughness S_{qr} vs. cell volume V_c of the fields for different screen rulings SR and velocities v_i ($v_1 = 0.62$ m/s, $v_2 = 1.25$ m/s, $v_3 = 2.5$ m/s, $v_4 = 5.0$ m/s). Supplementally to Figure 4.23 on page 118.

C.3 MATLAB codes

C.3.1 4-dimensional curve fitting

nlinfit4D.m

```
function [ output_args ] = nlinfit4D( input_args )
% performs a non-linear fitting of 4-dimensional data

data1 = csvread('data_v_all_h_matlab.csv');   % read file
[n,m] = size(data1);
X = zeros(n,4);
X(:,1) = data1(:,11);  % corresponding cell volumes
X(:,2) = data1(:,8);   % corresponding screen ruling
X(:,3) = data1(:,6);   % corresponding printing velocity
y = data1(:,13);       % resulting mean dry film thickness

% define function with b() as fit paramters
```

```
func = @(b,x)( b(1).*(x(:,1)).^b(2).*(x(:,3)).^b(4).*(x(:,2)).^b(3));

% set robust fitting options
opts = statset('nlinfit');
opts.RobustWgtFun = 'bisquare';
opts.MaxIter = 1000;

beta0 = [1;1;1;1]; %set initial fit parameters
[beta,r,J,cov] = nlinfit(X,y,func,beta0,opts);
beta
Rsq = 1-mean(r.^2)/var(y)

%Check whether [1;3;2] is in a 95% confidence interval using the Jacobian
%argument:
ci = nlparci(beta,r,'Jacobian',J);

(beta - ci(:,1))./beta*100

end
```

C.3.2 Radial averaged power spectral density

The following two scripts compute the 1-dimensional radial averaged power spectral density of 2-dimensional input surface data, either based on CSV files or on images.

PSD_radial.m

```
function out = PSD_radial(hij);

% Load 2-dimensional *.csv matrix file of surface
hij = csvread('file.csv');

%or

% Load image file and convert to gray-scale image
%hij = rgb2gray(imread('image.tif'));

% Get size of the data
[N M] = size(hij);

% Find minimum dimension of data
minSize=min(N,M);

% Distance of minimum dimension of input data in millimeter
minDist=29.2;

% Scaling factor in [mm/pixel]
scale = minDist/minSize;

% Perform FFT using MATLAB's built-in function 'fft2'
FFT = fft2(hij,N,M);

% Determine PSD, the square of FFT and shifting the zero-frequency to the
% center with 'fftshift'
```

```
PSD2D = (abs(fftshift(FFT))).^2./(N*M);

% Radial averaging using the function 'radial.m'
PSD1D_radial = radial(PSD2D);

% Determing the new size in pixel of PSD1D_radial
p = max(size(PSD1D_radial));

% Normalizing the frequency to length scale
PSD1_freq_normalized = (0:p-1)*scale;

% Rearranging the data from radial frequency to the radial wavelength
for j = 1:p
    PSD1D_radial_ampl_wavelength(1,p+1-j) = PSD1D_radial(1,j);
    PSD1D_wavelength(1,p+1-j) = 1/PSD1_freq_normalized(1,j);
end

% Plotting
 subplot(2,2,1); imagesc(hij); axis image; title('{\bf Original h(i,j)}');
 subplot(2,2,2); imagesc(PSD2D,[0 255]); axis image; title('{\bf PSD}');
 subplot(2,2,3); plot(PSD1D_wavelength,PSD1D_radial_ampl_wavelength);axis([0 3 0 ...
     5E3]); title('{\bf Radial}');

end
```

The `radial.m` function requires square matrices and is less commented than the first one.

`radial.m`

```
function result = radial(matrix);
% Find radial average of input matrix

%[m0,n0] = size(matrix0);
%d0=min(size(matrix0))-1;
%cx = (n0/2);
%cy = (m0/2);
%rect=[round(cx-d0/2) round(cy-d0/2) d0 d0];
%matrix=imcrop(matrix0,rect);

[m,n] = size(matrix);
center = round(n/2);

[i,j] = meshgrid(1:m,1:m);
i = i(:);
j = j(:);

dist = round(sqrt((i-center).^2 + (j-center).^2));
[dist,y] = sort(dist);

% this is because I need to find how many matrix values are located at each distance
% so I decided to use 'hist' function to find that
hh = hist(dist,max(dist)+1);

vec = matrix(:);
vec = vec(y); % sort the same way as dist
```

```
ini = 2;

result(1:max(dist))=0;

for k = 1:max(dist)

   index = [ini:ini+hh(k+1)-1];
   result(k) = mean(vec(index));
   ini = max(index)+1;

end
```

Appendix D

2D simulation of a full gravure printing process using OpenFOAM

Since a complete numerical simulation regarding all aspects of a gravure printing unit has not been reported so far, I started to implement a representative geometry in the open source software platform for computational fluid dynamics (CFD) OpenFOAM. This is based on the computer language C++ and provides different pre-defined so-called solvers for different purposes. Those numerically solve the underlying Navier-Stokes equations under numerous boundary conditions one has to define apart from the physical geometry. I set up a fully automated geometry and mesh generation using GMSH which is also an open source software [81].The mesh defines the numerical "grid" on which the differential equations are solved for the different variables.

Treating free surface flows in OpenFOAM is implemented using the so-called volume of fluid (VOF) method which tracts a two-phase problem of gas and fluid [191]. Thereby, an additional differential equation is simultaneously solved per numerical cell and time step which accounts for a continuous variable between $[0, 1]$, 1 for solely representing the fluid and 0 for solely the gas. The values in between are extended over several computational cells whether the free fluid interface is not sharply defined using VOF. Coupling this to a moving computational mesh has been implemented as the so-called `interDynMFoam` solver in OpenFOAM [191].

For the computational geometry to match a real system, I decided to use dimensions of the smallest gravure cylinder commercially available. That is a Microgravure™cylinder with a radius of 10 mm from Yasui Seiki, Japan. Without gravure cells, the computational implementation of a geometry and its numerical solution would be less complex because the substrate and the cylinder motion could be only defined by appropriate boundary conditions. This means no moving computational mesh would be required. Taking into account gravure cells completely changes the situation. The gravure cells have to move in respect to a static ink reservoir and a static doctor blade. Therefore, I used OpenFOAM's new implementation of the so-called arbitrary mesh interface (AMI), initially developed for turbomachinery applications [191]. This allows to define moving and static meshes while the computational interface is matched using sophisticated but numerically improvable methods.

Unfortunately, the performed numerical simulations were not completely successful within the scope of this thesis because I could not achieve numerical stability and the computation of the liquid phase gave non-realistic results. The afore mentioned variable within the VOF method for the liquid phase exceeds 1. Besides these issues which might be solvable with hard code modification of the underlaying C++ code, I decided to present the results in short. Therefore, I attached the complete

OpenFOAM case-files in Appendix D to show that the problem is trackable in principle and to possibly give a starting point for further investigations. For further details on CFD and OpenFOAM, I refer the reader to textbooks of Velten [255] and to OpenFOAM's user guide [191].

The resulting geometry and the different components of the gravure printing setup including the initial tetrahedral-based computational mesh of a total number of 26653 numerical cells is shown in Figure D.1 and clipped to the doctor blade region in Figure D.2.

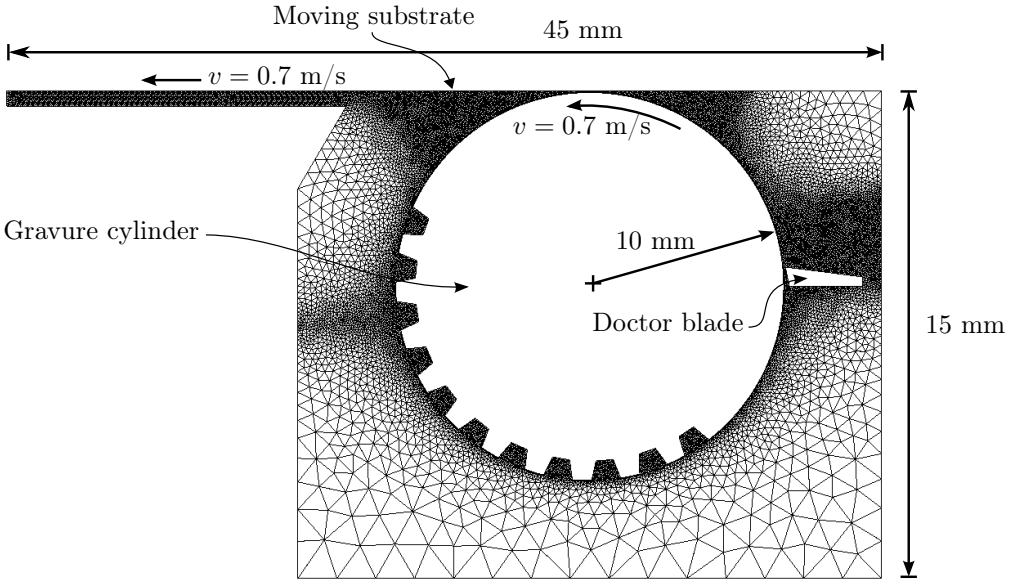

Figure D.1: Full numerical mesh of the computational gravure printing geometry in 2D as generated by GMSH using the case-files in Appendix D.

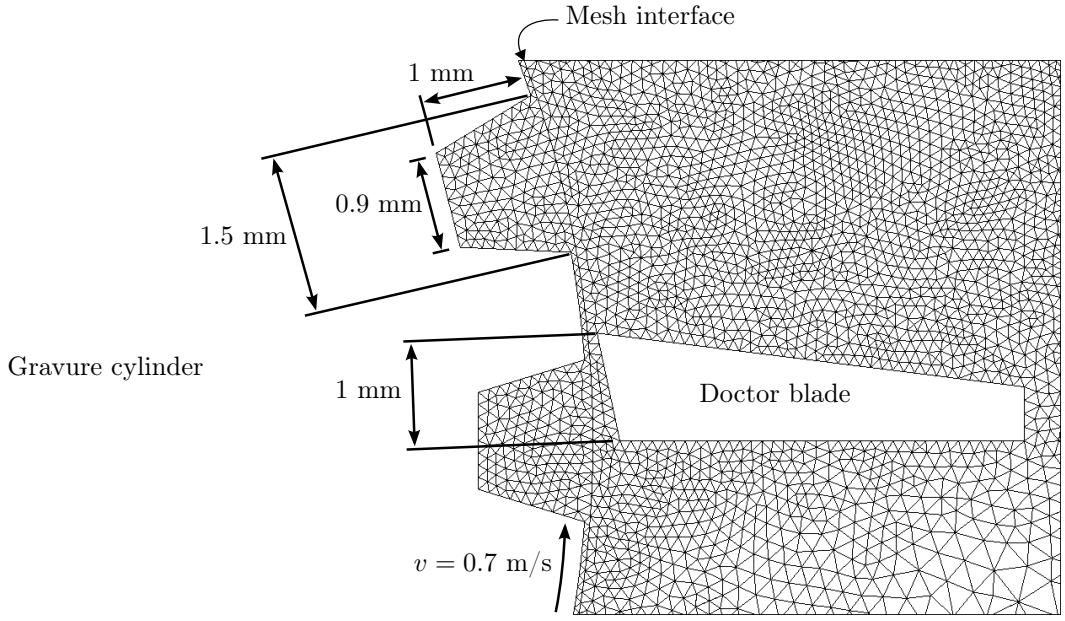

Figure D.2: Magnified doctor blade region of the generated geometry shown the numerical cells.

The generated gravure cell geometry was about factor of about 10 above realistic values. The printing velocity was defined to 0.7 m/s, the Newtonian viscosity to 10 mPa·s, the surface tension

to 30 mN/m and the critical distance between blade tip−gravure cell and cylinder−substrate were both 50 µm. The numerical time-step was set to 10^{-6} s and the last simulation step corresponds to $t = 0.08$ s. The computation was performed using a standard notebook[1] on an operating system Ubuntu 10.04 LTS with an installed standard OpenFOAM version 2.1.0. The real time duration for the computation on the Notebook on a single CPU core took about 8 hours.

The resulting liquid phase fractions (red for the ink, blue for air and green for the interface) for the computed time-steps at $t = 0$ s, $t = 0.356$ s, $t = 0.046$ s are shown in Figure D.3, D.4 and D.5. Figure D.4 and D.5 show interesting aspects of the afore mentioned sub-processes in Section

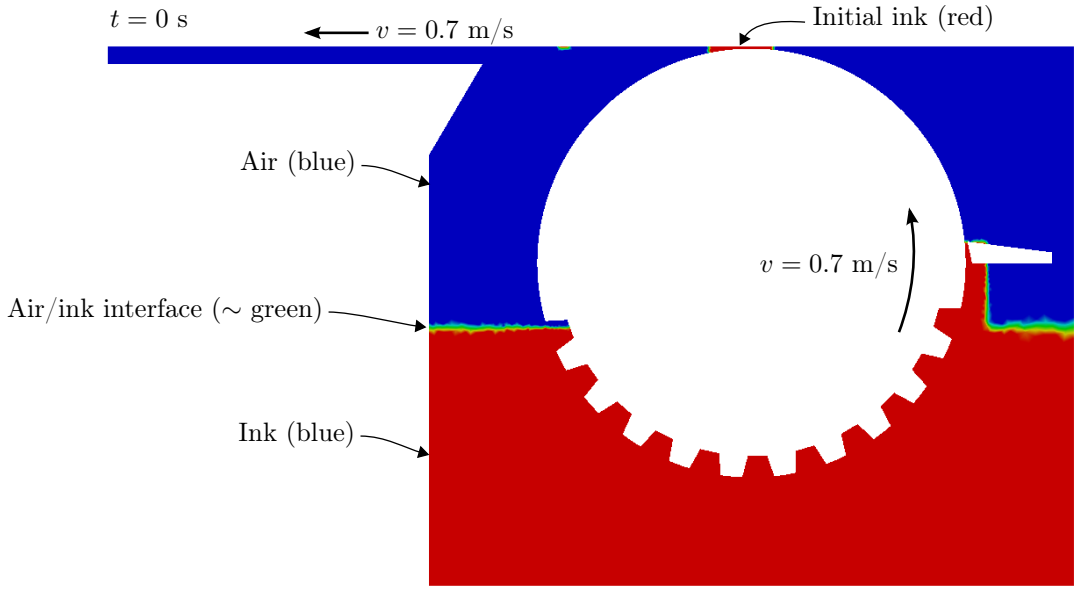

Figure D.3: Defined liquid phase (red) at the initial, starting time step $t = 0$ s of the numerical simulation.

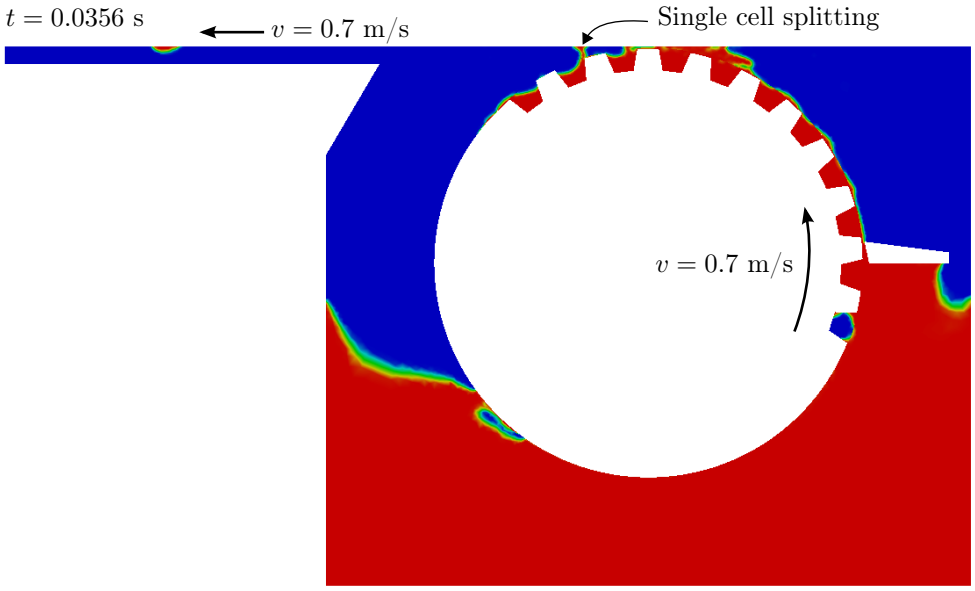

Figure D.4: Computed liquid phase (red) at the time step $t = 0.0356$ s, single cell splitting occurred.

[1]Lenovo R400, with 8GB RAM and an Inter® Core™ Duo T6570 with 2.1 GHz

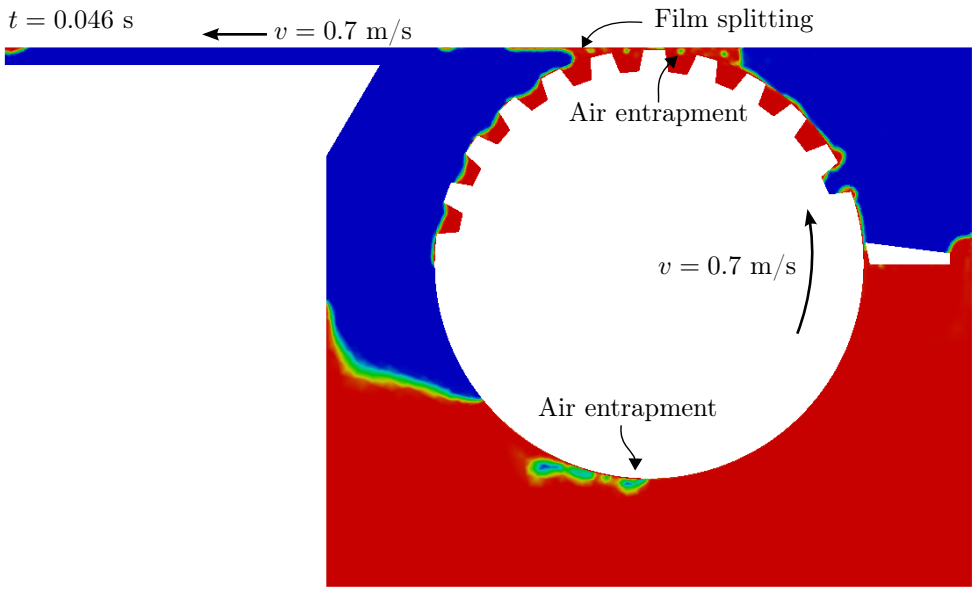

Figure D.5: Computed liquid phase (red) at the time step $t = 0.046$ s, ink transfer mechanism has changed to film splitting.

3.2 on page 62. The ink transfer reveals initially single cell splitting (Figure D.4) which changed to film splitting after a few gravure cells had passed the nip, as shown in Figure D.5. Actually, this behavior could be expected for real setups processing low viscous inks, especially in gravure coating operations.

The numerical experiments show that ink has been accumulated at the entrance of the printing nip which I also assign an important role in the printing experiments discussed in Chapter 4. Furthermore, strong air entrapment has evolved at the immersion region of the gravure cells into the reservoir. This, however, could originate from the reduction to 2D.

The following aspects have to be improved for further investigations:

- Gravure cells, and minimal distances between substrate−cylinder and blade−cylinder have to be lowered by a factor of 10 while providing numerically stability.
- Dynamic contact angles at the triple lines seem to behave unrealistically.
- Validation with experimental results has to be performed.
- Ideally, extension to 3D might resolve also nip instabilities along the printing nip. Therefore, the computation might be parallelized and transferred to multi-core platforms.

D.1 OpenFOAM case files of a gravure printing setup

In the following, I present the complete program code of the CFD simulation based on OpenFOAM. This is intended for experienced OpenFOAM users, since I reduced my comments only to aspects deviating from the standard test cases provided by OpenFOAM and therefore refer to the documentation [191] and to the numerous EXCELLENT forums and websites of the growing and changing OpenFOAM community.

The underlying folder and file structure of the OpenFOAM case is the following:

/0/p_rgh

/0/U

/0/alpha1.org

/constant/dynamicMeshDict

/constant/g

/constant/transportProperties

/constant/turbulenceProperties

/constant/polyMesh/

/system/controlDict

/system/fvSchemes

/system/fvSolution

/system/setFieldsDict

/system/topoSetDict

/GMSH/rotCyl2DIn1.geo

/GMSH/rotCyl2DOut1.geo

/GMSH/masterIn/constant/

/GMSH/masterIn/system/

/GMSH/slaveOut/constant/

/GMSH/slaveOut/system/

Allclean

meshBuild

sedApply

run

Apart from the `/GMSH/` folder, the case is normally structured for `icoDynMFoam` with the AMI interface. The complete case might be executed via `./run` in the command line. For the automated mesh generation it is important that the folders in `/GMSH/` do exist as shown above to successfully apply OpenFOAM's mesh merging tool `mergeMeshes`. Furthermore, it is important to transfer the correct value of `deltaT` in the `controlDict` file to the `run` file as commented therein.

The complete geometry of the gravure printing setup with its parameters of the number of cell, the distances, the definition of the blade etc. can be found in `/GMSH/rotCyl2DIn1.geo` and `/GMSH/rotCyl2DOut1.geo`. All other parameters of the motion and the algorithm can be found in the corresponding case files.

The corresponding files of the afore mention case structure is listed in the following:

/0/p_rgh

```
/*---------------------------------*- C++ -*----------------------------------*\
| =========                 |                                                 |
| \\      /  F ield         | OpenFOAM: The Open Source CFD Toolbox           |
|  \\    /   O peration     | Version:  2.1.0                                 |
|   \\  /    A nd           | Web:      www.OpenFOAM.org                      |
|    \\/     M anipulation  |                                                 |
```

```
\*---------------------------------------------------------------------------*/
FoamFile
{
    version     2.0;
    format      ascii;
    class       volScalarField;
    location    "0";
    object      p_rgh;
}
// * * * * * * * * * * * * * * * * * * * * * * * * * * * * * * * * * * * * * * * * * * * * //
dimensions      [1 -1 -2 0 0 0 0];
internalField   uniform 0;
boundaryField
{
    impellerWall
    {
        type            buoyantPressure;
        gradient        uniform 0;
        rho             rho;
        value           uniform 0;
    }
    baffleWall
    {
        type            buoyantPressure;
        gradient        uniform 0;
        value           uniform 0;
    }
    blade
    {
        type            buoyantPressure;
        gradient        uniform 0;
        value           uniform 0;
    }
    substrate
    {
        type            buoyantPressure;
        gradient        uniform 0;
        value           uniform 0;
    }
    AMI1
    {
        type            cyclicAMI;
        value           $internalField;
    }
    AMI2
    {
        type            cyclicAMI;
        value           $internalField;
    }
    atmosphere
    {
        type            totalPressure;
        p0              uniform 0;
        U               U;
        phi             phi;
        rho             rho;
```

```
        psi             none;
        gamma           1;
        value           uniform 0;
    }
    frontAndBack
    {
        type            empty;
    }
}
// ************************************************************************* //
```

/0/U

```
/*--------------------------------*- C++ -*----------------------------------*\
| =========                 |                                                 |
| \\      /  F ield         | OpenFOAM: The Open Source CFD Toolbox           |
|  \\    /   O peration     | Version:  2.1.0                                 |
|   \\  /    A nd           | Web:      www.OpenFOAM.org                      |
|    \\/     M anipulation  |                                                 |
\*---------------------------------------------------------------------------*/
FoamFile
{
    version     2.0;
    format      ascii;
    class       volVectorField;
    location    "0";
    object      U;
}
// * * * * * * * * * * * * * * * * * * * * * * * * * * * * * * * * * * * * * //
dimensions      [0 1 -1 0 0 0 0];
internalField   uniform (0 0 0);
boundaryField
{
    AMI1
    {
        type            cyclicAMI;
        value           $internalField;
    }
    AMI2
    {
        type            cyclicAMI;
        value           $internalField;
    }
    baffleWall
    {
        type            fixedValue;
        value           uniform (0 0 0);
    }
    blade
    {
        type            fixedValue;
        value           uniform (0 0 0);
    }
    substrate
    {
```

```
        type            fixedValue;  //deg/s * 0.000174533; v=2*pi*r*cycle/s
        value           uniform (-0.698132 0 0);
    }

    impellerWall
    {
        type            movingWallVelocity;
        value           uniform (0 0 0);
    }
    atmosphere
    {
        type            fluxCorrectedVelocity;
        value           uniform (0 0 0);
    }
    frontAndBack
    {
        type            empty;
    }
}
// ************************************************************************* //
```

/0/alpha1.org

```
/*--------------------------------*- C++ -*----------------------------------*\
| =========                 |                                                 |
| \\      /  F ield         | OpenFOAM Extend Project: Open Source CFD        |
|  \\    /   O peration     | Version:  1.6-ext                               |
|   \\  /    A nd           | Web:      www.extend-project.de                 |
|    \\/     M anipulation  |                                                 |
\*---------------------------------------------------------------------------*/
FoamFile
{
    version     2.0;
    format      ascii;
    class       volScalarField;
    location    "0";
    object      alpha1.org;
}
// * * * * * * * * * * * * * * * * * * * * * * * * * * * * * * * * * * * * * //
dimensions      [0 0 0 0 0 0 0];
internalField   uniform 0;
boundaryField
{
    impellerWall
    {
    // return theta0_ + (thetaA_ - thetaR_)*tanh(uwall/uTheta_);
      type           dynamicAlphaContactAngle;
      uTheta        1e-0;
    thetaA          40;
    theta0          25;
    thetaR      10;
        limit          none;
        value          uniform 1;
    }
```

```
    baffleWall
    {
      type           dynamicAlphaContactAngle;
      uTheta        1e-0;
    thetaA          40;
    theta0          25;
    thetaR      10;
        limit          none;
        value          uniform 1;
    }
    blade
    {
      type           dynamicAlphaContactAngle;
      uTheta        1e-0;
    thetaA          40;
    theta0          25;
    thetaR      10;
        limit          none;
        value          uniform 1;
    }
    substrate
    {
      type           dynamicAlphaContactAngle;
      uTheta        1e-0;
    thetaA          40;
    theta0          25;
    thetaR      10;
        limit          none;
        value          uniform 1;
    }
    AMI1
    {
        type            cyclicAMI;
        value           $internalField;
    }
    AMI2
    {
        type            cyclicAMI;
        value           $internalField;
    }
    atmosphere
    {
        type            inletOutlet;
        inletValue      uniform 0;
        value           uniform 0;
    }
    frontAndBack
    {
        type            empty;
    }
}
// ************************************************************************* //
```

/constant/dynamicMeshDict

```
/*--------------------------------*- C++ -*----------------------------------*\
| =========                 |                                                 |
| \\      /  F ield         | OpenFOAM: The Open Source CFD Toolbox           |
|  \\    /   O peration     | Version:  2.1.0                                 |
|   \\  /    A nd           | Web:      www.OpenFOAM.org                      |
|    \\/     M anipulation  |                                                 |
\*---------------------------------------------------------------------------*/
FoamFile
{
    version     2.0;
    format      ascii;
    class       dictionary;
    location    "constant";
    object      dynamicMeshDict;
}
// * * * * * * * * * * * * * * * * * * * * * * * * * * * * * * * * * * * * * //
dynamicFvMesh   solidBodyMotionFvMesh;
motionSolverLibs ( "libfvMotionSolvers.so" );
solidBodyMotionFvMeshCoeffs
{
    cellZone        impellerWall;
    solidBodyMotionFunction  rotatingMotion;
    rotatingMotionCoeffs
    {
        CofG        (0 0 0);
        radialVelocity (0 0 4000); //6000;// deg/s
    }
}
// ************************************************************************* //
```

/constant/g

```
/*--------------------------------*- C++ -*----------------------------------*\
| =========                 |                                                 |
| \\      /  F ield         | OpenFOAM: The Open Source CFD Toolbox           |
|  \\    /   O peration     | Version:  2.1.0                                 |
|   \\  /    A nd           | Web:      www.OpenFOAM.org                      |
|    \\/     M anipulation  |                                                 |
\*---------------------------------------------------------------------------*/
FoamFile
{
    version     2.0;
    format      ascii;
    class       uniformDimensionedVectorField;
    location    "constant";
    object      g;
}
// * * * * * * * * * * * * * * * * * * * * * * * * * * * * * * * * * * * * * //
dimensions      [0 1 -2 0 0 0 0];
value           ( 0 -9.81 0);
// ************************************************************************* //
```

/constant/transportProperties

```
/*--------------------------------*- C++ -*----------------------------------*\
| =========                 |                                                 |
| \\      /  F ield         | OpenFOAM: The Open Source CFD Toolbox           |
|  \\    /   O peration     | Version:  2.1.0                                 |
|   \\  /    A nd           | Web:      www.OpenFOAM.org                      |
|    \\/     M anipulation  |                                                 |
\*---------------------------------------------------------------------------*/
FoamFile
{
    version     2.0;
    format      ascii;
    class       dictionary;
    location    "constant";
    object      transportProperties;
}
// * * * * * * * * * * * * * * * * * * * * * * * * * * * * * * * * * * * * * //
phase1
{
    transportModel  Newtonian;
    nu              nu [ 0 2 -1 0 0 0 0 ] 1e-05;//1e-06
    rho             rho [ 1 -3 0 0 0 0 0 ] 1000;
}
phase2
{
    transportModel  Newtonian;
    nu              nu [ 0 2 -1 0 0 0 0 ] 1.48e-05;
    rho             rho [ 1 -3 0 0 0 0 0 ] 1;
}
sigma           sigma [ 1 0 -2 0 0 0 0 ] 0.03; //0.07;
// ************************************************************************* //
```

/constant/turbulenceProperties

```
/*--------------------------------*- C++ -*----------------------------------*\
| =========                 |                                                 |
| \\      /  F ield         | OpenFOAM: The Open Source CFD Toolbox           |
|  \\    /   O peration     | Version:  2.1.0                                 |
|   \\  /    A nd           | Web:      www.OpenFOAM.org                      |
|    \\/     M anipulation  |                                                 |
\*---------------------------------------------------------------------------*/
FoamFile
{
    version     2.0;
    format      ascii;
    class       dictionary;
    location    "constant";
    object      turbulenceProperties;
}
// * * * * * * * * * * * * * * * * * * * * * * * * * * * * * * * * * * * * * //
simulationType  laminar;
// ************************************************************************* //
```

/constant/controlDict

```
/*--------------------------------*- C++ -*----------------------------------*\
| =========                 |                                                 |
| \\      /  F ield         | OpenFOAM: The Open Source CFD Toolbox           |
|  \\    /   O peration     | Version:  2.1.0                                 |
|   \\  /    A nd           | Web:      www.OpenFOAM.org                      |
|    \\/     M anipulation  |                                                 |
\*---------------------------------------------------------------------------*/
FoamFile
{
    version     2.0;
    format      ascii;
    class       dictionary;
    object      controlDict;
}
// * * * * * * * * * * * * * * * * * * * * * * * * * * * * * * * * * * * * * * * * * * * * * * * * * * * * * * * * //
application     interDyMFoam;
startFrom       startTime;
startTime       0.00;//0;
stopAt          endTime;
endTime         0.5;
ΔT          1e-06;//08 0.00001;
writeControl    adjustableRunTime;
writeInterval   2e-04;//0.0001;
cycleWrite      0;
writeFormat     ascii;
writePrecision  12;//;12;//6;
writeCompression uncompressed;
timeFormat      general;
timePrecision   12;//12;//6;
runTimeModifiable yes;
adjustTimeStep yes;
maxCo           0.5;
maxAlphaCo      0.5;
maxDeltaT       1;
// ************************************************************************* //
```

/system/fvSchemes

```
/*--------------------------------*- C++ -*----------------------------------*\
| =========                 |                                                 |
| \\      /  F ield         | OpenFOAM: The Open Source CFD Toolbox           |
|  \\    /   O peration     | Version:  2.1.0                                 |
|   \\  /    A nd           | Web:      www.OpenFOAM.org                      |
|    \\/     M anipulation  |                                                 |
\*---------------------------------------------------------------------------*/
FoamFile
{
    version     2.0;
    format      ascii;
    class       dictionary;
    location    "system";
    object      fvSchemes;
}
```

```
// * * * * * * * * * * * * * * * * * * * * * * * * * * * * * * * * * * * * * * * * * * * * * * * * * * * * * * * * //
ddtSchemes
{
    default         Euler;
}
gradSchemes
{
    default         Gauss linear;
        grad(U)         Gauss linear;
        grad(alpha)     Gauss linear;
}
divSchemes
{
    div(rho*phi,U)  Gauss upwind;
    div(phi,alpha)  Gauss vanLeer;
    div(phirb,alpha) Gauss interfaceCompression;
}
laplacianSchemes
{
    default         Gauss linear corrected;
}
interpolationSchemes
{
    default         linear;
}
snGradSchemes
{
    default         corrected;
}
fluxRequired
{
    default         no;
    p_rgh;
    pcorr;
    alpha;
}
// ************************************************************************* //
```

/system/fvSolution

```
/*--------------------------------*- C++ -*----------------------------------*\
| =========                 |                                                 |
| \\      /  F ield         | OpenFOAM: The Open Source CFD Toolbox           |
|  \\    /   O peration     | Version:  2.1.0                                 |
|   \\  /    A nd           | Web:      www.OpenFOAM.org                      |
|    \\/     M anipulation  |                                                 |
\*---------------------------------------------------------------------------*/
FoamFile
{
    version     2.0;
    format      ascii;
    class       dictionary;
    location    "system";
    object      fvSolution;
}
```

```
// * * * * * * * * * * * * * * * * * * * * * * * * * * * * * * * * * * * * * * * * * * * * //
solvers
{
    pcorr
    {
        solver          PCG;
        preconditioner
        {
            preconditioner  GAMG;
            tolerance       0.001;
            relTol          0;
            smoother        GaussSeidel;
            nPreSweeps      0;
            nPostSweeps     2;
            nFinestSweeps   2;
            cacheAgglomeration false;
            nCellsInCoarsestLevel 10;
            agglomerator    faceAreaPair;
            mergeLevels     1;
        }
        tolerance       0.0001;
        relTol          0;
        maxIter         100;
    }
    p_rgh
    {
        solver          GAMG;
        tolerance       1e-08;
        relTol          0.05;
        smoother        GaussSeidel;
        nPreSweeps      0;
        nPostSweeps     2;
        nFinestSweeps   2;
        cacheAgglomeration false;
        nCellsInCoarsestLevel 10;
        agglomerator    faceAreaPair;
        mergeLevels     1;
    }
    p_rghFinal
    {
        solver          PCG;
        preconditioner
        {
            preconditioner  GAMG;
            tolerance       1e-08;
            relTol          0;
            nVcycles        2;
            smoother        GaussSeidel;
            nPreSweeps      0;
            nPostSweeps     2;
            nFinestSweeps   2;
            cacheAgglomeration false;
            nCellsInCoarsestLevel 10;
            agglomerator    faceAreaPair;
            mergeLevels     1;
        }
```

```
        tolerance       1e-08;
        relTol          0;
        maxIter         20;
    }
    U
    {
        solver          smoothSolver;
        smoother        GaussSeidel;
        tolerance       1e-06;
        relTol          0;
        nSweeps         1;
    }
    UFinal
    {
        $U;
        tolerance       1e-08;
        relTol          0;
    }

    "(k|B|nuTilda)"
    {
        solver          PBiCG;
        preconditioner  DILU;
        tolerance       1e-08;
        relTol          0;
    }
}
PIMPLE
{
    momentumPredictor no;//yes;//no;
    nCorrectors     3;
    nNonOrthogonalCorrectors 1;//5;//1;
    nAlphaCorr      1;//2;//1;
    nAlphaSubCycles 3;//4;//3;
    cAlpha          1;//2;//1;
}
relaxationFactors
{
    fields
    {
    }
    equations
    {
        "U.*"           1;
    }
// ************************************************************************* //
```

/system/setFieldsDict

```
/*--------------------------------*- C++ -*----------------------------------*\
| =========                 |                                                 |
| \\      /  F ield         | OpenFOAM: The Open Source CFD Toolbox           |
|  \\    /   O peration     | Version:  2.1.0                                 |
|   \\  /    A nd           | Web:      www.OpenFOAM.org                      |
|    \\/     M anipulation  |                                                 |
```

```
\*---------------------------------------------------------------------------*/
FoamFile
{
    version     2.0;
    format      ascii;
    class       dictionary;
    location    "system";
    object      setFieldsDict;
}
// * * * * * * * * * * * * * * * * * * * * * * * * * * * * * * * * * * * * * * * * * * * * * * * * * * * * * * * * * * * * * * * * //
defaultFieldValues
(
    volScalarFieldValue alpha1 0
);
regions
(
    boxToCell
    {
        box ( -0.5 -0.5 -5 ) ( 0.5 -0.003 5 );
        fieldValues
        (
            volScalarFieldValue alpha1 1
        );
    }
//blade
    boxToCell
    {
        box ( 0 -0.005 -5 ) ( 0.011 0.001 5 );
        fieldValues
        (
            volScalarFieldValue alpha1 1
        );
    }
//substrate
    boxToCell
    {
        box ( -0.009 0.01 -5 ) ( -0.0085 0.1 5 );
        fieldValues
        (
            volScalarFieldValue alpha1 1
        );
    }
    boxToCell
    {
        box ( -0.002 0.009 -5 ) ( 0.001 0.1 5 );
        fieldValues
        (
            volScalarFieldValue alpha1 1
        );
    }
 );
// ************************************************************************* //
```

/system/topoSetDict

```
/*--------------------------------*- C++ -*----------------------------------*\
| =========                 |                                                 |
| \\      /  F ield         | OpenFOAM: The Open Source CFD Toolbox           |
|  \\    /   O peration     | Version:  2.1.0                                 |
|   \\  /    A nd           | Web:      www.OpenFOAM.org                      |
|    \\/     M anipulation  |                                                 |
\*---------------------------------------------------------------------------*/
FoamFile
{
    version     2.0;
    format      ascii;
    class       dictionary;
    object      topoSetDict;
}
// * * * * * * * * * * * * * * * * * * * * * * * * * * * * * * * * * * * * * * * * * * * * * * * * * * * * * * * * //
actions
(
    // Get both sides of ami
    // ¬¬¬
```

```
    cellDepth   = 1000e-06;
    cellPeriod     =  cellWidth + cellWallWidth; // period of cell pattern as ...
        length [m]
    cellStartAngle = -160*Pi/180; //to 3 o'clock
    rGravCellBo    = rGravCy - cellDepth;

/*****************************************************
Points, lines and circles
*****************************************************/

// Inner part ------------------------------------------------
// Inside slider ---------------------------------------
   // points:
   pInSl[1] = newp; Point(pInSl[1]) = {0,  rInSlCy,  0,  lcarInSl};
   pInSl[2] = newp; Point(pInSl[2]) = {-rInSlCy,  0,  z,  lcarInSl};
   pInSl[3] = newp; Point(pInSl[3]) = {0,  -rInSlCy,  z,  lcarInSl};
   pInSl[4] = newp; Point(pInSl[4]) = {rInSlCy,  0,  z,  lcarInSl};
   pInSlNr  = 4;

   // circles:
   For i In {1:pInSlNr - 1}
       cInSl[i] = newreg; Circle(cInSl[i]) = {pInSl[i],r[0],pInSl[i+1]};
   EndFor
   cInSl[pInSlNr] = newreg; Circle(cInSl[pInSlNr]) = {pInSl[pInSlNr],r[0],pInSl[1]};

// Gravure Cylinder ------------------------------------------
   // points:
    j1=4; // period of entries in the following FOR-loop
   For i In {0:nrOfCells-1}
    pGrav[1+i*j1] = newp; Point(pGrav[1+i*j1]) = {rGravCy*Cos(cellStartAngle - ...
        Asin(cellWidth/2/rGravCy) + i*2*Asin(cellPeriod/2/rGravCy)),  ...
        rGravCy*Sin(cellStartAngle - Asin(cellWidth/2/rGravCy) + ...
        i*2*Asin(cellPeriod/2/rGravCy)),  z,  lcarGravCy};
    pGrav[2+i*j1] = newp; Point(pGrav[2+i*j1]) = {rGravCellBo*Cos(cellStartAngle ...
        -Asin(cellBoWidth/2/rGravCellBo) + i*2*Asin(cellPeriod/2/rGravCy)),  ...
        rGravCellBo*Sin(cellStartAngle-Asin(cellBoWidth/2/rGravCellBo) + ...
        i*2*Asin(cellPeriod/2/rGravCy)),  z,  lcarGravCy};
    pGrav[3+i*j1] = newp; Point(pGrav[3+i*j1]) = {rGravCellBo*Cos(cellStartAngle ...
        +Asin(cellBoWidth/2/rGravCellBo) + i*2*Asin(cellPeriod/2/rGravCy)),  ...
        rGravCellBo*Sin(cellStartAngle + Asin(cellBoWidth/2/rGravCellBo) + ...
        i*2*Asin(cellPeriod/2/rGravCy)),  z,  lcarGravCy};
    pGrav[4+i*j1] = newp; Point(pGrav[4+i*j1]) = {rGravCy*Cos(cellStartAngle ...
        +Asin(cellWidth/2/rGravCy) + i*2*Asin(cellPeriod/2/rGravCy)),  ...
        rGravCy*Sin(cellStartAngle+Asin(cellWidth/2/rGravCy) + ...
        i*2*Asin(cellPeriod/2/rGravCy)),  z,  lcarGravCy};
   EndFor
    pGrav[5+i*j1] = newp; Point(pGrav[5+i*j1]) = {rGravCy*Cos(cellStartAngle+Pi ...
        +(nrOfCells*2*Asin(cellPeriod/2/rGravCy) - ...
        4*Asin(cellWallWidth/2/rGravCy))/2),  rGravCy*Sin(cellStartAngle+Pi + ...
        (nrOfCells*2*Asin(cellPeriod/2/rGravCy) - ...
        4*Asin(cellWallWidth/2/rGravCy))/2),  z,  lcarGravCy};  //this point is ...
        needed for the last circle line to connect with the first point in the loop ...
        below, it is on the other site of the cylinder

// circles:
    j2=3; // period of entries in the following FOR-loop
```

```
    For i In {0:nrOfCells-1}
        lGrav[1+i*j2] = newreg; Line(lGrav[1+i*j2]) = {pGrav[1+i*j1],pGrav[2+i*j1]};
        lGrav[2+i*j2] = newreg; Line(lGrav[2+i*j2]) = {pGrav[2+i*j1],pGrav[3+i*j1]};
        lGrav[3+i*j2] = newreg; Line(lGrav[3+i*j2]) = {pGrav[3+i*j1],pGrav[4+i*j1]};
        lGrav[4+i*j2] = newreg; Circle(lGrav[4+i*j2]) = ...
            {pGrav[4+i*j1],r[0],pGrav[5+i*j1]};
    EndFor
        lGrav[5+i*j2] = newreg; Circle(lGrav[5+i*j2]) = {pGrav[5+i*j1],r[0],pGrav[1]};
        nrOfLi=5+i*j2;

   lineLoopIn  = newreg; Line Loop(lineLoopIn) = {cInSl[1]:cInSl[pInSlNr], ...
       lGrav[1]:lGrav[nrOfLi]};
   planeSurfIn = newreg; Plane Surface(planeSurfIn) = lineLoopIn;

Exlist[] = Extrude {0,0,0.01} {
    Surface{planeSurfIn};
    Layers{1};
    Recombine;
} ;
Physical Surface("impellerWall") = {Exlist[{6:nrOfCells*j1+1+6-1}]};
Physical Volume("impellerWall") = {1};
Physical Surface("AMI1") = {Exlist[{2:5}]};
Physical Surface("frontAndBack") = {planeSurfIn, Exlist[0]};
```

/GMSH/rotCyl2DOut1.geo

```
// Gravure printing simulation by Nils Bornemann
// Mesh
   rGravCy    = 10e-03;             // radius of the gravure cylinder
   distBlade  = 50e-06;             // distance of blade tip to cylinder
                                    //   = distance of substrate to cylinder
                                    //   = distance between ousider slider cylinder and
                                    //     gravure cylinder
   rSlCy = rGravCy + distBlade;     // radius of sliding cylinder
   leftDistWall  = 5e-03;           // width of left wall from ousideslider to ...
       outer wall
   leftDistSubst = 15e-03;
   leftHeightSub  = 0.8e-03;
   leftTopDistNip = 2e-03;
   leftDipPos     = 0;              // position of center region of left dip (in)
   leftDipHeight     = 5e-03;       // height of dip region
   downDistWall  = 5e-03;
   topDistWall  = 1*distBlade;
   rightDistWall  = 5e-03;          // width of left wall from ousideslider to ...
       outer wall
   rightTopDistNip = 8e-03;

// blade definitions
   bladeAngle = 30*Pi/180;
   bladeTipAngle = 10*Pi/180;
   bladeStartAngle = 0*Pi/180;
   bladeThick = 1000e-06;
   bladeLength = 4.0e-03;  // < rightDistWall
   alphaOffOut = 0.003; // reference point below y=0 for determine finer mesh for ...
       left dip in region
```

```
   alphaOffSl  = 0;
   lcarOut = 200e-05;
   lcarOutSl = 10e-05;
   lcarBlade = 10e-05;
   z=0;
   r[0] = newp; Point(r[0]) = {0,  0,  z};   // origin

/*******************************************************
Points, lines and circles
*******************************************************/
// Outer part ----------------------------------------------------
// points:
   pOut[1] = newp; Point(pOut[1]) = {rSlCy + 1*rightDistWall,  rSlCy + topDistWall, ...
        z,  lcarOut/2};   //right upper corner point
   pOut[2] = newp; Point(pOut[2]) = {rightTopDistNip,  rSlCy + topDistWall,  z,  ...
       lcarBlade};
   pOut[3] = newp; Point(pOut[3]) = {-leftTopDistNip,  rSlCy + topDistWall,  z,  ...
       lcarBlade};
   pOut[4] = newp; Point(pOut[4]) = {-(rSlCy + leftDistWall+leftDistSubst),  rSlCy ...
       + topDistWall,  z,  lcarBlade};
   pOut[5] = newp; Point(pOut[5]) = {-(rSlCy + leftDistWall+leftDistSubst),  rSlCy ...
       + topDistWall-leftHeightSub,  z,  lcarBlade};
   pOut[6] = newp; Point(pOut[6]) = {-(rSlCy + 0.5*leftDistWall),  rSlCy + ...
       topDistWall-leftHeightSub,  z,  lcarBlade};
   pOut[7] = newp; Point(pOut[7]) = {-(rSlCy + leftDistWall),  (rSlCy + ...
       topDistWall)/2,  z,  lcarOut/2};
   pOut[8] = newp; Point(pOut[8]) = {-(rSlCy + leftDistWall),  0-alphaOffOut,  z,  ...
       lcarOutSl};
   pOut[9] = newp; Point(pOut[9]) = {-(rSlCy + leftDistWall),  -(rSlCy + ...
       downDistWall),  z,  lcarOut};
   pOut[10] = newp; Point(pOut[10]) = {(rSlCy + rightDistWall), -(rSlCy + ...
       downDistWall),  z,  lcarOut};
   pOut[11] = newp; Point(pOut[11]) = {rSlCy + rightDistWall, 0,  z,  lcarOutSl};
   pOut[12] = newp; Point(pOut[12]) = {rSlCy + rightDistWall, (rSlCy + ...
       topDistWall)/2,  z,  lcarOutSl};
   pOutNr  = 12;

// lines:
   For i In {1:pOutNr - 1}
       lOut[i] = newreg; Line(lOut[i]) = {pOut[i],pOut[i+1]};
   EndFor
   lOut[pOutNr] = newreg; Line(lOut[pOutNr]) = {pOut[pOutNr],pOut[1]};

// Outside slider ------------------------------------------------
   // points:
   pOutSl[1] = newp; Point(pOutSl[1]) = {0, rSlCy,  z,  lcarOutSl};
   pOutSl[2] = newp; Point(pOutSl[2]) = {rSlCy*Cos(Pi+Asin(alphaOffSl/rSlCy)),  ...
       rSlCy*Sin(Pi+Asin(alphaOffSl/rSlCy)), z,  lcarOutSl}; //{-rSlCy,  0,  z,  ...
       lcarOutSl};
   pOutSl[3] = newp; Point(pOutSl[3]) = {0,  -rSlCy,  z,  lcarOutSl};
   pOutSl[4] = newp; Point(pOutSl[4]) = {rSlCy, 0, z,  lcarOutSl};
   pOutNrSl  = 4;

// circles:
   For i In {1:pOutNrSl - 1}
       cOutSl[i] = newreg; Circle(cOutSl[i]) = {pOutSl[i],r[0],pOutSl[i+1]};
```

```
   EndFor
   cOutSl[pOutNrSl] = newreg; Circle(cOutSl[pOutNrSl]) = ...
       {pOutSl[pOutNrSl],r[0],pOutSl[1]};

// blade ------------------------------------------
   // points:
   pBlade[1] = newp; Point(pBlade[1]) = {(rSlCy+bladeThick/4)* ...
       Cos(bladeStartAngle),  (rSlCy+bladeThick/4) *Sin(bladeStartAngle),  z,  ...
       lcarBlade};//pOutSl[5];
   pBlade[2] = newp; Point(pBlade[2]) = {(rSlCy+bladeLength),  (rSlCy+bladeLength)* ...
       Sin(bladeStartAngle),  z,  lcarBlade};
   pBlade[3] = newp; Point(pBlade[3]) = {(rSlCy+bladeLength),  ...
       (rSlCy+bladeLength)*Sin(bladeStartAngle + ...
       2*Asin(bladeThick/4/(rSlCy+bladeLength))),  z,  lcarBlade};
   pBlade[4] = newp; Point(pBlade[4]) = {(rSlCy+1*distBlade) *Cos(bladeStartAngle + ...
       1*Asin(bladeThick/2/(rSlCy+1*distBlade))),  (rSlCy+1*distBlade) * ...
       Sin(bladeStartAngle+2*Asin(bladeThick/2/(rSlCy+1*distBlade))),  z,  lcarBlade};
   pBladeNr  = 4;

// lines:
   For i In {1:pBladeNr - 1}
       lBlade[i] = newreg; Line(lBlade[i]) = {pBlade[i],pBlade[i+1]};
   EndFor
   lBlade[pBladeNr] = newreg; Line(lBlade[pBladeNr]) = {pBlade[pBladeNr],pBlade[1]};
   lineLoopOut  = newreg; Line Loop(lineLoopOut) = {lOut[1]:lOut[pOutNr], ...
       cOutSl[1]:cOutSl[pOutNrSl], lBlade[1]:lBlade[pBladeNr]};
   planeSurfOut = newreg; Plane Surface(planeSurfOut) = lineLoopOut;
   Exlist[] = Extrude {0,0,0.01} {
   Surface{planeSurfOut};
   Layers{1};
   Recombine;
} ;

Physical Volume("internal") = {1};
Physical Surface("baffleWall") = {Exlist[{2+6:pOutNr+1-1}]};
Physical Surface("AMI2") = {Exlist[{pOutNr+2:pOutNr+2+pOutNrSl-1}]};
Physical Surface("frontAndBack") = {planeSurfOut, Exlist[0]};
Physical Surface("substrate") = {Exlist[{2:4}]};
Physical Surface("atmosphere") = {Exlist[{5:7}], Exlist[pOutNr+1]};
Physical Surface("blade") = {Exlist[{pOutNr+2+pOutNrSl:pOutNr+5+pOutNrSl}]};
```

Allclean

```
#!/bin/sh
cd ${0%/*} || exit 1    # run from this directory

# Source tutorial clean functions
. $WM_PROJECT_DIR/bin/tools/CleanFunctions
rm -f constant/polyMesh/boundary
rm -rf constant/polyMesh/sets
cleanCase
# ------------------------------------------------------------------------- end-of-file
```

meshBuild

```
#!/bin/sh
# Source tutorial run functions
. $WM_PROJECT_DIR/bin/tools/RunFunctions

# make dummy cases in the two folders
cp -r constant/dynamicMeshDict GMSH/masterIn/constant/
cp -r system/controlDict GMSH/masterIn/system/
cp -r system/controlDict GMSH/slaveOut/system/
cp -r constant/dynamicMeshDict GMSH/slaveOut/constant/

gmsh GMSH/rotCyl2DIn1.geo -3
gmshToFoam -case GMSH/masterIn GMSH/rotCyl2DIn1.msh
gmsh GMSH/rotCyl2DOut1.geo -3
gmshToFoam -case GMSH/slaveOut GMSH/rotCyl2DOut1.msh
rm -rf GMSH/slaveOut/constant/polyMesh/sets
rm -rf GMSH/slaveOut/constant/polyMesh/cellZones
rm -rf GMSH/slaveOut/constant/polyMesh/faceZones
rm -rf GMSH/slaveOut/constant/polyMesh/pointZones
mergeMeshes GMSH/masterIn GMSH/slaveOut
```

sedApply

```
#!/bin/sh
#sed -i s/patch/ggi/ constant/polyMesh/boundary

sed -i '22d' constant/polyMesh/boundary #delete row
sed -i '21a        type     empty;' constant/polyMesh/boundary

sed -i '28d' constant/polyMesh/boundary #delete row
sed -i '27a        type     cyclicAMI;' constant/polyMesh/boundary
sed -i '30a                transform       noOrdering;' constant/polyMesh/boundary
sed -i '30a                neighbourPatch  AMI2;' constant/polyMesh/boundary
sed -i '30a                matchTolerance  0.0001;' constant/polyMesh/boundary

sed -i '37d' constant/polyMesh/boundary #delete row
sed -i '36a        type     wall;' constant/polyMesh/boundary

sed -i '43d' constant/polyMesh/boundary #delete row
sed -i '42a        type     wall;' constant/polyMesh/boundary

sed -i '55d' constant/polyMesh/boundary #delete row
sed -i '54a        type     wall;' constant/polyMesh/boundary

sed -i '61d' constant/polyMesh/boundary #delete row
sed -i '60a        type     cyclicAMI;' constant/polyMesh/boundary
sed -i '63a                transform       noOrdering;' constant/polyMesh/boundary
sed -i '63a                neighbourPatch  AMI1;' constant/polyMesh/boundary
sed -i '63a                matchTolerance  0.0001;' constant/polyMesh/boundary

sed -i '70d' constant/polyMesh/boundary #delete row
sed -i '69a        type     wall;' constant/polyMesh/boundary
```

run

```
#!/bin/sh
# Source tutorial run functions
. $WM_PROJECT_DIR/bin/tools/RunFunctions

application="interDyMFoam"
runApplication ./Allclean
runApplication ./meshBuild
cp -r GMSH/masterIn/1e-06/polyMesh constant #Important: the timestep .../1e-06... ...
    must match the "△T" of the file in /system/controlDict
runApplication ./sedApply
cp -r 0/alpha1.org 0/alpha1
runApplication topoSet
runApplication setFields
runApplication $application
```

Symbols and abbreviations

List of symbols

A, A_1, A_2	amplitudes of planar waves
$A_\mathrm{r}, A_\mathrm{t}$	reflecting and transmitting amplitudes of planar waves
A_TR	transfer ratio of ink from the gravure cylinder
A_eff	effective transfer ratio of ink from the gravure cylinder
A_fill	fill ratio of ink in the gravure cells after the doctor blade process and before the transfer region
$\tilde{A}_\mathrm{TR}$	fit function of the experimental data of the transfer ratio $\overline{h}$
a, b, c, d	constants used for various regressions
a_c	radial acceleration within the rotating reference frame [m/s^2]
Bo	dimensionless Bond number
Bo_c	dimensionless modified Bond number
Ca	dimensionless capillary number
Cd	color depth of digital $\mathcal{RGB}$ image data for all color channels, usually 24-bit or 48-bit
c	speed of light in vacuum [m/s]
c_k	theoretical contrast values per color channel k
$\tilde{c}_k^{ij}$	measured contrast values per color channel k at pixel position ij
C_dry	drying constant of the ink under ambient conditions [nm/s]
c_spiro	mass concentration of spiro-MeOTAD in a solvent [wt-%]
d_l	thickness of layer l [m]
$d_{q,\mathrm{max}}$	maximim thickness of layer q [m]
d_l^{ij}	thickness of layer l at pixel position ij [m]
$d_{q,r}, d_{q,r}^\mathrm{wide}, d_{q,r}^\mathrm{narrow}$	theoretical thickness range of the top layer q for $r \in [1, p]$
$d_{q,\mathrm{est}}^{ij}$	resulting estimated thickness of the top layer q at pixel position ij [m]
d_c	cell depths of the single pyramidal gravure cells [µm]
d_inl	distance from contact line of cylinder and substrate to the meniscus position of the inlet ink bead [m]
$F_k(\lambda)$	spectral filter transfer function for color channels k
g	gravitational accelaration [m/s^2]
$h(i, j)$	measured dry film thickness of a printed field at discrete position image pixel position i, j
$h(x_j, y_i)$	measured dry film thickness of a printed field at discrete position $x_j y_i$ [nm]
$\overline{h}$	mean dry film thickness of a printed field [nm]
$\mathcal{H}$	Fourier transform of the dry film thickness $\overline{h}$

$\overline{h}_\mathrm{s}$	mean dry film thickness at a distinct step [nm]
$\delta\overline{h}_\mathrm{s}$	dry film thickness difference of a distinct step [nm]
$\delta\overline{h}_\mathrm{sr}$	relative dry film thickness difference of a distinct step
h_w	transferred wet film thickness [µm]
$\tilde{h}$	fit function of the experimental data of the dry film thickness $\overline{h}$
$\mathfrak{i}$	complex imaginary unit
i_m	pixel resolution of rows (in y-direction) of an image or thereof determined topography data
i, j	running variables denoting the pixel position in two dimensions (row, column or y, x-direction), usually of an image or thereof determined topography data
I	spectral irradiance of a planar wave or an arbitrary optical wave
$I_\mathrm{i}, I_\mathrm{t}$	incoming and transmitting spectral irradiances of light
I_r	reflecting spectral radiant exitance of light
j_m	pixel resolution of columns (in x-direction) of an image or thereof determined topography data
k	index denoting the color channels $k \in \{\mathcal{R}, \mathcal{G}, \mathcal{B}\}$
$K^{ij}, K_0, K_1^{ij}, \tilde{K}^{ij}, \tilde{K}_0, \tilde{K}_1^{ij}$	constants within the optical model representing various constant variations
$L(\lambda)$	spectral power distribution or spectrum of a light source
l	running integer index denoting the layer of a thin film stack from $l = 1, \ldots, q$ and the substrate for $l = 0$
$\mathcal{L}_c$	coherence length of a light spectrum
l_c	length of the contact zone [m]
L	a characteristic length [m]
M_l	Abele matrix representing layer l
M	Abele matrix representing the complete layer stack
$m_{[1,2][1,2]}$	matrix entries of the Abeles matrix M
$N(\lambda)$	complex refractive index
n	real part of the complex refractive index N
$N_\mathrm{air}(\lambda)$	complex refractive index of air
$N_l(\lambda)$	complex refractive index of layer l
$\tilde{N}_l^\mathrm{p}$	pseudo index of layer l for p-polarized light
$\tilde{N}_l^\mathrm{s}$	pseudo index of layer l for s-polarized light
O_max	maximum digital value of $\mathcal{RGB}$ image values per color channel
$O_k^{ij}, \tilde{O}_k^{ij}$	total optoelectronic response at pixel position ij for color channel k
$o_k^{ij}, \tilde{o}_k^{ij}$	optoelectronic response at pixel position ij for color channel k for $K^{ij} \stackrel{!}{=} 1$
$P(\lambda)$	spectral transfer function of the optical path
PSD	power spectral density
q	integer index denoting the top layer of a thin film stack
$R_\mathrm{total}(\lambda)$	total reflectance of a sample
$R_\mathrm{f}(\lambda)$	front-side reflectance originating from a thin film stack
$R'_\mathrm{f}(\lambda)$	front-side reflectance originating from a thin film stack in reverse order
$R_\mathrm{bs}(\lambda)$	backside reflectance of a sample (substrate and thin film stack)
$R_{0-\mathrm{air}}(\lambda)$	backside reflectance within the substrate

$\tilde{R}^{\mathrm{p}}_{\mathrm{total}}(\theta)$	total spectral reflectance of p-polarized light of the thin film sample for arbitrary incident angles θ
$\tilde{R}^{\mathrm{s}}_{\mathrm{total}}(\theta)$	total spectral reflectance of s-polarized light of the thin film sample for arbitrary incident angles θ
Re	dimensionless Reynolds number
R^2	coefficient of determination when used in the context of curve fitting
r_c	radius of the gravure cylinder [m]
Δr	difference of radii [m]
r'	radius of a tube [m]
$S(\lambda)$	optoelectronic transfer function of a photo sensor
$S_{\mathrm{QE}}(\lambda)$	quantum efficiency of a photo sensor
SR	screen ruling of a gravure cylinder [L/cm]
S_{q}	root mean squared (RMS) roughness of a surface
S_{qr}	relative root mean squared (RMS) roughness of a surface
S_{sk}	skewness of a surface
S_{ku}	kurtosis of a surface
$T_{\mathrm{total}}(\lambda)$	total transmittance of a sample
$T_{\mathrm{f}}(\lambda)$	transmittance through a thin film stack
$T'_{\mathrm{f}}(\lambda)$	transmittance through a thin film stack in reverse order
t	general variable denoting time
t_{d}	drying time of the ink under ambient conditions [s]
t_c	time of contact of gravure cylinder and substrate via the ink in nip [s]
Ta	dimensionless Taylor number
$U_k(\lambda)$	optoelectronic transfer filter function
V_{c}	cell volume of a gravure cylinder [ml/m^2]
$V_{\mathrm{c,s}}$	mean cell volume between data points which exhibit a distinct thickness step
$\overline{V}_{\mathrm{c,s}}$	averaged mean cell volume $V_{\mathrm{c,s}}$
v	tangential printing velocity at the contact zone of cylinder and substrate [m/s]
V_{fill}	ink volume in the gravure cells after the doctor blade process before ink transfer
V_{print}	remaining ink volume in the gravure cells after ink transfer
V_{trans}	ink volume transferred to the substrate
W	probability, dimensionless $\in [0, 1]$
We	dimensionless Weber number
Δx	step size of discrete data in x-direction
x_j	discrete lateral position in x-direction with $x_j = j\,\Delta x$ for $j \in [0, j_{\mathrm{m}}]$ in [m]
X	maximum width or value in x direction of the image and thickness data [m]
Δy	step size of discrete data in y-direction
y_i	discrete lateral position in y-direction with $y_i = i\,\Delta y$ for $i \in [0, i_{\mathrm{m}}]$ in [m]
Y	maximum height or value in y direction of the image and thickness data [m]
α	half the opening angle defined by the numerical aperture [°]
γ	value used for the gamma correction of images
$\delta^{\,ij}$	Euclidian distance of measured $\mathcal{RGB}$ contrast values to the list of theoretical ones per pixel
$\delta^{\,ij}_{\mathrm{min}}$	minimum of $\delta^{\,ij}$

$\overline{\delta}_{\text{min}}$	δ_{min}^{ij} averaged over all pixels
ε	error added to selected variables
η	dynamic viscosity of a fluid [mPa $\cdot$ s]
θ	incident and reflecting angle of the light enclosing to the normal of the surface [°]
κ	imaginary part of the complex refractive index N
λ	optical wavelength [nm]
λ_{min}	minimum optical wavelength of the visible spectrum [nm]
λ_{max}	maximum optical wavelength of the visible spectrum [nm]
λ_c	peak wavelength of a Gaussian spectrum
$\Delta\lambda_c$	width of a Gaussian spectrum around its peak wavelength
λ_{iso}	dominant isotropic wavelength of a surface
λ_x	dominant isotropic wavelength in x direction [m]
λ_y	dominant isotropic wavelength in y direction [m]
μ_q	spatial frequency of the 2D discrete Fourier transform $\mathcal{H}$ of the dry film thickness $\overline{h}$ corresponding to the integer i in the spatial image domain
ν_p	spatial frequency of the 2D discrete Fourier transform $\mathcal{H}$ of the dry film thickness $\overline{h}$ corresponding to the integer j in the spatial domain
π	number $\pi = 3.14159\ldots$
ρ	mass density [g/cm]
ρ_{tol}	mass density of toluene [g/cm]
ρ_{spiro}	mass density of spiro-MeOTAD of the solid phase [g/cm]
ρ_{sol}	mass density of the ink solution spiro-MeOTAD solved in toluene [g/cm]
ϱ	spatial radial frequency coordinate in a polar coordinate system in the Fourier frequency domain
ϱ	Fresnel reflection coefficient
ϱ_{f}	Fresnel reflection coefficient of a thin film stack
σ	surface tension of a fluid [mN/m]
τ	Fresnel transmission coefficient
τ_{f}	Fresnel transmission coefficient of a thin film stack
Φ, Φ_1, Φ_2	total phases of planar waves
$\Phi^\circ, \Phi_1^\circ, \Phi_2^\circ$	constant phase offsets of planar waves
$\varphi_l, \tilde{\phi}_l$	phase difference light experiences when traveling through the layer l
φ	angle in a polar coordinate system in the Fourier frequency domain
ω	angular frequency of a planar wave

List of abbreviations

1D	one dimensional
2D	two dimensional
3D	three dimensional
AFM	atomic force microscopy
AMI	arbitrary mesh interface
a.u.	arbitrary unit
bit	binary digit
BS	beam-splitter

CCD	charge-coupled device
CFD	computational fluid dynamics
CMOS	complementary metal oxide semiconductor
CSV	comma-separated values
DFT	discrete Fourier transformation
DHM	digital holographic microscopy
DPI	dots per inch
FFT	fast Fourier transformation
FOV	field of view
GMSH	open-source software for generating comptutational meshes
ICR	imaging color reflectometry
IDD	Institute of Printing Science and Technology, Technische Universität Darmstadt, Germany
ITO	indium tin oxide
LED	light emitting diode
LS	least-square
MA	magnification
MATLAB	**mat**rix **lab**oratory: numerical computing software from Mathworks, USA
$M_{1,\ldots,5}$	mirrors in an optical system
NA	numerical aperture
NSE	Navier-Stokes equations
OFET	organic field-effect transistor
OLED	organic light emitting diode
OpenFOAM	registered trademark of ESI, France, **Open** Source **F**ield **O**peration **A**nd **M**anipulation, a open-source software for CFD
OPV	organic photovoltaics
PET	polyethylene terephthalate
PSI	phase-shifting interferometry
$\mathcal{RGB}$	red green blue
RMS	root mean squared
RS232	a serial port interface standard defined by the Electronic Industries Association in 1969
SE	spectroscopic ellipsometry
Si	silicon
SiO_2	silicon dioxide
SPD	spectral power distribution in color science
spiro-MeOTAD	$2,2'7,7'$-tetrakis-(N,N-di-p-methoxyphenyl amine)-$9,9'$-spirobi-fluorene
TEM	transmission electron microscopy
UV	ultra-violet light
VOF	volume of fluid method
VSI	vertical scanning interferometry
XPS	X-ray photoelectron spectroscopy

References

[1] Abeles, F. "Optical properties of very thin films". In: *Thin Solid Films* 34 (May 1976), pp. 291–302.

[2] Afanasiev, K., Münch, A., and Wagner, B. "Landau-Levich problem for non-Newtonian liquids". In: *Physical Review E* 76.3 (Sept. 2007).

[3] Ahmed, D. H., Sung, H. J., and Kim, D.-S. "Simulation of non-Newtonian ink transfer between two separating plates for gravure-offset printing". In: *International Journal of Heat and Fluid Flow* 32.1 (Feb. 2011), pp. 298–307.

[4] Ahn, S., Lee, S., and Na, Y. "Elasticity Effect on the Ink Transfer Process in Gravure Printing". In: *Computational Science and Its Applications ICCSA 2008*. Ed. by Gervasi, O., Murgante, B., LaganÃ, A., Taniar, D., Mun, Y., and Gavrilova, M. Vol. 5072. Lecture Notes in Computer Science. Springer Berlin / Heidelberg, 2008, pp. 565–575.

[5] Ahn, S. and Na, Y. "On the Ink Transfer Process in Gravure Printing". In: *Computational Science and Its Applications ICCSA 2007*. Ed. by Gervasi, O. and Gavrilova, M. Vol. 4706. Lecture Notes in Computer Science. Springer Berlin / Heidelberg, 2007, pp. 907–918.

[6] Alex Lee, J., Rothstein, J. P., and Pasquali, M. "Computational study of viscoelastic effects on liquid transfer during gravure printing". In: *Journal of Non-Newtonian Fluid Mechanics* (May 2013).

[7] Amar, M. and Bonn, D. "Fingering instabilities in adhesive failure". In: *Physica D: Nonlinear Phenomena* 209.1-4 (Sept. 2005), pp. 1–16.

[8] Archambeau, S., Seguy, I., Jolinat, P., Farenc, J., Destruel, P., Nguyen, T., Bock, H., and Grelet, E. "Stabilization of discotic liquid organic thin films by ITO surface treatment". In: *Applied Surface Science* 253.4 (Dec. 2006), pp. 2078–2086.

[9] Asinovski, L., Beaglehole, D., and Clarkson, M. T. "Imaging ellipsometry: quantitative analysis". In: *Physica Status Solidi (a)* 205.4 (Apr. 2008), pp. 764–771.

[10] Bass, M. HANDBOOK OF OPTICS VOL. 2: DEVICES, MEASUREMENTS, AND PROPERTIES. Ed. by America., O. S. of. New York: McGraw-Hill, 1995.

[11] Bauman, T., Sullivan, T., and Middleman, S. "Ribbing instability in coating flows: effect of polymer additives". In: *Chemical Engineering Communications* 14.1-2 (Feb. 1982), pp. 35–46.

[12] Becker, J., Grün, G., Seemann, R., Mantz, H., Jacobs, K., Mecke, K. R., and Blossey, R. "Complex dewetting scenarios captured by thin-film models". In: *Nature Materials* 2.1 (Dec. 2002), pp. 59–63.

[13] Behler, H. "Die Randstruktur von Druckpunkten - Eine experimentelle Untersuchung der Farbspaltungsströmung". Ph.D. Thesis. Darmstadt: Technische Universität Darmstadt, 1993.

[14] Ben Amar, M. "Viscous fingering in a wedge". In: *Physical Review A* 44.6 (Sept. 1991), pp. 3673–3685.

[15] Benkreira, H. "Dynamic wetting in metering and pre-metered forward roll coating". In: *Chemical Engineering Science* 57.15 (Aug. 2002), pp. 3025–3032.

[16] Benkreira, H. and Cohu, O. "Direct forward gravure coating on unsupported web". In: *Chemical Engineering Science* 53.6 (1998), pp. 1223–1231.

[17] Bertran, F. L., Pursals, R. A., and Artigues, C. C. “Dual technology optical profilometer”. U.S. Patent US 2007/0165241 Al. July 19, 2007.

[18] Bery, E. “Gravure printing on non-absorbing materials”. In: *Proc. Taga*. Technical Association of the Graphic Arts, Rochester NY, 1978, pp. 207–220.

[19] Bery, J. “Mechanisms Governing Gravure Printing”. In: *Coating Conference*. Atlanta, GA: Tappi Press, 1985, pp. 149–159.

[20] Bigas, M., Cabruja, E., Forest, J., and Salvi, J. “Review of CMOS image sensors”. In: *Microelectronics Journal* 37.5 (May 2006), pp. 433–451.

[21] Binnig, G. and Quate, C. F. “Atomic Force Microscope”. In: *Physical Review Letters* 56.9 (Mar. 1986), pp. 930–933.

[22] Bonn, D., Eggers, J., Indekeu, J., Meunier, J., and Rolley, E. “Wetting and spreading”. In: *Reviews of Modern Physics* 81.2 (May 2009), pp. 739–805.

[23] Born, M. PRINCIPLES OF OPTICS: ELECTROMAGNETIC THEORY OF PROPAGATION, INTERFERENCE AND DIFFRACTION OF LIGHT. 7th expanded ed. Cambridge ; New York: Cambridge University Press, 1999.

[24] Bornemann, N., Sauer, H. M., and Dörsam, E. “Thin Film Behaviour after Ink Transfer in Printing Processes”. In: *Large-area, Organic and Printed Electronics Convention (LOPE-C)*. 9.4. Frankfurt, Germany: OE-A (Organic and Printed Electronics Association), 2010, pp. 138 –142.

[25] Bornemann, N., Sauer, H. M., and Dörsam, E. “Evaluation and Determination of Gravure Cylinders for Functional Printing”. In: *Large-area, Organic and Printed Electronics Convention (LOPE-C)*. Frankfurt, Germany: OE-A (Organic and Printed Electronics Association), 2011, pp. 309–313.

[26] Bornemann, N., Guck, T., Bitsch, T., and Dörsam, E. “Determination of gravure cells using confocal microscopy”. In: *Proceedings: 39th International Research Conference of Iariga*. Ljubljana, Slovenia, Sept. 2012.

[27] Bornemann, N., Sauer, H. M., and Dörsam, E. “Gravure Printed Ultrathin Layers of Small-Molecule Semiconductors on Glass”. In: *Journal of Imaging Science and Technology* 55.4 (2011), p. 040201.

[28] Bornemann, N., Sauer, H. M., and Dörsam, E. “Experimental Investigation of the Filling and Emptying of Gravure Cells”. In: *Materials Science and Engineering Congress (MSE)*. Poster. Darmstadt, Germany, Sept. 2012.

[29] Bracewell, R. N. THE FOURIER TRANSFORM AND ITS APPLICATIONS. English. Boston: McGraw Hill, 2000.

[30] Brethour, J. M. “Filling and Emptying of Gravure Cells - A CFD Analysis”. In: *4th European Coating Symposium*. Brussels, Belgium, 2001.

[31] Burns, P. D. “Analysis of image noise in multispectral color acquisition”. Ph.D. Thesis. Rochester N.Y., USA: Rochester Institute of Technology, 1997.

[32] Cahn, J. W. “Phase Separation by Spinodal Decomposition in Isotropic Systems”. In: *The Journal of Chemical Physics* 42.1 (1965), p. 93.

[33] Carlson, B. "Comparison of modern CCD and CMOS image sensor technologies and systems for low resolution imaging". In: vol. 1. IEEE, 2002, pp. 171–176.

[34] Carvalho, M. S. and Scriven, L. E. "Deformable roll coating flows: steady state and linear perturbation analysis". In: *Journal of Fluid Mechanics* 339 (May 1997), pp. 143–172.

[35] Carvalho, M. and Scriven, L. "Three-Dimensional Stability Analysis of Free Surface Flows: Application to Forward Deformable Roll Coating". In: *Journal of Computational Physics* 151.2 (May 1999), pp. 534–562.

[36] Casademunt, J. "Viscous fingering as a paradigm of interfacial pattern formation: Recent results and new challenges". In: *Chaos: An Interdisciplinary Journal of Nonlinear Science* 14.3 (2004), p. 809.

[37] Cassie, A. B. D. and Baxter, S. "Wettability of porous surfaces". In: *Transactions of the Faraday Society* 40 (1944), p. 546.

[38] Castillo, M. E. G. and Patera, A. T. "Three-dimensional ribbing instability in symmetric forward-roll film-coating processes". In: *Journal of Fluid Mechanics* 335 (1997), p. 323.359.

[39] Castillo, M. E. G. "Modelling and Parallel Simulation of Three-Dimensional Ribbing Instability in Symmetric Forward-Roll Coating Processes". Ph.D. Thesis. Cambridge: Massachusetts Institute of Technology, 1994.

[40] *CCD image sensor KAF-8300 datasheet*. Rochester, USA: Truesense Imaging, Inc.

[41] Chen, Y. *et al.* "Rapid Determination of the Thickness of Graphene Using the Ratio of Color Difference". In: *The Journal of Physical Chemistry C* 115.14 (Apr. 2011), pp. 6690–6693.

[42] Cheng, J.-A., Chen, C. H., and Liao, C. H. "Solution-Processible Small Molecular Organic Light-Emitting Diode Material and Devices Based on the Substituted Aluminum Quinolate". In: *Chemistry of Materials* 16.15 (July 2004), pp. 2862–2868.

[43] Clay Mathematics Institute and American Mathematical Society. THE MILLENNIUM PRIZE PROBLEMS. Providence, R.I. : Cambridge, MA: American Mathematical Society, 2006.

[44] *CMOS image sensor KAC-00401 datasheet*. Rochester, USA: Truesense Imaging, Inc.

[45] Cook, C. "Spectroscopic ellipsometry for in-line monitoring of silicon nitrides". In: *Thin Solid Films* 455-456 (May 2004), pp. 794–797.

[46] Couder, Y., Gérard, N., and Rabaud, M. "Narrow fingers in the Saffman-Taylor instability". In: *Physical Review A* 34.6 (Dec. 1986), pp. 5175–5178.

[47] Coyle, D. J., Macosko, C. W., and Scriven, L. E. "Film-splitting flows in forward roll coating". In: *Journal of Fluid Mechanics* 171.-1 (1986), p. 183.

[48] Coyle, D. J., Macosko, C. W., and Scriven, L. E. "The fluid dynamics of reverse roll coating". In: *AIChE Journal* 36.2 (Feb. 1990), pp. 161–174.

[49] Darlington, R. B. "Is kurtosis really peakedness?" In: *The American Statistician* 24.2 (1970), pp. 19–22.

[50] De Carlo, L. T. "On the meaning and use of kurtosis." In: *Psychological Methods* 2.3 (1997), pp. 292–307.

[51] De Grace, J. H. and Mangin, P. J. "A mechanistic approach to ink transfer. Part I: Effect of substrate properties and press conditions". In: *Advances in Printing Science and Technology* 17 (1984), pp. 312–332.

[52] De Grace, J. H. and Mangin, P. J. "A Mechanistic Approach to Ink Transfer. Part 2: The Splitting Behaviour of Inks in Printing Nips". In: *Advances in Printing Science and Technology* 21 (1988), pp. 146–141.

[53] Deegan, R., Bakajin, O., Dupont, T., Huber, G., Nagel, S., and Witten, T. "Contact line deposits in an evaporating drop". In: *Physical Review E* 62.1 (July 2000), pp. 756–765.

[54] Deegan, R. D., Bakajin, O., Dupont, T. F., Huber, G., Nagel, S. R., and Witten, T. A. "Capillary flow as the cause of ring stains from dried liquid drops". In: *Nature* 389.6653 (1997), pp. 827–829.

[55] Derjaguin, B. "On the thickness of a layer of liquid remaining on the walls of vessels after their emptying, and the theory of the application of photoemulsion after coating on the cine film (presented by academician A.N. Frumkin on July 28, 1942)". In: *Progress in Surface Science* 43.1-4 (May 1993), pp. 129–133.

[56] Diaz, F. J. K. "Effect of the Flow in a Printing Nip on Paper Runnability During Sheetfed Offset Printing". In: *Appita Journal: Journal of the Technical Association of the Australian and New Zealand Pulp and Paper Industry* 64.2 (2011), pp. 158–164.

[57] Ding, I.-K., Tétreault, N., Brillet, J., Hardin, B. E., Smith, E. H., Rosenthal, S. J., Sauvage, F., Grätzel, M., and McGehee, M. D. "Pore-Filling of Spiro-OMeTAD in Solid-State Dye Sensitized Solar Cells: Quantification, Mechanism, and Consequences for Device Performance". In: *Advanced Functional Materials* 19.15 (Aug. 2009), pp. 2431–2436.

[58] Dodds, S., Carvalho, M. d. S., and Kumar, S. "Stretching and slipping of liquid bridges near plates and cavities". In: *Physics of Fluids* 21.9 (2009), p. 092103.

[59] Drelich, J., Fang, C., and White, C. L. "Measurement of interfacial tension in fluid-fluid systems". In: *Encyclopedia of Surface and Colloid Science* (2002), pp. 3152–3166.

[60] Dörsam, E. and Bornemann, N. *Printing Technology for Electronics*. Lecture Notes, TU Darmstadt, Germany. 2011.

[61] Dubé, M., Drolet, F., Daneault, C., and Mangin, P. J. "Hydrodynamics of Ink Transfer". In: *Proc. Printing and Graphics Arts Conference*. Cincinnati, Ohio, USA, Sept. 2006.

[62] Duhamel, P. and Vetterli, M. "Fast Fourier transforms: a tutorial review and a state of the art". In: *Signal processing* 19.4 (1990), pp. 259–299.

[63] Dumouchel, W. and O'Brien, F. "Integrating a robust option into a multiple regression computing environment". In: *Computing and graphics in statistics*. Springer-Verlag New York, Inc., 1991, pp. 41–48.

[64] El Gamal, A. and Eltoukhy, H. "CMOS image sensors". In: *Circuits and Devices Magazine, IEEE* 21.3 (2005), pp. 6–20.

[65] Elsayad, S., Morsy, F., El-Sherbiny, S., and Abdou, E. "Some factors affecting ink transfer in gravure printing". In: *Pigment and Resin Technology* 31.4 (2002), pp. 234–240.

[66] *Epson Perfection 3170 Photo, datasheet*.

[67] Fantacci, S., De Angelis, F., Nazeeruddin, M. K., and Grätzel, M. "Electronic and Optical Properties of the Spiro-MeOTAD Hole Conductor in Its Neutral and Oxidized Forms: A DFT/TDDFT Investigation". In: *The Journal of Physical Chemistry C* 115.46 (Nov. 2011), pp. 23126–23133.

[68] Fell, D. “Dynamic wetting of complex liquids”. eng. Ph.D. Thesis. Mainz, Germany: Johannes Gutenberg-Universität, 2013.

[69] Fernandez, J., Krechetnikov, R., and Homsy, G. M. “Experimental study of a surfactant-driven fingering phenomenon in a Hele-Shaw cell”. In: *Journal of Fluid Mechanics* 527 (Mar. 2005), pp. 197–216.

[70] Fields, R. J. and Ashby, M. F. “Finger-like crack growth in solids and liquids”. In: *Philosophical Magazine* 33.1 (Jan. 1976), pp. 33–48.

[71] Fornefeld-Schwarz, U. M. and Svejda, P. “Refractive Indices and Relative Permittivities of Liquid Mixtures of γ-Butyrolactone, γ-Valerolactone, δ-Valerolactone, or ε-Caprolactone + Benzene, + Toluene, or + Ethylbenzene at 293.15 K and 313.15 K and Atmospheric Pressure”. In: *Journal of Chemical and Engineering Data* 44.3 (May 1999), pp. 597–604.

[72] Fowkes, F. M. “Dispersion Force Contributions to Surface and Interfacial Tensions, Contact Angles, and Heats of Immersion”. In: *Contact Angle, Wettability, and Adhesion*. Ed. by Fowkes, F. M. Vol. 43. Washington, D. C.: American Chemical Society, Jan. 1964, pp. 99–111.

[73] Frank, E. and Rupp, R. “Printing Inks”. In: *Ullmann’s Encyclopedia of Industrial Chemistry*. Weinheim, Germany: Wiley-VCH Verlag GmbH & Co. KGaA, July 2006.

[74] Garcia-Sucerquia, J., Xu, W., Jericho, S. K., Klages, P., Jericho, M. H., and Kreuzer, H. J. “Digital in-line holographic microscopy”. In: *Applied Optics* 45.5 (2006), p. 836.

[75] Gaskell, P. H., Innes, G. E., and Savage, M. D. “An experimental investigation of meniscus roll coating”. In: *Journal of Fluid Mechanics* 355 (Jan. 1998), pp. 17–44.

[76] Gaskell, P., Rees, S., Savage, M., and Storey, S. “A Mathematical Model of Roll-to-Web Kiss Coating”. In: *Chemical Engineering Research and Design* 76.1 (Jan. 1998), pp. 29–37.

[77] Gasvik, K. J. OPTICAL METROLOGY. Third Edition. West Sussex, England: John Wiley & Sons Ltd, 2002.

[78] Gennes, P. de. “Wetting: statics and dynamics”. In: *Reviews of Modern Physics* 57.3 (July 1985), pp. 827–863.

[79] Gennes, P.-G. de. CAPILLARITY AND WETTING PHENOMENA : DROPS, BUBBLES, PEARLS, WAVES. New York: Springer, 2004.

[80] George, H. F. “Electrostatically Assisted Ink Transfer in Gravure Printing”. In: *Colloids and Surfaces in Reprographic Technology*. Ed. by Hair, M. and Croucher, M. D. Vol. 200. Washington, D. C.: American Chemical Society, Oct. 1982, pp. 359–370.

[81] Geuzaine, C. and Remacle, J.-F. “Gmsh: A 3-D finite element mesh generator with built-in pre- and post-processing facilities”. In: *International Journal for Numerical Methods in Engineering* 79.11 (2009), pp. 1309–1331.

[82] Ghadiri, F., Ahmed, D. H., Sung, H. J., and Shirani, E. “Non-Newtonian ink transfer in gravure–offset printing”. In: *International Journal of Heat and Fluid Flow* 32.1 (Feb. 2011), pp. 308–317.

[83] Gibbs, J. W. SCIENTIFIC PAPERS OF J. WILLARD GIBBS. Vol. 1. Longmans, Green and Company, 1906.

[84] Giesekus, H. PHÄNOMENOLOGISCHE RHEOLOGIE: EINE EINFÜHRUNG. Berlin; New York: Springer-Verlag, 1994.

[85] Gingras, M. and Rácz, Z. “Noise and the linear stability analysis of viscous fingering”. In: *Physical Review A* 40.10 (Nov. 1989), pp. 5960–5965.

[86] Gokhale, V. V. “Bounds for Region of Ribbing Instability in Some Free Surface Coating Flows”. In: *Journal of Rheology* 25.4 (1981), p. 421.

[87] Good, R. “Contact Angles and the Surface Free Energy of Solids”. English. In: *Surface and Colloid Science*. Ed. by Good, R. and Stromberg, R. Springer US, Jan. 1979, pp. 1–29.

[88] Gramlich, C. M., Mazouchi, A., and Homsy, G. M. “Time-dependent free surface Stokes flow with a moving contact line. II. Flow over wedges and trenches”. In: *Physics of Fluids* 16.5 (2004), p. 1660.

[89] Gravure Education Foundation and Gravure Association of America. GRAVURE: PROCESS AND TECHNOLOGY. English. Rochester, N.Y., 2003.

[90] Greener, J., Sullivan, T., Turner, B., and Middleman, S. “Ribbing instability of a two-roll coater: Newtonian fluids”. In: *Chemical Engineering Communications* 5.1-4 (Jan. 1980), pp. 73–83.

[91] Griesheimer, S. “Experimentelle Untersuchung zur Farbspaltung und Farbübertragung im Flexodruck”. Ph.D. Thesis. Darmstadt: Technische Universität Darmstadt, 2013.

[92] Groot, P. de and Deck, L. “Surface Profiling by Analysis of White-light Interferograms in the Spatial Frequency Domain”. In: *Journal of Modern Optics* 42.2 (Feb. 1995), pp. 389–401.

[93] Groot, P. de, Lega, X. Colonna de, Kramer, J., and Turzhitsky, M. “Determination of Fringe Order in White-Light Interference Microscopy”. In: *Applied Optics* 41.22 (Aug. 2002), p. 4571.

[94] Hager, W. H. “Wilfrid Noel Bond and the Bond number”. In: *Journal of Hydraulic Research* 50.1 (Feb. 2012), pp. 3–9.

[95] Haidinger, W. “Die Interferenzlinien am Glimmer. Berührungsringe und Plattenringe”. In: *Annalen der Physik und Chemie* 172.11 (1855), pp. 453–468.

[96] Hambsch, M., Reuter, K., Kempa, H., and Hübler, A. “Comparison of fully printed unipolar and complementary organic logic gates”. In: *Organic Electronics* 13.10 (Oct. 2012), pp. 1989–1995.

[97] Hanumanthu, R. “Variation of gravure coating thickness during early stages of doctor blade wear”. In: *AIChE Journal* 45.12 (Dec. 1999), pp. 2487–2494.

[98] Hardeberg, J. Y. “Spectral characterization of electronic cameras”. In: vol. 3409. SPIE, 1998, pp. 100–109.

[99] Hasegawa, T. and Sorimachi, K. “Wavelength and depth of ribbing in roll coating and its elimination”. In: *AIChE Journal* 39.6 (June 1993), pp. 935–945.

[100] Hele-Shaw, H. S. “The Flow of Water”. In: *Nature* 58.1489 (May 1898), pp. 34–36.

[101] Henning, G. “Laser Precision Micro Fabrication in the Printing Industry”. In: *Journal of Laser Micro/Nanoengineering* 1.2 (July 2006), pp. 89–98.

[102] Hernandez-Sosa, G., Bornemann, N., Ringle, I., Agari, M., Doersam, E., Mechau, N., and Lemmer, U. “Ink Properties Optimization for Gravure-printed Flexible Organic Light-emitting Diodes”. In: *Symposium WW: Roll-to-Roll Processing of Electronics and Advanced Functionalities*. Talk. Boston, USA, Nov. 2012.

[103] Hernandez-Sosa, G., Bornemann, N., Ringle, I., Agari, M., Dörsam, E., Mechau, N., and Lemmer, U. "Rheological and Drying Considerations for Uniformly Gravure-Printed Layers: Towards Large-Area Flexible Organic Light-Emitting Diodes". In: *Advanced Functional Materials* (Feb. 2013).

[104] Hewson, R, Kapur, N, and Gaskell, P. "A theoretical and experimental investigation of trihelical gravure roll coating". In: *Chemical Engineering Science* 61.16 (Aug. 2006), pp. 5487–5499.

[105] Hewson, R. W. "Tri-Helical Direct Gravure Coating". Ph.D. Thesis. Leeds, England: University of Leeds, 2006.

[106] Hlubina, P., Lunacek, J., Ciprian, D., and Chlebus, R. "Spectral interferometry and reflectometry used to measure thin films". In: *Applied Physics B* 92.2 (June 2008), pp. 203–207.

[107] Holmvall, M. "Nip Mechanics, Hydrodynamics and Print Quality in Flexo Post-Printing". Ph.D. Thesis. Sundsvall, Sweden: Mid Sweden University, Department of Natural Sciences, Engineering and Mathematics, 2010.

[108] Homsy, G. M. "Viscous Fingering in Porous Media". In: *Annual Review of Fluid Mechanics* 19.1 (Jan. 1987), pp. 271–311.

[109] Hrehorova, E., Pekarovicova, A., Bliznyuk, V. N., and Fleming, P. D. "Polymeric Materials for Printed Electronics and Their Interactions". In: Anchorage, Alaska, Sept. 2007.

[110] Hu, H. and Larson, R. G. "Evaporation of a Sessile Droplet on a Substrate". In: *The Journal of Physical Chemistry B* 106.6 (Feb. 2002), pp. 1334–1344.

[111] Hu, H. and Larson, R. G. "Analysis of the Effects of Marangoni Stresses on the Microflow in an Evaporating Sessile Droplet". In: *Langmuir* 21.9 (Apr. 2005), pp. 3972–3980.

[112] Hu, H. and Larson, R. G. "Marangoni Effect Reverses Coffee-Ring Depositions". In: *The Journal of Physical Chemistry B* 110.14 (Apr. 2006), pp. 7090–7094.

[113] Hu, H. and Larson, R. G. "Drying a sessile droplet: imaging and analysis of transport and deposition patterns". In: *Evaporative Self-Assembly Of Ordered Complex Structures*. World Scientific, Feb. 2012, pp. 1–57.

[114] Huang, W., Lee, S., Sung, H., Lee, T., and Kim, D. "Simulation of liquid transfer between separating walls for modeling micro-gravure-offset printing". In: *International Journal of Heat and Fluid Flow* 29.5 (Oct. 2008), pp. 1436–1446.

[115] Hübner, H. "Ein Beitrag zum Problem der Flüssigkeitsspaltung in der Drucktechnik". DE. Ph.D. Thesis. Darmstadt: Technische Universität Darmstadt, 1991.

[116] Iliopoulos, I. and Scriven, L. E. "A blade-coating study using a finite-element simulation". In: *Physics of Fluids* 17.12 (2005), p. 127101.

[117] Irie, K, McKinnon, A. E., Unsworth, K, and Woodhead, I. M. "A model for measurement of noise in CCD digital-video cameras". In: *Measurement Science and Technology* 19.4 (Apr. 2008), p. 045207.

[118] Isaksson, P. and Rigdahl, M. "Numerical simulation of blade coating with short dwell and roll application coaters". In: *Rheologica Acta* 33.5 (1994), pp. 454–467.

[119] Ishii, H. T. and Dannoura, M. “Measurement of Three-Dimensional Morphology and Surface Area of Conifer Shoots and Roots using the Desktop Scanner and Silhouette Image Analysis”. In: *Eurasian Journal of Forest Research* 7.1 (Feb. 2004), pp. 27–32.

[120] Israelachvili, J. INTERMOLECULAR AND SURFACE FORCES. 2nd ed. Academic Press London, 1991.

[121] Jacobs, K., Seemann, R., and Mecke, K. “Dynamics of Structure Formation in Thin Liquid Films: A Special Spatial Analysis”. In: *Statistical Physics and Spatial Statistics. The Art of Analyzing and Modeling Spatial Structures and Pattern Formation*. Ed. by Stoyan K., M. D. Vol. 554. Lecture Notes in Physics, Berlin Springer Verlag. 2000, pp. 72–91.

[122] Joyce, E. and Fuchs, G. L. “Study of gravure ink transfer”. In: *Proc. Taga*. Technical Association of the Graphic Arts, Rochester NY, 1966, pp. 291–311.

[123] Jung, I., Pelton, M., Piner, R., Dikin, D. A., Stankovich, S., Watcharotone, S., Hausner, M., and Ruoff, R. S. “Simple Approach for High-Contrast Optical Imaging and Characterization of Graphene-Based Sheets”. In: *Nano Letters* 7.12 (Dec. 2007), pp. 3569–3575.

[124] Kalliadasis, S., Bielarz, C., and Homsy, G. M. “Steady free-surface thin film flows over topography”. In: *Physics of Fluids* 12.8 (2000), p. 1889.

[125] Kang, H. W., Sung, H. J., Lee, T.-M., Kim, D.-S., and Kim, C.-J. “Liquid transfer between two separating plates for micro-gravure-offset printing”. In: *Journal of Micromechanics and Microengineering* 19.1 (Jan. 2009), p. 015025.

[126] Kashiwagi, H., Hashimoto, T., Tanaka, Y., Kubota, H., and Makita, T. “Thermal conductivity and density of toluene in the temperature range 273–373 K at pressures up to 250 MPa”. English. In: *International Journal of Thermophysics* 3.3 (Sept. 1982), pp. 201–215.

[127] Kawaguchi, M. “Comparison of viscous fingering patterns in polymer and newtonian solutions”. In: *Physica D: Nonlinear Phenomena* 105.1-3 (June 1997), pp. 121–129.

[128] Kemper, B., Langehanenberg, P., and Von Bally, G. “Digital holographic microscopy”. In: *Optik & Photonik* 2.2 (2007), pp. 41–44.

[129] Kheshgi, H. S. “Profile equations for film flows at moderate Reynolds numbers”. In: *AIChE Journal* 35.10 (Oct. 1989), pp. 1719–1727.

[130] Kheshgi, H. S. and Scriven, L. “Dewetting: Nucleation and growth of dry regions”. In: *Chemical Engineering Science* 46.2 (1991), pp. 519–526.

[131] Kim, A., Lee, H., Lee, J., Cho, S. M., and Chae, H. “Bi-Layer Gravure Printed Nanoscale Thick Organic Layers for Organic Light Emitting Diode”. In: *Journal of Nanoscience and Nanotechnology* 11 (Jan. 2011), 546–549(4).

[132] Kim, H. J., Krane, M. J. M., Trumble, K. P., and Bowman, K. J. “Analytical Fluid Flow Models for Tape Casting”. In: *Journal of the American Ceramic Society* 0.0 (June 2006), 2769Ũ2775.

[133] Kim, I., Kwak, S.-W., Kim, K.-S., Lee, T.-M., Jo, J., Kim, J.-H., and Lee, H.-J. “Effect of ink cohesive force on gravure offset printing”. In: *Microelectronic Engineering* 98 (Oct. 2012), pp. 587–589.

[134] Kim, M. K. DIGITAL HOLOGRAPHIC MICROSCOPY. Springer, 2011.

[135] Kim, S. and Na, Y. “Study on the web deformation in ink transfer process for R2R printing application”. In: *International Journal of Precision Engineering and Manufacturing* 11.6 (Dec. 2010), pp. 945–954.

[136] Kipphan, H. HANDBOOK OF PRINT MEDIA: TECHNOLOGIES AND PRODUCTION METHODS. Berlin; New York: Springer, 2001.

[137] Kitsomboonloha, R., Morris, S. J. S., Rong, X., and Subramanian, V. “Femtoliter-Scale Patterning by High-Speed, Highly Scaled Inverse Gravure Printing”. In: *Langmuir* (Nov. 2012), pp. 16711–16723.

[138] Kleeberger, K. S. and Moser, B. C. “Flatbed Scanners: An Alternative Tool for Gathering Horticultural Data”. In: *HortTechnology* 12.3 (Sept. 2002), pp. 444–446.

[139] Kline, J. “The dynamics of Blade Coater Rheology”. In: *Proceedings*. Atlanta, GA: Tappi Press, 1985, pp. 181–188.

[140] Kopola, P., Tuomikoski, M., Suhonen, R., and Maaninen, A. “Gravure printed organic light emitting diodes for lighting applications”. In: *Thin Solid Films* 517.19 (2009), pp. 5757–5762.

[141] Korochkina, T, Jewell, E, Claypole, T, and Gethin, D. “Experimental and numerical investigation into nonlinear deformation of silicone rubber pads during ink transfer process”. In: *Polymer Testing* 27.6 (Sept. 2008), pp. 778–791.

[142] Krechetnikov, R. and Homsy, G. M. “Experimental study of substrate roughness and surfactant effects on the Landau-Levich law”. In: *Physics of Fluids* 17.10 (2005), p. 102108.

[143] Krug, J. DIE ENTSTEHUNG FRAKTALER OBERFLÄCHEN: UNTERSUCHUNGEN ZUR STATISTISCHEN MECHANIK VON WACHSTUMSPROZESSEN. Deutsch Harri GmbH, 1990.

[144] Kunz, W. “Ink transfer in gravure process”. In: *Proc. Taga*. Technical Association of the Graphic Arts, Rochester NY, 1975, pp. 151–176.

[145] Kuria, J. M., Schön, R., and Börret, R. “A Flatbed Scanner Based Wavefront Sensing Unit for Optics Quality Control”. In: *Proceedings: 18th World Conference on Nondestructive Testing*. Durban, South Africa, Apr. 2012.

[146] Kuzmak, J. M. “Bevelled-Blade Coating”. In: *Proceedings*. Atlanta, GA: Tappi Press, 1985, pp. 5–12.

[147] Lai, G. and Yatagai, T. “Generalized phase-shifting interferometry”. In: *Journal of the Optical Society of America A* 8.5 (May 1991), p. 822.

[148] Lam, C. N. C., Wu, R, Li, D, Hair, M. L., and Neumann, A. W. “Study of the advancing and receding contact angles: liquid sorption as a cause of contact angle hysteresis”. eng. In: *Advances in colloid and interface science* 96.1-3 (Feb. 2002). PMID: 11911113, pp. 169–191.

[149] Landau, L. and Levich, B. “Dragging of a liquid by a moving plate”. In: *Acta Physicochim. URSS*. 17 (1942), pp. 42–54.

[150] Landau, L. FLUID MECHANICS. 2. ed., repr. with corr. Amsterdam [u.a]: Elsevier [u.a.], 2007.

[151] Laplace, P. “Theory of capillary attraction”. In: *Supplements to the 10th book of Celestial Mechanics* (1807).

[152] Larouche, S. and Martinu, L. "OpenFilters: open-source software for the design, optimization, and synthesis of optical filters". In: *Applied Optics* 47 (Jan. 2008), p. C219.

[153] Larson, D. T., Lott, L. A., and Cash, D. L. "Surface Film Thickness Determination by Reflectance Measurements". In: *Applied Optics* 12.6 (June 1973), p. 1271.

[154] Leach, R. K. OPTICAL MEASUREMENT OF SURFACE TOPOGRAPHY. English. Berlin; Heidelberg: Springer, 2011.

[155] Lécuyer, H., Mmbaga, J., Hayes, R., Bertrand, F., and Tanguy, P. "Modelling of forward roll coating flows with a deformable roll: Application to non-Newtonian industrial coating formulations". In: *Computers & Chemical Engineering* 33.9 (Sept. 2009), pp. 1427–1437.

[156] Lee, H., Kim, A., Cho, S. M., and Chae, H. "Characterization of thermal annealing of gravure printed PVK/Ir(ppy)3 organic light emitting layers". In: *Current Applied Physics* 10.4 (Nov. 2010), e143–e146.

[157] Lee, J, Mun, K, and Yoo, Y. "A comparative study on roll-to-roll gravure printing on PET and BOPP webs with aqueous ink". In: *Progress in Organic Coatings* 64.1 (Jan. 2009), pp. 98–108.

[158] Lee, J. H., Han, S. K., Lee, J. S., Jung, H. W., and Hyun, J. C. "Ribbing instability in rigid and deformable forward roll coating flows". In: *Korea-Australia Rheology Journal* 22.1 (2010), pp. 75–80.

[159] Lee, S. and Na, Y. "Analysis on the ink transfer mechanism in R2R application". In: *Journal of Mechanical Science and Technology* 24.1 (Mar. 2010), pp. 293–296.

[160] Lee, S. and Na, Y. "Effect of roll patterns on the Ink transfer in R2R printing process". In: *International Journal of Precision Engineering and Manufacturing* 10.5 (Jan. 2010), pp. 123–130.

[161] Lindner, A., Bonn, D., Ben Amar, M., Meunier, J., and Kellay, H. "Controlling Viscous Fingering". In: *Europhysics News* 30.3 (July 1999), pp. 77–78.

[162] Lindner, A., Coussot, P., and Bonn, D. "Viscous Fingering in a Yield Stress Fluid". In: *Physical Review Letters* 85.2 (July 2000), pp. 314–317.

[163] Lukac, R. and Plataniotis, K. "Color filter arrays: design and performance analysis". In: *IEEE Transactions on Consumer Electronics* 51.4 (Nov. 2005), pp. 1260–1267.

[164] Lummer, O. "Die „Interferenzkurven gleicher Neigung" im polarisierten Lichte". In: *Annalen der Physik* 327.1 (1906), pp. 49–63.

[165] Macleod, H. THIN-FILM OPTICAL FILTERS. 4th ed. Boca Raton FL: CRC,Press/Taylor & Francis, 2010.

[166] Macosko, C. W. RHEOLOGY: PRINCIPLES, MEASUREMENTS, AND APPLICATIONS. English. New York: John Wiley & Sons, Inc., 1994.

[167] Magnan, P. "Detection of visible photons in CCD and CMOS: A comparative view". In: *Nuclear Instruments and Methods in Physics Research Section A: Accelerators, Spectrometers, Detectors and Associated Equipment* 504.1-3 (May 2003), pp. 199–212.

[168] Maher, J. "Development of Viscous Fingering Patterns". In: *Physical Review Letters* 54.14 (Apr. 1985), pp. 1498–1501.

[169] Maleki, M., Reyssat, M., Restagno, F., Quéré, D., and Clanet, C. "Landau–Levich menisci". In: *Journal of Colloid and Interface Science* 354.1 (Feb. 2011), pp. 359–363.

[170] Manoharan, V. N. "Frontiers of Engineering: Reports on Leading-Edge Engineering from the 2009 Symposium". In: vol. p. 5-12. The National Academies Press, 2010.

[171] Mantz, H., Jacobs, K., and Mecke, K. "Utilizing Minkowski functionals for image analysis: a marching square algorithm". In: *Journal of Statistical Mechanics: Theory and Experiment* 2008.12 (Dec. 2008), P12015.

[172] Manukyan, S. "Fundamental Investigation of Forced Wetting on Structured Surfaces". URN: tuda-tuprints-34097. Ph.D. Thesis. Darmstadt: TU Darmstadt, 2013.

[173] Marangoni, C. "Study on surface tension of fluid". In: *Ann Phys Chem* 143 (1871), pp. 337–354.

[174] Mark, H. ENCYCLOPEDIA OF POLYMER SCIENCE AND TECHNOLOGY. Concise 3rd ed. Hoboken N.J.: Wiley-Interscience, 2007.

[175] Matney, J. E., Parker, B. C., Neck, D. W., Henkelmann, G., and Rosen, I. I. "Evaluation of a commercial flatbed document scanner and radiographic film scanner for radiochromic EBT film dosimetry". In: *Journal of applied clinical medical physics / American College of Medical Physics* 11.2 (2010). PMID: 20592699, p. 3165.

[176] Maxwell, J. C. "A Dynamical Theory of the Electromagnetic Field". In: *Philosophical Transactions of the Royal Society of London* 155 (Jan. 1865). ArticleType: research-article / Full publication date: 1865 /, pp. 459–512.

[177] McKinley, G. H. "Dimensionless groups for understanding free surface flows of complex fluids". In: *Soc. Rheol. Bull* 2005 (2005), pp. 6–9.

[178] Mecke, K. R. "Additivity, Convexity, and Beyond: Applications of Minkowski Functionals in Statistical Physics". In: *Statistical Physics and Spatial Statistics. The Art of Analyzing and Modeling Spatial Structures and Pattern Formation*. Ed. by Mecke, K. R. and Stoyan, D. Vol. 554. Lecture Notes in Physics, Berlin Springer Verlag. 2000, p. 111.

[179] Michels, J. J., Winter, S. H. de, and Symonds, L. H. "Process optimization of gravure printed light-emitting polymer layers by a neural network approach". In: *Organic Electronics* 10.8 (Dec. 2009), pp. 1495–1504.

[180] Michelson, A. A. STUDIES IN OPTICS. Chicago, USA: University of Chicago Press, 1927.

[181] Mora, S. and Manna, M. "Saffman-Taylor instability for generalized Newtonian fluids". In: *Physical Review E* 80.1 (July 2009).

[182] Müllen, K, Scherf, U., and John Wiley & Sons. ORGANIC LIGHT EMITTING DEVICES SYNTHESIS, PROPERTIES AND APPLICATIONS. English. Weinheim: Wiley-VCH, 2006.

[183] Murakami, T., Ono, S., Tamura, M., and Kurata, M. "On the Theory of Surface Tension of Regular Solution". In: *Journal of the Physical Society of Japan* 6.5 (May 1951), pp. 309–312.

[184] Myers, T. G. "Thin Films with High Surface Tension". In: *SIAM Review* 40.3 (1998), p. 441.

[185] Nakayama, T. and Motogami, S. "A finite element approach to the numerical computation of viscous fingering phenomena". In: *Fluid Dynamics Research* 22.2 (Feb. 1998), pp. 73–87.

[186] *Nanocalc NC-10 software, Ocean Optics, Germany.*

[187] Neff, J. E. "Investigation of the Effects of Process Parameters on Performance of Gravure Printed ITO on Flexible Substrates". Master Thesis. Atlanta, GA: Georgia Institute of Technology, 2009.

[188] Newton, I. and Motte, A. NEWTON'S PRINCIPIA: THE MATHEMATICAL PRINCIPLES OF NATURAL PHILOSOPHY (1846). Kessinger Publishing, 2010.

[189] Ollech, B. TIEFDRUCK: GRUNDLAGEN UND VERFAHRENSSCHRITTE DER MODERNEN TIEFDRUCKTECHNIK. German. Frankfurt/Main: Polygraph Verl., 1999.

[190] Ondarçuhu, T. and Piednoir, A. "Pinning of a Contact Line on Nanometric Steps during the Dewetting of a Terraced Substrate". In: *Nano Letters* 5.9 (Sept. 2005), pp. 1744–1750.

[191] *OpenFOAM®, User Guide, Version 2.1.0*.

[192] Orchard, S. "On surface levelling in viscous liquids and gels". In: *Applied Scientific Research* 11.4 (1963). 10.1007/BF03184629, pp. 451–464.

[193] Oron, A. and Bankoff, S. G. "Long-scale evolution of thin liquid films". In: *Reviews of Modern Physics* 69.3 (July 1997), pp. 931–980.

[194] Owens, D. K. and Wendt, R. C. "Estimation of the surface free energy of polymers". In: *Journal of Applied Polymer Science* 13.8 (Aug. 1969), pp. 1741–1747.

[195] Parisio, F., Moraes, F., Miranda, J., and Widom, M. "Saffman-Taylor problem on a sphere". In: *Physical Review E* 63.3 (Feb. 2001).

[196] Patel, R. and Benkreira, H. "Gravure roll coating of newtonian liquids". In: *Chemical Engineering Science* 46.3 (Jan. 1991), pp. 751–756.

[197] Pearson, J. R. A. "The instability of uniform viscous flow under rollers and spreaders". In: *Journal of Fluid Mechanics* 7.04 (1960), p. 481.

[198] Pedrini, G., Fröning, P., Fessler, H., and Tiziani, H. J. "In-Line Digital Holographic Interferometry". In: *Applied Optics* 37.26 (Sept. 1998), p. 6262.

[199] Peli, E. "Contrast in complex images". In: *Journal of the Optical Society of America. A, Optics and image science* 7.10 (Oct. 1990). PMID: 2231113, pp. 2032–2040.

[200] Petrie, C. J. "Extensional viscosity: A critical discussion". In: *Journal of Non-Newtonian Fluid Mechanics* 137.1-3 (Aug. 2006), pp. 15–23.

[201] *PLu neox 3D Optical Profiler user manual*. Sensofar-Tech, S.L. Terrassa, Spain, 2002.

[202] Pranckh, F. R. and Scriven, L. E. "The physics of blade coating of a deformable substrate". In: *Tappi Journal* 73.1 (1990), pp. 163–1.

[203] Press, W. H. NUMERICAL RECIPES 3RD EDITION: THE ART OF SCIENTIFIC COMPUTING. Cambridge university press, 2007.

[204] Probstein, R. PHYSICOCHEMICAL HYDRODYNAMICS: AN INTRODUCTION. 2nd ed., [pbk. ed.]. Hoboken N.J.: Wiley-Interscience, 2003.

[205] Quate, C. "The AFM as a tool for surface imaging". In: *Surface Science* 299-300 (Jan. 1994), pp. 980–995.

[206] Quintans Carou, J., Wilson, S. K., Mottram, N. J., and Duffy, B. R. "Asymptotic and numerical analysis of a simple model for blade coating". In: *Journal of Engineering Mathematics* 63.2-4 (Apr. 2008), pp. 155–176.

[207] Rabaud, M., Michalland, S., and Couder, Y. "Dynamical regimes of directional viscous fingering: Spatiotemporal chaos and wave propagation". In: *Physical Review Letters* 64.2 (Jan. 1990), pp. 184–187.

[208] Raman, C. V. and Rajagopalan, V. S. "L. Haidinger's rings in non-uniform plates". In: *Philosophical Magazine* 29.196 (1940), pp. 508–514.

[209] Ramdane, O. O. and Quéré, D. "Thickening Factor in Marangoni Coating". In: *Langmuir* 13.11 (May 1997), pp. 2911–2916.

[210] Ramiasa, M., Ralston, J., Fetzer, R., and Sedev, R. "The influence of topography on dynamic wetting". In: *Advances in Colloid and Interface Science* (May 2013).

[211] Reddy, A., Narakathu, B., Atashbar, M., Rebros, M., Rebrosova, E., and Joyce, M. "Fully Printed Flexible Humidity Sensor". In: *Procedia Engineering* 25 (Jan. 2011), pp. 120–123.

[212] Reiter, G. "Unstable thin polymer films: rupture and dewetting processes". In: *Langmuir* 9.5 (May 1993), pp. 1344–1351.

[213] Riseman, J. and Ullman, R. "The Concentration Dependence of the Viscosity of Solutions of Macromolecules". In: *The Journal of Chemical Physics* 19.5 (1951), p. 578.

[214] Ritzoulis, G., Papadopoulos, N., and Jannakoudakis, D. "Densities, viscosities, and dielectric constants of acetonitrile + toluene at 15, 25, and 35 .degree.C". In: *Journal of Chemical & Engineering Data* 31.2 (Apr. 1986), pp. 146–148.

[215] Roddaro, S., Pingue, P., Piazza, V., Pellegrini, V., and Beltram, F. "The Optical Visibility of Graphene: Interference Colors of Ultrathin Graphite on SiO_2". In: *Nano Letters* 7.9 (Sept. 2007), pp. 2707–2710.

[216] Römpp, H., Falbe, J., and Regitz, M. RÖMPP-CHEMIE-LEXIKON. Thieme, 1992.

[217] Rong, X. and Pekarovicova, A. "The Study of Missing Dots of Electromechanical and Laser-Engraved Cylinders". In: *Proc. Taga*. Technical Association of the Graphic Arts, Rochester NY, 2007, pp. 596–604.

[218] Ruckenstein, E. and Jain, R. K. "Spontaneous rupture of thin liquid films". In: *Journal of the Chemical Society, Faraday Transactions 2* 70 (1974), p. 132.

[219] Sachs, W. and Meyn, V. "Pressure and temperature dependence of the surface tension in the system natural gas/water principles of investigation and the first precise experimental data for pure methane/water at 25°C up to 46.8 MPa". In: *Colloids and Surfaces A: Physicochemical and Engineering Aspects* 94.2-3 (Jan. 1995), pp. 291–301.

[220] Saffman, P. G. and Taylor, G. "The Penetration of a Fluid into a Porous Medium or Hele-Shaw Cell Containing a More Viscous Liquid". In: *Proceedings of the Royal Society A: Mathematical, Physical and Engineering Sciences* 245.1242 (June 1958), pp. 312–329.

[221] Saita, F. A. and Scriven, L. E. "Coating Flow Analysis and the Physics of Flexible Blade Coating". In: *Proceedings*. Atlanta, GA: Tappi Press, 1985, pp. 13–22.

[222] Sankaran, A. K. and Rothstein, J. P. "Effect of viscoelasticity on liquid transfer during gravure printing". In: *Journal of Non-Newtonian Fluid Mechanics* 175-176 (May 2012), pp. 64–75.

[223] Sauer, H. M., Bornemann, N., and Dörsam, E. "Viscous fingering in functional flexo printing: an inevitable bug ?" In: *Large-area, Organic and Printed Electronics Convention (LOPE-C)*. Frankfurt, Germany: OE-A (Organic and Printed Electronics Association), 2011.

[224] Schaffer, B., Mitterbauer, C., Pogantsch, S., Rentenberger, S., Zojer, E., Schertel, A., and Hofer, F. "TEM Investigations of Cross-Sectional Prepared Organic Light Emitting Devices". In: *Microscopy and Microanalysis*. Vol. 9 (Suppl. 03). Dresden, 2003, pp. 266–267.

[225] Schröder-Turk, G., Kapfer, S., Breidenbach, B., Beisbart, C., and Mecke, K. "Tensorial Minkowski functionals and anisotropy measures for planar patterns". In: *Journal of Microscopy* 238.1 (Apr. 2010), pp. 57–74.

[226] Schwartz, L. and DeGregoria, A. "Simulation of Hele-Shaw fingering with finite-capillary-number effects included". In: *Physical Review A* 35.1 (Jan. 1987), pp. 276–279.

[227] Schwartz, L. W., Weidner, D. E., and Eley, R. R. "An Analysis of the Effect of Surfactant on the Leveling Behavior of a Thin Liquid Coating Layer". In: *Langmuir* 11.10 (Oct. 1995), pp. 3690–3693.

[228] Schwartz, L. "Numerical modeling of liquid withdrawal from gravure cavities in coating operations; the effect of cell pattern". In: *Journal of Engineering Mathematics* 42 (Apr. 2002), 243–253(11).

[229] Schwartz, R. W, Voigt, J. A, Boyle, T. J, Christenson, T. A, and Buchheit, C. D. "Control of thin film processing behavior through precursor structural modifications". In: *Presented at the 19th Annual Conference on Advanced Ceramics, Materials and Structures, Cocoa Beach, FL, 9-12 Jan. 1995*. 1995, pp. 9–12.

[230] Seemann, R., Herminghaus, S., and Jacobs, K. "Dewetting Patterns and Molecular Forces: A Reconciliation". In: *Physical Review Letters* 86.24 (June 2001), pp. 5534–5537.

[231] Seemann, R., Herminghaus, S., and Jacobs, K. "Gaining control of pattern formation of dewetting liquid films". In: *Journal of Physics: Condensed Matter* 13.21 (2001), p. 4925.

[232] Seiwert, J., Clanet, C., and Quéré, D. "Coating of a textured solid". In: *Journal of Fluid Mechanics* 669 (Feb. 2011), pp. 55–63.

[233] Sidick, E. "Power spectral density specification and analysis of large optical surfaces". In: *Proc. SPIE 7390*. Ed. by Bosse, H., Bodermann, B., and Silver, R. M. Munich, Germany, June 2009, p. 12.

[234] Sorbie, K. "Linear viscous fingering: New experimental results, direct simulation and the evaluation of averaged models". In: *Chemical Engineering Science* 50.4 (Feb. 1995), pp. 601–616.

[235] SPRINGER HANDBOOK OF EXPERIMENTAL FLUID MECHANICS. Berlin: Springer, 2007.

[236] Stahl, S., Sauer, H. H., and Dörsam, E. "Investigation in the homogeneity of gravure printed polymer films for printed electronics". In: *Proceedings: 39th International Research Conference of Iariga*. Ljubljana, Slovenia, Sept. 2012.

[237] Stahl, S. "Einfluss der Druckform und der Fluidviskosität auf die Schichtdicke von im Tiefdruck hergestellten Funktionsschichten und deren Charakterisierung". URN: tuda-tuprints-35295. Ph.D. Thesis. Darmstadt: Technische Universität Darmstadt, 2013.

[238] Stauffer, C. E. "The Measurement of Surface Tension by the Pendant Drop Technique". In: *Journal of Physical Chemistry* 69.6 (June 1965), pp. 1933–1938.

[239] Stillwagon, L. E. and Larson, R. G. "Fundamentals of topographic substrate leveling". In: *Journal of Applied Physics* 63.11 (1988), p. 5251.

[240] Stout, K. DEVELOPMENT OF METHODS FOR THE CHARACTERISATION OF ROUGHNESS IN THREE DIMENSIONS. English. London: Penton Press, 1993.

[241] Tabeling, P., Zocchi, G., and Libchaber, A. "An experimental study of the Saffman-Taylor instability". In: *Journal of Fluid Mechanics* 177.-1 (Apr. 2006), p. 67.

[242] Takahashi, T., Koyama, Y., and Masaki, E. "Ink Transfer in Gravure Process". In: *Bulletin of the Technical Association of Graphic Arts of Japan* 10.1 (1968), pp. 25–38.

[243] Taylor, G. I. "Stability of a Viscous Liquid Contained between Two Rotating Cylinders". In: *Philosophical Transactions of the Royal Society A: Mathematical, Physical and Engineering Sciences* 223.605-615 (Jan. 1923), pp. 289–343.

[244] THE PRINTING INK MANUAL. 5th ed. London ; New York: Blueprint, 1993.

[245] Thiele, U. "Thin film evolution equations from (evaporating) dewetting liquid layers to epitaxial growth". In: *J. Phys.-Cond. Mat.* 22 (2010), p. 084019.

[246] Thiele, U., Vancea, I., Archer, A. J, Robbins, M. J, Frastia, L., Stannard, A., Pauliac-Vaujour, E., Martin, C. P, Blunt, M. O, and Moriarty, P. J. "Modelling approaches to the dewetting of evaporating thin films of nanoparticle suspensions". In: *J. Phys.-Cond. Mat.* 21 (2009), p. 264016.

[247] Thiele, U., Mertig, M., and Pompe, W. "Dewetting of an Evaporating Thin Liquid Film: Heterogeneous Nucleation and Surface Instability". In: *Phys. Rev. Lett.* 80.13 (1998), 2869–2872.

[248] Thieme, R. "Experimentelle Untersuchung der Farbübertragung in Anilox Kurzfarbwerken des wasserlosen Offsetdrucks". PhD Thesis, TU Chemnitz, Germany, in preparation.

[249] THIN FILMS ON GLASS. Schott series on glass and glass ceramics. Berlin ; New York: Springer, 1997.

[250] Thrasher, M. E. "Geometry and dynamics of fluid-fluid interfaces". Ph.D. Thesis. Austin, USA: University of Texas at Austin, 2007.

[251] Tone, R., Bornemann, N., Mechau, N., Al Helwi, M., Sauer, H. M., and Dörsam, E. "Impedance Spectroscopy as a Tool for the Detection of Mixed Layers in Solution Processed Semiconductors". In: *Large-area, Organic and Printed Electronics Convention (LOPE-C)*. Munich, Germany: OE-A (Organic and Printed Electronics Association), 2012, pp. 419–422.

[252] Trouton, F. T. "On the Coefficient of Viscous Traction and Its Relation to that of Viscosity". In: *Proceedings of the Royal Society of London. Series A* 77.519 (1906), pp. 426–440.

[253] Urban, P., Rosen, M. R., and Berns, R. S. "A Spatially Adaptive Wiener Filter for Reflectance Estimation". In: Portland, Oregon, 2008, p. 279–284.

[254] Varela López, F., Pauchard, L., Rosen, M., and Rabaud, M. "Non-Newtonian effects on ribbing instability threshold". In: *Journal of Non-Newtonian Fluid Mechanics* 103.2-3 (Mar. 2002), pp. 123–139.

[255] Velten, K. MATHEMATICAL MODELING AND SIMULATION: INTRODUCTION FOR SCIENTISTS AND ENGINEERS. Weinheim [Germany]: Wiley-VCH, 2009.

[256] Vlad, D. and Maher, J. "Tip-splitting instabilities in the channel Saffman-Taylor flow of constant viscosity elastic fluids". In: *Physical Review E* 61.5 (May 2000), pp. 5439–5444.

[257] Voss, C. "Analytische Modellierung, experimentelle Untersuchungen und dreidimensionale Gitter-Boltzmann Simulation der quasistatischen und instabilen Farbspaltung". Ph.D. Thesis. Wuppertal: University of Wuppertal, 2002.

[258] Vrij, A. “Possible mechanism for the spontaneous rupture of thin, free liquid films”. In: *Discussions of the Faraday Society* 42 (1966), p. 23.

[259] Welch, P. “The use of fast Fourier transform for the estimation of power spectra: A method based on time averaging over short, modified periodograms”. In: *IEEE Transactions on Audio and Electroacoustics* 15.2 (June 1967), pp. 70–73.

[260] Wenzel, R. N. “Resistance of solid surfaces to wetting by water”. In: *Industrial & Engineering Chemistry* 28.8 (Aug. 1936), pp. 988–994.

[261] White, F. FLUID MECHANICS. 4th ed. Boston ; Toronto: McGraw-Hill, 1999.

[262] Xie, R., Karim, A., Douglas, J., Han, C., and Weiss, R. “Spinodal Dewetting of Thin Polymer Films”. In: *Physical Review Letters* 81.6 (Aug. 1998), pp. 1251–1254.

[263] Xu, J., Xia, J., Hong, S. W., Lin, Z., Qiu, F., and Yang, Y. “Self-Assembly of Gradient Concentric Rings via Solvent Evaporation from a Capillary Bridge”. In: *Physical Review Letters* 96.6 (Feb. 2006).

[264] Yang, Y. H. and Abelson, J. “Spectroscopic ellipsometry of thin films on transparent substrates: A formalism for data interpretation”. In: *Journal of Vacuum Science & Technology A: Vacuum, Surfaces, and Films* 13.3 (May 1995), p. 1145.

[265] Yeh, C., Hung, C., Chang, T. C., Lin, H., and Lin, Y. “An immunoassay using antibody-gold nanoparticle conjugate, silver enhancement and flatbed scanner”. In: *Microfluidics and Nanofluidics* 6.1 (May 2008), pp. 85–91.

[266] Yin, X. and Kumar, S. “Lubrication flow between a cavity and a flexible wall”. In: *Physics of Fluids* 17.6 (2005), p. 063101.

[267] Young, T. “An Essay on the Cohesion of Fluids”. In: *Philosophical Transactions of the Royal Society of London (1776-1886)* 95.-1 (Jan. 1805), pp. 65–87.

[268] Yu, B., Chen, Y., Wang, W., Hsu, M., Tsai, S., Lin, W., Lin, Y., Jou, J., Chu, C., and Shyue, J. “Depth Profiling of Organic Films with X-ray Photoelectron Spectroscopy Using C60+ and Ar+ Co-Sputtering”. In: *Analytical Chemistry* 80.9 (May 2008), pp. 3412–3415.

[269] Zang, Y.-H. “A new approach for modelling ink transfer”. In: *Tappi Journal* 76.7 (1993), pp. 97–103.

[270] Zhan, Q. and Leger, J. R. “High-Resolution Imaging Ellipsometer”. In: *Applied Optics* 41.22 (Aug. 2002), p. 4443.

List of own publications

Journal articles

Bornemann, N. and Dörsam, E. "A flatbed scanner for large-area thickness determination of ultrathin layers in printed electronics". In: *Opt. Express* 21.19 (Sept. 2013), 21897–21911.

Bornemann, N., Sauer, H. M., and Dörsam, E. "Gravure Printed Ultrathin Layers of Small-Molecule Semiconductors on Glass". In: *Journal of Imaging Science and Technology* 55.4 (2011), p. 040201.

Hernandez-Sosa, G., Bornemann, N., Ringle, I., Agari, M., Dörsam, E., Mechau, N., and Lemmer, U. "Rheological and Drying Considerations for Uniformly Gravure-Printed Layers: Towards Large-Area Flexible Organic Light-Emitting Diodes". In: *Advanced Functional Materials* (Feb. 2013).

Patents

Bornemann, N., Neuroth, P., Urban, P., Sauer, H. M., and Dörsam, E. "Verfahren zur Ermittlung einer Schichtdicke". German Patent Application (DRN) 2013071815340800DE. July 18, 2013.

Conferences papers

Bornemann, N., Sauer, H. M., and Dörsam, E. "Evaluation and Determination of Gravure Cylinders for Functional Printing". In: *Large-area, Organic and Printed Electronics Convention (LOPE-C)*. Frankfurt, Germany: OE-A (Organic and Printed Electronics Association), pp. 309–313.

Bornemann, N., Sauer, H. M., and Dörsam, E. "Thin Film Behaviour after Ink Transfer in Printing Processes". In: *Large-area, Organic and Printed Electronics Convention (LOPE-C)*. 9.4. Frankfurt, Germany: OE-A (Organic and Printed Electronics Association), 2010, pp. 138 –142.

Bornemann, N., Guck, T., Bitsch, T., and Dörsam, E. "Determination of gravure cells using confocal microscopy". In: *Proceedings: 39th International Research Conference of Iariga*. Ljubljana, Slovenia, Sept. 2012.

Sauer, H. M., Bornemann, N., and Dörsam, E. "Viscous fingering in functional flexo printing: an inevitable bug ?" In: *Large-area, Organic and Printed Electronics Convention (LOPE-C)*. Frankfurt, Germany: OE-A (Organic and Printed Electronics Association), 2011.

Tone, R., Bornemann, N., Mechau, N., Al Helwi, M., Sauer, H. M., and Dörsam, E. "Impedance Spectroscopy as a Tool for the Detection of Mixed Layers in Solution Processed Semiconductors". In: *Large-area, Organic and Printed Electronics Convention (LOPE-C)*. Munich, Germany: OE-A (Organic and Printed Electronics Association), 2012, pp. 419–422.

Talks and posters

Bornemann, N. "Verhalten von dünnen Farbfilmen nach der Farbspaltung im Druckprozess". In: *Seminar vom Verein Deutscher Druckingenieure*. Talk. Darmstadt, Germany, 2010.

Bornemann, N. "Dewetting of printed ultra-thin layers of small-molecule semiconductors". In: *Symposium Funktionalisierung und Prozessierung dünner Schichten (Evonik Industries)*. Talk. Hanau, Germany, 2012.

Bornemann, N. "Dewetting Patterns of Gravure Printed Ultra-Thin Layers of Small Molecule Semiconductors". In: *8th Zsigmondy Kolloquium of the German Colloid Society*. Talk. Darmstadt, Germany, Mar. 2012.

Bornemann, N. "From Graphical to Functional Gravure Printing: A Discussion of Several Issues". In: *Forschungsvorträge zur gedruckten und organischen Elektronik am InnovationLab*. Talk. Heidelberg, Germany, Oct. 2012.

Bornemann, N., Sauer, H. M., and Dörsam, E. "Experimental Investigation of the Filling and Emptying of Gravure Cells". In: *Materials Science and Engineering Congress (MSE)*. Poster. Darmstadt, Germany, Sept. 2012.

Hernandez-Sosa, G., Bornemann, N., Ringle, I., Agari, M., Doersam, E., Mechau, N., and Lemmer, U. "Ink Properties Optimization for Gravure-printed Flexible Organic Light-emitting Diodes". In: *Symposium WW: Roll-to-Roll Processing of Electronics and Advanced Functionalities*. Talk. Boston, USA, Nov. 2012.

Hernandez-Sosa, G., Bornemann, N., Ringle, I., Agari, M., Doersam, E., Mechau, N., and Lemmer, U. "Ink Properties Optimization for Gravure-printed Flexible Organic Light-emitting Diodes". In: *Symposium WW: Roll-to-Roll Processing of Electronics and Advanced Functionalities*. Talk. Boston, USA, Nov. 2012.

Sauer, H. M., Bornemann, N., and Dörsam, E. "Drucken dünner organischer Funktionsschichten: Eine Herausforderung". In: *Workshop "Organische Dünne Schichten – Grundlagen und Anwendungen", Europäische Forschungsgesellschaft Dünne Schichten eV*. Talk. Dresden, Germany.